ABSTRACT

Title of dissertation: FUNDAMENTAL UNDERSTANDING OF HELICOPTER AEROMECHANICS ON MARS THROUGH CHAMBER TESTING AND HIGH-FIDELITY ANALYSIS

Daniel Escobar
Doctor of Philosophy, 2020

Dissertation directed by: Professor Anubhav Datta
Department of Aerospace Engineering

The fundamental aeromechanics of rotary-wing flight on Mars is explored. The exploration is based on chamber testing of Mars-like low Reynolds number rotors and the development of comprehensive analysis and comprehensive analysis coupled with computational fluid dynamics for systematic investigation of aeromechanical phenomena–critical for weights and packaging for Mars. The investigation includes rotor airloads, structural loads, and control loads, comparison of hingeless and articulated hubs, hover and forward flight, and the impact of fuselage aerodynamics. The coaxial configuration is the baseline platform for this work.

The use of a helicopter on Mars would dramatically increase the speed, range, and coverage of exploration by providing access to caves, craters, over polar ice, along icy scarps and recurring slope lineae that are just plain inaccessible or too dangerous for rovers. Many factors go into the design of a Mars helicopter from launch/entry loads to power to controls to packaging. Aeromechanics is only one factor, but the principal factor for efficient and effective flight that impacts everything else. This work is focused on this principal factor.

Current knowledge extrapolated from Earth would allow for short hops into the Mars atmosphere. Deeper understanding of Martian aeromechanics is needed to design larger more capable aircraft. Accurate predictions are needed for performance, blade loads, control loads, and blade strike behavior. True high-fidelity is needed for unlike on Earth decades of data sets do not exist on Mars. In fact there is not even a single data set. Thus clever and innovative means of verification and validation must be found. The objective of this thesis is to carry out all of these tasks.

The key conclusions are: (1) the design of aircraft, hub, blades, and controls are substantially different on Mars because of its unique aeromechanics, (2) an articulated hub can in fact have lesser danger of blade strike, (2) a hingeless hub can experience lower or only marginally higher $(6-7\%)$ flap bending moments, (3) control / pitch link loads are dramatically impacted more by choice of Mars airfoils than rotor hubs, (4) lifting-line analysis does not even begin to capture the precise magnitudes of blade passage impulsive loads, and (5) fuselage aerodynamics is irrelevant in preliminary design. These, and other interesting phenomena will be the topics of this dissertation.

FUNDAMENTAL UNDERSTANDING OF HELICOPTER AEROMECHANICS ON MARS THROUGH CHAMBER TESTING AND HIGH-FIDELITY ANALYSIS

by

Daniel Fernando Escobar

Dissertation submitted to the Faculty of the Graduate School of the
University of Maryland, College Park in partial fulfillment
of the requirements for the degree of
Doctor of Philosophy
2020

Advisory Committee:
Professor Anubhav Datta, Chair/Advisor
Professor Inderjit Chopra
Professor James Baeder
Professor Christine Hartzell
Professor Nikhil Chopra

Dedication

To my family for their love and encouragement

Acknowledgments

This work, like my entire academic career, has been a collaborative effort. I could have never reached this point without the help, support and advice of all my professors, colleagues, friends, and family. I would first like to thank my PhD advisor, Dr. Anubhav Datta, for all the help, advice, and mentorship throughout my PhD career. He gave me the opportunity to work on an amazing project and the exciting research in this thesis. His commitment everyday to mentor and grow his students is invaluable. He is a wonderful advisor and mentor. Thank you. I would also like to thank my other committee members Dr. Inderjit Chopra, Dr. James Baeder, Dr. Christine Hartzell, and Dr. Nikhil Chopra for their advice, expertise, and contributions throughout my graduate school career. Their feed back has been extremely helpful in the formulation of this thesis. Dr. VT Nagaraj is also owed many thanks. He has taught me countless lessons during Helicopter Design and the hundreds of visits to his office.

During the course of my PhD, I have been lucky enough to enjoy two internship experiences. I would like to thank the US Army Aviation Development Directorate and especially Dr. Roger Strawn, and Dr. Beatrice Roget for their advice and mentorship. I thoroughly enjoyed my summer learning and growing my skill set. I look forward to working with them again. I would also like to thank everyone I worked with at JPL. Because the project was outside my field of expertise, I was continuously learning and enjoyed the opportunity to understand the Mars Helicopter project from a different point of view. I would like to thank Teddy Tzanetos, Gene Merewether, and Gerik Kubiak for all their help, patience, and advice.

I would not have received the education I did without the many senior students who took the time to help me. Ananth Sridharan, Bharath Govindarajan, and Vikram Hrishikeshavan were always available teach me something new or the same thing they taught me the week before. I will always be thankful for their help and

advice. Thank you to Elena Shrestha and James Lankford for showing me the ropes of the MAV lab. Thanks to Elizabeth Ward for showing me all the fun you can have being VFS chapter president. I would also like to thank all of the friends I have made over the years here at Maryland who made this adventure as enjoyable as it was educational. I will miss all my cube farm friends for all the conversations (some were productive).

Thank you to all the friends I have made through research and other activities. We may have never won an intramural championship but it was definitely fun and the reprieve from research helped with my sanity. I enjoyed every game. I will never forget all the fond memories of going to Deep Creeks, camping, going out in DC or just hanging out. I would especially like to thank Bharath, Dylan, Tyler, and Brandyn. These friendships forged over sleepless nights in the cube farm or lab are irreplaceable and create a wonderful support network.

I would like to acknowledge my whole family, who have been a wonderful source of love and support throughout my academic career. Mom, Dad, David, and Cristina have always been there for me with a loving smile and positive energy. I look forward to spending full vacations together and being able to visit my siblings who live only a short car ride away. My parents are my role models. Their endless encouragement, understanding, and love have made this whole endeavor possible. Having my family's support means the world to me and I not could imagine being here without it.

Finally, I would like to express my enduring gratitude to Michelle. Michelle has been a simply wonderful girlfriend over the past three years. Patiently helping me through late nights and constantly sliding deadlines. I know spending the weekend in the lab is not ideal, but I thank her for understanding. I cannot properly express how much I appreciate all the support, care, and love, and how it has helped in achieving my dreams. I would not have achieved any of this without her. I also appreciate all her patience with my antics.

Table of Contents

List of Tables

List of Figures

List of Abbreviations

ADD	(US Army) Aviation Development Directorate
AHS	American Helicopter Society (now re-named VFS)
AMR	Adaptive mesh refinement
ARES	Aerial Regional-scale Environmental Survey
AV	Air vehicles
BEMT	Blade element momentum theory
CA	Comprehensive Analysis
CFD	Computational Fluid Dynamics
CFL	Courant–Friedrichs–Lewy (number)
CSD	Computational Structural Dynamics
CREATE	Computational Research and Engineering Acquisition Tools and Environments
DADI	Diagonalized Alternating Direction Implicit (preconditioner)
DoD	(US) Department of Defense
FEA	Finite element analysis
FEM	Finite element method
FM	Figure of Merit
Garfield	GPU-Accelerated Rotor Flow Field (solver)
GPS	Global Positioning System
GPU	Graphics Processing Unit
JPL	Jet Propulsion Laboratory
MABVAP	Mars Balloon Validation Program
MARCC	Maryland Advanced Research Computing Center
MARV	Mars Autonomous Rotory-wing Vehicle
MAV	Micro-aerial vehicle
MH	Mars Helicopter
MUSCL	Monotone Upstream-centered Scheme for Conservation Laws
NACA	National Advisory Committee for Aeronautics
NASA	National Aeronautics and Space Administration
PAN	Polyacrylonitrile
PPSF	Polyphenylsulfone
RANS	Reynolds-Averaged Navier–Stokes
RCAS	Rotorcraft Comprehensive Analysis System
RPM	Revolutions per minute
SMR	Single Main Rotor
SA	Spalart–Allmaras
TURNS2D	Transonic Unsteady Rotor Navier-Stokes 2D
UMARC	University of Maryland Advanced Rotorcraft Code
UMD	University of Maryland

UTA	University of Texas at Austin
VTOL	Vertical take-off and landing
VFS	Vertical Flight Society (formerly called AHS)
X3D	Experimental 3D Dynamic solver

Chapter 1: Introduction

1.1 Motivation

Rotary-wing aircraft are viewed as a natural progression of ground-based rovers providing greater access and deeper coverage of the Martian terrain in preparation of eventual human exploration. They are also envisioned to assist the rover or the astronaut of the future, to interrogate targets of interest that are otherwise inaccessible. Thus, Martian aeromechanics can become an important discipline in the future. The objective is to lay the ground work for that discipline.

A coaxial configuration is used as the basis of investigation. It is an important configuration, viewed historically as one of the most compact yet offering the best power-loading in the thin Martian air. It is an interesting configuration, deemed critical to in-depth understanding of rotors as well as intricate validation of high-fidelity tools. It is also the most relevant configuration, selected presently for the first Mars Helicopter on board Mars 2020.

The objective of the current research is to build a fundamental understanding of rotorcraft aeromechanics on Mars. Aeromechanics is the study of flexible aircraft in equilibrium flight; it includes structural dynamics, aerodynamics, stability and control; in a rotorcraft these disciplines are intimately coupled.

The NASA Mars 2020 mission will be launched aboard an Atlas V rocket in July 2020, and will land on Mars in February 2021. The rocket will be carrying *Perseverance*, a 2315 lb (1050 kg) rover. Tucked into the rover, attached to its

underbelly, will be *Ingenuity*, the 4.0 lb (1.8 kg) Mars Helicopter. The helicopter will attempt 5 flights over a 30 day period with a maximum endurance of 90 seconds. A culmination of nearly three decades of work, the Mars Helicopter marks the first attempt at extraterrestrial flight by humankind.

Many recent advances in vertical take-off and landing (VTOL) and micro-aerial vehicle (MAV) technology have primed aerial exploration of Mars with rotary-wing flight. Greater understanding of low Reynolds number aerodynamics, light-weight composite structures, robust and reliable micro electronics, compact power, and autonomous control have made the feasibility of flying on Mars real. If successful, the horizons of planetory science will only expand and countless possibilities opened for future missions, with larger aircraft with longer flights, greater range, and increased payload.

Exploration of Mars began in the 1960s. The first missions consisted of flybys, and hard (impact) landers. Over time, these missions progressed to orbiters and soft landers. As the success rate of soft landings improved, landers grew in size and capability. Eventually the first wheeled vehicle landed on Mars in July 1997; the mobile rover *Sojourner* was a small 23 lb demonstrator deployed from the larger *Pathfinder* lander (1973 lbs). In January 2004, two rovers *Spirit* and *Opportunity* landed on either side of Mars with greater mobility than *Sojourner*. In 2012, the most recent of the rovers, *Curiosity* (1982 lb), landed on Mars. It has since provided countless scientific discoveries, traveled a distance of 13.5 miles, and remains operational (as of July 9, 2020). Today, rovers can conduct science investigations independently of a lander.

Over the two decades spent on the planet, the Mars rovers have collectively covered less than 50 miles. The terrain explored was relatively smooth, flat, and open, without any potentially dangerous locales such as cliffs, gullies, caves, or slopes, as seen for example in Figure 1.1. Using a rotorcraft would increase the scope and range

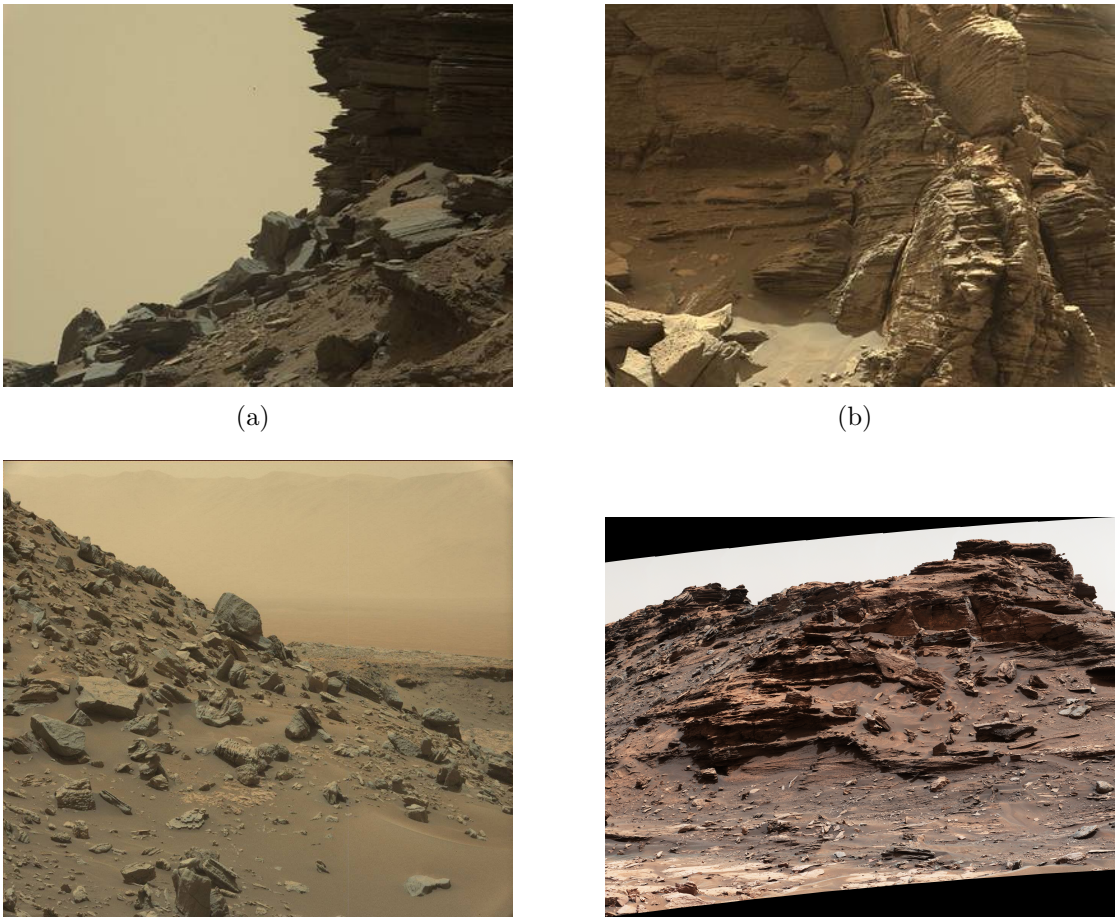

(a) (b)

(c) (d)

Figure 1.1: Inaccessible Martian terrain from *Curiosity* rover.

of possible exploration. These may vary from a small aircraft acting as a scout for a rover to a larger aircraft that can conduct science investigations independently of a rover. As a scout, aerial mapping could identify treacherous terrain too dangerous for the rover, speeding up travel. As a science platform, it can provide access to potentially dangerous locales that are currently inaccessible. Aerial explorers with hover and low speed flight capability provide better view than rovers and better resolution than orbiters.

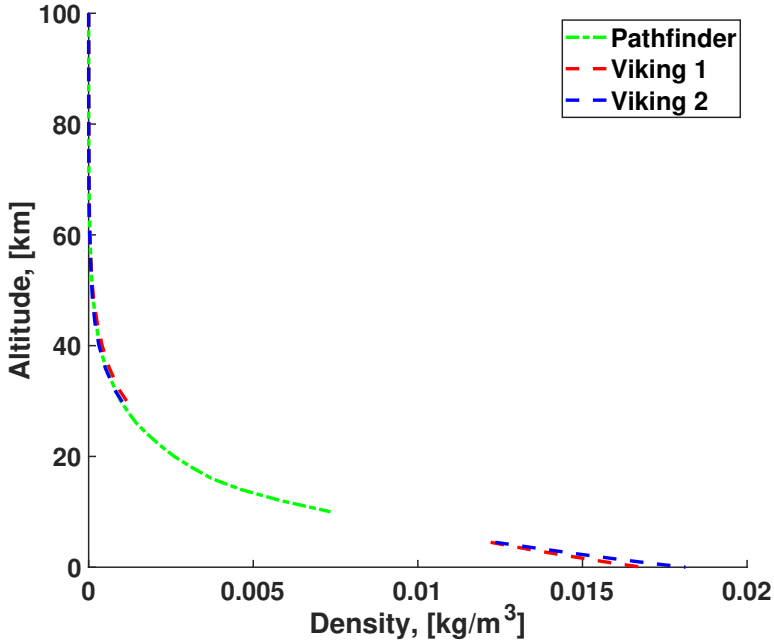

Figure 1.2: Atmospheric density versus altitude from past Mars missions collected during entry and descent (from Seiff and Kirk 1977).

1.1.1 Unique Conditions

The Martian environment presents a unique set of aeronautical challenges. Much is now known from past missions [1, 2]. For example, Figure 1.2 shows atmospheric density versus altitude. Table 1.1 summarizes the conditions on Earth and Mars. On Mars, the thin carbon dioxide atmosphere, with a density of only–1.26% of Earth yet a speed of sound 67% of Earth, can immerse the rotors in a simultaneously very low Reynolds number ($< 10,000$), and relatively high Mach number (> 0.6). Hence the flow is influenced by both viscous and compressibility effects. Due to the poor aerodynamic performance associated with such flows, optimizing both weight and performance are crucial for sustained flight with a meaningful payload. The thin atmosphere also means that there is little convective cooling for the motor or batteries during flight. At night, on the other hand, considerable energy must be spent to keep the aircraft warm.

Table 1.1: Comparison of atmospheric conditions on Earth and Mars.

Properties	Earth	Mars	Ratio
Gravity, (g) m/s^2	9.81	3.71	38%
Density, (ρ) kg/m^3	1.2285	0.0155	1.26%
Temperature, K	288.16	210.56	73%
Viscosity, (μ) kg/ms	$1.983e-05$	$1.422e-5$	72%
Adiabatic Coefficient (γ)	1.4	1.29	92%
Speed of Sound, m/s	343	230	67%

There are however several advantages on Mars. The gravitational acceleration is 38% of Earth, which reduces the lift requirement. The high rotational speeds prompted by low Reynolds numbers produce very low tip speed ratios (ratio of forward flight speed to tip speed). This is advantageous for gust tolerance and avoiding blade strike in a coaxial configuration. Flying on an uninhabited planet means that there are no restrictions on noise or concerns for operator safety so tip speeds can be designed for performance alone.

Because of all these factors, the aeromechanics on Mars quickly deviate from Earth. To counter low Reynolds numbers, the rotor must grow in size. With a significant payload to deliver and a premium on weight and packaging, a small, soft, and symmetric airframe is likely, which increases the danger of rotor-body frequency coalescence. High pitching and propeller moments on the rotor, from large chord and high rotation speeds produce high unsteady and steady control loads. Chordwise center of gravity offsets are likely if best airfoils (more like flat plates and less like airfoils) are used, which can increase oscillatory control loads further due to flap-torsion coupling. At a minimum, the very low density leads to very low Lock numbers. Lock number is the ratio of aerodynamic to inertial forces on the blade. Aerodynamic damping in flap motion taken for granted on Earth (typically up to 50% critical) disappears on Mars. However, low Lock number also has a beneficial impact on aeroelastic stability; many instabilities that are a serious concern on Earth disappear on Mars.

The lack of aerodynamic damping in flap will cause any natural oscillations to persist. A stiff hingeless hub will reduce the magnitude of these oscillations, but accrue more fatigue cycles and produce high hub moments. Hub moments are good for control but bad for weight. The high rotational speeds produce high cyclic stresses, which leads to a heavier rotor. The combination of a heavy rotor and a light airframe further aggravates the danger of rotor–fuselage coupling. An articulated hub would relieve the loads, but may require greater inter-rotor separation to allow larger flap angles, and generate smaller hub moments for controls. A flap hinge however might make it easier to fold and package inside the spacecraft. Thus dynamics and aerodynamics are closely intertwined, in ways that are unconventional, yet with critical impact on weights and packaging for an aircraft that must be sent packed for deployment 80 million miles away.

1.1.2 Technical Barriers

The principal barrier to designing an effective rotorcraft for Mars is the lack of any validated high-fidelity first principles analyses. Over the past 50 years high-fidelity analyses have been developed, validated, refined, and matured for applications on Earth. Wind tunnel and flight tests provided indispensable data for discovery and validation, but these findings are not applicable for Mars.

Modern tools and solution procedures have not been validated, refined, or matured for conditions on Mars. There is no experimental data on Mars. Thus there is limited understanding of the similarities and dissimilarities in aeromechanics and which analysis components can be kept and what must change. Deeper understanding is essential to design a larger more capable Mars helicopter.

Figure 1.3: Illustrator Chesley Bonestell's airplane concept based on the ideas of Wernher von Braun.

1.2 Concepts of Mars Aerial Exploration

Before the Mariner 4 lander (1964-1967), the density of the Martian atmosphere was believed to be much higher than it actually is ($\approx$ 10% versus 1% of Earth). Significant work went into large manned fixed wing aircraft on Mars as part of the first detailed Mars lander design. The lander was a half-cone lifting-body with winglets [3, 4]. The concept was inspired by Wernher von Braun's scientific book *The Mars Project* which included winged aircraft for landing humans on Mars.

With the new found understanding of the Mars atmosphere from *Mariner* (mainly density and CO_2 composition), smaller unmanned aircraft were proposed. In the late 1970s, Dale Reed designed and built the *Mini Sniffer* (Figure 1.4(a))

for exploring the upper atmosphere of Earth, but it was also considered for the exploration of Mars [5]. The aircraft had a 22 ft wingspan and was powered by a hydrazine engine. It was designed to reach altitudes of $70,000 - 100,000$ ft, but never flew higher than $20,000$ ft because of a hydrazine leak. More recently, in 2011, NASA Langley proposed the Aerial Regional-scale Environmental Survey (ARES) for the NASA Mars Scout Mission [6, 7]. The aircraft had a 20.5 ft wingspan and an undetermined engine but perhaps powered by a bi-propellant rocket engine. It was designed to be an aerially launched folding aircraft that would fly roughly 1.5 km above the surface with a range of around 600 km. The proposed mission would last one hour. Ultimately the Mars Atmosphere and Volatile Evolution (MAVEN) orbiter was selected instead. Other conceptual designs of fixed wing aircraft have been proposed, but never progressed beyond preliminary concepts [8–12]. Fixed wing aircraft face two significant challenges. They must maintain high speed, due to the thin atmosphere, which precludes true observation and surface interrogation capability. The uneven terrain makes any attempt at landing and take-off impractical.

Over the past several decades, there has also been efforts in exploring lighter-than-air balloons for Mars. They were capable of aerial deployment and inflation. The two approaches considered were: (1) helium superpressure balloons, and (2) solar Montgolfiere balloons. The superpressure balloons would fill up to a high pressure with lighter-than-ambient gas to generate lift. The Montgoftiere balloons would use heated Martian air to inflate and generate lift. In 1997, NASA Jet Propulsion Laboratory (JPL) initiated Mars Balloon Validation Program (MABVAP) to develop and validate the technology necessary for superpressure balloons on Mars [13, 14]. Feasibility studies progressed to stability, strength, and performance studies. Beyond analysis, multiple test campaigns were conducted. These included successful tests of a 40 ft diameter balloon on Earth at an altitude of $99,500$ ft–where density is similar to Mars–for 9.5 hours. Another important study was the Mars Geoscience Aerobot,

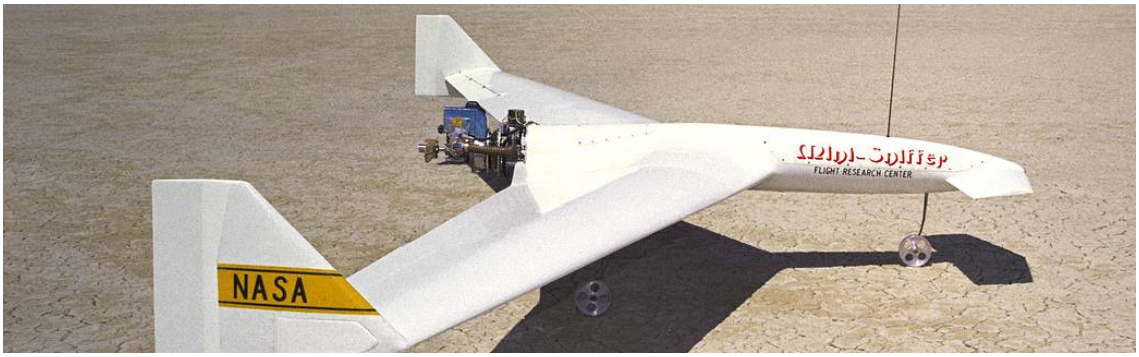

(a) Mini Sniffer airplane considered for use on Mars.

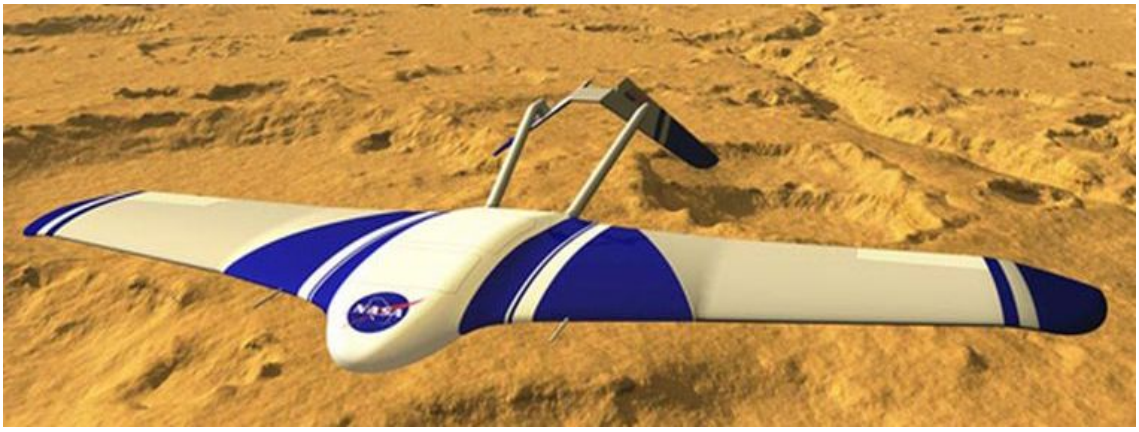

(b) Aerial Regional-scale Environmental Survey (ARES) concept aircraft for use on Mars.

Figure 1.4: Proposed fixed wing aircraft for Mars exploration.

which was a 90 ft diameter balloon, designed to float at 6.5 km above the surface for a 90 day mission that would have consisted of surface imaging and atmospheric science [15, 16]. A lighter-than-air aircraft are difficult to control and station keep and are at the mercy of gusts, winds, and changing atmospheric density.

1.3 The Case For Helicopters

A rotorcraft is the only aerial platform that is capable of hover and controlled low speed, low altitude flight with multiple take-offs and landings at needed. These capabilities open countless scout and science opportunities. It provides incomparable range, speed, and versatility over a rover. Multiple flights can be flown, each tailored to a specific scientific goal, increasing its tactical impact.

(a) Montgoftiere balloon concept for use on Mars.

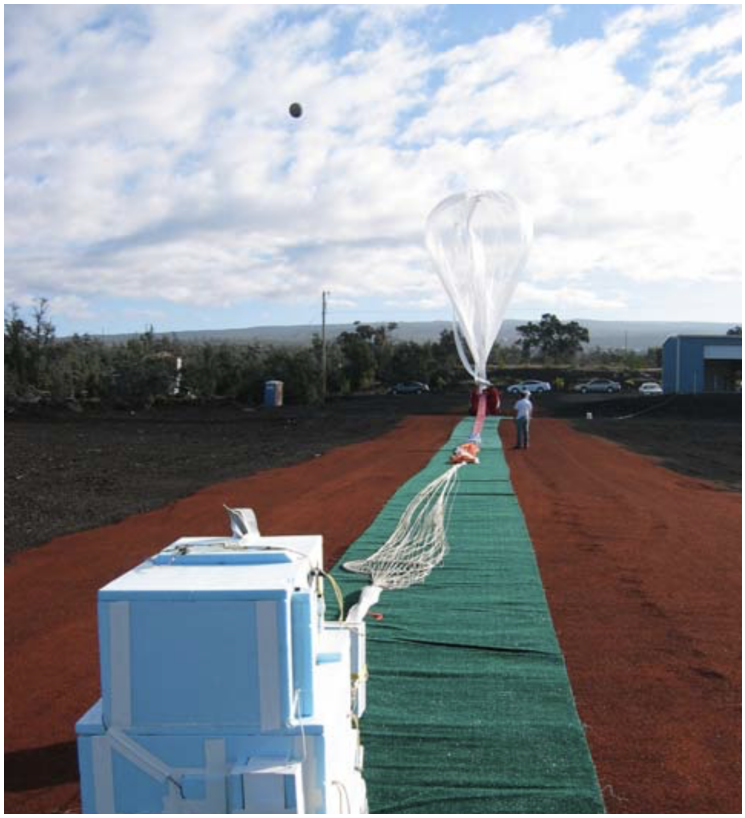

(b) NASA JPL MABVAP superpressure balloon concept for use on Mars (from Hall et al. 2009).

Figure 1.5: Proposed balloon aircraft for Mars exploration.

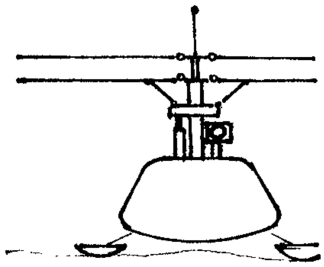

Figure 1.6: Savu and Trifu coaxial rotor concept (from Savu and Trifu 1995).

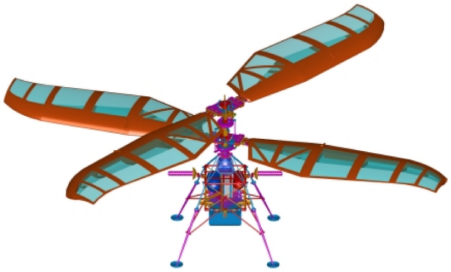

Figure 1.7: University of Maryland conceptual design of a Mars Autonomous Rotory-wing Vehicle (MARV) (from Datta et al. 2003).

A coaxial configuration is attractive because of its compact anti-torque, efficient hover, good gust tolerance, and attainment of relatively high blade Reynolds number within a fixed weight and volume. Single main rotors are lighter but require an extended tail boom with tail rotor for anti-torque which adds volume and packaging concerns. Multi-rotors have a higher empty weight fraction due to the structure and cannot in general achieve the same Reynolds number as a coaxial for a given volume.

The case for helicopters was never in doubt. The questions were whether it could be built to fly in the thin air, have sufficient structural integrity, have enough power, be packaged for journey, and unfold for deployment upon arrival.

1.4 Brief History of Mars Helicopters

The use of a helicopter was conceptually explored during the 1990s. Savu and Trifu [17] envisioned a coaxial helicopter powered by rotors with solar cells that

Figure 1.8: The NASA JPL-AeroVironment Mars Helicopter.

Figure 1.9: Notional research configuration used in present work.

would power a turbine engine (Figure 1.6). Based on momentum theory helicopters large (193 kg) and small (8.5 kg) were claimed as feasible.

Interest was renewed by the work of Young [18–21] at NASA Ames during 2000s. In 2000, the American Helicopter Society (now called Vertical Flight Society) annual student design competition called for a Mars aerial scout. It was sponsored by Sikorsky Aircraft and NASA Ames. The University of Maryland Martian Autonomous Rotary wing Vehicle (MARV) produced a 7 ft (2.13 m) radius 50 kg helicopter (Figure 1.7) with a 10.8 kg payload powered by a fuel cell [22]. The design established the merits of a 2-bladed counter-rotating coaxial helicopter for Martian flight and gave the method and basis for its design. Relying on the level of understanding of low Reynolds number rotors at the time and the fidelity of the available aeromechanics tools a coaxial rotor with two blades each was found to be the best configuration from the standpoint of energy, Reynolds number, payload weight fraction, and vehicle folding. A high solidity, twisted, and tapered rotor with a special-purpose high lift

Figure 1.10: Hover testing of baseline proof-of-concept Mars rotor in vacuum chamber at NASA Ames (from Young et al. 2002).

airfoil with gradual pressure recovery was found suitable for Mars. A stiff inplane teetering hub was chosen to eliminate ground resonance while reducing vibratory hub loads with a teetering flap hinge. The key elements of this work was documented subsequently in Ref [23].

In 2002, hover testing in the Ames Planetary Aeolian Laboratory vacuum chamber [21] on a 4 ft (1.219 m) radius single rotor (Figure 1.10) showed the desired thrust conditions were obtainable in the Martian conditions. A coaxial hover rig was also built but never reached testing.

Since then, greater understanding of low Reynolds number rotor aerodynamics has been gained through computational fluid dynamics (CFD) analysis [24] and small scale rotor and airfoil testing [25–27]. The CFD effort at the time lacked any validation data. An important conclusion from testing was that thin circular arc cambered plates provide optimal performance in the target Reynolds number

range [28]. Keeping the airfoil as thin as possible is best, and a sharp leading edge trips the laminar separation bubble and keeps the flow attached. More recently, research related to micro-air vehicles have produced deeper insights into low Reynolds number aerodynamics and how best to predict them [29–32]. These have generally revealed that thin cambered plates with sharp edges provide better performance than airfoils in the target Reynolds number range of a Mars helicopter.

On May 11-th, 2018, NASA announced the inclusion of a Mars Helicopter scout as part of the Mars 2020 mission. The vehicle is the result of a Jet Propulsion Laboratory (JPL) program that began around 2013. The Mars Helicopter developed by JPL/NASA and built by AeroVironment is a small 4.0 lb (1.8 kg) aircraft with a coaxial rotor with two blades each. The rotors are stiff inplane and out-of-plane with no hinges. The rotor diameter is 3.97 ft (1.21 m). The vehicle is designed for multiple short 90 sec flights. It is powered with a Li-ion battery charged from solar panels mounted on the top of the helicopter, above the rotors [33]. Development of engineering models and the final prototype included extensive testing in JPL Space Simulator Chamber. The chamber is 85 ft tall and 25 ft in diameter and capable of producing Mars atmospheric composition. With communication time between Earth and Mars being up to 22 minutes, true vehicle autonomy is essential. Most of the public domain documentation has focused on the guidance and control systems [34–36] developed through simulations based on system identification flights in the chamber.

Little to no information is available at present on the aeromechanics of the aircraft, such as rotor airloads, blade structural loads, or control system loads. Description of the rotor design and some structural analysis have begun to appear in the literature over the last couple of years [37, 38]. These focus on top level description of vehicle components, fabrication, and hardware testing. The components highlighted are the landing gear, swashplate, servos, motors, and some details on

(a)

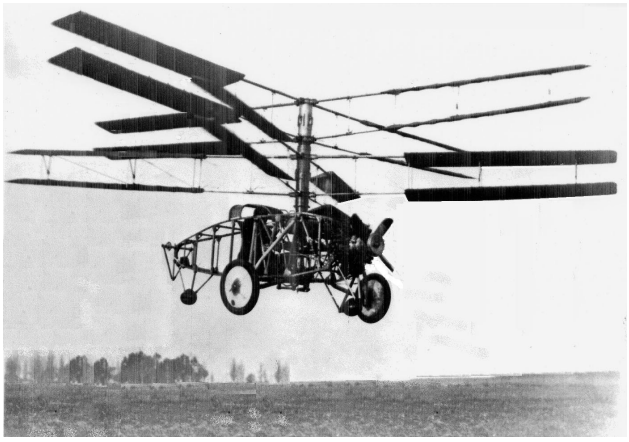

(b)

(c)

Figure 1.11: Early coaxial rotor designs.

blade fabrication and design philosophy.

1.5 The Lure of the Coaxial Rotor

The natural ability of a coaxial rotor to balance torque was obvious to even the earliest inventors. Mikhail Lomonosov's clock-spring driven device demonstrated to the Russian Academy of Sciences in 1754 and Launoy and Bienvenu's bow-string driven device demonstrated to the French Academy of Sciences in 1784 were both coaxial rotors. Indeed, the legendary model of Gustave de Ponton d'Amécourt

(France 1863), who coined the term helicopter, was a coaxial design (Figure 1.11(a)). Whereas these were ingenious toys and devices, the first controlled forward flight (but not hover) by Breguet and Dorand (France 1935) was a coaxial helicopter with two blades per rotor (Figure 1.11(c)). Even the first helicopter to demonstrate cyclic controls (Figure 1.11(b))—that is still the mainstay of all modern rotorcraft—was also a coaxial design by Raúl Pateras Pescara (France 1923). It is interesting that the first helicopter to ever attempt powered flight outside the Earth will also be a coaxial and also with two blades per rotor.

The aerodynamic advantages of a coaxial rotor (10% less induced power for same thrust compared to a single rotor) was gradually recognized over the next century. Not having to carry a tail rotor for counter-torque, made it compact. But the mechanical complication of having two rotors and its implication on structural weight meant it did not enter wide-spread production. Only Kamov mastered the art for a niche low speed naval application, with articulated blades that reduced loads at the rotor hub. During the 1970s, Sikorsky documented another advantage of the coaxial rotor, now at high speeds, and only realized with hingeless blades.

An authoritative review of the principal works on coaxial rotors in the last century (until 1997) is given by Coleman [39]. It categorized research and development by country of origin. The aerodynamic advantage of a coaxial counter-rotating rotor was clear in hover when compared to a single rotor with the same number of blades. Interference of flow around the two rotors had significant impact on wake geometry and convection. The impact of the upper rotor on the lower was identified as the most significant. Swirl recovery due to counter-rotation was only a secondary effect at best. At high tip speed ratios (flight speed divided by rotor tip speed), the interactions weaken as the upper rotor wake is washed clear of the lower rotor. The Coleman review highlighted the need to advance coaxial theoretical models in hopes of accurately capturing all interference effects, and recommended more experimental

studies to understand the impact of Reynolds number scaling.

1.6 Coaxial Rotor Experiments

Interest in hingeless coaxial rotors began with Sikorsky's high-speed advancing blade concept in the 1970s [40, 41]. Funded by US Army and NASA, the experimental XH-59A (Figure 1.12(a)) flight demonstration program carried out 106 hours of flight test until 1981[42, 43]. The goal of the Advancing Blade Concept (ABC) was to achieve high speeds with a coaxial rotor with hingeless blades. the hingeless blades carried hub moments deliberately (quantified as a lift-offset from the hub) to prevent loss of lift and propulsive force at high speed. The price to pay is a stronger and heavier hub. This approach is counter to the classical articulated approach that carried no moments but allowed large blade motions instead. The price to pay there was speed. At high speeds the rotor ran out of lift and propulsive force and blade flapping would produce blade strike. The well-documented test data from the XH-59A program form the basis for validation for all advanced analyses even today. The XH-59A program, while proving the basic viability of the concept, was compromised by many aerodynamic and structural dynamic factors, from heavy hub to high vibration which led to lower speeds than originally intended.

During the 2000s, Sikorsky revitalized the ABC rotor with the aim of fixing the compromises of the XH-59A. They carried out flight tests of the X2-Technology Demonstrator aircraft (Figure 1.12(b)) [44–47]. Subsequently, a larger coaxial system, the Sikorsky S-97 RAIDER (Figure 1.12(c)), was tested at the National Full-scale Aerodynamics Complex 40 by 80 ft wind-tunnel at Ames research center[48]. This test included the fuselage, fuselage and upper rotor, and fuselage and both rotors. However, unlike the XH-59A, the data and details in public domain are insufficient for validation of analysis tools.

In order to bridge this gap, several important model tests have been carried

(a) Sikorsky XH-59A flight demonstrator of the Advance Blade Concept (ABC) Rotor

(b) Sikorsky X2TD flight demonstrator

(c) Sikorsky S-97 RAIDER

Figure 1.12: High speed coaxial rotor designs.

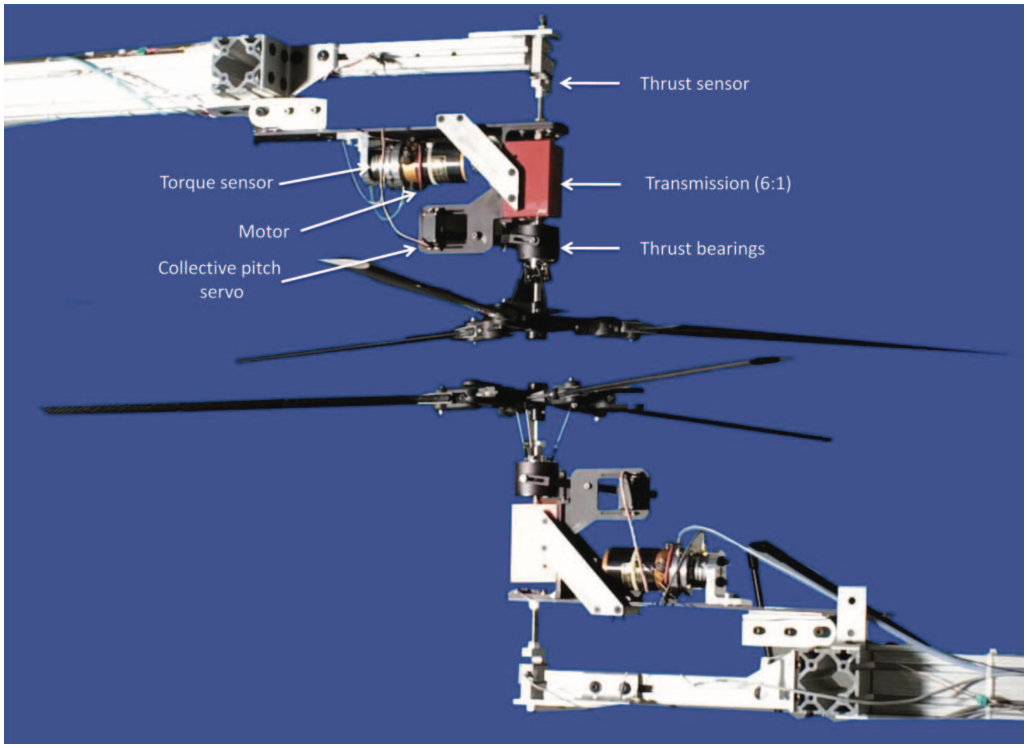

Figure 1.13: Ramasamy's coaxial test setup with independent rotors (from Ramasamy 2015).

out. These include hover tests by US Army/NASA at Ames by McAlister et al. [49], McAlister and Tung [50], and Ramasamy [51]. MacAlister's tests on model proprotor blades (highly twisted) documented comparisons with a single rotor, the effect of separation, and the impact of a ground plane. The data includes performance, and flow field measurements from particle image velocimetry (PIV). This provided greater insight into the contraction and convection of the coaxial wake. Ramasamy (Figure 1.13) tested both model proprotor blades and straight helicopter blades with NACA 0012 airfoils for a variety of twin rotor configurations—counter-rotating and co-rotating coaxial, and tandem. Sweeps of thrust and inter-rotor separation were carried out systematically. Coaxial rotors were compared with the individual rotors operating alone as well as with equivalent rotors with the same number of blades as the coaxial. These tests were all at low tip Mach numbers and Reynolds numbers closer to those anticipated on Mars.

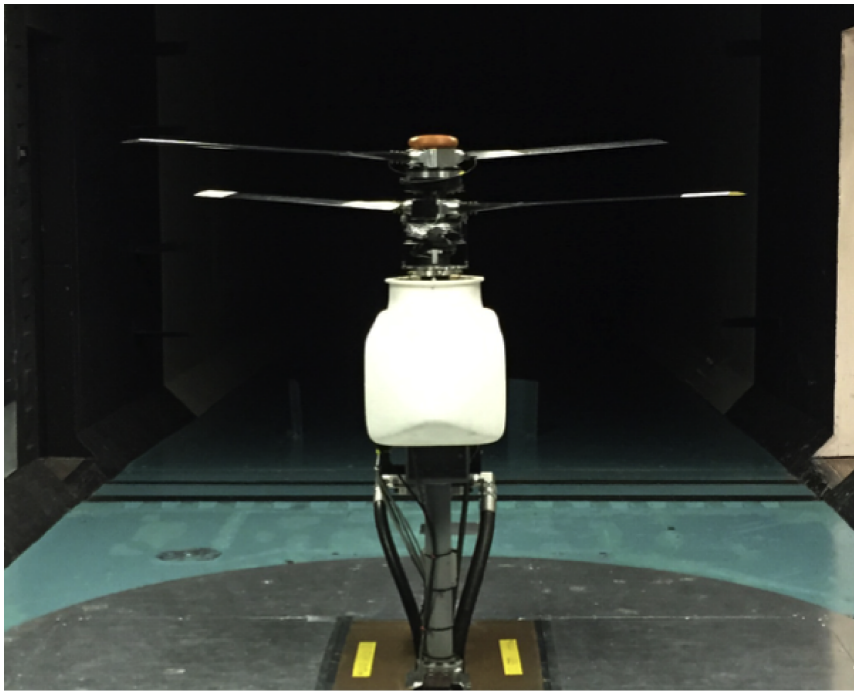

Figure 1.14: University of Texas-Austin hingeless coaxial rotor tested at the Maryland Glenn L. Martin tunnel (from Cameron and Sirohi 2019).

The University of Texas-Austin (UTA) has conducted coaxial hover tests on their hover tower[52] and forward flight tests in University of Maryland (UMD) 7.75- by 11-ft Glenn L Martin Wind Tunnel (Figure 1.14) [53, 54]. The inter-rotor separation was fixed but the tests were conducted at higher Mach numbers. The Reynolds numbers were too high to be of relevance to Mars. Nonetheless single rotors operating alone as well as an equivalent single rotor with the same number of blades as the coaxial confirmed the trends established earlier. The forward flight tests were conducted up to a tip speed ratio (forward flight speed to tip speed) of 0.5 and a lift offset of 20%. Lift offset was found to improve rotor performance (rotor lift to drag ratio) up to 30% at the expense of very high hub loads. Blade tip clearance was dictated more by lift offset and thrust than tip speed ratio. Modern coaxial analysis have used these datasets for advancing their state of the art.

1.7 Coaxial Rotor Analysis

Predicting coaxial rotor loads is more difficult than a single rotor. The difficulty arises mainly from the aerodynamic analysis. Accurate predictions of wake interactions are necessary for accurate predictions of vibratory structural loads.

Modern coaxial rotor analysis can be classified into three categories: 1) unsteady lifting-line aerodynamic models coupled with finite element structural dynamics and rotor/aircraft trim (called comprehensive analysis (CA) in rotorcraft terminology); 2) isolated CFD (unsteady three-dimensional Reynolds Averaged Navier-Stokes) with no structural dynamics or trim; and 3) analysis that couples CFD with the structural dynamics and trim of CA (CFD/CA, or loosely termed CFD/CSD for symmetry of terminology).

1.7.1 Category 1

The principal work on the modern coaxial helicopters mostly belong to Category 1, i.e. comprehensive analysis (CA). Comprehensive analysis consists of aerodynamics and structural dynamics coupled to a trim solution which calculates controls to ensure equilibrium flight. The principal work on modern analysis began with Johnson [55], which elucidated and quantified the lift-offset parameter. This was further expanded by Johnson, Moodie, and Yeo [56]. The power, rotor lift to drag, and controls were well predicted, showing the benefits of lift offset. Yeo and Johnson [57] focused on understanding how lift offset allowed rotors to break the McHugh stall boundary and achieve high blade loadings (C_T/σ). These used the XH-59A data for validation. Coaxial data obtained from UTA-UMD wind tunnel tests were used to validate, understand high speed coaxial flight, and refine University of Maryland's Advanced Rotorcraft Code (UMARC) comprehensive analysis by Schmaus and Chopra [58] (see also [59]). Later, this validation analysis will serve as the starting point of the

Mars comprehensive analysis developed here.

1.7.2 Category 2

CFD has been used to improve the understanding of coaxial aerodynamics. The large impulsive airloads from blade passage are in general better captured by CFD than lifting-line aerodynamic models. Thorough work on isolated CFD for coaxial rotors can be traced to Ruzicka and Strawn [60] and Lakshminarayanan and Baeder [61]. These work used NASA OVERFLOW2 and University of Maryland OVERTURNS, respectively, and were validated with the Harrington [62], and the McAlister and Tung [50] hover data. They provided insight into the spanwise and azimuthal variations in airloads, which have been impossible to measure so far, and confirmed accurately modeling the wake was important for performance predictions.

Juhasz et al. [63] compared three different aerodynamic analysis methods with validation using the Harrington hover data. The blade element momentum theory (BEMT) was able to capture the performance and average inflow well. Free wake and CFD were needed to capture the inflow distribution, particularly in the tip region. The BEMT and free wake were trimmed to thrust and zero total torque. The CFD was left un-trimmed with collective prescribed from experiment instead.

Reed and Egolf [64] studied the X2-TD aircraft including the rotor, fuselage, and stabilizers at a tip speed ratio up to 0.20. The results included limited full aircraft and tail performance. The details of the rotor were not included. Bowles et al. [65] ran a similar study on the S-97 Raider aircraft. This analysis used an embedded blade element method for the blades and CFD only for the fuselage and pusher prop. The objective was to predict aircraft drag and prop performance.

1.7.3 Category 3

With increase in availability of computational resources in recent years, coaxial rotors have been a major target of CFD validation [66–68]. These efforts have proven the advantage of CFD over lifting line methods for capturing the unsteady airloads. In summary however, isolated CFD might be adequate for hover, however in forward flight, structural dynamics and trim are essential for any meaningful solution. This belongs to Category 3, the most advanced and expensive of all analysis.

Coupling CFD with comprehensive analysis (CA) (referred to as CFD/CA) is a relatively new development in rotorcraft. Much like the coaxial rotor, this capability also matured over the last two decades [69]. Today, given adequate resources (processors and time) CFD/CA provides the highest-fidelity solution for performance, loads and vibration. Several contemporary studies have tried to apply CFD/CA on the modern coaxial rotors. But none carried to completeness or proper validation. Singh, Kang and Sirohi [70] and Singh et al. [71] analyzed the forward flight data from the UTA-UMD tests.

Passe et al. [72, 73] and Klimchenko and Baeder [74] included the fuselage and pusher propeller, in CFD in order to study the full X2TD aircraft in trim. There is no available data for validation however in public domain. These studies found strong interactions between the rotor, fuselage, and pusher propeller components that affected trim. Roll and yaw moments were generated by the fuselage because of rotor downwash. There was also a large pitching moment due to rotor wake impinging the horizontal tail. Strong impulsive loading in normal force and pitching moments were found on the blades at inter-rotor blade passage.

1.7.4 Other Notable Works

In addition to the above, over the years there have been many special purpose efforts focused on the coaxial wake. Interested readers can refer to the works of Bagai and Leishman [75], Brown 2000[76], Lim, McAlister, and Johnson 2009 [77], Singh and Friedmann 2018[78]. These were either all isolated aerodynamic analysis or demonstration of advanced simulation capability without any validation data to establish accuracy. Thus in summary, there is a dearth of coaxial data on Earth, in spite of a high level of interest. There is nothing that is directly applicable to Mars Reynolds numbers. Reliable analysis is still in its formative years of maturity. The expansions needed for applying them on Mars is unknown and unclear.

1.8 Objectives of This Thesis

The overall objectives of the present work is to bridge some of the above gaps and thereby build a fundamental understanding of rotorcraft aeromechanics on Mars. The technical approach categorizes the work under five tasks.

1. **Generate hover data at Mars-like conditions.** Vacuum chamber tests are conducted. Cambered plate blades are fabricated, and a single rotor test rig is constructed for testing inside a vacuum chamber. Thrust sweeps at low Reynolds numbers are carried out.

2. **Develop comprehensive analysis for a Mars helicopter.** A comprehensive analysis is developed with finite element blades, low Reynolds number aerodynamics, and Mars helicopter-like coaxial trim solution. This will be used to predict rotor performance, airloads, structural loads, and control loads. Performance is validated with data from task 1.

3. **Develop CFD/CA analysis for a Mars helicopter.** The comprehensive

analysis from task 2 is now coupled with 3D CFD. Development of CFD is not part of this thesis, only coupling comprehensive analysis with CFD. The well-established delta coupling method is used for this talk. The rotor performance, airloads, structural loads, and control loads are now predicted with the high-fidelity aerodynamic analysis. Performance is again validated with data from task 1. In absence of any Mars data for validation a different approach is followed. Two sets of CFD/CA analyses are carried out. One using in-house Maryland tools another using US DoD Helios. These tools together form the highest fidelity capability set in rotor analysis in the United States. Their general agreement, if achieved, would serve as the best scenario for verification.

4. **Fundamental understanding of aeromechanics in Mars conditions.** The results obtained from tasks 1-3 provide the most valuable contributions of the thesis—a new understanding and knowledge base for Martian rotorcraft flight. This includes similarities and differences in aeromechanics between Earth and Mars. In particular, the impact of hingeless and articulated hubs on blade loads and control loads that impact so much of the entire vehicle performance and weights that is affects everything from flight to packaging to even launch needs.

5. **Understand the importance of a fuselage on rotor airloads.** The question of how important it is to model the aerodynamics of the fuselage to design the rotor is answered in this task. This is more than an academic curiosity. If helicopters were to be used in future for science missions, very few restrictions on fuselage shape might be admissible. The ultra-thin air indicates that fuselage aerodynamics is not important. A precise assessment is needed nevertheless for more than 90 sec of flight.

1.9 Organization of the Dissertation

The dissertation is organized into seven chapters. Following this introduction, Chapter 2 covers vacuum chamber hover testing. The fabrication of the rotor and construction of the test stand are described. These are followed by low Reynolds number test data. Chapter 3 describes the development of the analyses and of the structural and aerodynamic models, which are built from testing of blade structural properties and 2D CFD calculations. Chapter 4 validates the CA first with the closest coaxial data available on Earth conditions. Then with the Chapter 2 hover data. Analysis of forward flight is focused on comparing the hingeless and articulated hubs. The impact of blade loading C_T/σ, inter-rotor separation, shaft angle, and advance ratio are studied. There is however no test data to back these predictions. Chapter 5 develops CFD/CA for the highest fidelity predictions. The analysis is first validated with the Chapter 2 hover data. Then investigates the impact of the higher-fidelity analysis in forward flight. Chapter 6 compares the CFD/CA analysis with another state-of-art analysis from US DoD. The aerodynamic impact of a fuselage is studied at this stage. Chapter 7 provides the key conclusions.

Chapter 2: Vacuum Chamber Testing

2.1 Overview

Little to no data exist for Mars rotors beyond what is available now at JPL and in Maryland. Very few experiments have been conducted and even less data published. The test facilities at the University of Maryland include a 3 ft diameter vacuum chamber. This chamber is typically used for testing the structural integrity and inertial loads on new kinds of composite rotor blades. By controlling the pressure Mars-like Reynolds and Mach numbers can be produced. This chapter covers the fabrication of the rotor blades, construction of the rotor rig, and acquisition of hover data. This data will be used later for analysis validation.

2.2 Blade and Rotor Design

The target tip Reynolds number of the Mars helicopter is very low ($Re_{Tip} < 10,000$). Recent low Reynolds number research on rotating cantilevered blades in the same chamber [29] guided the design of the blades. Systematic investigations of rotors with various cross sections at Reynolds numbers between 10^4 – 10^5 were used to inform the present work.

Earlier work found thin cambered plates showed better lift and drag performance over true airfoils. As the thickness decreased, the performance improved. Testing over the range of flat plate camber showed a camber of 6% produced the highest lift-to-drag ratio for the Reynolds numbers expected on the Mars rotor. Increasing

Figure 2.1: Blade cross section with 6% camber and 2% thickness.

Table 2.1: Model Mars rotor parameters.

Parameter	Value
Number of Blades per rotor	2
Radius, in (m)	9.2 (0.234)
Chord, in (m)	2.0 (0.0508)
Pitch Bearing	6%R
Pitch Horn	8%R
Root Cut-Out	13%R
Blade attachment	16%R
Hub	Hingeless
Solidity	0.1199
Twist	none
Taper	none
Blade Weight, lb (g)	0.0224 (10.16)
Airfoil	6% camber 2% thick circular arc
Chordwise C.G.	50%c

camber further increased the lift, but at an increased drag penalty. The study also found thinner plates have better performance. With thickness, pressure drag increased, although lift-curve slopes remain steeper, and stall onset delayed to higher angles of attack.

A camber of 6% and a thickness of 2% was selected. Thinning the blades further raised structural and fabrication concerns. The cross-section is shown in Figure 2.1. The leading and trailing edges were blunt. Sharp or beveled edges were avoided to ensure uniform and repeatable fabrication. Sharp edges proved difficult during fabrication. No twist or taper were included to minimize complexity and also facilitate basic insights. The rotor was two bladed. The geometry is given in Table 2.1.

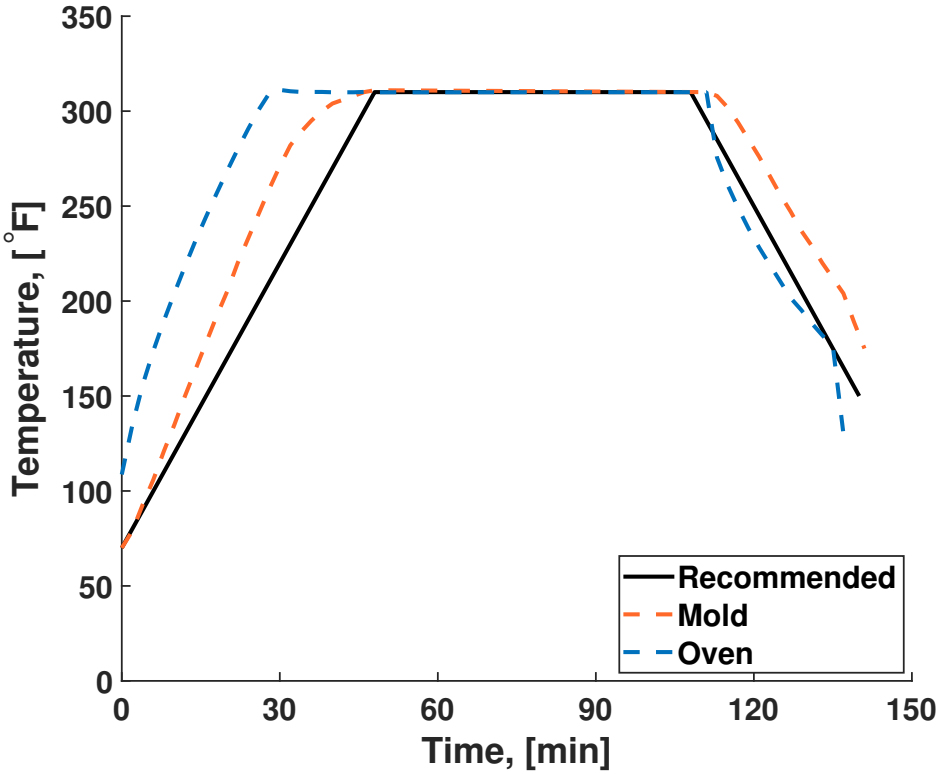

Figure 2.2: Oven curing temperature profile.

2.3 Blade Fabrication

The blades are fabricated from carbon fiber pre-preg fabric. It is a $\pm 45°$ 2×2 twill weave. The fibers are 3000 filament bundles of polyacrylonitrile (PAN) carbon. The manufacturer stated tensile modulus is 33 mega-pound per square inch (MSI). The epoxy content is 36% by weight. Each blade consists of three layers of plies. There is no spar. The blades are uniform along the span.

The plies are hand laid and wrapped in release film before being placed in the mold. The blade is then cured according to manufacturer's specifications:

1. ramp up to 310°F (154.4°C) at a rate of 5°F-per-minute,
2. hold at 310°F (154.4°C) for 1 hour, and
3. cool down to at least 150°F (65.5°C) at a rate of 5°F-per-minute before removal.

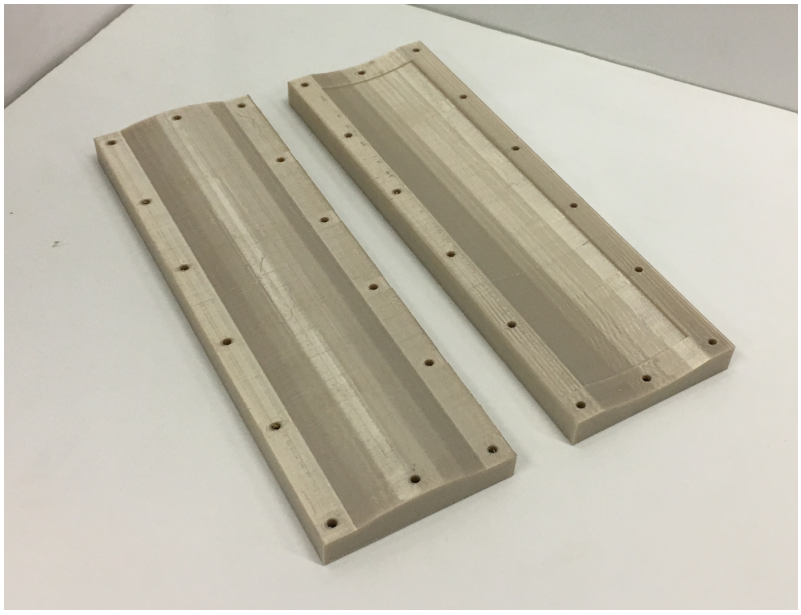

Figure 2.3: PPSF High Temperature, 6% Camber 2% Thick Blade Molds.

The oven was instrumented with thermocouples to measure the actual temperatures during a cure cycle. Both the oven and internal mold temperatures were recorded. Figure 2.2 shows the temperatures over a cure cycle. The mold internal temperature matches the recommended cycle well.

The mold was 3D printed to tight tolerances on a Stratasys Fortus 400mc printer at the University of Maryland Rapid Prototyping Laboratory. The molds are made of polyphenylsulfone (PPSF) plastic. The material is often used for automotive and medical applications that need thermal and chemical resistance. Initial molds were made of ULTEM 9085. Even though ULTEM 9085 has a higher heat deflection point than PPSF (410°F (210°C) versus 372°F (189°C)) the PPSF molds deformed less during the cure cycle and produced a higher quality blade. The mold has two halves, which are screw tightened. Even though not optimal for printing efficiency due to print time and support material, the molds were printed with the upper and lower surface contours aligned along each print layer. This produced the best surface smoothness, quality, and resolution. The mold is shown in Figure 2.3.

After the cure cycle, the blade was removed from the mold and machined using

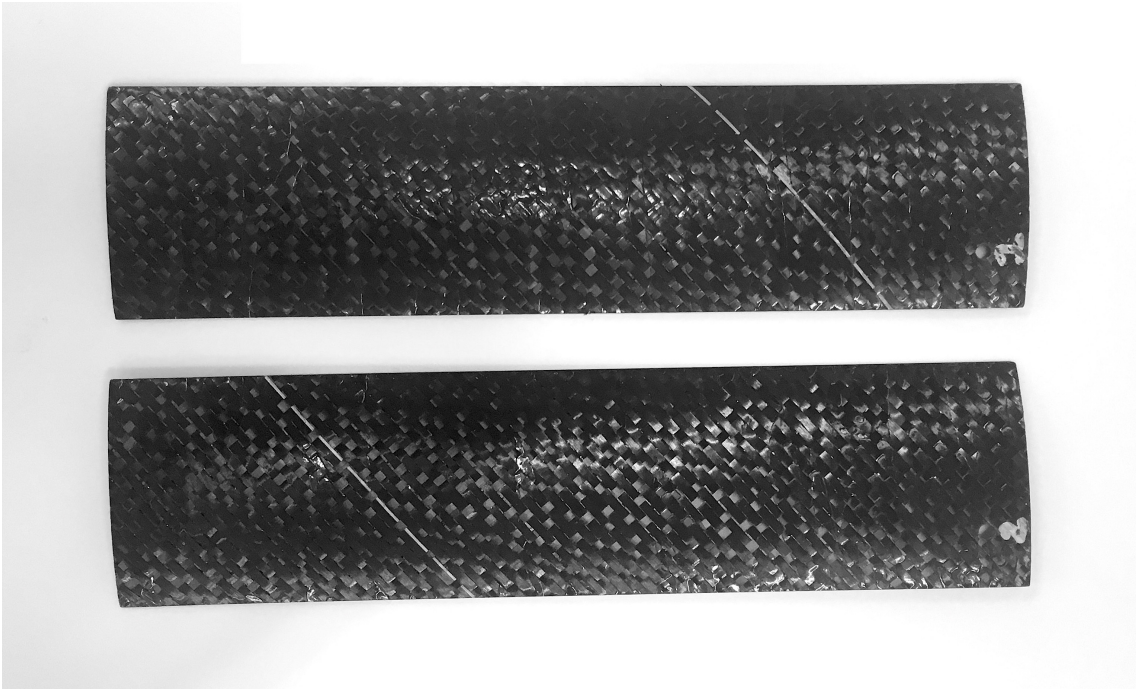

Figure 2.4: 6% Camber 2% Thick Composite Blades.

a CNC mill. The mold was slightly over sized in the span and chord directions. This ensured the blades were cut to the exact dimensions. The blades are shown in Figure 2.4. Each blade was weighed and the average was 0.0224 lb (10.16 g) with negligible variation. Being a cambered plate the chordwise center of gravity position is at 50% chord, which was also verified through measurements.

2.4 Center of Gravity

In addition to the baseline blade, two other blades were also fabricated. The goal was to move the chordwise center of gravity from 50% c nearer to 25% c, while keeping the profile intact as much as possible. This required the addition of Tungsten rod leading edge (LE) weights. The fabrication process is similar to the baseline blade except for a few modifications. Instead of three separate plies, a single ply was wrapped from the lower surface around the leading edge weights onto the upper surface. Inside are the leading edge weights and a middle ply. The middle ply is

Table 2.2: Results of chordwise center of gravity placement study.

	Baseline	Mod #1	Mod #2
LE Weights	None	4 × 0.04 in	1 × 0.04 in & 1 × 0.0625 in
Weight, lb (g)	0.0224 (10.16)	0.0468 (21.25)	0.0440 (19.98)
Chordwise CG	50.0%c	27.3%c	29.7%c

shorted, chordwise, in order to accommodate the leading edge weights. The weights are wrapped in Cytec FM 300 adhesive film before being placed in the blade. The same curing process was used. The first modified blade (Mod #1) used four weights with a diameter of 0.040 in, and the second (Mod #2) used a single 0.040 in weight and a 0.0625 in weight.

The blade weights and center of gravity locations are given in Table 2.2. Figure 2.5 shows the blade cross sections of the three designs. The figure shows the placement of the leading edge weights and how much the airfoil shape is altered. Although the modified blades were able to achieve (what was thought to be) more favorable center of gravity locations, this came at the cost of twice the weight. The two modified blades had 109% and 97% increase in weight compared to the baseline blade. The modified blades were not studied any further because of the large weight penalty. The conclusion was they could be produced if the weight budget allowed for it and aeroelastic stability needed it. Later, during analysis, no instabilities were revealed (due to the low Lock number), hence the additional weight was deemed unnecessary.

2.5 Experimental Setup

The experimental setup includes a vacuum chamber, the hover stand, sensors and data acquisition, and the rotor. The main goal is to collect hover data at low of Reynolds numbers on a rotor with a pitch bearing and control inputs.

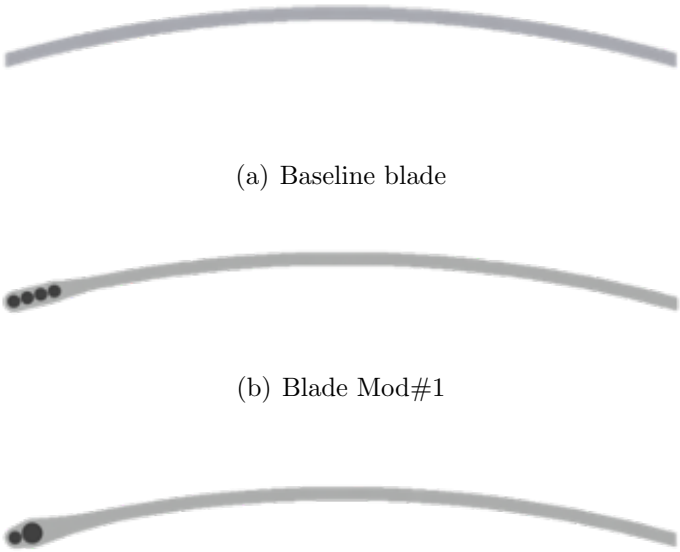

(a) Baseline blade

(b) Blade Mod#1

(c) Blade Mod#2

Figure 2.5: Blade cross sections.

2.5.1 Vacuum Chamber

The tests were conducted inside an existing, custom built, cylindrical vacuum chamber (Figure 2.6). The rotor rig and instrumentation were built for this work. A vacuum pump, Welch-ILMVAC DuoSeal, was used to achieve the desired pressures for testing. The pump is capable of reaching a minimum pressure of 1.3×10^{-5} lb/in^2 (0.089 Pa, 8.85×10^{-7} atmosphere). The stainless steel chamber has a single view port and six feedthrough ports. All the feedthrough ports are ISO designated NW40 KF flanges, which are rated for pressure far below the pump capability. The two ports on the top of the chamber were used for the pump and pressure sensor. The four ports on the side used variety of wire feedthroughs for data acquisition, including power for the motor and all the data signals. All the wire feedthroughs were UHV Kapton insulated to ensure no wire bursts at vacuum and are rated down to 2×10^{-12} lb/in^2 (1.38×10^{-8} Pa, 1.36×10^{-13} atmosphere).

Figure 2.6: Exterior of 3 ft diameter vacuum chamber.

In order to quantify the atmospheric conditions inside the chamber, the pressure and temperature were recorded. The pressure sensor was a Mensor CPT6100 Precision Pressure Transducer. The sensor has a range of -15 to $6,000$ lb/in^2 and was manufacturer calibrated. The temperature was measured with an Analog Devices TMP36 Temperature Sensor. The TMP36 sensor has a range of $-40°$ to $125°$ C and a $\pm$ 1° C accuracy. This sensor was calibrated with a K type thermocouple, and was found to have a 9.3 mV/°C scale factor. The manufacturer stated scale factor is 10 mV/°C.

Only the pressure was controlled, the chamber has no control over temperature or gas composition. Controlling the pressure (while reading the temperature) provides control over density, which in turn controls Reynolds number. The vacuum chamber proved capable of reaching and maintaining pressure levels down to 0.05 lb/in^2 (0.34% Earth's atmosphere) which allows for density levels as low as 0.004 kg/m^3 (25.8%

Mars' atmosphere). This range was sufficient for simulating the desired Reynolds numbers.

2.5.2 Hover Stand

Figure 2.7 shows the hover stand designed and built for testing the small 2 bladed Mars rotor. The stand places the rotor 2.9 radii above the ground to ensure there is no ground effect. However, recirculation inside the vacuum chamber is unavoidable. The stand is constructed from stainless steel MakerBeam and an aluminum mounting plate. The mounting plate extends 0.25R at a distance of 0.6R below the rotor, and provides only a small blockage. Efforts to reduce the size of the plate further resulted in a less stable stand with unacceptable levels of vibration, and therefore discarded.

The stand uses a combination of in-house fabricated and commercial off the shelf components. The structure is made from a single 3D printed ABSplus plastic part. It was designed to mount both the rotor and all the instrumentation. The disassembled parts and pieces are shown in Figure 2.8 and the assembled setup is shown in Figure 2.9.

The blades are attached to the hub through 3D printed ABSplus plastic blade grips. The adapters are designed to fit the 6% camber 2% thick geometry. This component can be quickly re-designed to fit other geometries, and therefore allows other blade designs to be easily tested without the need to alter the hub. The hub is hingeless in flap and lag but has a pitch bearing. The pitch bearing is at 0.06 R, with a pitch horn 0.08 R. The root cut out is 0.13 R, and the blade attachment bolt at 0.16 R. The effective flap hinge is outboard of the pitch bearing so there is no pitch-flap kinematic coupling.

The rotor has full cyclic control through custom built pitch links, a commercial 450 mm Class RC helicopter swashplate, and three analog rotary servos to actuate

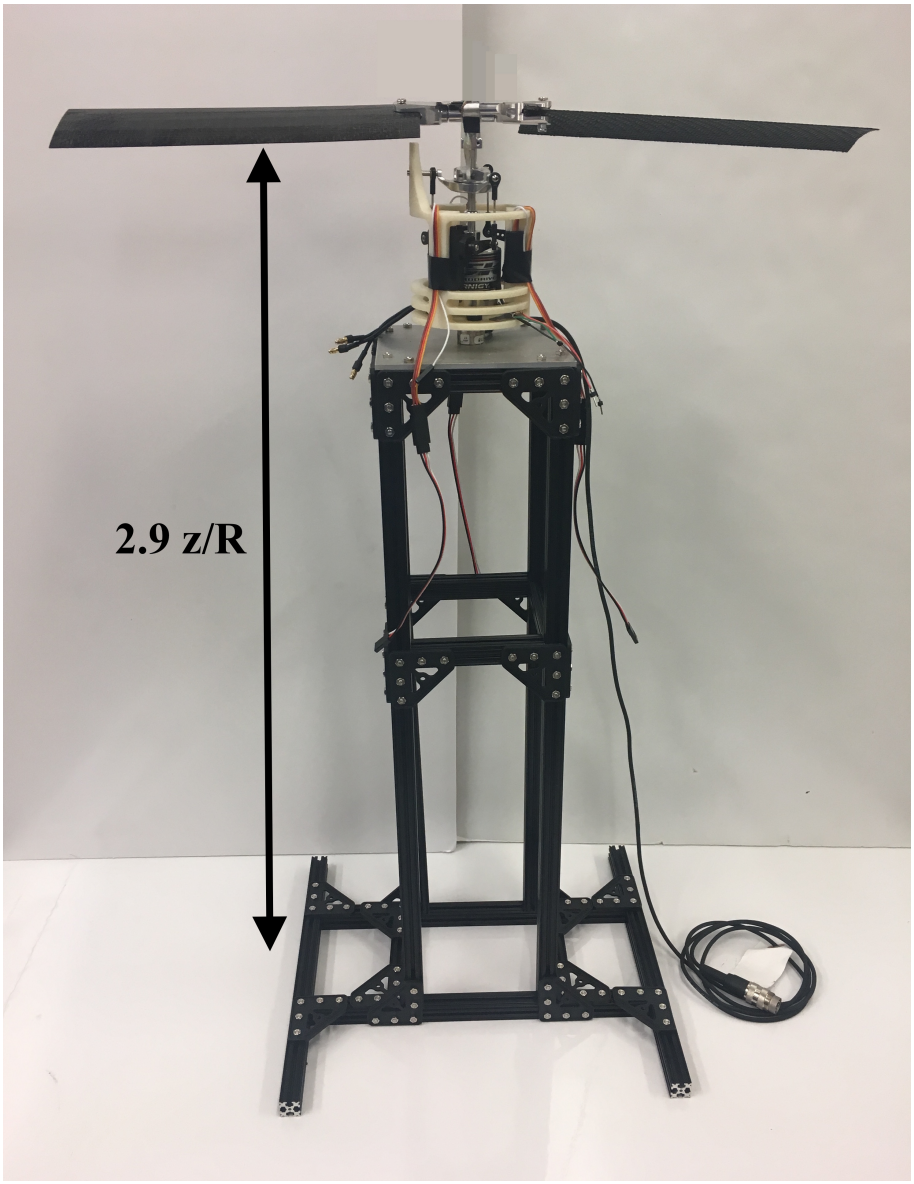

Figure 2.7: Hover stand with test rotor.

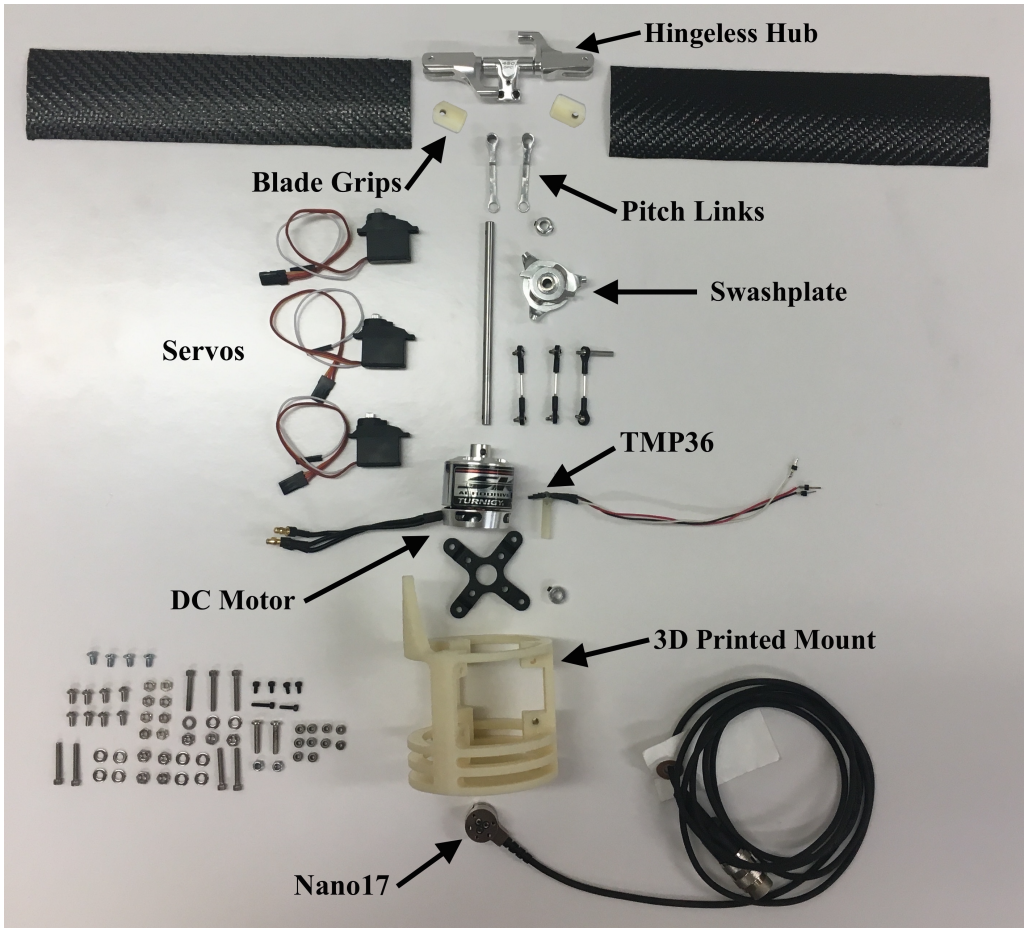

Figure 2.8: Disassembled test rotor.

the swashplate. The servos are Batan B2122 analog feedback servos, which have a maximum torque of 25 oz in (0.1765 Nm). The high torque and metal construction allow the servos to hold the pitch steady under the pitch link loads. Each servo weighs 16 g.

The servos are independently controlled through serial commands, using pulse width modulated (PWM) communication. The servo commands are sent thrrough an Arduino Uno board which converts the desired pitch angle to a PWM value and then generates the corresponding signal. The servos were calibrated with a pitch inclinometer for collectives from $-10°$ to $+40°$ at $5°$ increments. The calibration was found to have an allowable $\pm 0.2°$ variation around the azimuth after spinning up the rotor. Figure 2.10 shows the calibration curves for the servo positioning commands.

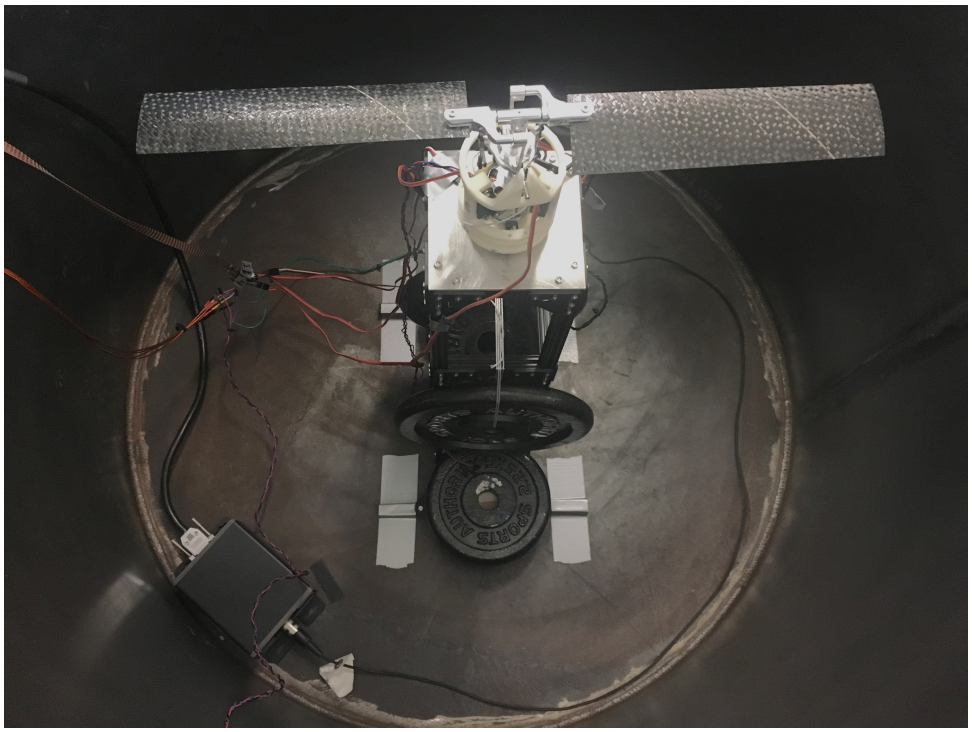

Figure 2.9: Hover stand and test rotor inside vacuum chamber.

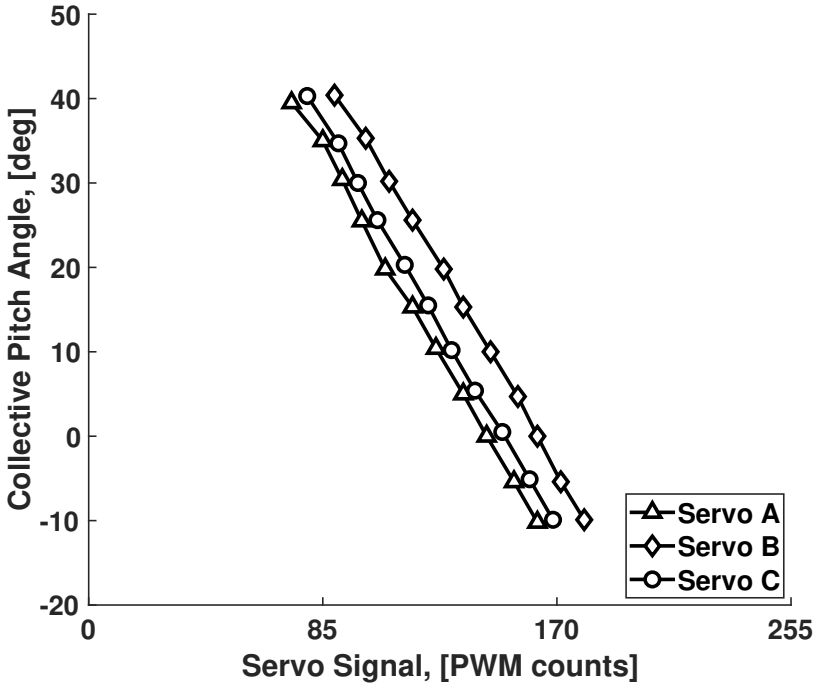

Figure 2.10: Servo calibration for blade collective pitch control.

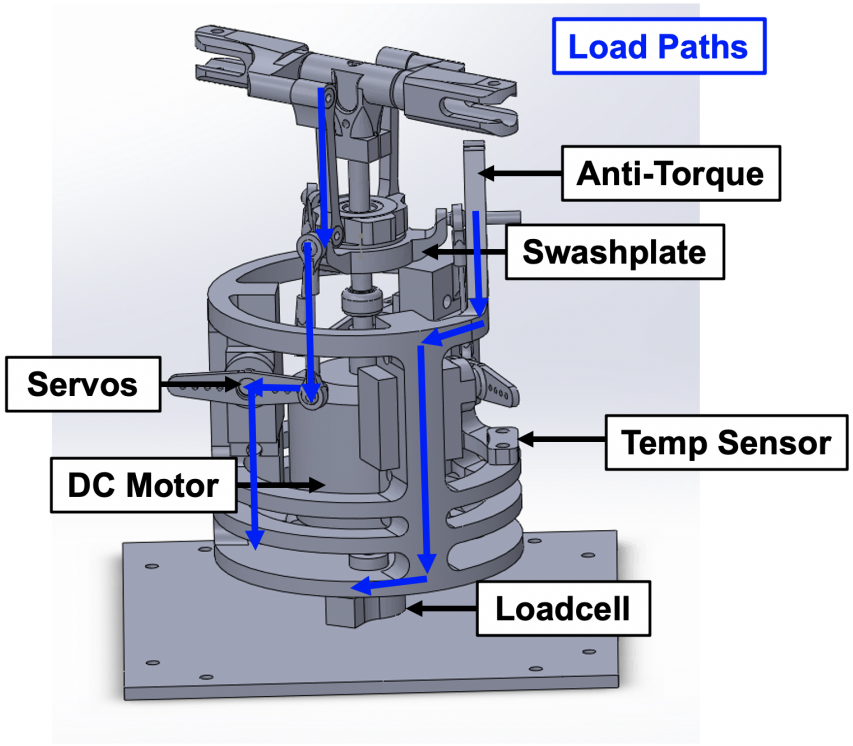

Figure 2.11: Test stand diagram with auxiliary load paths to the load cell.

The rotor is directly driven by a Turnigy Aerodrive SK3–3542–800KV DC brushless out-runner motor. The motor has a K_v rating of 800 (meaning the unloaded motor spins at 800 rpm per volt) and a power rating of 625 W. The power is fed through the vacuum chamber feedthrough ports on high power wires rated for 5 A. The motor operates at 15 V nominally and speed is controlled using an electronic speed controller (ESC) and PWM.

Operating near vacuum meant the motor could not dissipate heat through convection. This is a real problem on Mars and one of the reasons why the first flights are limited to 90 secs. To ensure the motor did not overheat, it was only allowed to operate up to 80° C. The temperature was monitored using a TMP36 temperature sensor. The motor could operate for six minutes before spinning-down for cooling. The temperature sensor was calibrated using a K type thermocouple and was found to have a 9.7 mV/°C scale factor.

The rotor was directly driven. The motor frame was directly mounted to the ATI Nano17 Force/Torque Sensor. The Nano17 is a small (17 mm diameter) six axis silicon foil load cell. Special care was taken in designing the test stand so that all rotor forces and moments travel through the load cell. No load paths could bypass the load cell. The main load path was through the motor. Thrust had a second load path through the pitch link. The torque had a second load path through the scissor (anti-torque bar in Figure 2.11) into the swashplate. Because the control system is also mounted entirely on the 3D frame and therefore on the load cell the second load path also passes into the load cell.

The primary measurements for these tests are the vertical force and moment F_z and M_z, which correspond to the rotor thrust and torque. The load cell range is ± 25 N for side forces, ± 35 N for vertical force, and ± 0.250 Nm for all three moments. The resolution is 0.00625 N for forces and 0.03125 Nm for moments. Tare measurements were taken with the blades attached for thrust, and blades removed and spinning for the torque.

The rotor speed is measured using a Monarch PLT200 Laser Tachometer. The Monarch Tachometer is an optical sensor that is mounted outside the vacuum chamber and measures the rotational speed through the glass view port sensing a small square piece of T-5 reflective tape, mounted on top of the motor.

The data from the test stand is passed through the vacuum chamber ports to a 16 channel National Instruments (NI) SCC2345 signal conditioning block, which in turn is connected to a NI M-series USB-6251 DAQ Input/Output block with 16-bit accuracy, 1.25 Megasamples per second (MS/s) and a 1 kHz internal clock. All readings, except for the rotor speed, are fed through the NI DAQ. A LabView VI code, using a Timed Loop, is used to collect data samples at 1 kHz. In order to attain this sampling rate, all data are taken as raw voltages. During post-processing, the voltages were reduced. The wire connection schematics from inside the chamber

Table 2.3: Summary of data collected during testing and their instruments.

Measurement	Device
Pressure	Mensor 6100 Pressure Sensor
Temperature	Analog Devices TMP36
Thrust and Torque	ATI Nano17 F/T Transducer
Rotational Speed	Monarch PLT200 Tachometer
Motor Temperature	Analog Devices TMP36

to the NI DAQ are given in Appendix A.

Table 2.3 provides a summary of all the data measured during testing.

2.6 Test Description

The rotor was tested at tip Reynolds numbers, 3000, 5000, and $10,000$. The tip Mach number was a constant 0.07. This allowed pure low Reynolds number effects to be studied in the near incompressible range. To achieve these conditions, the chamber density was varied from 0.0343 to 0.1142 kg/m^3 and the rotor was spun at 1000 RPM. Collective pitch was swept from $-10°$ to $40°$, at $5°$ increments.

2.7 Results

All results are presented in non-dimensional form. Table 2.4 summarizes the average atmospheric conditions for each tip Reynolds number. The Reynolds number was controlled via pressure. At each Reynolds number three trials were conducted. The data shown is the average of the three trials. There was negligible variation between trials.

Figure 2.12 shows the variation of blade loading C_T/σ versus collective pitch. The collective sweeps produced a wide range of blade loadings from -0.12 to 0.22. At a given collective, higher Reynolds numbers resulted in higher thrust. This effect is more pronounced at lower collectives. There is no indication of stall even at

Table 2.4: Average chamber conditions for each Reynolds number sweep.

Measurement	Re = 3000	Re = 5000	Re = 10,000
Pressure, N/m^2	2873.244	4786.815	9574.008
Temperature, K	292.95	292.15	293.45
Density, kg/m^3	0.0343	0.0571	0.1142
Rotational Speed, RPM	1003.00	1004.50	1002.25

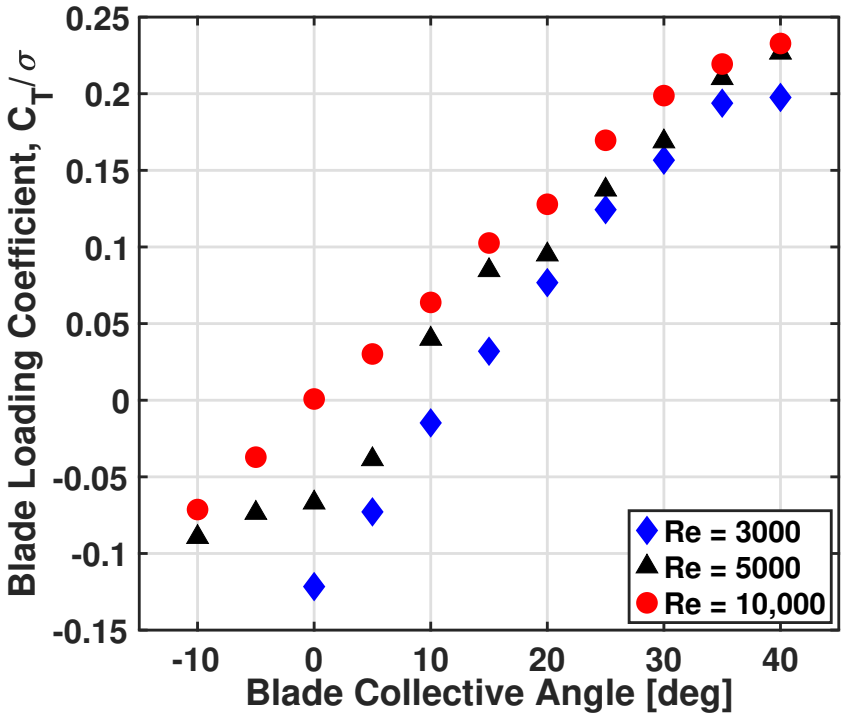

Figure 2.12: Variation of Blade Loading Coefficient C_T/σ with collective, for different Reynolds numbers.

collectives of 40°. The Re 5000 data is more erratic for reasons unclear.

Figure 2.13 shows the variation of power coefficient C_P/σ versus the collective pitch. Unlike the blade loading, power shows less dependence on Reynolds number.

Figure 2.14 shows the same data as power versus thrust. At a given blade loading the power increases as the Reynolds number decreases. This trend flips for negative thrust; although negative thrust is of no practical importance.

The Figure of Merit (FM) is the metric for hover efficiency. It is the ratio of

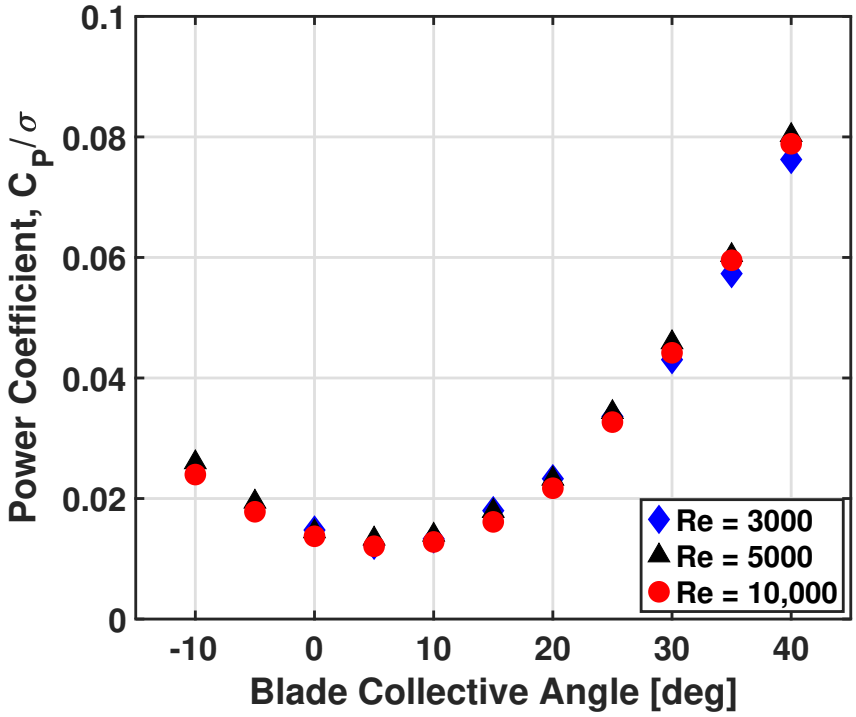

Figure 2.13: Variation of Power Coefficient C_P/σ with collective, for different Reynolds numbers.

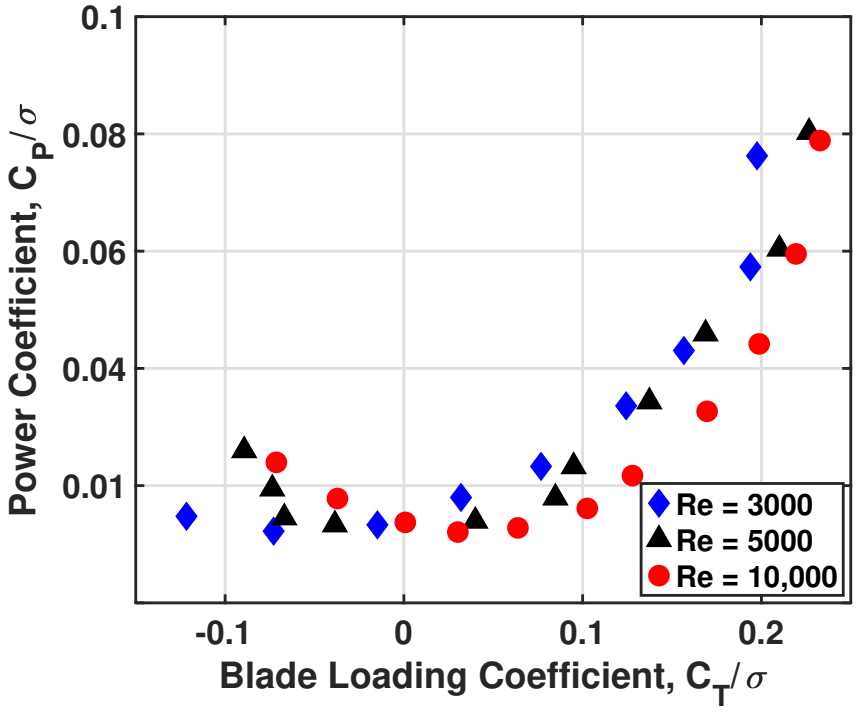

Figure 2.14: Variation of Coefficient of Power C_P/σ with Blade Loading C_T/σ for different Reynolds numbers.

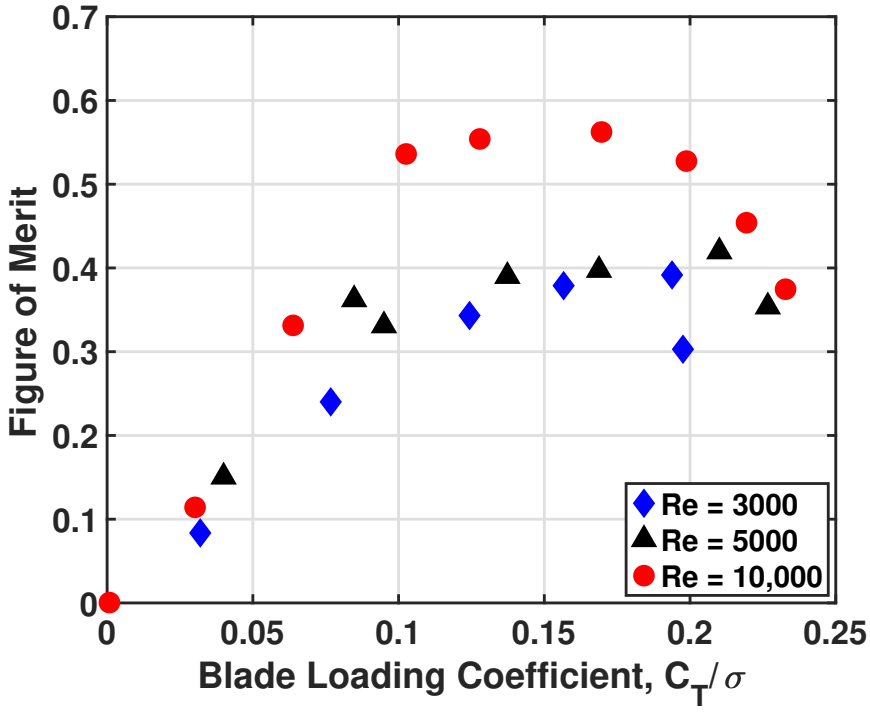

Figure 2.15: Variation of Figure of Merit, with Blade Loading Coefficient C_T/σ, for different Reynolds numbers.

ideal power to the actual power, given by Equation 2.1.

$$FM = \frac{C_T^{3/2}/\sqrt{2}}{C_P} \tag{2.1}$$

where C_T and C_P are the measured thrust and power coefficients, respectively. These coefficients are defined in Equation 2.2.

$$C_T = \frac{T}{\rho A(\Omega R)^2} \quad \text{and} \quad C_P = C_Q = \frac{Q}{\rho A(\Omega R)^2 R} \tag{2.2}$$

where T is thrust, P is power, Q is torque, ρ is air density, A is disk area, Ω is rotational speed, and R is radius.

Figure 2.15 shows the variation in Figure of Merit versus blade loading. As expected the maximum Figure of Merit increases with Reynolds number. For a Reynolds number of $10,000$, the maximum Figure of Merit is 0.56, while for the lower

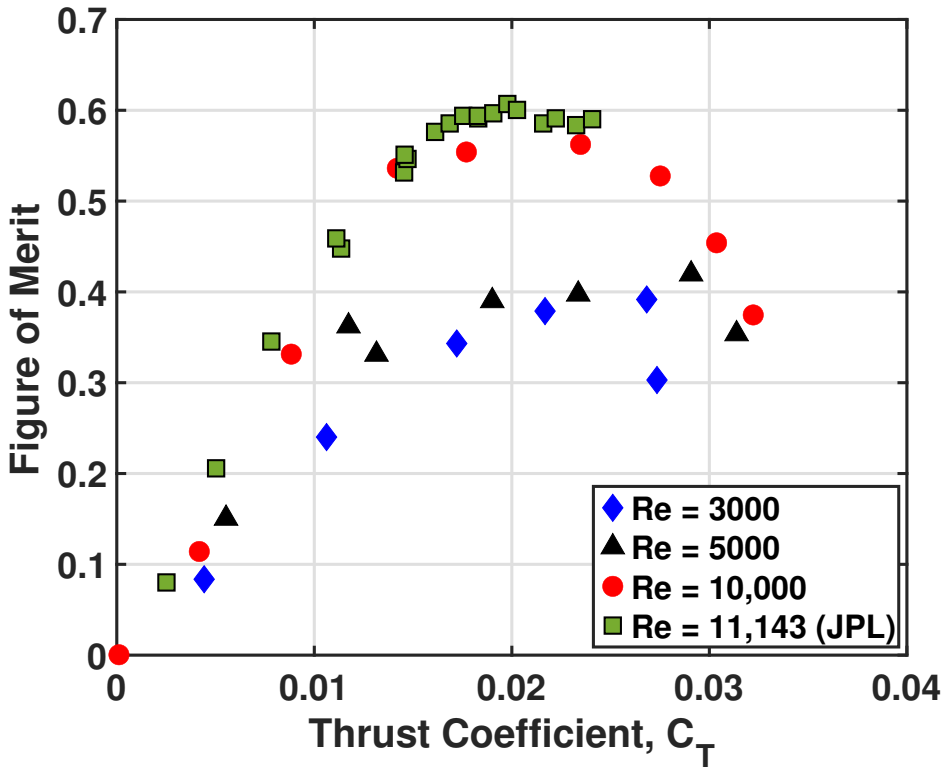

Figure 2.16: Comparison of NASA JPL hover data with the present study, showing variation of Figure of Merit with Thrust Coefficient C_T.

Reynolds numbers (3000 and 5000) the maximum is only 0.39 and 0.42, respectively. Thus, tip Reynolds numbers of at least $10,000$ is desired on Mars.

A contemporary data set from JPL at Reynolds number $11,143$ is compared in Figure 2.16. Note that the JPL rotor has an airfoil. It is also the full aircraft with two rotors and twice the number of blades. Nonetheless the close proximity of the two data sets serves as a verification for both.

Chapter 3: Developing Models for Analysis

3.1 Overview

This chapter covers the multiple analysis methods used in the present work. There are two primary predictive tools that are used for this work: (1) Comprehensive analysis (CA) UMARC, which includes a lifting-line aerodynamic model, a structural model, and a trim solver, and (2) three-dimensional computational fluid dynamics (CFD) GARFIELD. The two analyses are then coupled to perform CFD/CA analysis (often referred to as CFD/CSD merely for symmetry of terminology). For CFD/CA the delta coupling method is used. All the tools were developed in-house at the University of Maryland.

3.2 Reference Aircraft and Model Rotor

A reference aircraft (or objective aircraft) was needed for deciding the test and analysis conditions. It was decided that tip Reynolds numbers of 3000-10,000 should always be maintained. This range was considered representative of Mars helicopters of the future. The model for test and model for analysis were required to fall in this range. The reference aircraft is the Maryland design MARV [23], scaled down in size to fit the rotor in the vacuum chamber. That gave the reference rotor. MARV was a large 50 kg coaxial helicopter, whereas the reference aircraft is smaller than even the JPL Mars Helicopter (MH) of 1.8 kg. That is simply the constraint of the vacuum chamber. The reference aircraft is shown in Table 3.1. The reference aircraft

Table 3.1: Mars aircraft flight conditions.

	MARV	MH	Reference Aircraft
Rotational Speed [RPM]	645	2575	2400
Tip Reynolds	64,800	11,412	4687
Tip Mach	0.625	0.70	0.255
Lock number	0.354	0.30	0.075
Advance Ratio	0.08	0.05	0.10
Blade Loading, C_T/σ	0.1464	0.10	0.08
Solidity	0.1585	0.148	0.1199
Weight [kg]	50.0	1.80	0.200
Radius [m]	2.130	0.605	0.234
Chord [m]	0.530	0.605	0.0508
Intra-rotor Spacing	16%R	16.5%R	10%R
Hub Type	Teetering	Hingeless	Articulated and Hingeless

is an imaginary aircraft, neither built nor designed, but serves only as assessment of scaling.

Now for the rotor. The model for test was the reference rotor but only a single rotor, constrained again by resources (two rotors will generate significant re-circulation in a small chamber). The model for analysis was the full coaxial rotor. The analysis focuses primarily on the rotor. The aerodynamic unimportance of the fuselage is shown later in Chapter 6. The coaxial rotor used in analysis is a pair of the single rotors built and tested in Chapter 2. The analysis is conducted with two different hub types–hingeless and articulated–although the rotor built and tested is only hingeless. In the analysis, the rotor operates with a tip Reynolds number of 4,687, tip Mach number of 0.255, and Lock number of 0.075–as per the Reference aircraft(Table 3.1). In the coaxial system, the upper rotor spins counter-clockwise, whereas the lower rotor spins clockwise–same convention as Earth, and also MARV and the JPL MH.

3.3 Comprehensive Analysis: UMARC

The University of Maryland Advanced Rotorcraft Code (UMARC) is used as the baseline analysis platform. The formulation is described in Refs [79, 80] (see also [81]) for single rotors. Extension to coaxial rotors is described in Ref [58] (see also [59]). These work extensively validated UMARC for single and coaxial rotors on Earth. The work on the coaxial rotor is the starting point of the present work. That analysis is extended here to couple with CFD and refined for application on Mars.

3.3.1 Structural Model

The structural model includes flexible blades, hub type (hingeless or articulated), and pitch links. Flexible blades are modeled as second order, nonlinear, Euler-Bernoulli beams. The finite element discretization is based on Hamilton's principle. Inputs are sectional stiffness and inertial properties, which were measured in detail in Section 3.6.1. Each beam element undergoes coupled flap, lag, torsion, and axial deformations. The model has 20 spanwise elements. Boundary conditions are applied to the assembled finite element matrices allowing this method to be very adaptable to different blade boundary conditions, or hub types. Pitch link stiffness is introduced by modifying the properties of the torsion spring at the root end. Modal reduction is used to solve the equations of motion. The first eight modes are used.

Periodic response is obtained by finite element in time. Twenty-four time elements are used, with Hermite polynomials inside, ensuring continuity of displacements and velocities. The polynomials are fifth order with six internal nodes. Finite element in time allows for direct extraction of the periodic solution.

3.3.2 Aerodynamic Model

The aerodynamic analysis is a Weissinger-L type second-order unsteady lifting line model.

The blade is divided into 50 spanwise segments. The Weissinger-L model calculates the angle of attack at three-quarter chord with bound circulation at one-quarter chord. The bound circulations are obtained using a near-wake model. A non-linear near-wake (or second order lifting-line) is used; which iterates bound circulations and airfoil tables for a consistent Kutta-Joukowski solution. Relaxation is needed and about 10-20 iterations. The near-wake extends 30° behind the trailing edge. The analysis also includes indicial unsteady aerodynamics (Leishman-Beddoes). The airfoil tables include Mach and angle of attack variations. Reynolds number is accounted for by different tables across the span. This is the inner problem of the aerodynamics model.

The near wake is assumed to roll-up into a single tip vortex. The tip vortices from all the blades and rotors constitute the far wake. The far wake contributes inflow at the blade three-quarter chord. This is the outer problem of the aerodynamic model. The inner and outer problems constitute the aerodynamic model combining the unsteady lifting-line (supplying the blade airloads) with free wake (supplying the inflow).

The free-wake analysis is used to model far field inflow, rotor-to-rotor interactions, and blade-to-blade interactions. A single vortex was trailed from the blade tip, although options for multiple trailers could be used. The released vortex trailer strength is given by the magnitude of the maximum bound circulation on the blade. Additionally, the blade deformations (three deflections and three rotations) from the structural analysis is passed to the free-wake to define the release points of the trailers and control points for inflow calculation. The free-wake azimuthal discretization is

15° and carried for three turns in forward flight and six turns in hover. More turns are necessary in hover to ensure the end of the wake is far enough from the rotor.

There were modifications made in the aerodynamic model due to the thin Mars atmosphere. UMARC did not include Reynolds number correction. For the Mars cases, airfoil decks for the same airfoil at different Reynolds numbers were generated and used to model the variation with radial location. Only the drag correction was ultimately used based on validation with low Reynolds number coaxial data. The diffusion constant in the vortex core-growth model was reduced by two orders of magnitude in accordance with Reynolds number scaling due to atmospheric conditions on Mars. The relaxation in the near wake model was increased (update factor was reduced from 10% to 1%) to converge the near-wake iterations.

3.3.3 Trim Solver

The goal of an aircraft trim solver is to calculate the necessary inputs to achieve a desired equilibrium flight condition. The inputs can be a combination of pilot controls and body angles. For a rotorcraft, steady level flight trim is achieved by a steady response in the fixed frame, which means the rotor response must be periodic. Full aircraft trim balances the rotor forces and moments as well as forces and moments from all other components of the aircraft, such as fuselage, wings, stabilizers and/or anti-torque devices. There are two types of trim: coupled, or free flight, trim (where rotor forces and moments keep the aircraft in equilibrium), and uncoupled, or isolated rotor, trim (where rotor forces and moments or flapping motion satisfies some prescribed targets).

In the free flight trim problem, there are six degrees-of-freedom and therefore six equilibrium equations. There are then six trim variables to solve for. There are many different control schemes, but they must ultimately result in six variables. The six equations describe the balance of lateral force (F_Y), longitudinal force (F_X),

vertical force (F_Z), roll moment (M_X), pitch moment (M_Y), and yaw moment (M_Z). Aircraft pitch and roll are always two of the six trim variables. In a single main rotor helicopter the others are rotor collective θ_o, lateral cyclic θ_{1c}, longitudinal cyclic θ_{1s}, and tail rotor collective θ_{TR}.

For classical articulated coaxial rotors (such as Kamov), the upper rotor collective θ_o^U solves for the vertical force balance (thrust), same as the single main rotor. The lower rotor collective θ_o^L solves for the yaw moment balance (torque), replacing the tail rotor collective. The yaw moment is now balanced through differential torque instead of tail rotor side force. Similar to the single main rotor, the roll and pitch moment equations are solved with a single lateral ($\theta_{1c} = \theta_{1c}^U = \theta_{1c}^L$) and longitudinal ($\theta_{1s} = \theta_{1s}^U = \theta_{1s}^L$) cyclic control, respectively. These coaxial rotors have the same cyclic given to both rotors; through two swashplates that are mechanically linked. The inputs control flapping which tilts the thrust vector. This solution is acceptable because the hub moments are not a concern for the articulated rotors.

For hingeless coaxial rotors (such as XH-59 and X2TD), the same solution cannot be used because of the concern of high moments. The coaxial configuration enjoys the benefit of having the roll moment naturally balanced. This means changing the lateral cyclic will only impact the size of the roll moment carried between the rotors. This arbitrary roll moment is characterized as the lift-offset (moment divided by thrust). The trim solution is similar to the classical coaxial rotors except the pitch moment is now solved with the individual rotor longitudinal cyclics ($\theta_{1s}^U \neq \theta_{1s}^L$). This leaves the lateral cyclic (single value for both rotors) for lift-offset, a performance parameter, not a trim variable.

For hingeless rotors with a high flap frequency, lateral cyclic θ_{1c} does not produce pure lateral flapping β_{1s} but also longitudinal β_{1c}. The same is true for the longitudinal cyclic θ_{1s}. For rotors with very high flap frequencies $> 1.5/rev$, the controls nearly reverse. Lateral cyclic θ_{1c} produces mostly longitudinal flapping β_{1c}

and longitudinal cyclic β_{1s} produces mostly lateral flapping β_{1c}. For these rotors, both cyclic controls are used and the lift-offset (LOS) is added to one. It is found best added to the longitudinal cyclic θ_{1s}. The lateral cyclic $\theta_{1c} = \theta_{1c}^U = \theta_{1c}^L$ solves the pitch moment equilibrium. The longitudinal cyclic is used for roll moment equilibrium with $\theta_{1s}^U = \theta_{1s} + LOS$ and $\theta_{1s}^L = \theta_{1s} - LOS$.

The Mars hingeless rotor models also have very high flap frequency, but the trim solution studied is slightly different from convention on Earth. At the Mars flight speeds lift-offset is not necessary. Therefore, fully independent rotor controls are employed. In this manner the hingeless and articulated rotors could be compared at the same hub loads. The six trim targets are total thrust, zero torque, and zero lateral and longitudinal moments on each rotor. The trim variables are six independent rotor controls: collective (θ_o^U and θ_o^L), lateral cyclic (θ_{1c}^U and θ_{1c}^L) and longitudinal cyclic (θ_{1s}^U and θ_{1s}^L).

For the forward flight cases, the target thrust was set to $C_T/\sigma = 0.08$, at an advance ratio of $\mu = 0.10$, which corresponds to a flight velocity of 11.4 kn (5.87 m/s). The longitudinal shaft angle was fixed at $\alpha = 5°$ nose down, and the lateral shaft angle at $\phi = 0^\circ$.

The solution method formulates the equations of motion in the implicit form, and then use an iterative scheme to update the controls. The iterative scheme used in the present work is the Newton-Raphson method. Iterations are performed until the residuals of the force and moment equations meet a user defined convergence criterion. The CA uses a forward finite difference formulation in the form of a Jacobian matrix; initialized about the user input initial guess. The Jacobian matrix is a first-order partial derivative, with the residuals as the dependent variables and the control inputs as independent variables. The Jacobian is computed by perturbing each control independently and calculating the response using uniform inflow and linear aerodynamics for computational speed. Once the Jacobian is calculated, iterations

are conducted to find the desired controls. In the present analysis, increased control update relaxation was used for improved convergence. The update fraction was reduced from 0.8 to 0.5. Convergence is measured by two criteria: (1) how close the trim residuals are to zero and (2) the convergence of the blade tip response between successive iterations. In the present work, the criteria was set to 0.00005 and 0.0005, respectively.

3.3.4 Coaxial Implementation

The comprehensive analysis UMARC has only recently been expanded and validated for aircraft having coaxial rotors spin in opposite directions [58, 59]. The coaxial analysis was implemented with the goal of allowing arbitrary configurations, with multiple rotors spinning in counter-clockwise (CCW) and clockwise directions (CW). The implementation includes interferences, but only from the wake. There is no dynamic interference. The first modification was to make the trim procedure compatible with an arbitrary number of rotors. This is done by summing all the component forces and moments. It is important to ensure consistent sign convention with rotors spinning in opposite directions. In addition, modifications were made to allow for coupled controls. Coaxial rotors have multiple options for trim, and some are only possible with coupled controls. To couple controls, all controls must be in the global azimuth. The global azimuth ψ is simply indicative of time and defined as the counter-clockwise rotor azimuth and the negative of the clockwise rotor azimuth.

$$\psi = \psi^{CCW} = -\psi^{CW} \tag{3.1}$$

To model the clockwise rotor, instead of re-deriving the governing equations with new rotation direction, the rotor calculations are done as a CCW rotor, but the relevant outputs change sign before interacting with the rest of aircraft. Because

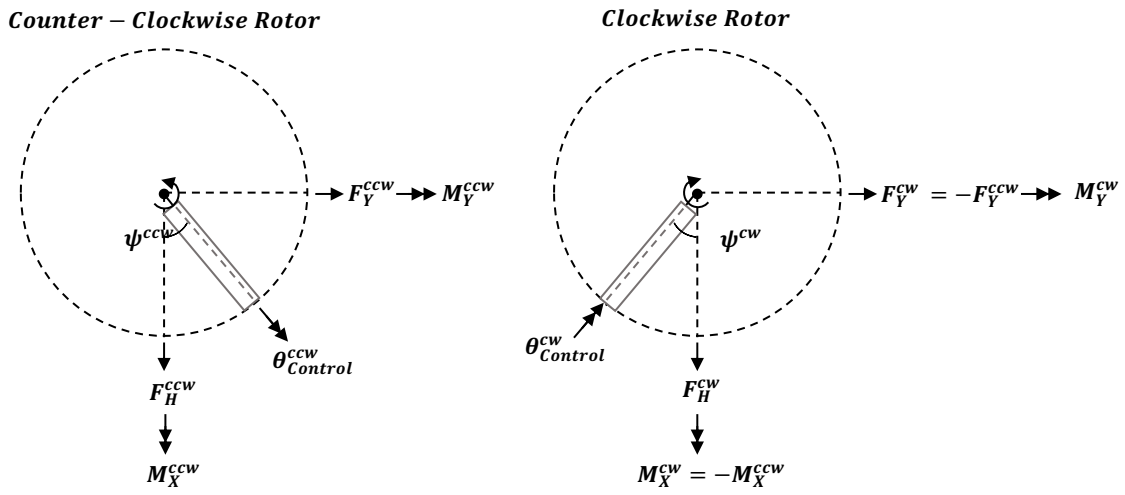

Figure 3.1: Reflected Model showing counter-clockwise and clockwise rotor with reflected control inputs, resulting in similar but reflected loads.

the rotor controls are defined in the global azimuth, the input longitudinal cyclic θ_{1s} must change sign before being used for the CW rotor calculations θ_{1s}^{CW}.

$$\theta_{1s}^{CW} = -\theta_{1s} \tag{3.2}$$

The rotor forces and moments change sign according to the following relationships. These relationships are also illustrated in Figure 3.1.

$$T^{CCW} = T^{CW} \tag{3.3}$$

$$Y^{CCW} = -Y^{CW} \tag{3.4}$$

$$H^{CCW} = H^{CW} \tag{3.5}$$

$$Q^{CCW} = -Q^{CW} \tag{3.6}$$

$$M_Y^{CCW} = M_Y^{CW} \tag{3.7}$$

$$M_X^{CCW} = -M_X^{CW} \tag{3.8}$$

When interfacing with external modules (outside the single rotor calculations), it is

important to also transform fixed-frame coordinates as follows

$$\begin{Bmatrix} x \\ y \\ z \end{Bmatrix}^{CCW} = \begin{bmatrix} 1 & 0 & 0 \\ 0 & -1 & 0 \\ 0 & 0 & 1 \end{bmatrix} \begin{Bmatrix} x \\ y \\ z \end{Bmatrix}^{CW} \tag{3.9}$$

Similar adjustments must be made when interfacing with the free wake, as deformations and sectional airloads are in local rotor azimuth. If coordinates are needed in fixed frame they can be found by Equation 3.9. To summarize, the procedure to implement a clockwise rotor would be:

1. Define the rotor controls in the global azimuth frame (representing time)
2. Reflect the longitudinal cyclic θ_{1s}
3. Calculate the rotor loads as if it were a counter-clockwise rotor
4. Change sign of the resulting rotor loads

Consider two identical isolated rotors, where the only difference is the rotation direction. The forces and moments should be identical but for some with opposite sign. Executing UMARC with the same inputs but for the rotation direction will not produce this expected result. This would result in identical forces and moments. The longitudinal cyclic θ_{1s} must be reflected for the clockwise rotor in order to obtain the right results. For example, Table 3.2 shows how a CCW rotor can be executed in CW mode.

Table 3.2: Controls to model identical rotors spinning in opposite directions.

	CCW	CW
θ_0	10°	10°
θ_{1s}	3°	−3°
θ_{1c}	2°	2°

3.4 Computational Fluid Dynamics

The GPU-Accelerated rotor flow FIELD (GARFIELD) is a University of Maryland in-house three-dimensional computational fluid dynamics (CFD) solver. Development of the CFD solver is not part of this research. How it is coupled to CA is part of this work. The coupling process replaces the lifting-line aerodynamics model of the CA with the high-fidelity CFD model.

A brief description is provided here for completeness, see Refs [82, 83] for details. GARFIELD is an unsteady structured mesh solver for Reynolds Averaged Navier-Stokes (RANS) equations discretized with a cell centered hybrid finite-volume and finite-difference method. Fifth order spatial accuracy and first order temporal accuracy is used. The Diagonalized Alternating Direction Implicit (DADI) approximate factorization preconditioner was applied on the left-hand-side. The Spalart-Allmaras turbulence model was employed.

GARFIELD is an overset grid solver allowing for different mesh sizes, from body-fitted to far field, with increasing cell size. All meshes use the same solver. The CFD is able to read periodic blade motion and deformations, and deform meshes accordingly. This allows for the coupling with the structural analysis. The near-body blade mesh is completely enclosed by a fine nested rotor mesh. Deformations are applied only on the near-body blade mesh. All cells at a radial station receive the same deformations. Deformations are linearly interpolated between the discrete points given by CA. Deformations are provided along a single spanwise line. CA typically uses the quarter-chord line. Once deformed, the near-body blade mesh is then reconnected to the nested rotor mesh at each time step. The details of the CFD/CA exchange are given in Section 3.5. GARFIELD has recently been validated against other state-of-the-art codes and test data [84, 85].

The grids used in the present work are structured and curvilinear. They were

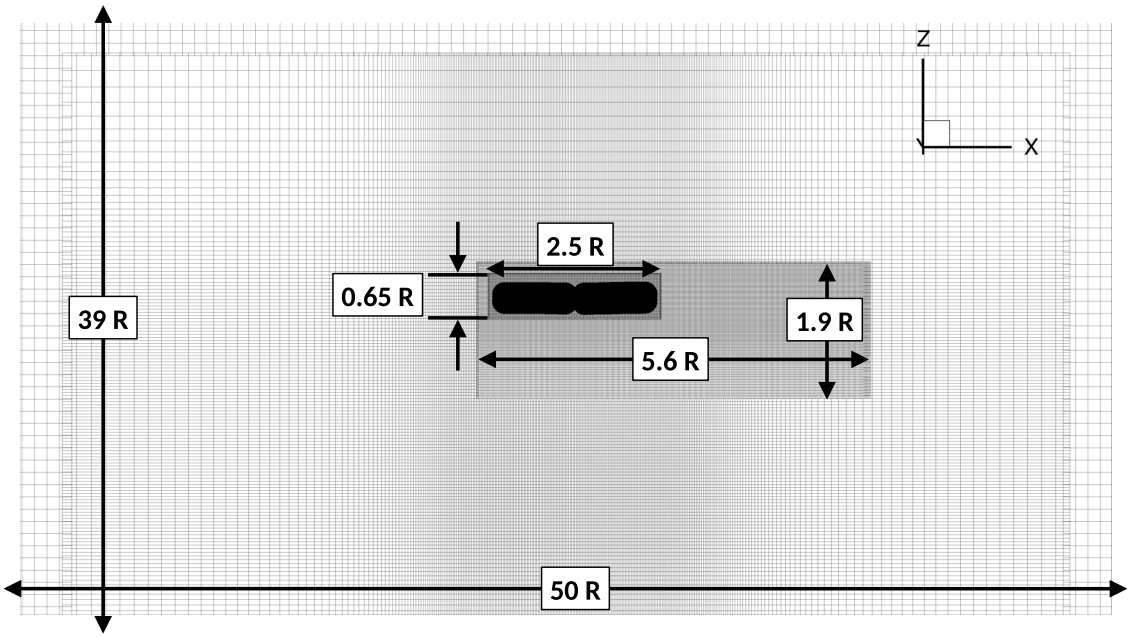

Figure 3.2: Mesh system of the coaxial Mars rotor.

elliptically generated using the blade surface and specified far-field extent as boundary conditions. For the Mars rotor blades, the nearbody mesh has a O-O structure, which is preferable over a C mesh because of the airfoil's abrupt trailing edge and sharp corners. The blade meshes are completely enclosed within a nested rotor mesh, that has a grid size of $0.2c$ (blade root chords). All grid motion and re-connectivity is limited to the blade meshes and this single nested mesh. There are three more layers of background meshes; each with growing cell size. The maximum cell at the far field boundary is $5c$ blade root chords. The mesh extends a total distance of $87c$ in the plane of the rotor and $68c$ in the vertical direction. Each blade nearbody mesh has 2.9 million points with the total mesh size of 34.73 million points. The mesh setup is shown in Figure 3.2.

The CFD solutions were all conducted with 32 sub-iterations, a Courant-Friedrichs-Lewy (CFL) number of 5.0, and an azimuthal step size of a quarter of a degree, $\Delta\psi = 0.25°$. These values were selected to give suitable convergence of at lease two orders of magnitude. The calculations were carried out on the Maryland

Table 3.3: CFD grid convergence results at $Re_{Tip} = 10,000$, $M_{Tip} = 0.07$, and $C_T/\sigma = 0.18$.

Grid	Time/step	FM
Fine	63.16 s	0.5011
Medium	39.08 s	0.4906
Coarse	29.46 s	0.4645

Advanced Research Computer Center (MARCC) cluster, Blue Crab. Each revolution took roughly 18 hours using three Nvidia K80 GPUs and 36 CPUs.

A convergence study was conducted for mesh refinement. Accurate resolution of skin friction is particularly important at low Reynolds numbers and is highly dependent on wall normal mesh spacing. As the mesh becomes finer, the accuracy is improved but there is also an increase in computational time. These have to be balanced. Single rotor hover was used for the convergence study. The Figure of Merit (FM) was chosen as the metric. Wall normal spacings of 0.0005, 0.001, and 0.005 chord were compared. The rotor reached steady state by six revolutions. The thrust and torque over the final revolution were used to calculate the Figure of Merit. A summary of the results are given in Table 3.3. The medium mesh was selected for the remaining calculations because of similar accuracy as the fine mesh with only 62% of the time.

3.5 CFD/CA Coupling: Overview

CFD/CA coupling for rotorcraft allows for the combination of CFD with structural dynamics and trim. The analyst has to exchange rotor motions and airloads. The motions include flexible deformations and controls. The underlying algorithm require the use of lifting-line airloads from CA for efficient convergence of successive substitution. The formulation is found in Ref [80].

The CA calculates structural dynamics, trim controls, and lifting-line airloads.

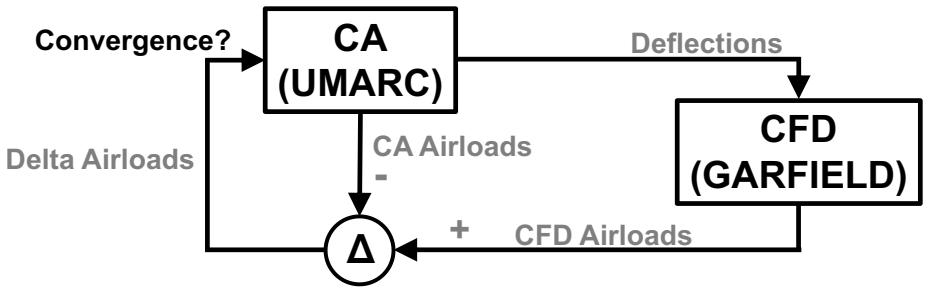

Figure 3.3: CFD/CA coupling with delta method.

The lifting-line airloads are used only as a pre-conditioner. In fact any airload calculation that is sensitive to blade deformations (i.e. supply aerodynamic damping) suffice; lifting-line is not necessary per se. Quasi-steady airloads (including non-circulatory) with uniform inflow are admissible just as well. Thus, these airloads are called the internal airloads. Coupling is achieved by passing blade deformations from CA to CFD and the sectional airloads back from CFD to CA. This method is also termed loose coupling in the rotary-wing community but that nomenclature can be confusing with loose coupling of fixed-wing literature that bears no relation to the present method.

The first delta formulation was introduced by Tung, Caradonna, and Johnson in 1986 [86] (termed loose coupling at the time). The modern method emerged in 2006 from Datta, Sitaraman, Chopra, and Baeder [80, 87] and Potsdam, Yeo, and Johnson [88]. They differed in implementation of the updates, but was the same underlying method. The method begins with a baseline comprehensive analysis (with a non-CFD aerodynamic model, perhaps lifting-line). This creates the first internal airloads F^0_{AE} and deformations u^0. The deformations u^0 are passed to CFD, which then calculates new airloads $F^1_{CFD}(u^0)$. These deformations include flexibility and controls. CFD airloads are passed back to CA as delta airloads. The deltas F^1_Δ are

calculated by subtracting the CA airloads (F^0_{AE}) from the CFD airloads $F^1_{CFD}(u^0)$.

Comprehensive analysis is performed again. But this time the delta airloads are applied in addition to the internal airloads $F^1_{AE} + F^1_{\Delta}$. F^1_{Δ} remains fixed. F^1_{AE} changes with controls to achieve trim. It also provides aerodynamic damping. The process is repeated until the deformations and airloads converge. And at that point the F_{AE} and F_{Δ} becomes equal to F_{CFD} A diagram of this procedure is shown in Figure 3.3. Convergence is usually achieved in $5 - 6$ iterations. Figure 3.4 shows a sample of delta airloads during an exchange from CFD to CA.

For the Mars rotor cases, after the initial CA solution, two revolutions of CFD are allowed to let the solution settle into periodicity before the first coupling, thereafter a single revolution in CFD is sufficient. Blade deformations are calculated at 120 radial stations and at every 2.5° azimuth. The deformations are calculated exactly from underlying space and time shape functions. Once inside CFD, these deformations are interpolated linearly in the spanwise direction and spectrally in the azimuthal direction (to avoid discontinuities in grid velocities) before used for mesh motions. CFD airloads are calculated at 155 radial stations and every 0.25° azimuths. These are passed back to CA which interpolates them linearly.

3.5.1 CFD/CA Coupling: Relaxation

Flap damping stems from quasi-steady aerodynamics and is proportional to air density. The delta method was designed to take advantage of this damping. This damping nearly disappears on Mars due to the reduced density. Therefore, it was found beneficial to relax the delta airloads by a fraction $r = 0.5$ to minimize oscillations and allow for more stable convergence.

Each CA solution is now executed twice, a second execution is with fixed controls. The fixed controls are a relaxed update from the previous controls. The formulation is shown by equation 3.10, where r is the relaxation factor.

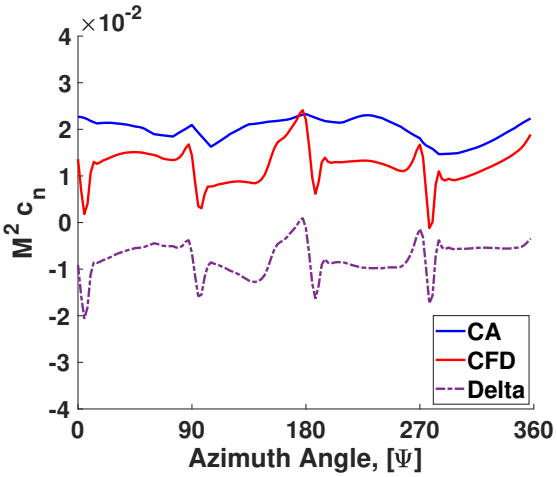

(a) Normal force.

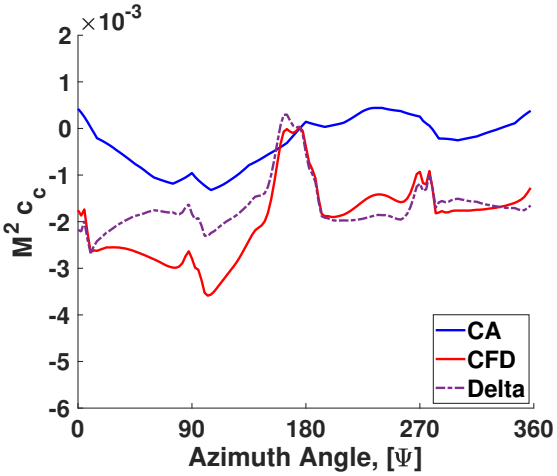

(b) Chord force.

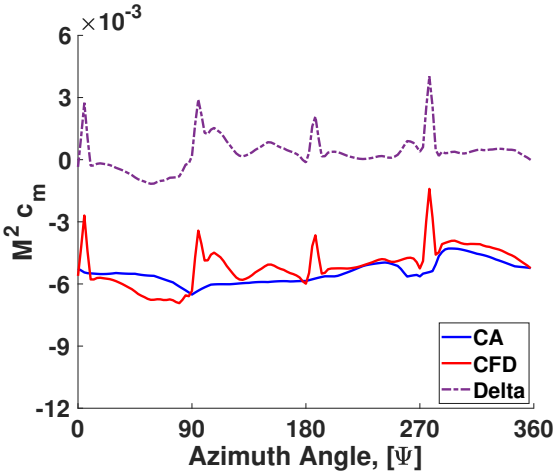

(c) Quarter-chord pitching moment.

Figure 3.4: A sample of sectional airloads; from CA and CFD, and delta needed for CFD/CA coupling; delta = CFD - CA.

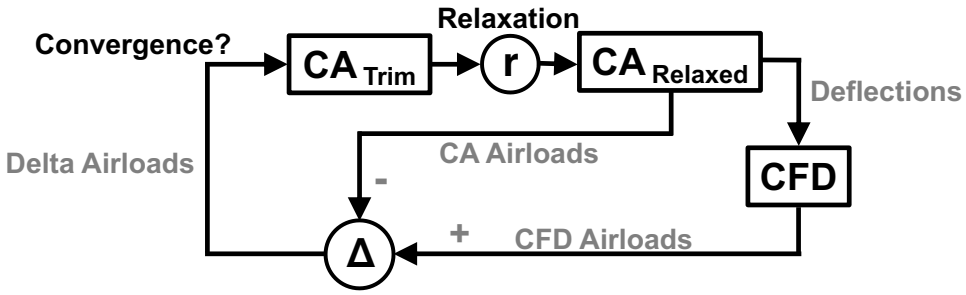

Figure 3.5: CFD/CA coupling delta method with relaxation.

$$\theta_{relaxed} = \theta_{n-1} + r \times (\theta_n - \theta_{n-1}) \tag{3.10}$$

From this solution, the deflections are passed to the CFD for the next coupling iteration, a diagram of this coupling procedure is shown in Figure 3.5. It is important to note: (1) the internal, or CA, airloads used in the delta calculation are now from the $CA_{relaxed}$ solution since these deflections are used in CFD, and (2) the same delta airloads, from the previous iteration, are applied both CA_{trim} and $CA_{relaxed}$. The delta airloads are not updated or changed between the two CA executions within a coupling iteration. The relaxation reduced oscillations in the coupling iterations and allowed for convergence in approximately 10 coupling iterations.

3.5.2 CFD/CA Coupling: Coordinate Systems

The structural model is a beam which passes deformations along the blade quarter-chord line to CFD. The undeformed quarter-chord line is also passed from CA to CFD. The structural dynamics outputs radially and azimuthally varying deformations.

$$u, \quad v, \quad w, \quad v', \quad w', \quad \phi \tag{3.11}$$

Table 3.4: Relaxed coupling scheme.

Step	CA Iteration	CFD Iteration	Delta
Baseline	CA^0		
	$F^0_{AE}, \quad u^0, \quad \theta^0$	$F^0_{CFD}(u^0, \theta^0)$	$\Delta^0 = F^0_{CFD} - F^0_{AE}$
1	$CA^1(\Delta^0)$		
	$F^1_{AE}, \quad u^1, \quad \theta^1$		
	$\theta^1_R = \theta^0 + r \times (\theta^1 - \theta^0)$		
	$CA^1_R(\Delta^0, \theta^1_R)$		
	$F^1_{AE_R}, \quad u^1_R, \quad \theta^1_R$	$F^1_{CFD}(u^1_R, \theta^1_R)$	$\Delta^1 = F^1_{CFD} - F^1_{AE_R}$
2	$CA^2(\Delta^1)$		
	$F^2_{AE}, \quad u^2, \quad \theta^2$		
	$\theta^2_R = \theta^1_R + r \times (\theta^2 - \theta^1_R)$		
	$CA^2_R(\Delta^1, \theta^2_R)$		
	$F^2_{AE_R}, \quad u^2_R, \quad \theta^2_R$	$F^2_{CFD}(u^2_R, \theta^2_R)$	$\Delta^2 = F^2_{CFD} - F^2_{AE_R}$
	...	...	...
k	$CA^k(\Delta^{k-1})$		
	$F^k_{AE}, \quad u^k, \quad \theta^k$		
	$\theta^k_R = \theta^{k-1}_R + r \times (\theta^k - \theta^{k-1}_R)$		
	$CA^k_R(\Delta^{k-1}, \theta^k_R)$		
	$F^k_{AE_R}, \quad u^k_R, \quad \theta^k_R$	$F^k_{CFD}(u^k_R, \theta^k_R)$	$\Delta^k = F^k_{CFD} - F^k_{AE_R}$

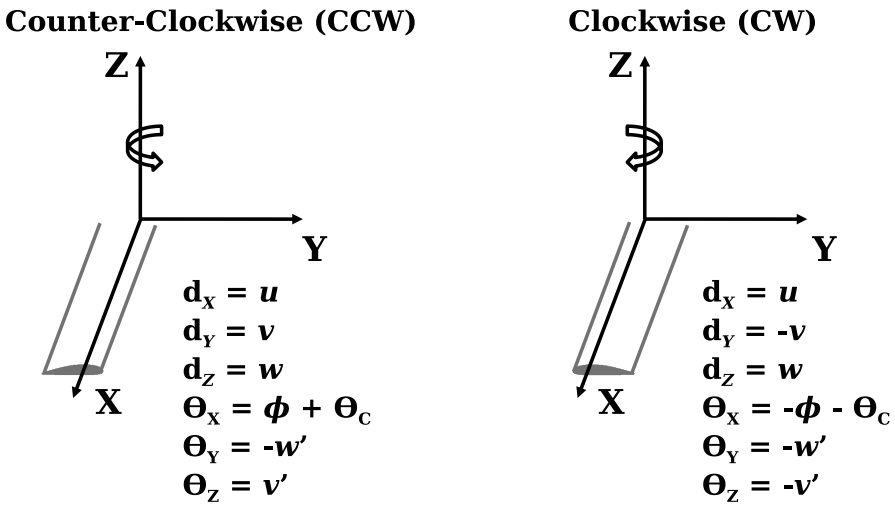

Figure 3.6: Interface convention for deformation transfer from CA to CFD.

where each is a function of (r, ψ). u, v, w are the axial, lead-lag, and flap deflections defined in the blade undeformed frame. v', w' are the lead-lag and flap-up slopes, and ϕ is the nose-up torsion plus the control angle. These deformations are transformed into the interface frame of reference.

$$d_x, \quad d_y, \quad d_z, \quad \theta_x, \quad \theta_y, \quad \theta_z \tag{3.12}$$

The slopes are assumed to be rotations, consistent with the Euler-Bernoulli assumption. The transformations are given in Figure 3.6. Note the relations change for counter-clockwise and clockwise spinning rotors. CA operates in the local rotor azimuth for both rotation directions. CFD uses the global (counter-clockwise) azimuth. The deformations for the clockwise rotor must be flipped from local to global azimuth.

For the exchange of airloads, similar steps must be followed. The clockwise airloads must be flipped from global to local rotor azimuth. The airloads are sectional normal and chord forces, and the sectional quarter-chord pitching moment in the

on-dimensional form (Eq. 3.13).

$$M^2 c_n = \frac{dN/dr}{\frac{1}{2}\rho a^2 c} \qquad M^2 c_c = \frac{dC/dr}{\frac{1}{2}\rho a^2 c} \qquad M^2 c_m = \frac{dM_{25}/dr}{\frac{1}{2}\rho a^2 c^2} \tag{3.13}$$

where M is the incident Mach number, a is the speed of sound, ρ is the density, c is the local chord length, r is the radial coordinate, and N, C, and M_{25} are the normal and chord force (i.e. force per span, N/m or lbf / ft), and pitching moment about quarter-chord (i.e. moment per span, N-m/m or lbf-ft/ ft), respectively. The airloads are in the deformed frame. The sign convention of normal force is positive up (to upper surface), chord force is positive to leading-edge, and pitching moment is positive nose-up. The chord and normal axes, and quarter-chord are all well defined. In rotors, the incident Mach number and the airfoil coefficients–c_n, c_c, and $c_{m_{25}}$–are strictly undefined in CFD or in test (since local velocities are unknown), the combined $M^2 c$ form is always well-defined (since temperature and hence speed of sound is known).

3.6 Model Development

This section describes the development of the comprehensive model for UMARC, including both the structural and aerodynamic properties.

3.6.1 Structural Properties

The comprehensive analysis structural model requires both stiffness and inertial properties as inputs. The model's structural properties are derived from the rotor tested in the vacuum chamber. The blades are made of carbon fiber composites and oven cured. A more detailed description of the blade design and fabrication process is included in Chapter 2. The flapwise stiffness EI_F was measured, the chordwise and torsional stiffnesses were predicted by a 3D finite element analysis. The material

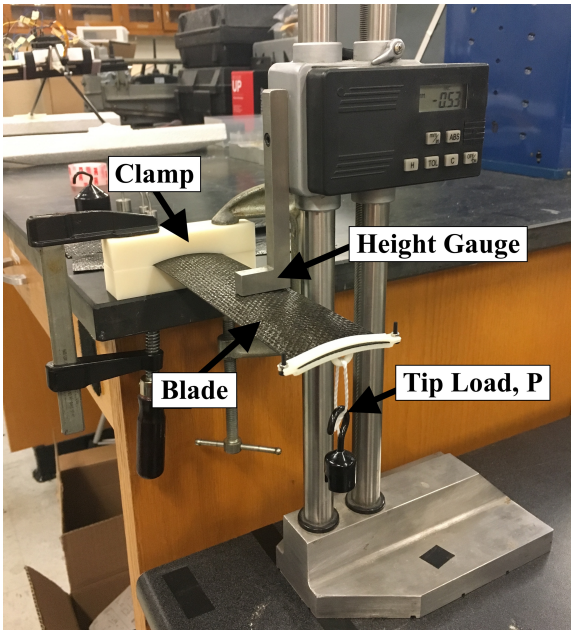

Figure 3.7: Experimental setup with height gauge to measure blade flapwise stiffness under static deflections.

properties were calibrated with the flapwise data. Non-rotating frequencies were compared between measurement and prediction.

Measuring structural properties is difficult for blades that are too stiff because of the very small deformations. This was a problem for chordwise and torsion stiffnesses. The flapwise stiffness was measured by loading the blade, measuring the deflection, and using the Euler-Bernoulli result for a tip load:

$$\delta = \frac{Pl^3}{3EI_F} \tag{3.14}$$

Load P was applied along the mid-chord at the blade tip (a distance l from the root), and the resulting deflection δ was measured. For a symmetric section and $\pm 45°$ (quasi-isotropic) layup the elastic axis is at mid-chord. The blade root was clamped. Figure 3.7 shows the setup. A height gauge is used to measure the deflection. Three loads were applied and deflections measured at two spanwise locations. Each trial was repeated three times for a total of eighteen individual data points. The deflection

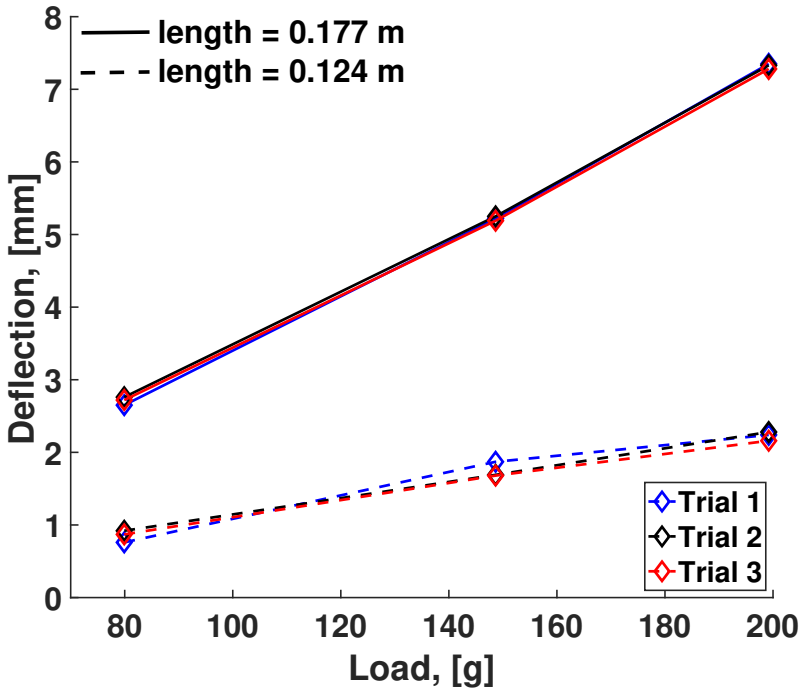

Figure 3.8: Deflection versus load data from flapwise stiffness measurements with loading at two spanwise locations.

is shown in Figure 3.8. The blade flapwise stiffness was found to be 0.539 Nm^2 with a standard deviation of 0.039.

With flapwise stiffness measured, a 3D finite element analysis (FEA) tool X3D was used to calculate chordwise and torsional stiffnesses. A model was created using the manufacturer provided material properties. The model was loaded and flapwise stiffness extracted. The manufacturer properties resulted in a flapwise stiffness of $EI_F = 0.90$ Nm^2. This is a 67% over-prediction. The material inputs were then corrected to match the measured flapwise stiffness. A 40% reduction in Carbon Fiber properties was needed. Once calibrated, the model was loaded and used to extract the chordwise and torsional stiffnesses. The chordwise stiffness was calculated to be 7 Nm^2 and the torsional stiffness was 0.155 Nm^2/rad.

Figure 3.9 shows the predicted deflection for the three loading conditions. The solid lines are 3D FEA results and the symbols are equivalent beam results. The

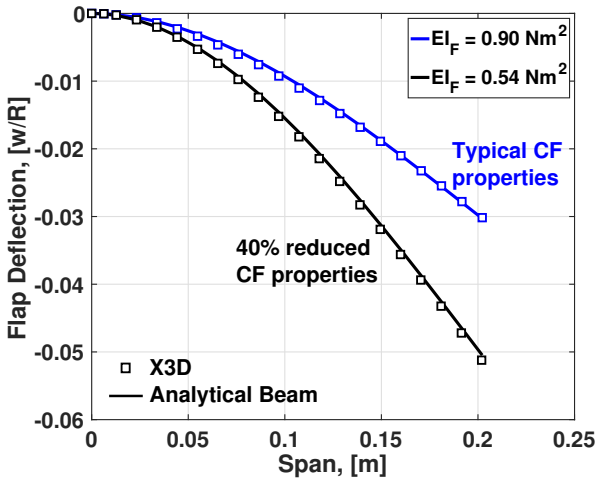

(a) Flap deflection under load; $F_z = 2$ N.

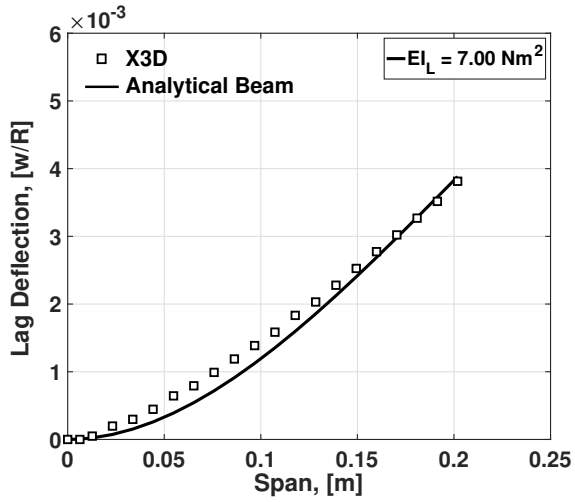

(b) Lag deflection under load; $F_y = 20$ N.

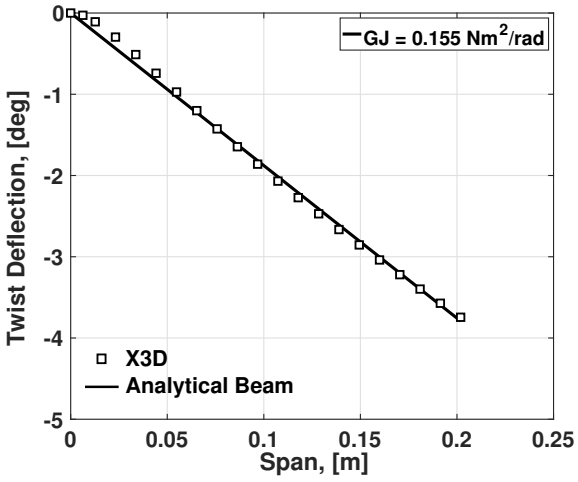

(c) Twist deflection under load; $M_x = 1$ Nm.

Figure 3.9: Mars rotor blade stiffness properties calculated in X3D.

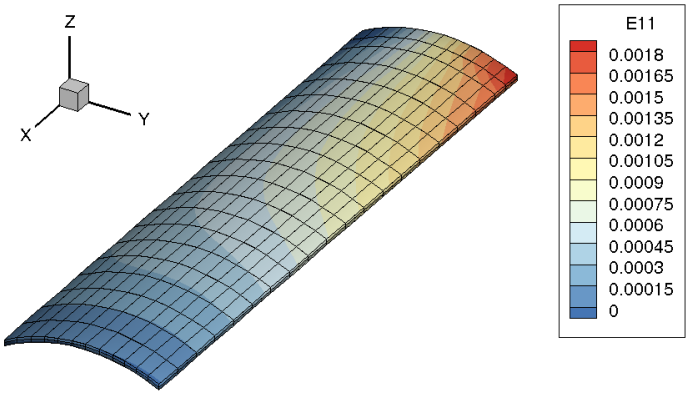

Figure 3.10: Blade strains under centrifugal loading at 3000 RPM; Tip to the left, root to the right, leading edge facing reader; E11 is axial strain.

two match for the same properties, which means the stiffnesses can be backed out from the equivalent beam. The blue solid line uses manufacturer provided typical material properties in 3D FEA. The black solid line uses corrected properties based on match with test data. Then the black symbols give the right equivalent beam from which stiffness can be extracted.

Measured and computed blade mass $10.16g$ agreed without correction. X3D was also used to find flap inertia. X3D was used to calculate blade stresses at 3000 RPM (25% over speed), in order to verify structural stress/strains were within limits. The axial strain $E11$, is shown in Figure 5.6(b). The strains are modest due to light weight with a maximum of 1800 microns. The highest stress and strain occurs at the leading edge near the root due to the mid-chord center of gravity (C.G.)causing centrifugal force to pull the blade back (lag).

The last input for the structural model is inertia. The cross-sectional area moment of inertia and mass per span are needed as input. The input for moment of inertia is the radius of gyration. The axes are flap and lag. The radius of gyration is

Table 3.5: CA structural inputs.

Parameter	Value
EI_F, Nm^2	0.539
EI_L, Nm^2	7.00
GJ, Nm^2/rad	0.155
CG Offset, in	1 (0.50c)
k_F, ft	0.003112
k_L, ft	0.063763
Mass per span, slug/ft	0.000944
Flap Inertia, slug ft^2	0.000141798

given by:

$$I = Ak^2; \qquad k = \sqrt{\frac{I}{A}} \tag{3.15}$$

where I is the area moment of inertia, A is the area, and k the radius of gyration. For a blade cross-section with axes x and y corresponding to lag and flap directions, respectively, the area moment of area is given by the equations:

$$I_x = \iint_A y^2 \, dx \, dy \quad \text{and} \quad I_y = \iint_A x^2 \, dx \, dy \tag{3.16}$$

For integration, the double integral was converted to a definite integral about a closed curve using Green's Theorem and carried out by the midpoint method. It was found if a rectangle with the same chord and thickness were used, a 70.23% under-prediction of flap radius of gyration would result, while the chordwise would still be correct. So the camber affects flap inertia significantly. The structural inputs are summarized in Table 3.5.

The first step was to validate non-rotating blade frequencies. The blade was clamped at the root, and a shake test was conducted. The setup is shown in Figure 3.11. A harmonic shaker was mounted close to the root at 20%R, and a smooth continuous frequency sweep from 10 Hz to 300 Hz was input to find any resonances in this range. Higher modes could not be excited reliably. Blade deflection

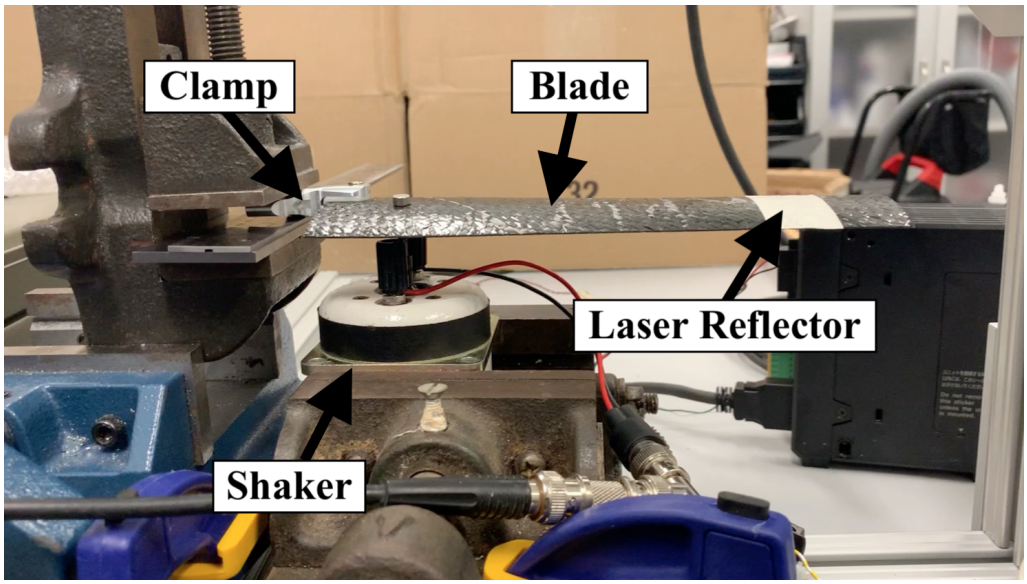

Figure 3.11: Shake test for measurement of non-rotating frequencies.

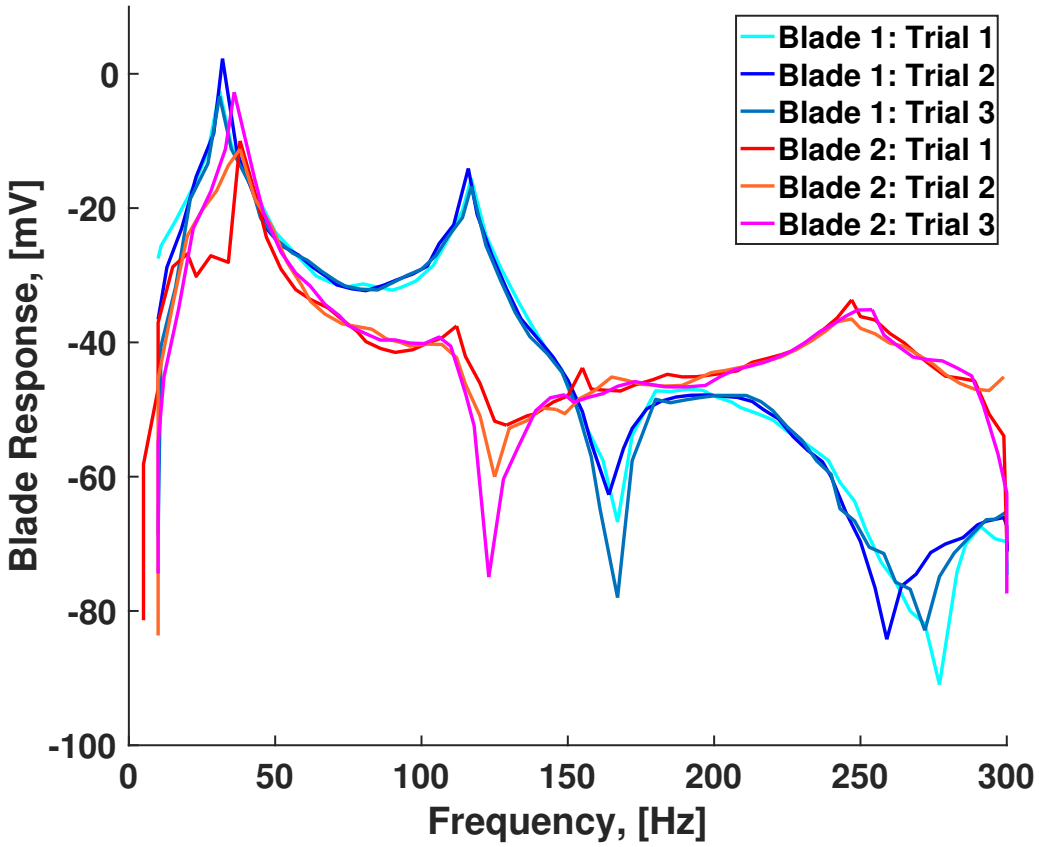

Figure 3.12: Shake test data; blade frequency response (measured near blade tip with laser height gauge) to shaker input frequency sweep.

Table 3.6: Non-rotating blade frequencies.

Mode	Measured [Hz]	Predicted [Hz]	Percent Error
1	34.3	40.8	19.0%
2	114.8	88.1	23.3%
3	166.0	160.2	3.5%
4	257.7	243.5	5.5%

was recorded, at 80%R, using a laser height gauge and reflector tape. Two blades were tested; each with three trials. The resulting transfer functions are shown in Figure 3.12. The first four modes were captured easily and are shown in Table 3.6, along with the predicted values from the structural model. The analysis picked up the modes below 300 Hz, and the predictions match reasonably well. The structural inputs were left as is, without any correction.

3.6.2 Aerodynamic Properties

3.6.2.1 Overview

The lifting-line aerodynamic model requires 2D sectional aerodynamic coefficients, c_l, c_d, c_m, at the section operating conditions (angle of attack, Reynolds number, and Mach number). Unique Mars conditions mean special wind-tunnels are required to measure these quantities. There are such wind-tunnels [25, 27, 89], but given the constraints of resources and time, these quantities were found numerically instead. A computational study was conducted to simulate flows at the low Reynolds numbers ($Re < 10^4$) in order to accurately extract the airfoil sectional coefficients.

The two-dimensional (2D) computational fluid dynamics tool used is a Reynolds-averaged Navier-Stokes solver, Transonic Unsteady Rotor Navier-Stokes 2D (TURNS2D), developed, matured, and validated over the last two decades at the University of Maryland. TURNS2D uses a dual-volume formulation, where the inviscid fluxes are computed using a third-order MUSCL reconstruction scheme and the viscous

fluxes are computed with a second-order central difference scheme. TURNS2D was originally developed for higher Reynolds number cases, but has more recently been validated at low Reynolds numbers [29], including the range of interest on Mars ($Re < 10^5$).

A key feature in TURNS2D for low speeds is the inclusion of low Mach number pre-conditioning [90]. A special pre-conditioning is needed when the flow becomes near incompressible to help with convergence. Additionally, the software also includes a correlation-based laminar-turbulent boundary-layer transition model [91]. Previous research has identified the flow at these conditions to have tendencies to begin as laminar and transitioning to turbulent while attached to the airfoil; meaning a transition model is necessary for accurate modeling.

A broad range of conditions were tested to ensure complete coverage of the rotor operating conditions. Angle of attack sweeps were run at Re = 1000, 3000, 5000, 7000, and $10,000$, and for each Reynolds number the Mach number was varied 0.05, 0.10, and 0.30, for a total of 15 different operating conditions. Angle of attack sweeps were from $-18°$ to $+18°$ at each operating condition. The mean c_l, c_d, c_m data for each operating condition was compiled into tables for the CA. The blade is divided into twenty spanwise segments and different Reynolds number tables are used over each. Thus, Re variation is modeled by varying airfoil decks, instead of a three-dimensional table look-up.

3.6.2.2 Mesh Definition

The airfoil geometry is simple – 2% thick 6% cambered circular arc. The leading and trailing edges are deliberately sharp, with nearly right angled corners. Meshing is important to generate good quality solutions around these corners. An O-mesh allowed for the best fit around the sharp corners. Figure 3.13 shows the final airfoil mesh. The close-ups of the leading and trailing edges are shown in

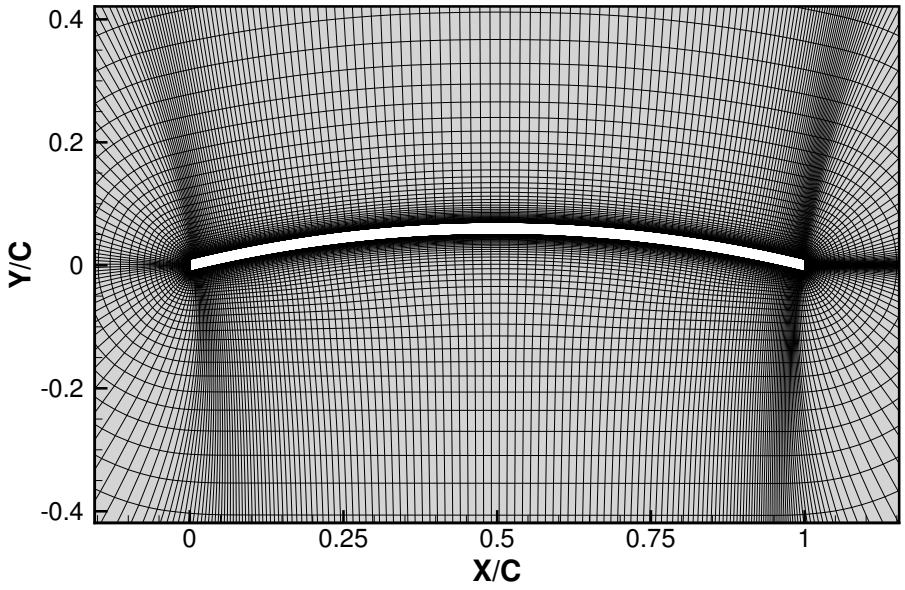

Figure 3.13: 2D mesh with wall spacing 0.001% of chord and extending 30 chord lengths.

Figures 3.14. Generating this mesh was not straight forward. Care was taken to ensure low skew. The mesh underwent seven iterations of stretching, smoothing, and spacing. Two different wall normal spacings were tested 0.01%c and 0.001%c. Both showed similar results. Because computational time was similar, the finer mesh was used for all calculations. The mesh contained 401 grid points in the wrap-around direction and 104 grid points in the wall-normal direction. Within the boundary layer, the wall normal spacing was 0.001% of the chord length, which is a crucial factor in capturing the boundary layer effects. The outer boundary is set at 30 chord lengths from the airfoil surface.

3.6.2.3 Results

The coefficients from the CFD studies are used as inputs for CA. Naturally only the mean value of each angle of attack can be used in airfoil decks.

In the low Reynolds number range, airfoils have a significant amount of un-

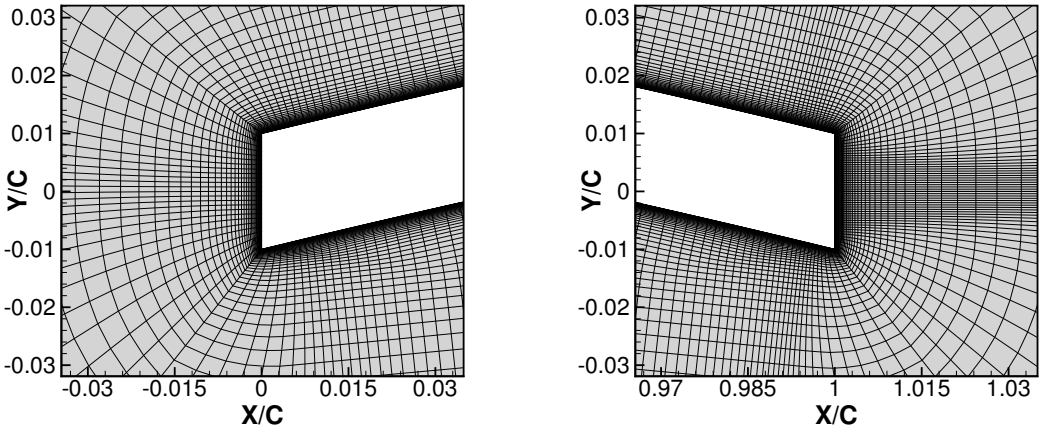

(a) Leading Edge.

(b) Trailing Edge.

Figure 3.14: Close up of mesh near leading and trailing edges.

steady vortex shedding from boundary layer separation. These impact the sectional coefficients of the airfoil. For example, the time history of the coefficients for the airfoil at an angle of attack of 9°, Re = 5000, and Ma = 0.30, is shown in Figure 3.15. All three coefficients show periodic oscillations, but with greater magnitudes in the lift and pitching moment. This is caused by the shedding of vortices along the upper surface of the airfoil, as seen in Figure 3.16. When the low pressure vortex is attached to the upper surface, Figure 3.16(a), the lift increases, but as soon as the vortex separates the pressure on the upper surface increases and the lift drops, Figure 3.16(b). Additionally, the vortex traveling along the chord length impacts the center of pressure and therefore alters the pitching moment. The magnitude of the unsteady effects changes with angle of attack. Figure 3.17 shows the aerodynamic coefficient variation over angle of attack. The vertical bars show the magnitude of oscillations at each angle while the symbol denote the mean. Unsteadiness increases dramatically at high or negative angles of attack. The 2D airfoil table inputs for CA can only include the mean value. The unsteady aerodynamics in CA will capture blade motion and dynamic stall, but not low Reynolds number vortex shedding.

Henceforth only the steady values at each angle of attack are shown. Figure 3.18

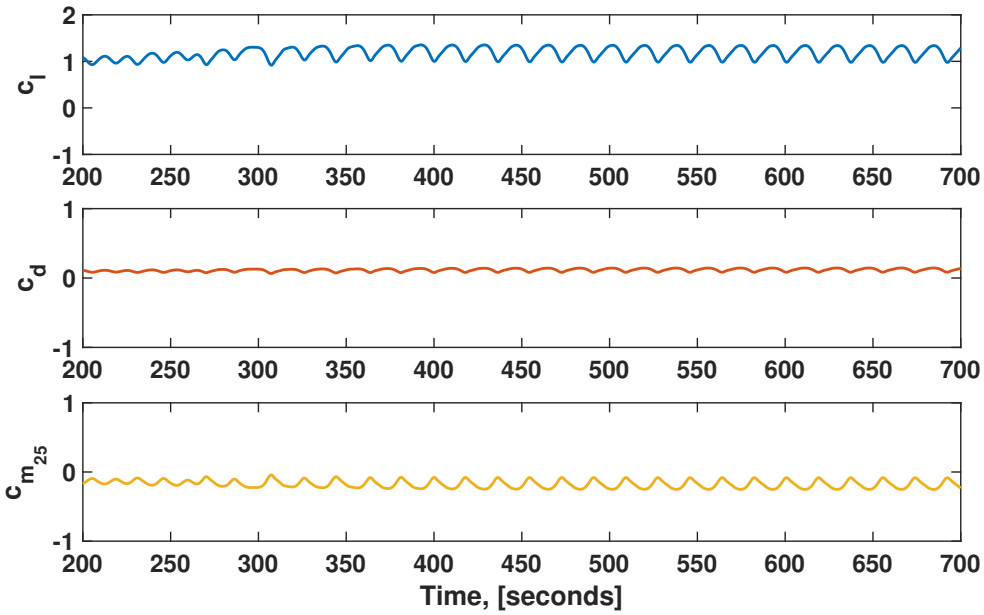

Figure 3.15: Time History of Coefficients at $\alpha = 7°$, $Re = 5000$, and $M = 0.05$.

shows the coefficient of lift versus angle of attack data for all tested Reynolds and Mach numbers. The symbols denote Mach number and colors denote Reynolds number. It can be seen that the colors form bands indicating an independence of Mach number and strong dependence on Reynolds number. This is expected for incompressible flow at low Reynolds numbers. As Reynolds number increases, the lift curve slope increases and the maximum coefficient of lift also increases. The Reynolds number trends are clearly visible for positive angles of attack, but for negative angles the trends are not clear and the values collapse toward to a single band. Figures 3.19. 3.20, and 3.21 show the same lift data, but separated by Mach number; the Reynolds number trends are easier to distinguish.

Next, Figure 3.22 shows the coefficient of drag versus angle of attack. Again, the expected low Reynolds number characteristics are evident. The variations in Reynolds number are clear, while the Mach number has little impact. The zero lift drag c_{d_o} decreases with Reynolds number, and the drag bucket has similar shapes for all except the lowest $Re = 1000$. This Reynolds number has a much higher c_{d_o}

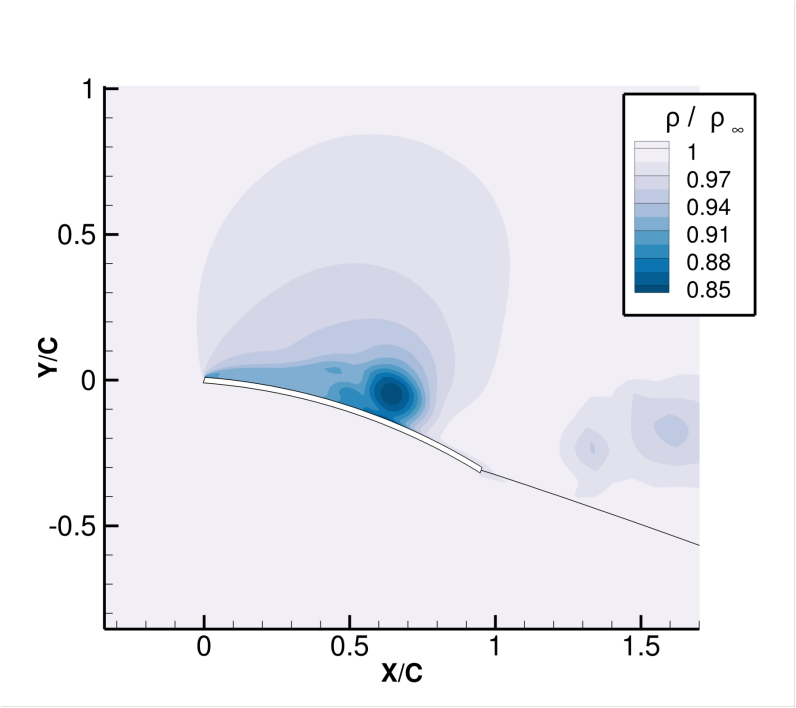

(a) Vortex attached to upper surface.

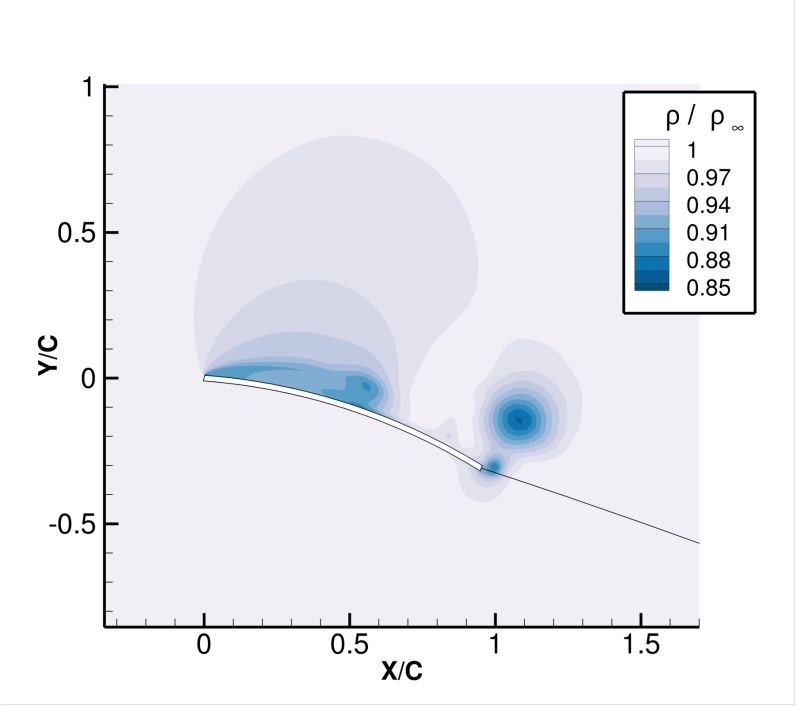

(b) Vortex separated and rolled off upper surface.

Figure 3.16: Vortex shedding and unsteady behavior of thin cambered airfoil at $\alpha = 7°$, $Re = 5000$, and $M = 0.05$; flow field shows local density normalized by far-field density.

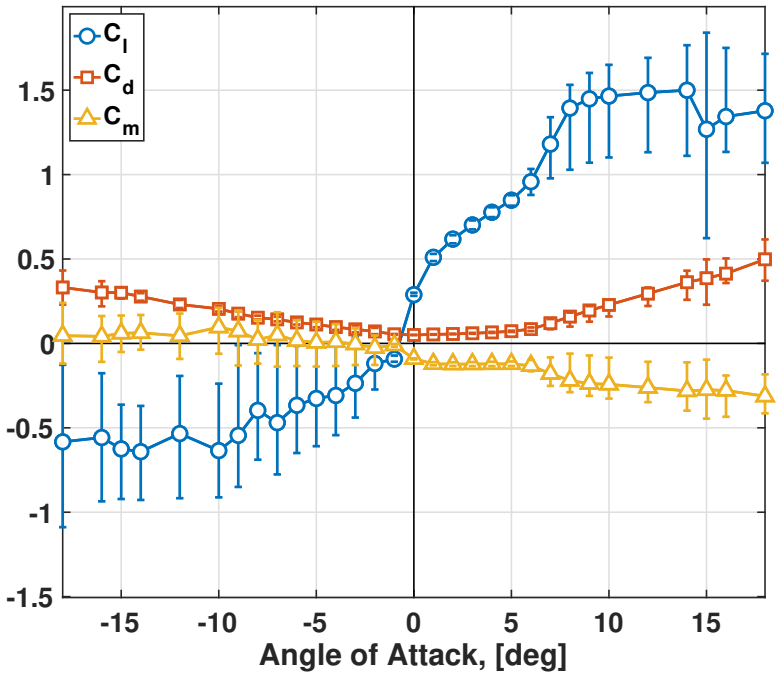

Figure 3.17: Aerodynamic coefficients of circular arc airfoil with 6% camber 2% thickness at $Re = 5000$, $M = 0.05$; vertical bars denote maximum and minimum oscillations at each angle of attack.

and a wider bucket. Figures 3.23. 3.24, and 3.25 show the same data, but separated by Mach number; the Reynolds number trends are easier to distinguish.

Figure 3.26 shows the coefficient of pitching moment about the quarter-chord versus angle of attack. The symbol and color schemes remain the same, with symbols denoting Mach numbers and colors denoting Reynolds numbers. For positive angles of attack, all conditions have a large negative pitching moment but interestingly, the lower Reynolds numbers are beneficial, for the smallest pitching moment. For lift and drag, it was beneficial to increase the Reynolds number, but not for pitching moments. Figures 3.27. 3.28, and 3.29 show the same data, but separated by Mach number; the Reynolds number trends are easier to distinguish. For negative angles of attack, the pitching moment increases as angle of attack decreases, but there are no clear trends.

The influence of Reynolds number on airfoil performance is more apparent

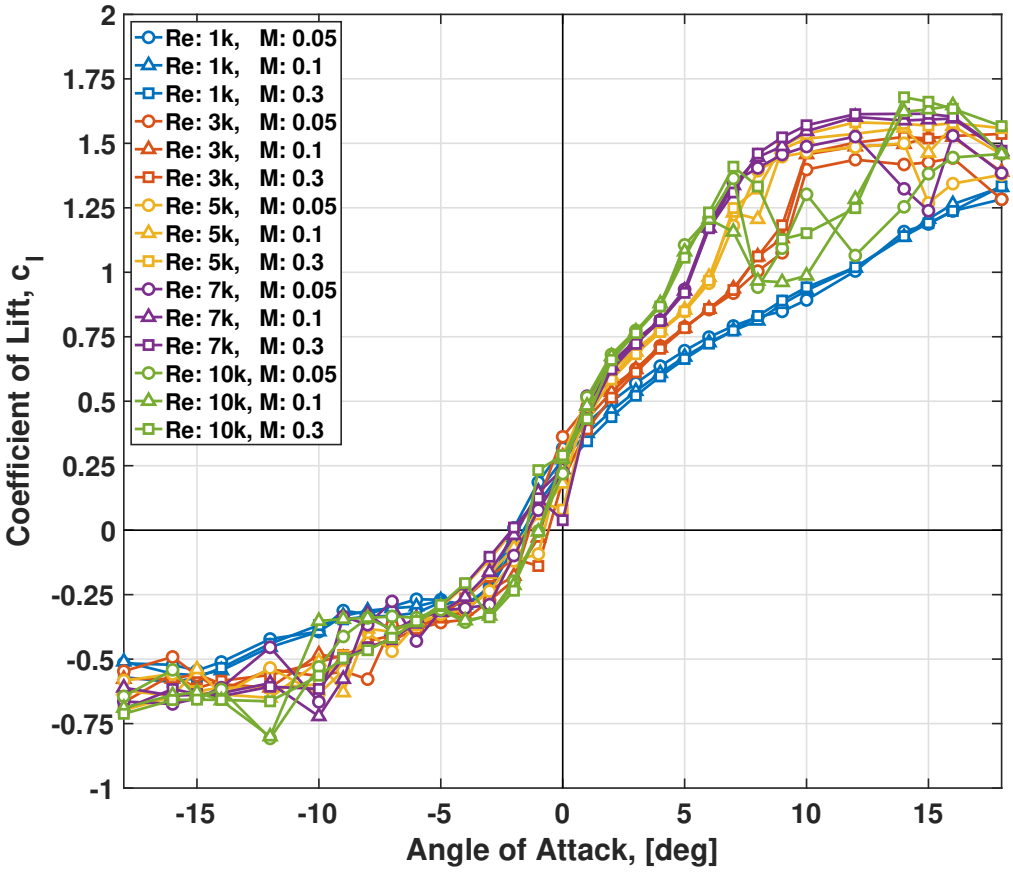

Figure 3.18: Coefficient of lift at all tested Reynolds and Mach numbers.

in the lift to drag ratio. The lift to drag ratio at one Mach number is shown in Figure 3.30 for example. The maximum nearly quadruples between $Re = 1000$ and $Re = 10,000$. The peaks for all Reynolds numbers occur near angle of attack $\alpha = 5° - 7°$. From these results it is evident that maximizing the blade Reynolds number is crucial for performance on Mars.

3.6.3 Aerodynamic Center Movement

The location of the aerodynamic center has enormous implications on rotor aeroelastic stability. From thin airfoil theory (valid for inviscid, incompressible flow) the aerodynamic center (AC) is at quarter-chord (25%c). At high Re regimes

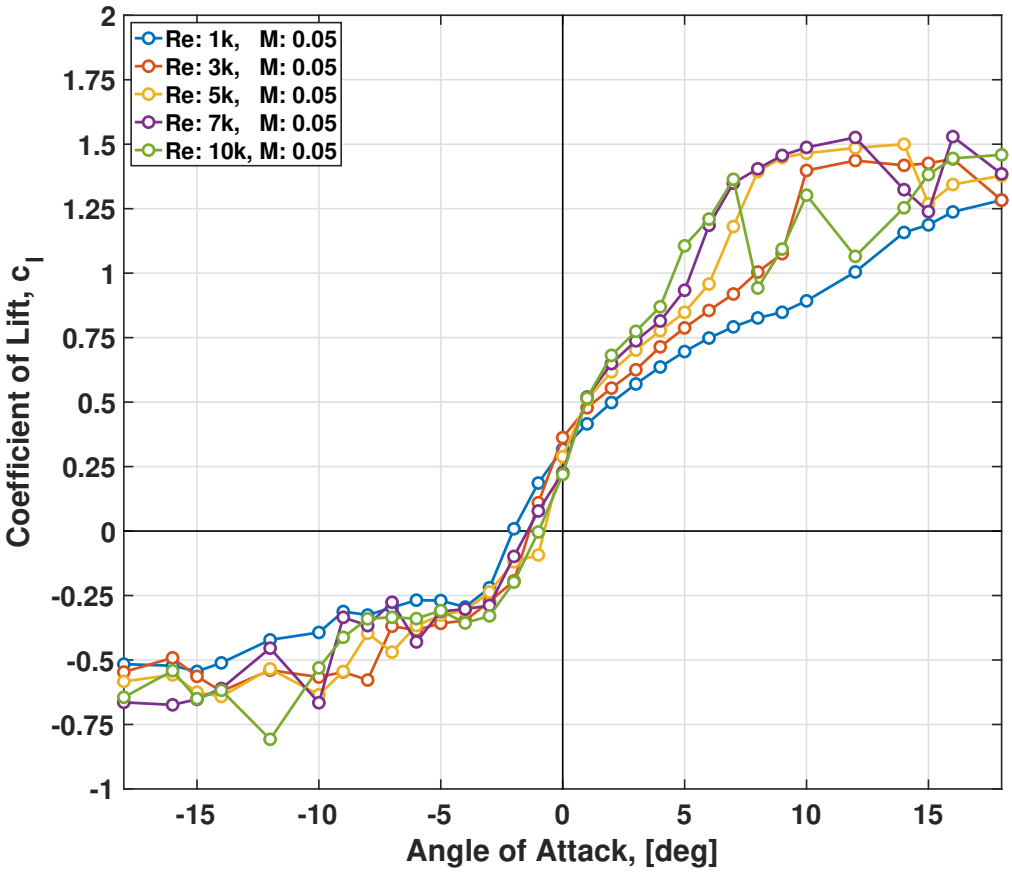

Figure 3.19: Coefficient of lift at $M = 0.05$ with all Reynolds numbers.

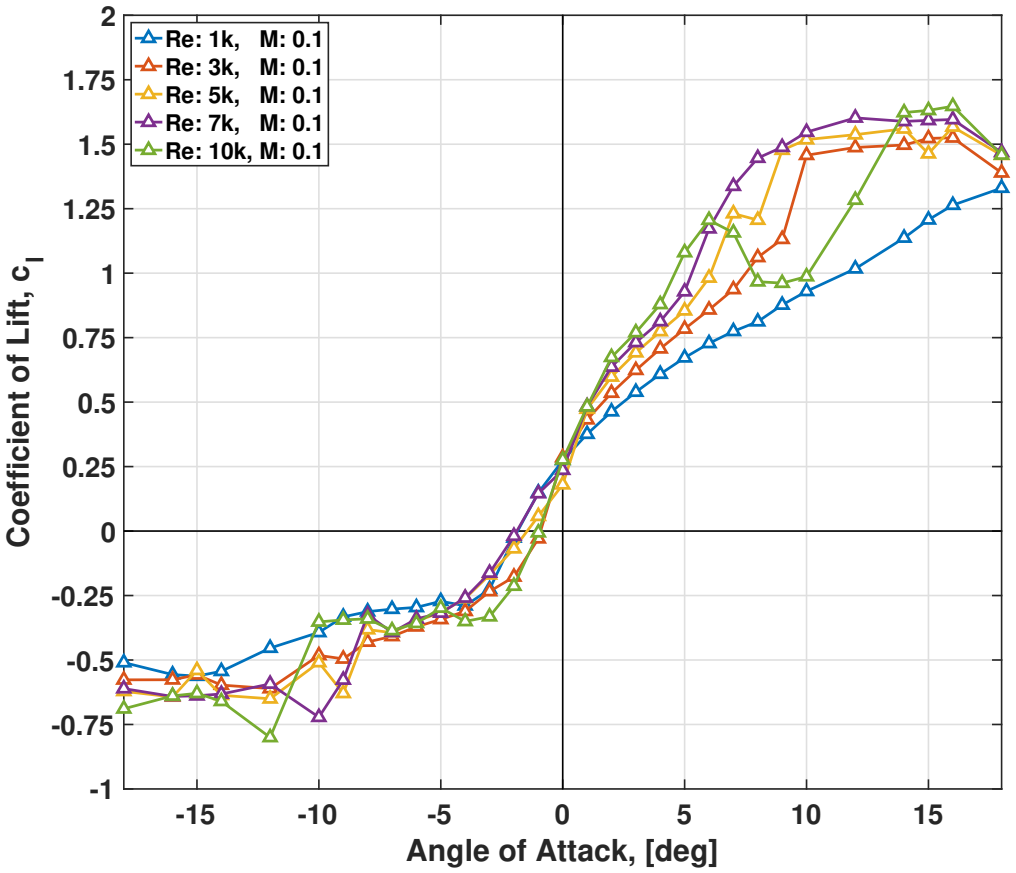

Figure 3.20: Coefficient of lift at $M = 0.1$ with all Reynolds numbers.

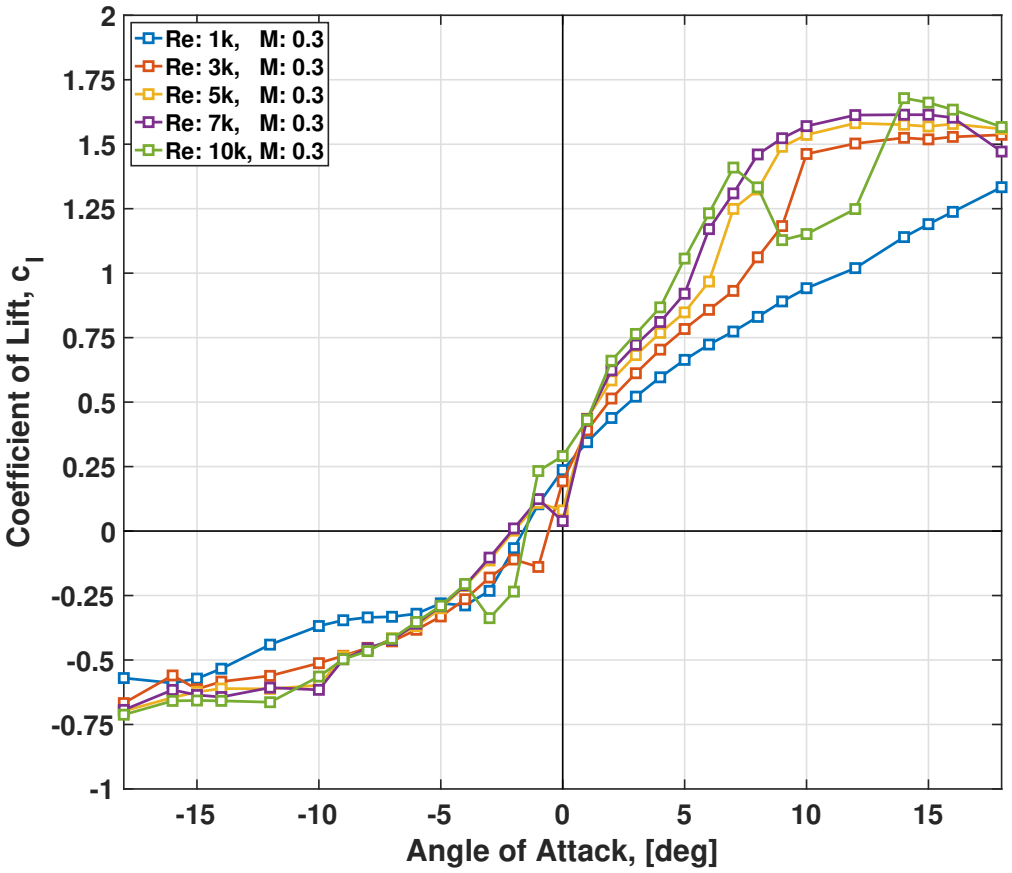

Figure 3.21: Coefficient of lift at $M = 0.3$ with all Reynolds numbers.

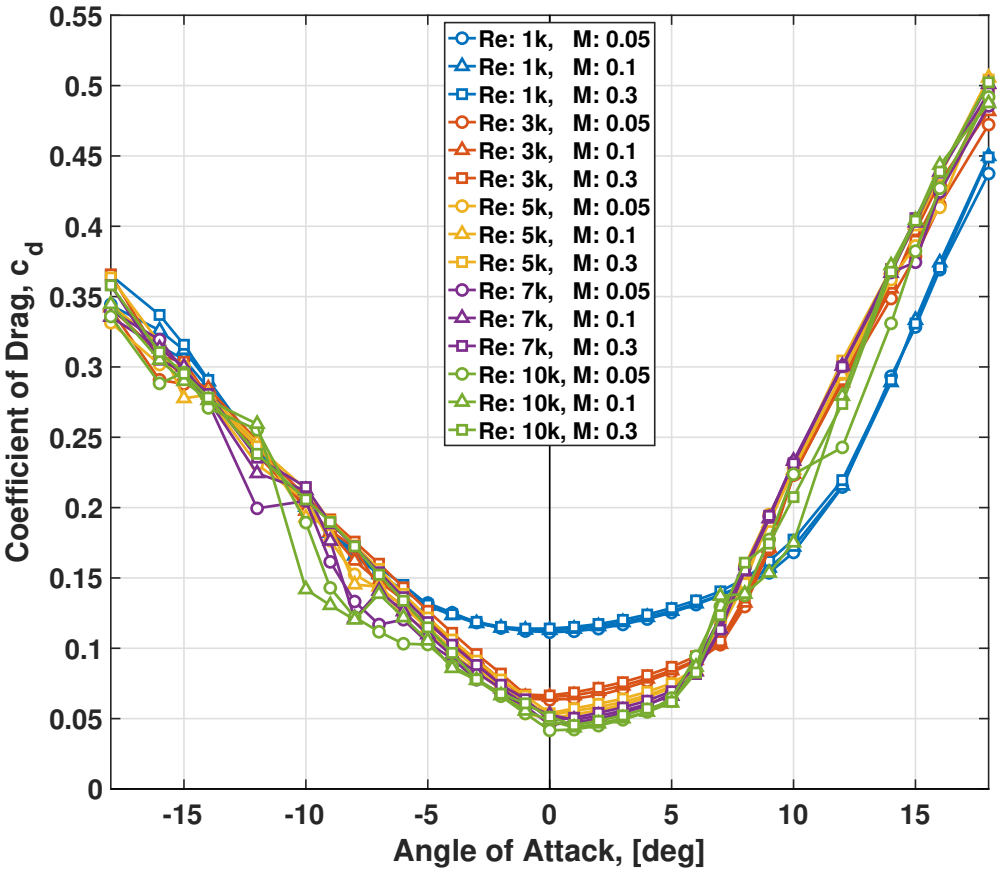

Figure 3.22: Coefficient of drag at all tested Reynolds and Mach numbers.

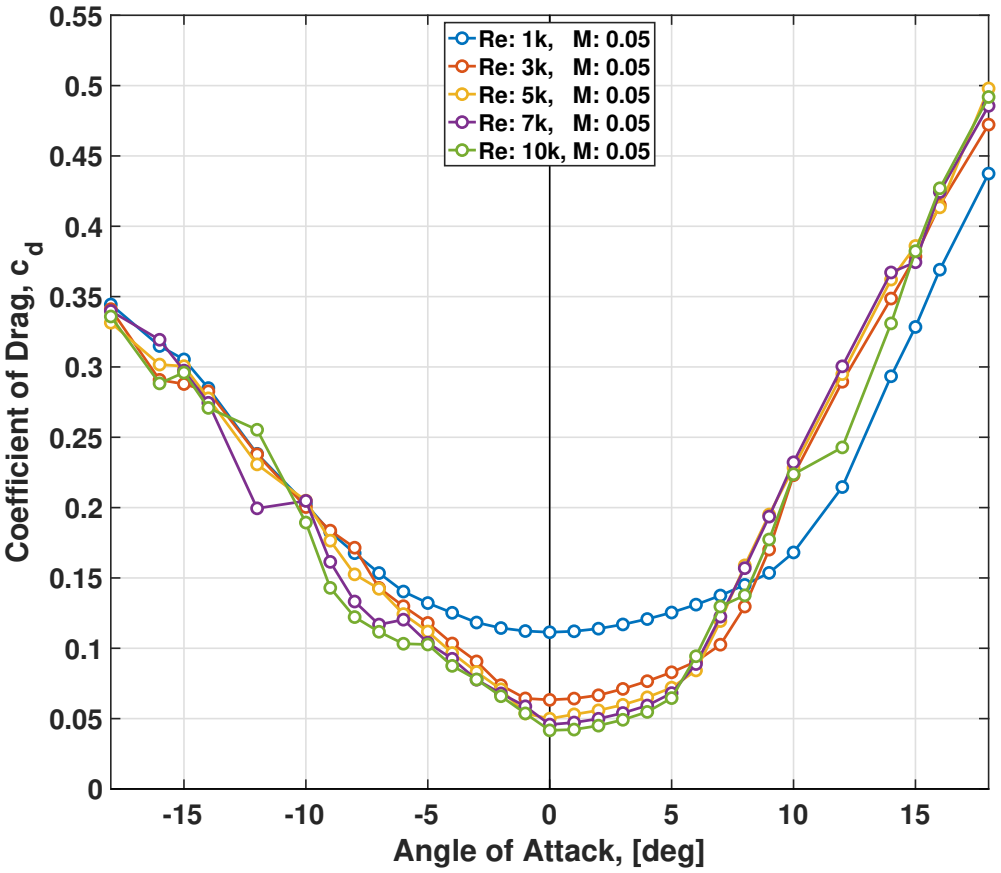

Figure 3.23: Coefficient of drag at $M = 0.05$ with all Reynolds numbers.

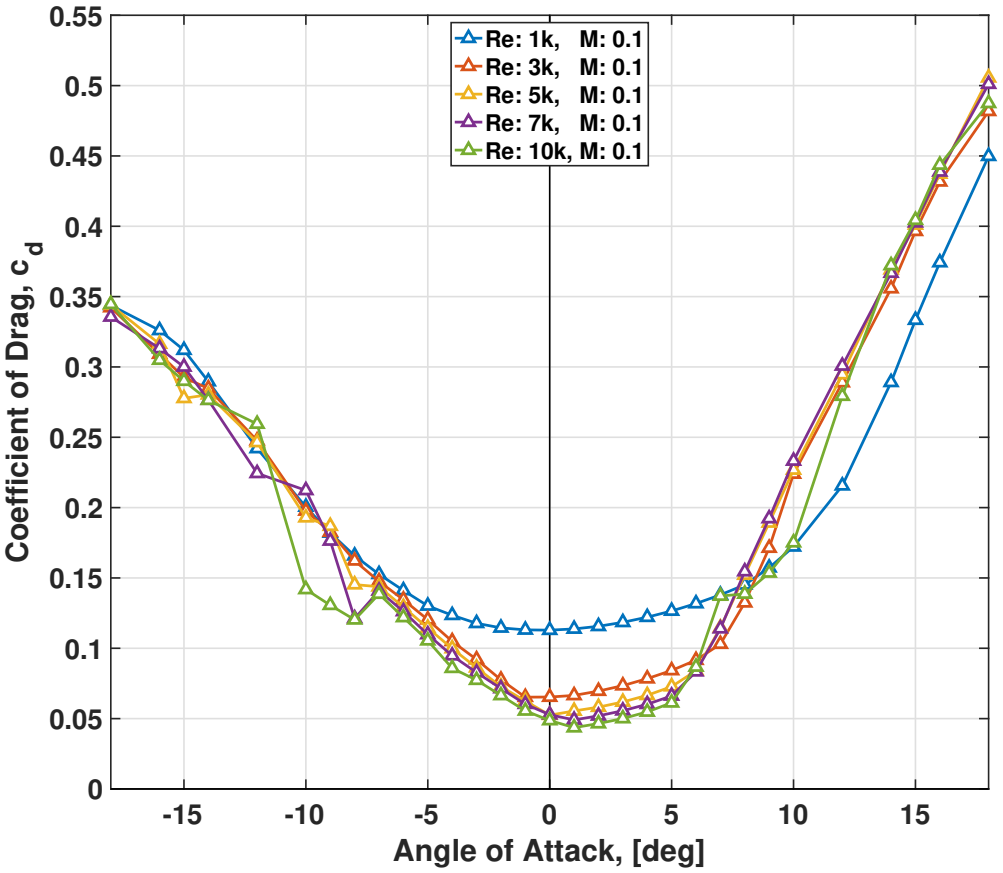

Figure 3.24: Coefficient of drag at $M = 0.1$ with all Reynolds numbers.

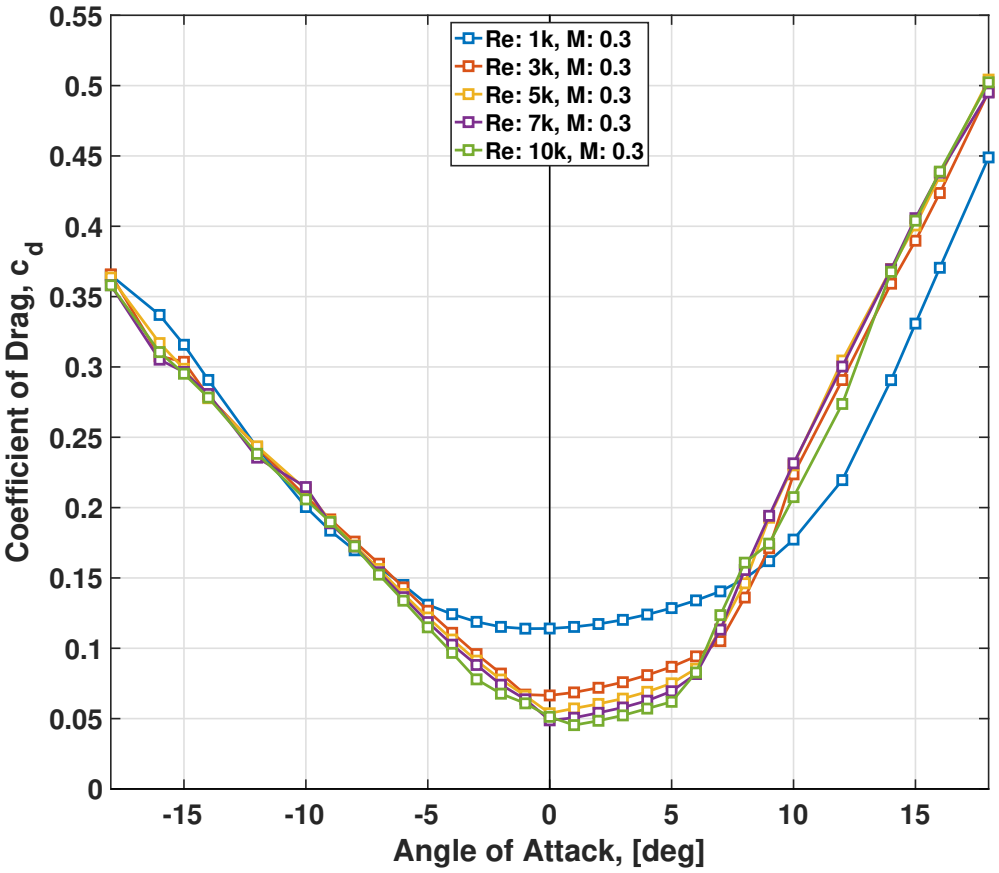

Figure 3.25: Coefficient of drag at $M = 0.3$ with all Reynolds numbers.

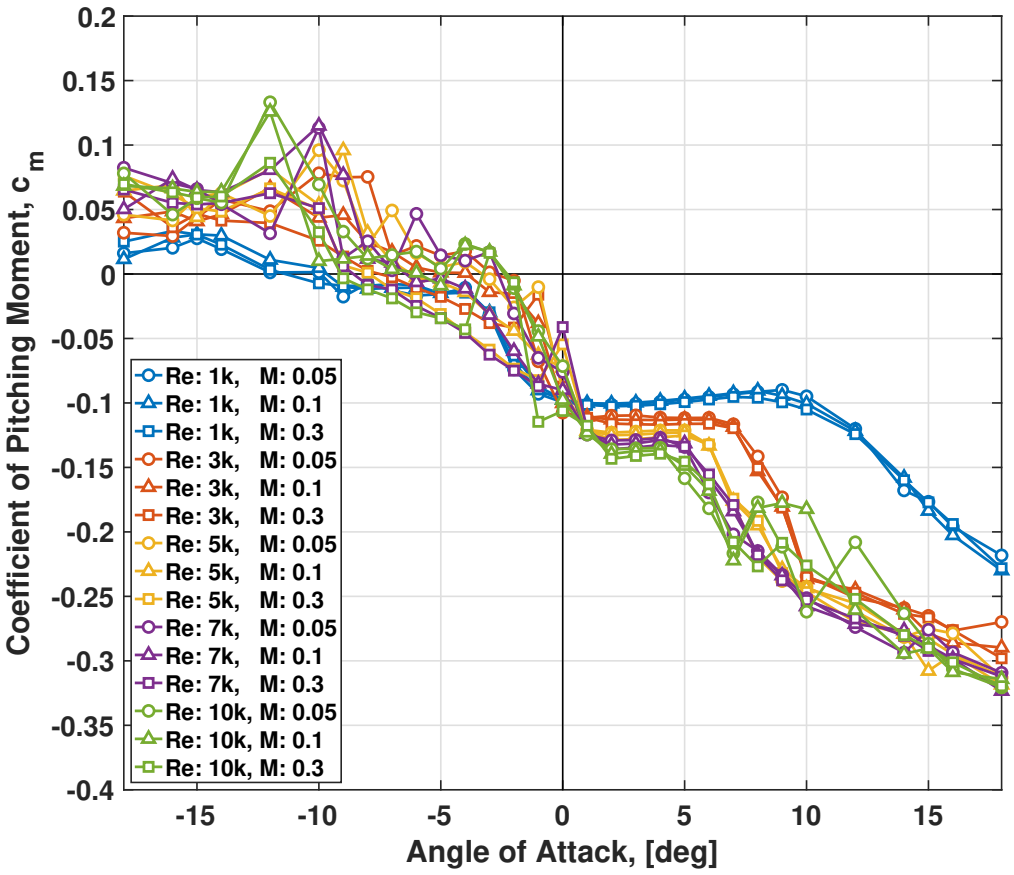

Figure 3.26: Coefficient of pitching moment at quarter-chord at all tested Reynolds and Mach numbers.

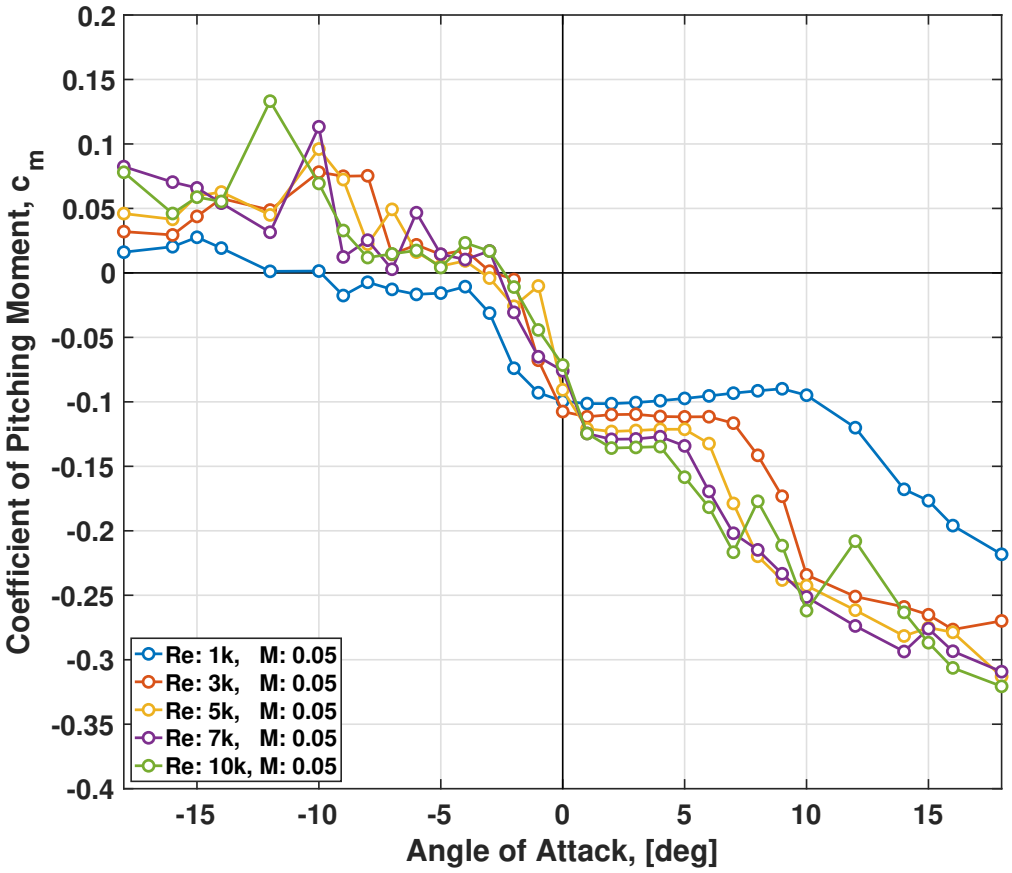

Figure 3.27: Coefficient of pitching moment at quarter-chord at $M = 0.05$ with all Reynolds numbers.

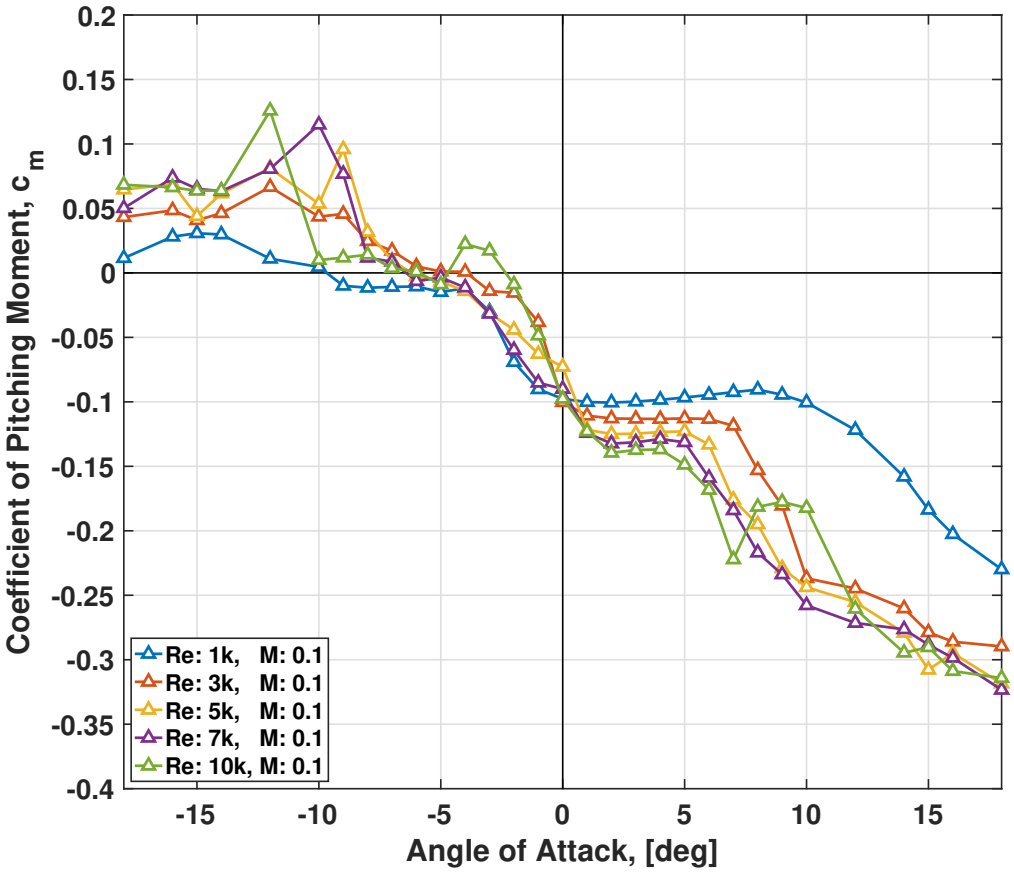

Figure 3.28: Coefficient of pitching moment at quarter-chord at $M = 0.1$ with all Reynolds numbers.

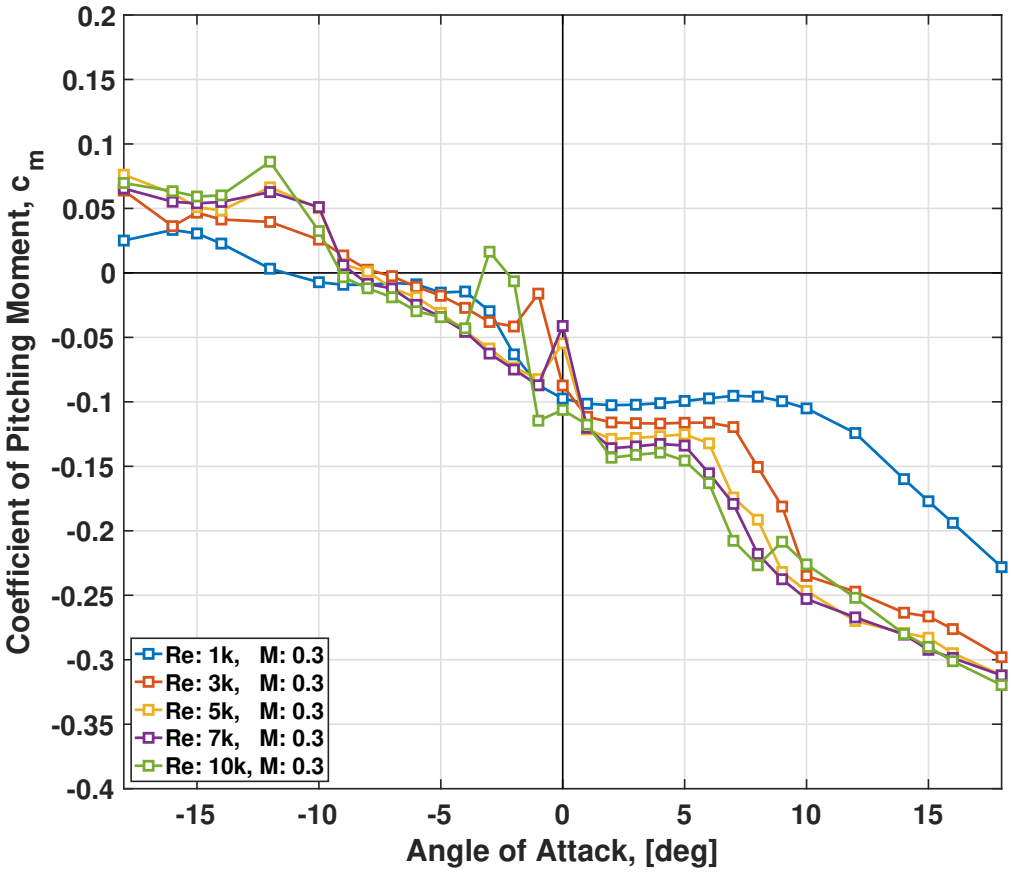

Figure 3.29: Coefficient of pitching moment at quarter-chord at $M = 0.3$ with all Reynolds numbers.

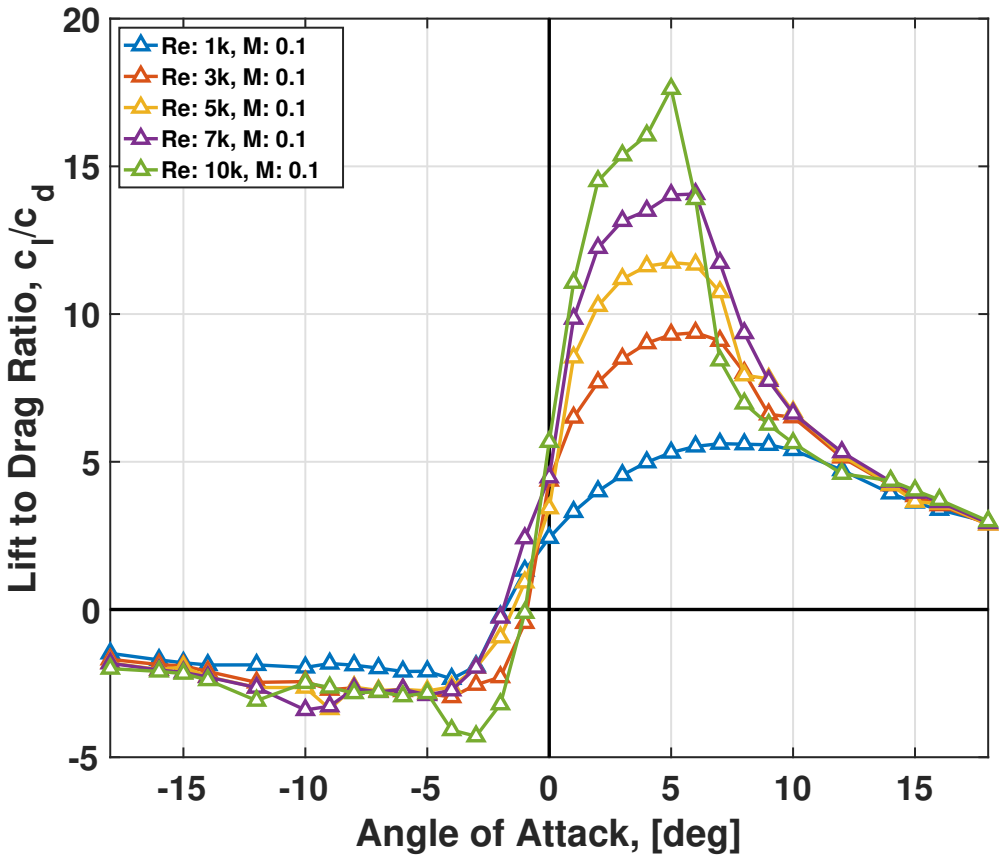

Figure 3.30: Lift to drag ratio variation with Reynolds number at M=0.10.

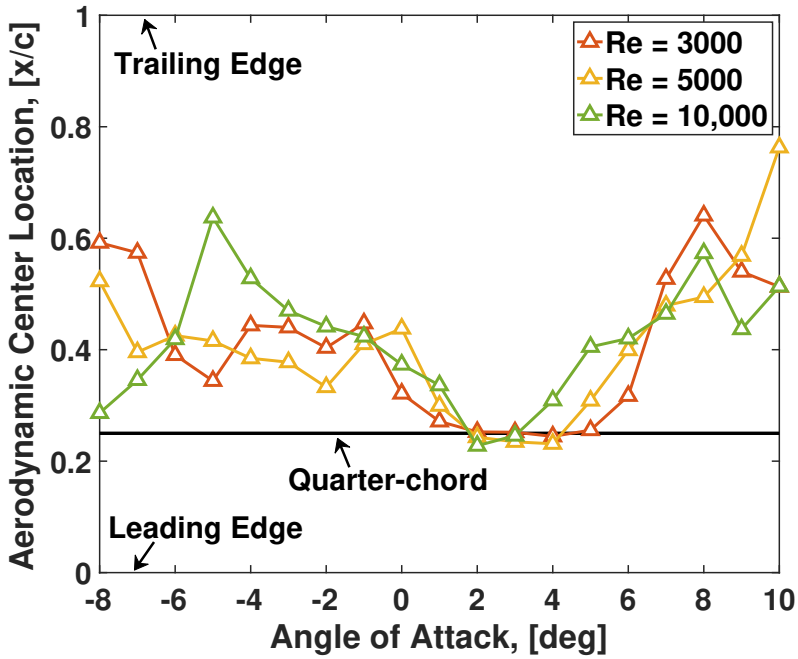

Figure 3.31: Aerodynamic center movement with angle of attack at multiple Reynolds numbers (Re = 3000, 5000, and 10,000); M = 0.10.

(Re$> 10^6$), this holds true for nearly all rotor airfoils even for viscous flows as long as in low subsonic range (Mach < 0.4). The relative locations of the AC and chordwise center of gravity is important for rotary-wing pitch-flap flutter. Using the 2D airfoil results, the location of the AC is calculated at several Re numbers and shown in Figure 3.31. At low positive angles the AC remains close to quarter-chord. This is similar to nominal behavior on Earth. For large ($\alpha > 5°$) or negative angles, the AC moves further back ($40 - 60\%$c). This is special to Mars. Thus the Earthly requirement of maintaining CG always ahead of quarter-chord could be relaxed. It implies leading edge weights might no longer be necessary. But there are certain low angles of attack where it comes close, so the danger of pitch-flap flutter is not entirely eliminated.

As the Re number increases the range of angles at which, the AC comes close to quarter-chord is reduced. For example, at Re = 3000, the AC stays close to quarter-chord between 1° to 7° whereas at Re = 5000 the range is 2° to 5°.

Chapter 4: Comprehensive Analysis

4.1 Overview

Having completed the development of models for comprehensive analysis, this chapter deals with validation and then application to the study of Mars helicopter flight.

The first section deals with the validation with best available coaxial hover data at low Reynolds numbers. The focus then shifts to Mars and begins with the structural dynamics of the rotor blade. This is followed by single rotor hover validation at Mars conditions. For this purpose the data collected in Chapter 2, must be used. Next, aeromechanics is investigated in forward flight beginning with a baseline condition representative of the mission for the JPL Mars Helicopter. Finally, excursions from the baseline are explored; with effects of advance ratio, pitch angle, inter-rotor separation, and blade loading. Throughout this chapter all results are from the lifting-line comprehensive analysis (CA). Results from CFD/CA coupling will be described in Chapter 5.

4.2 Coaxial Aerodynamics in Hover

The starting point was the comprehensive analysis (CA) validated and calibrated with hover and wind-tunnel data by Schmaus and Chopra [58]. That data is not sufficient for Mars. Martian flight will be at very low Reynolds numbers, and very low advance ratios. At low advance ratios the loads are dominated by the wake.

These run counter to how any wind-tunnel test is conducted on Earth. Tests on Earth focus on high speed and high Mach numbers (low speed tests are unreliable due to tunnel re-circulation unless conducted at the Ames National Full-scale Complex). High Mach numbers on Earth puts Reynolds numbers in 1 to 10 million range. Thus it is entirely ignored. In addition, inter-rotor separation is a critical parameter on Mars, far more than it is on Earth, not only due to the danger of blade strike under high Martian gusts, but also packaging the aircraft for delivery and deployment on a desolate destination 300 million miles away. Thus coaxial data is needed at low Reynolds numbers, in hover and with varying inter-rotor separation, preferably (at least for this thesis) at low tip Mach numbers. There is only one data-set that comes close.

4.2.1 Ames Coaxial Data

The data used to validate the coaxial aerodynamic analysis is from Ramasamy 2015 [51]. A series of tests were conducted at NASA Ames Research Center in the U.S. Army test facility ($8.0 \times 7.3 \times 6.0\ m$) with the aim of understanding the aerodynamic interference in twin-rotor systems. The tests include a single rotor setup and a twin-rotor setup, shown in Figure 4.1. The twin-rotors are independent, which allows for easy positioning into coaxial and tandem configurations. The system allows for independent rotor measurements. Both the inter-rotor separation and the percentage overlap could be varied. Additionally, tests were carried out with a straight blade with the NACA 0012 airfoil and with a special-purpose twisted blade with tiltrotor airfoils. The present work used the straight NACA 0012 blades and the single and coaxial rotor configurations. These are the most relevant and representative conditions for Mars. The validation cases include three main test series: (1) single rotor thrust sweeps, with both three and six blades, (2) coaxial rotor thrust sweep at constant inter-rotor separation, and (3) coaxial rotor inter-rotor

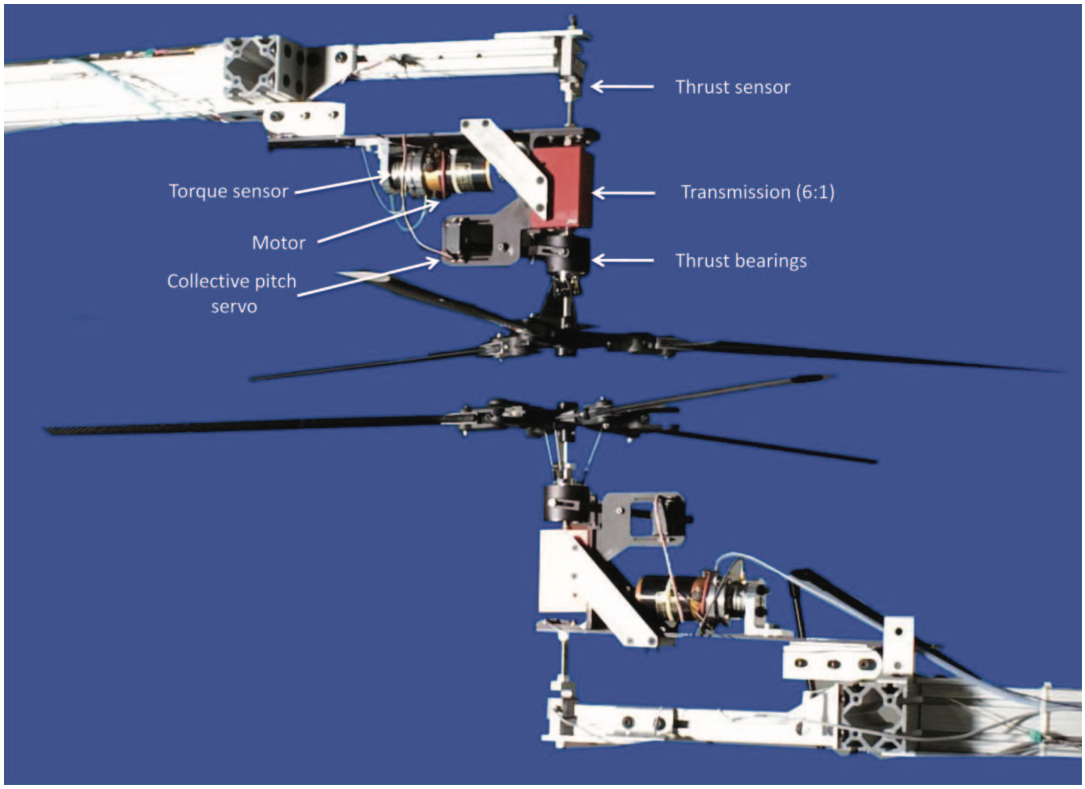

Figure 4.1: Coaxial rotor test setup from Ramasamy.

separation sweep, at two thrust settings.

4.2.2 Setup

Table 4.1 summarizes the parameters of the rotors used for validation. The tests are split between two rotational speeds; 1200 and 800 RPM. The test data includes thrust and torque for each individual rotor. To achieve thrust sweeps, the rotor collective was swept. For the inter-rotor separation sweeps, the trim condition of constant total thrust was applied ($T_u + T_l = \text{constant}$). Yaw trim, meaning zero torque ($Q_u + Q_l = 0$), was always applied.

This is an aerodynamic study and the blades are considered rigid (no property data available to model flexibility). This meant inputing a high structural stiffness until further increase in stiffness resulted in no change in performance (thrust and power) and deflections (flap, lag, and twist). Additionally, the pitch links are also

Table 4.1: Ramasamy rotor parameters.

Parameter	Value
Number of Blades	3 or 6
Radius, ft (m)	2.17 (0.66)
Chord, in (m)	2.29 (0.0647)
Root cutout	19.1%
Solidity	0.0679 or 0.1359
Twist	none
Taper	none
Airfoil	NACA 0012

locked. The analysis used a lifting-line model with airfoil lookup tables coupled with free-wake. The models are described in greater detail in Section 3.3. Most of the cases were performed with 6 free-wake turns, but for the inter-rotor separation sweeps it was increased to 12 to ensure that even at largest separation ($h/D = 1.5$) the upper wake would travel far enough downstream to reach the lower rotor. The model included the following eight features:

1. nonlinear nearwake with a prescribed geometry that extends 30° behind each blade, after each one

2. free wake with a single rolled-up trailer released from the tip and azimuthal discretization of 15°

3. initial core size of 10% of chord-length

4. vortex diffusion constant in the Squire core growth set to $a = 0.05$. The model varies core radius as $r_c = 1.12\sqrt{4\nu\delta t}$ with $\delta = 1 + a\frac{\Gamma_\nu}{\nu}$, where r_c is the core radius, ν is kinematic viscosity, t is the wake age, and Γ_ν is the circulation

5. tip vortex strength of 70% maximum bound circulation outboard of 50%R

6. motions–deformations and control angles–to deform the lifting-line (locus of bound circulation at 1/4-c, collocation points at 3/4-c, and vortex release

points at trailing edge)

7. inclusion of the effect of bound circulation on angle of attack on other blades, important to capture blade passage loads, and

8. Reynolds number correction on airfoil drag per Yamauchi and Johnson [92], with constant $n = \frac{1}{8}$.

The tip vortex strength related bound circulation was identified by McAlister [93] on models similar to the model used in this study. McAlister experiments used particle image velocimetry to identify, track, and measure the tip vortex from a two-bladed rotor. Applying vortex models to the data, McAlister found the vortex core was initially 10% of the chord and the circulation was approximately 67% of the maximum bound circulation on the blade. This reduction, possibly related to viscosity, is inconsistent with inviscid lifting-line theory, and hence must be an empirical correction. This correction resulted in limiting the rise of induced power with thrust, and as seen later, helped match the experimental data better. The Reynolds number correction was essential to predict the profile power. The Reynolds number of the NACA 0012 airfoil tables are in fact unknown but assumed to be at $Re_{table} = 10$ million per Ames guidance. The blade operating conditions, including tip Reynolds number for the two rotational speeds is given in Table 4.2. The Reynolds number corrections are:

$$c_l(\alpha) = K c_{l_{table}}(\overline{\alpha}) \; ; \qquad c_d(\alpha) = \frac{c_{d_{table}}(\alpha)}{K} \; ; \qquad \overline{\alpha} = \alpha_z + \frac{(\alpha - \alpha_z)}{K} \tag{4.1}$$

where c_l is the resulting coefficient of lift, α is the angle of attack, K is the correction factor, $c_{l_{table}}$ is the coefficient of lift from the table, c_d is the resulting coefficient of drag, $c_{d_{table}}$ is the coefficient of drag from the table, and α_z is the angle of attack for

Table 4.2: Ramasamy operating conditions; Re is Reynolds number, M is Mach number.

	800 RPM	1200 RPM
Re_{Tip}	$210,000$	$315,000$
M_{Tip}	0.1667	0.25

zero lift. The correction factor is given as:

$$K = \left(\frac{Re_{Local}}{Re_{table}} \right)^{n} \tag{4.2}$$

where Re_{Local} and Re_{table} are the local and table Reynolds numbers, respectively, and n is an adjustable constant, between 1/8 to 1/5 (turbulent flat plate limit). There is no model to correct the pitching moment. In the present work only the drag correction was used with $n = 1/8$ because it gave the best predictions. Larger values of n resulted in over-prediction of power.

4.2.3 Figure of Merit

For both a single rotor and a coaxial rotor, the Figure of Merit is defined as:

$$FM = \frac{P_{Ideal}}{P_{Measured}} = \frac{\frac{T^{3/2}}{\sqrt{2\rho A}}}{P_{Measured}} = \frac{\frac{{C_T}^{3/2}}{\sqrt{2}}}{C_{P_{Measured}}} \tag{4.3}$$

where T is thrust, P is power, ρ is density, A is projected area, and C_T and C_P are the coefficients of thrust and power, respectively. It is important to highlight that A is the projected area, so for coaxial rotors remains the same as the single rotor. It is not the total disk area of the two rotors.

This definition treats the coaxial rotor as a single system, where half the blades spin in the opposite direction. The thrust is the total thrust, $T = T^U + T^L$ or $C_T = C_T^U + C_T^L$. As will be seen in the results section (Figures 4.10(c), 4.11(c), and 4.12(c)) the thrust sharing is dependent upon many factors.

There is a second, less used, approach to define Figure of Merit for coaxial rotors. In this case, the numerator is the ideal power of two rotors in isolation with no interference. This requires the thrust sharing to be known for Figure of Merit. The individual rotor thrust is unknown a priori and as can be seen in, Figure 4.8, the rotor flow field have strong interactions. This second approach is not a proper basis to compare coaxial with a single rotor system and is therefore not used in the present work.

4.2.4 Single Rotor Validation

The first validation case is the performance of a single rotor. This validates essentially all pieces of the aerodynamic analysis but for the effect of separation. Runtime was much shorter (5 min) than the coaxial (30 min). Figure 4.2 shows the comparison between data and predictions of thrust versus power and FM at two different operating speeds. The CA predicts the data correctly below stall at both operating speeds, but predicts a marginally higher Figure of Merit at the higher speed.

Several sets of successive refinements were required to produce this level of validation. These are documented below.

1. **Reynolds number correction:** The test Re is well defined. It is the table Re that was uncertain. The table data is from Ames and the guidance was to consider the table Re as an adjustable parameter. This process was followed by Ho, Yeo, and Bhagwat [94] and also in this work. Thereafter, only the correction factor, n, remained to be determined. Using a higher value ($n = 1/5$) resulted in an over-prediction of power; $n = 1/8$ produced the best validation.

2. **Free-wake:** The inflow converged after 6 wake turns (Figure 4.6). With fewer turns the wake was not fully developed and under-predicted the induced

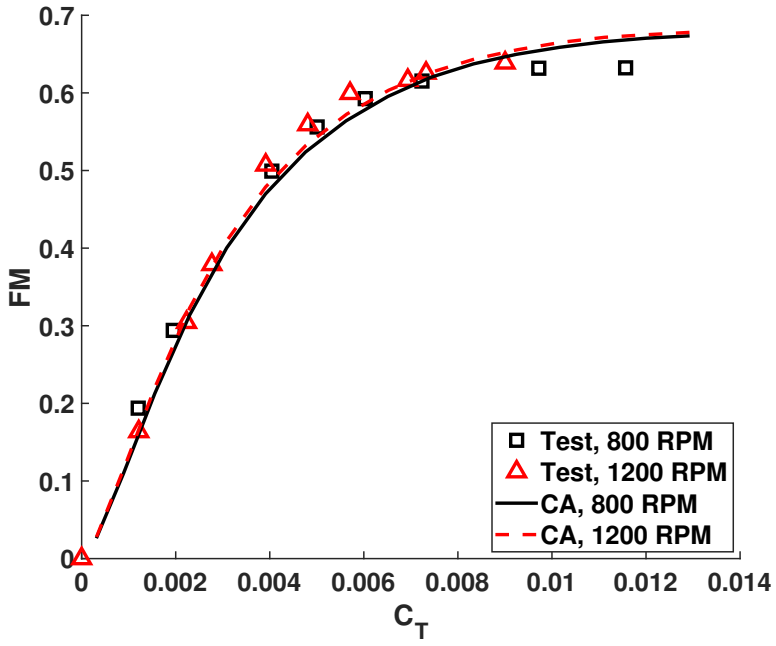

Figure 4.2: Single rotor performance at two rotational speeds (800 and 1200 RPM).

power. Increasing azimuthal resolution beyond 15° produced no change in rotor performance and simply increased run time.

3. **Tip Vortex Strength:** The nominal tip vortex strength was the maximum bound circulation strength consistent with lifting-line theory, but the induced power was over-predicted significantly. As suggested by Harrington for model-scale rotors, the modification to 70% of the maximum bound circulation showed the proper rise of induced power with thrust and resulted in much a better prediction. Adjusting the initial core size of 10%c to 5%c and 15%c was inconsequential. Adjustments of the vortex diffusion constant from baseline value of 0.005, to 0.05 and 0.0005, also made negligible difference.

4. **Nearwake:** Two nearwake geometries were explored–a flat geometry (in plane of the rotor) and another that deflects down with the rotor inflow. Both resulted in the same performance. The flat geometry was used for simplicity. The nearwake extends 30° behind the blade and remains prescribed, always,

with no distortion. Adjusting the nearwake extension had some impact on the rotor performance but 30° was selected for the best validation.

4.2.5 Coaxial Validation

Having matched well with the single rotor, validation moved onto the coaxial rotor. For the coaxial rotor, a thrust sweep was conducted at an inter-rotor separation of $h/D = 0.07$ at 1200 RPM, where h is the inter-rotor separation distance and D is the rotor diameter.

The performance of the individual rotors while operating within the coaxial system is compared with their isolated operation in Figure 4.3. Figure 4.3(a) shows power versus thrust, and Figure 4.3(b) shows the same data formatted as Figure of Merit versus thrust. The coaxial matches the profile power (zero thrust) well, but with increase in thrust the power grows more quickly in the analysis than the data. The analysis predicts stronger interference than the data suggests. The analysis does predict correctly that the lower rotor should be less efficient than the upper, and that they both should be worse than a single rotor. This comparison shows that a rotor is more efficient in isolation than in a coaxial system in generating the same thrust. But the question remains which system is more efficient for the same total thrust. Then the coaxial rotor is more efficient.

Figure 4.4 shows a comparison of a coaxial rotor, each rotor with $N_b = 3$, and an isolated rotor, with $N_b = 6$. Note that this comparison ensures that the total number of blades remain the same. Thus the skin friction losses hence profile power remain the same, and differences can be attributed primarily to induced power due to interference. The results of this comparison show the coaxial rotor is more efficient compared to the isolated rotor. Even though there is an offset between the data and predictions, both show the same trend. The improved efficiency of the coaxial rotor stems from two effects. A secondary effect may be swirl recovery. The swirl

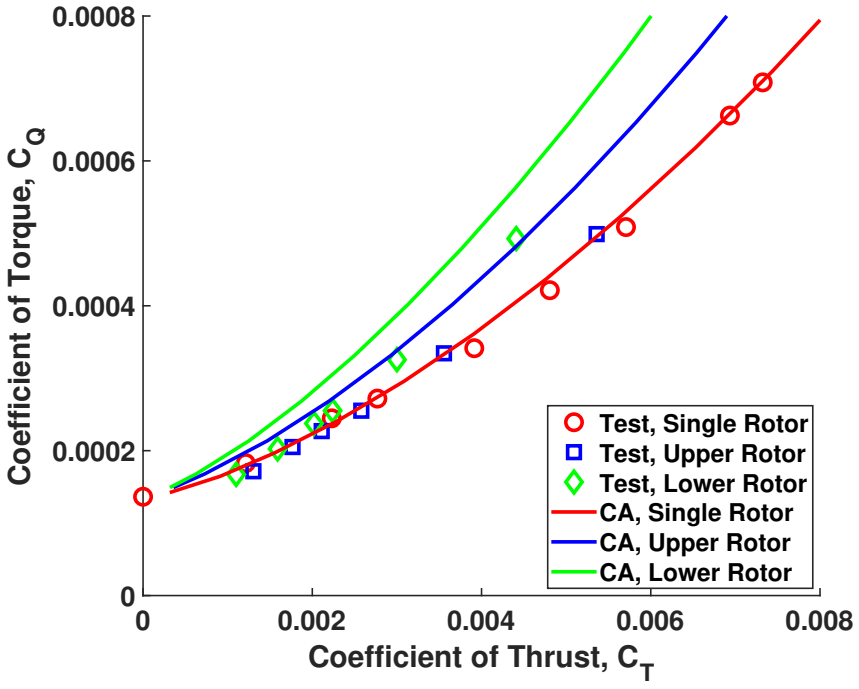

(a)

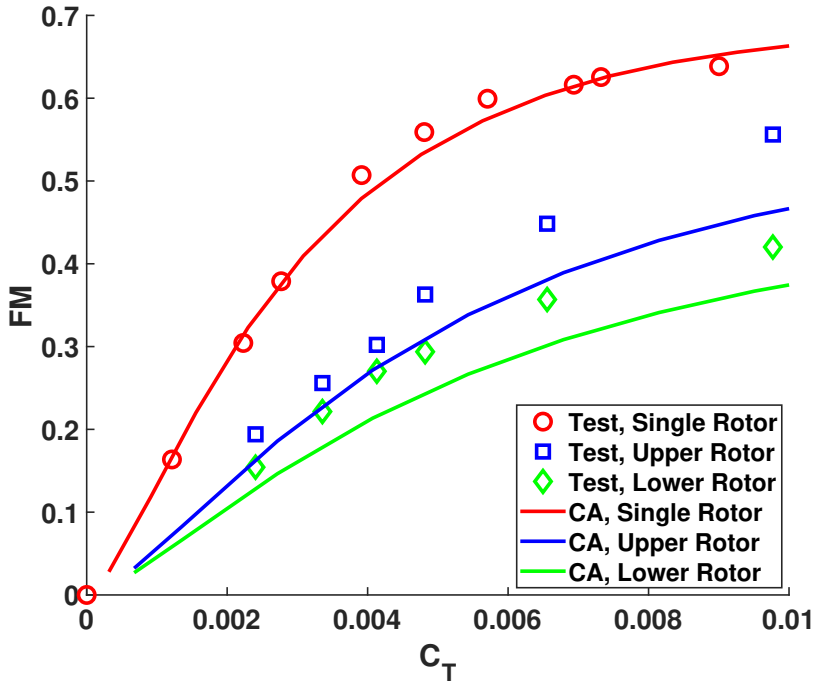

(b)

Figure 4.3: Performance comparison of single rotor and individual rotors within coaxial system ($h/D = 0.07$); all at 1200 RPM.

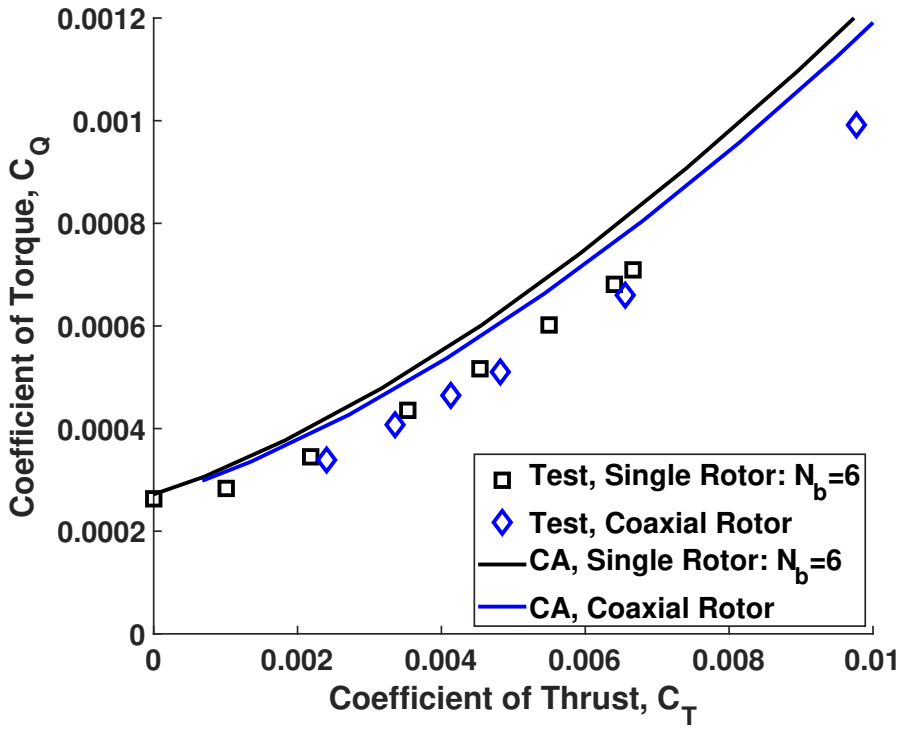

Figure 4.4: Performance comparison of single rotor and coaxial rotor ($h/D = 0.07$); both have the same total number of blades ($N_b = 6$); 1200 RPM.

of each rotor counteracts the other and reduces net momentum loss due to swirl. The primary benefit is from inter-rotor separation. The upper wake contracts before reaching the lower rotor. Therefore the lower rotor effectively provides additional disk area. This benefit is dependent on wake contraction and therefore inter-rotor separation. Momentum theory predicts a 9% benefit in power for a fully contracted upper wake without accounting for the viscous losses. The test data shows a 6% benefit and the predictions show a 4% benefit.

To complete the understanding, Figure 4.5 shows the comparison of three rotors: single rotor with $N_b = 3$, single rotor with $N_b = 6$, and coaxial rotor with $N_b = 6$. From Figure 4.5(a), its clear to see that the comparison to the single rotor with $N_b = 3$ is not fair because of the difference in profile power that accompanies change in blade number. The Figure of Merit highlights the trends between rotor types. The coaxial rotor has a higher Figure of Merit compared to a single rotor

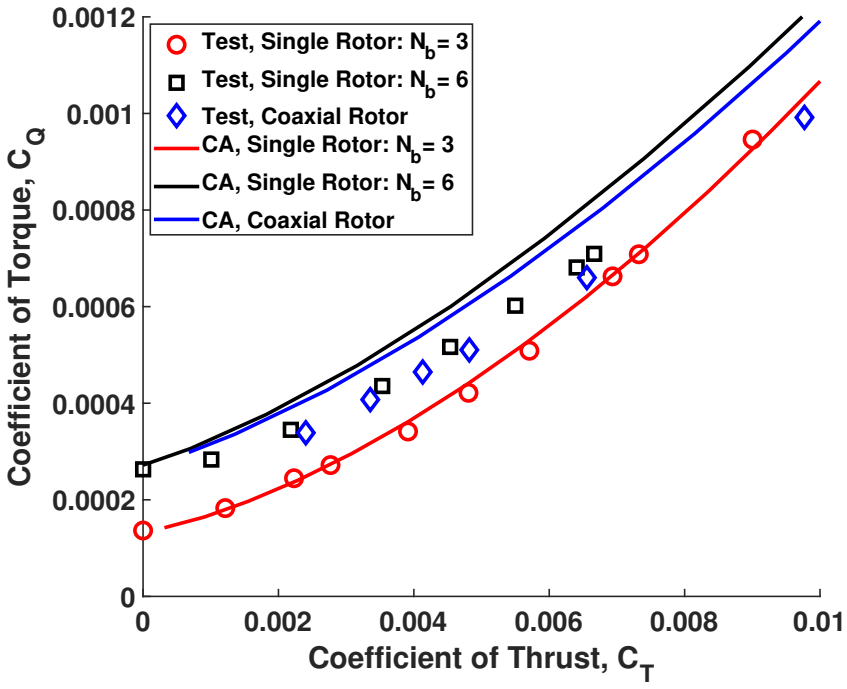

(a)

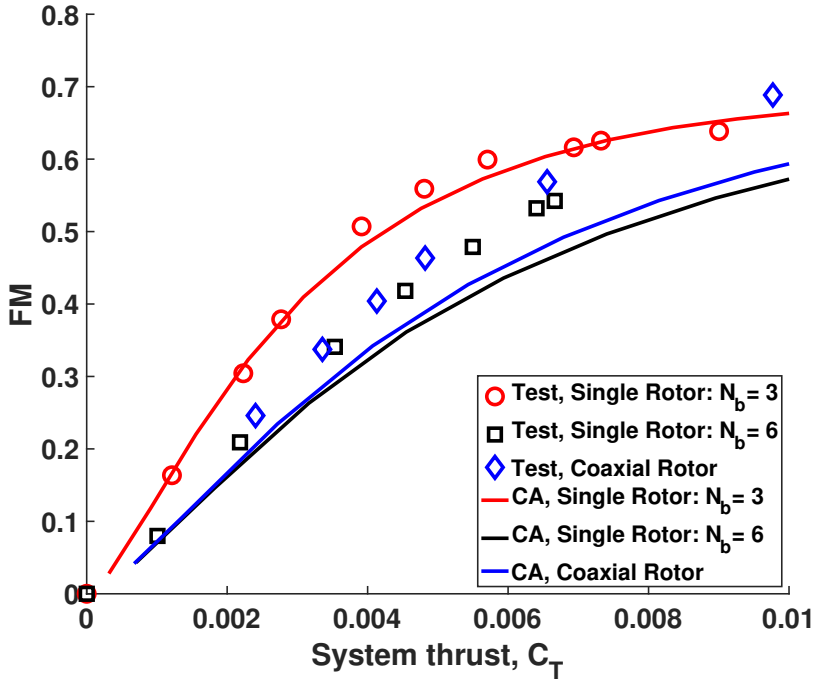

(b)

Figure 4.5: Performance comparison of single rotor ($N_b = 3$), and single rotor and coaxial rotor ($h/D = 0.07$); both have the same total number of blades ($N_b = 6$); 1200 RPM.

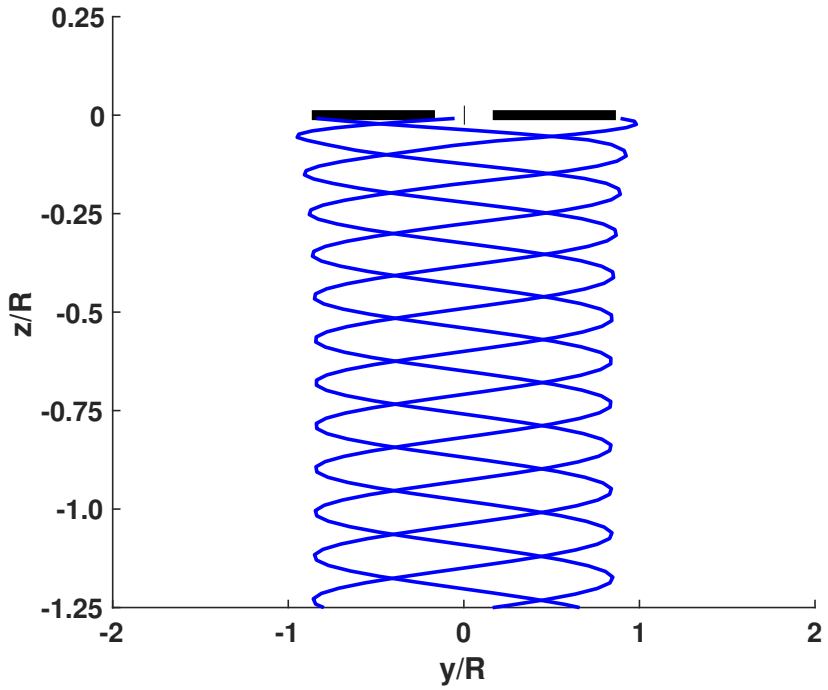

Figure 4.6: Tip vortex trajectory of the single rotor with three blades, at 1200 RPM, and thrust $C_T = 0.00564$.

with the same total number of blades. It is clear that the analysis captures all of these key trends precisely, even though there are differences in the exact magnitudes of the changes.

Figures 4.6, 4.7, and 4.8 show the tip vortex geometries. The cases have similar thrust values. The strong rotor-rotor interactions can be seen in Figure 4.8. The wake of the upper rotor contracts within the wake of the lower rotor, and travels through faster, roughly at twice the speed of the lower rotor. Both of these phenomena result from the flow induced by the lower rotor.

Figure 4.9 studies the radial lift distribution on a blade. Figures 4.9(a) and 4.9(b) show the distribution of sectional normal force and angle of attack along the span. The lower rotor produces less lift inboard, where the sections are in climb due to downwash from the upper rotor, but more lift near the tip.

The thrust sharing between the rotors is shown in Figure 4.10, plotted versus

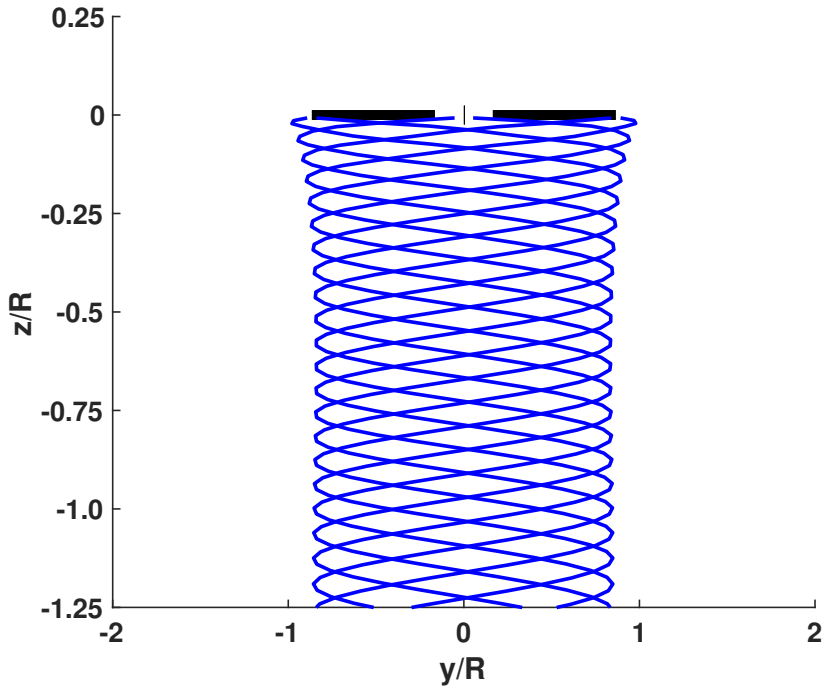

Figure 4.7: Tip vortex trajectory of the single rotor with six blades, at 1200 RPM, and thrust $C_T = 0.00594$.

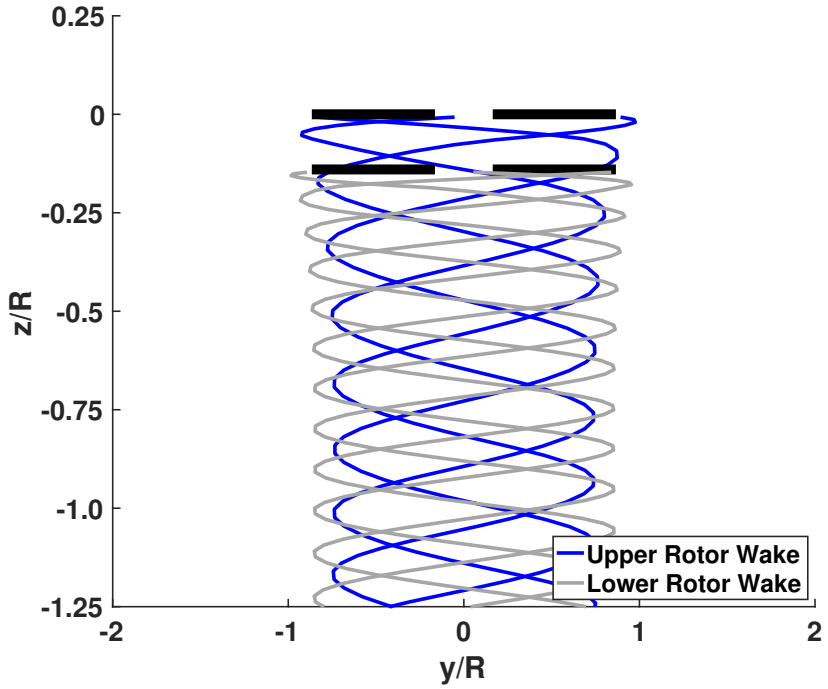

Figure 4.8: Tip vortex trajectory of the coaxial rotor, at 1200 RPM, and thrust $C_T = 0.00543$.

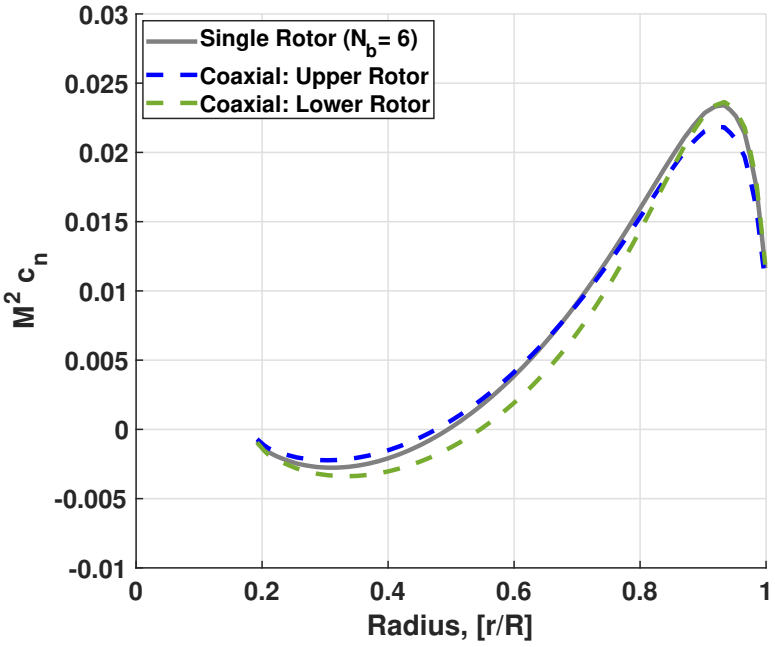

(a)

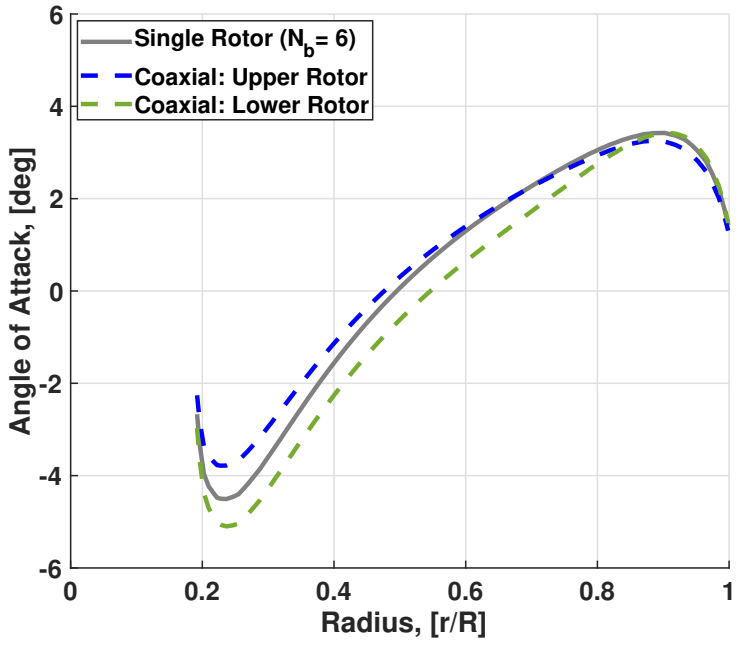

(b)

Figure 4.9: Radial distribution of sectional normal force and angle of attack; single rotor $N_b = 6$ ($C_T = 0.00594$) and coaxial rotor with $N_b = 3$ each ($C_T = 0.00543$).

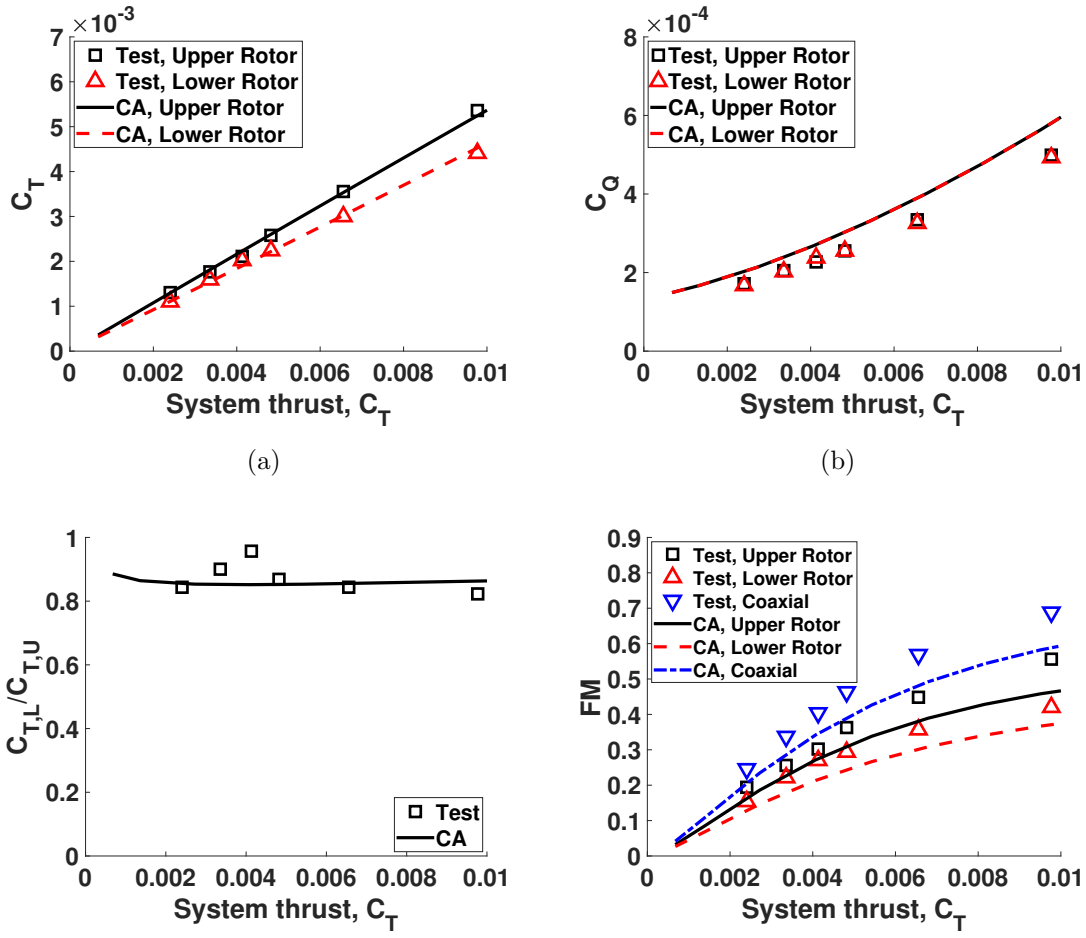

Figure 4.10: Performance of coaxial rotor over thrust sweep, at 1200 RPM, $h/D = 0.07$.

total thrust, as the upper rotor collective is fixed, the lower rotor collective is trimmed to balance torque, $C_Q^U + C_Q^L = 0$. Normally difficult to predict and also to measure, the analysis and data agree very well, Figure 4.10(a). The upper rotor carries a larger share of the thrust. The upper and lower rotors produce about 55% and 45% of the total thrust, respectively. The ratio is insensitive to thrust level across the sweep. Figure 4.10(b) shows the torque balance. The rotors are trimmed correctly to the same torque, only the magnitude is over-predicted. This results in an under-prediction of the Figure of Merit especially at higher thrust levels, Figure 4.10(d), but the physics is well captured. The coaxial system outperforms a single rotor, and

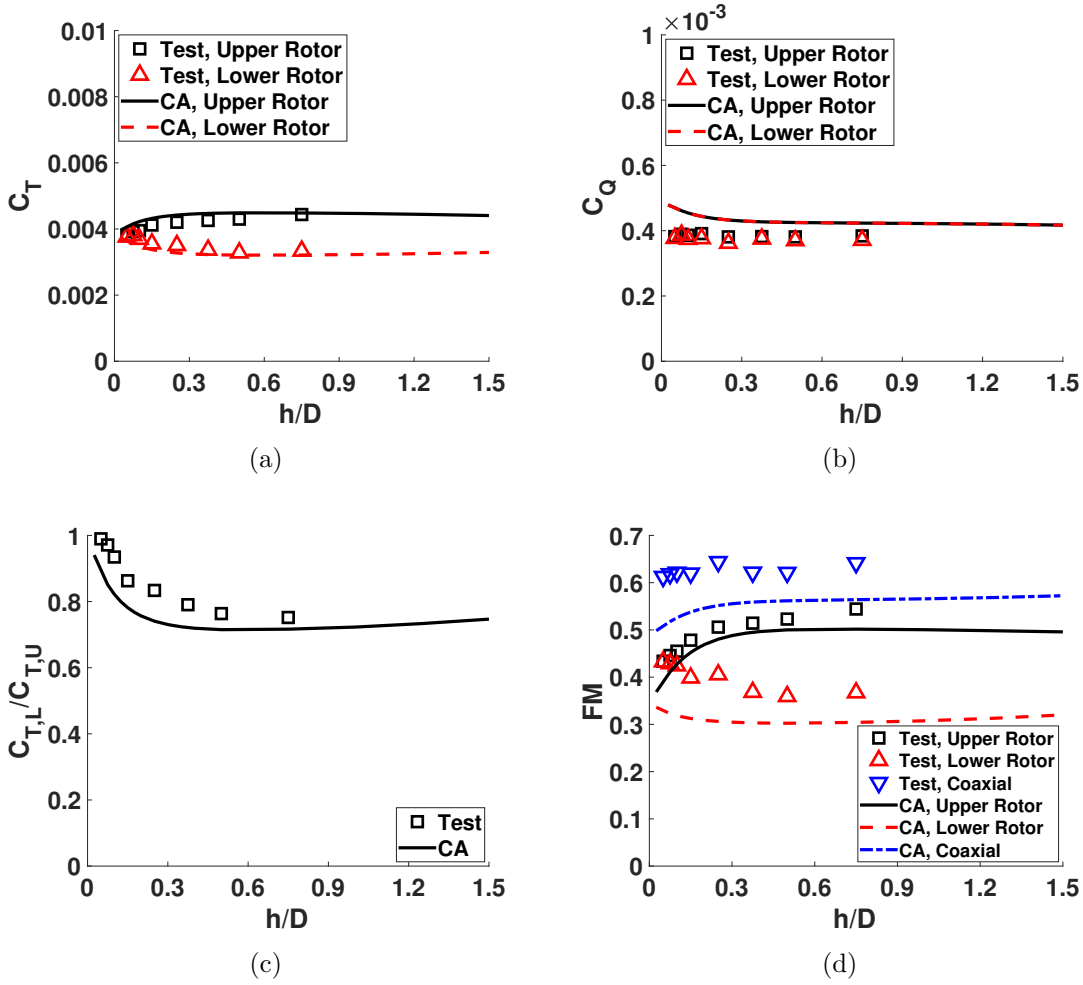

Figure 4.11: Performance of coaxial rotor over separation sweep, at 800 RPM, $C_T \approx 0.007$.

the upper rotor outperforms the lower rotor. This sweep was conducted at 1200 RPM and at a single separation distance, $h/D = 0.07$, to investigate the impact of thrust.

The following sweeps are far more critical for design, and also important, for it is beyond what momentum theory can predict and where the fidelity of the free wake is tested most severely. It is a sweep of inter-rotor separation, when the upper rotor wake is no longer fully contracted and vanishes at the limit to produce a rotor with twice the number of blades. The sweeps are each conducted at a single thrust level (one low and one high), but over a range of separation distances to reveal its impact

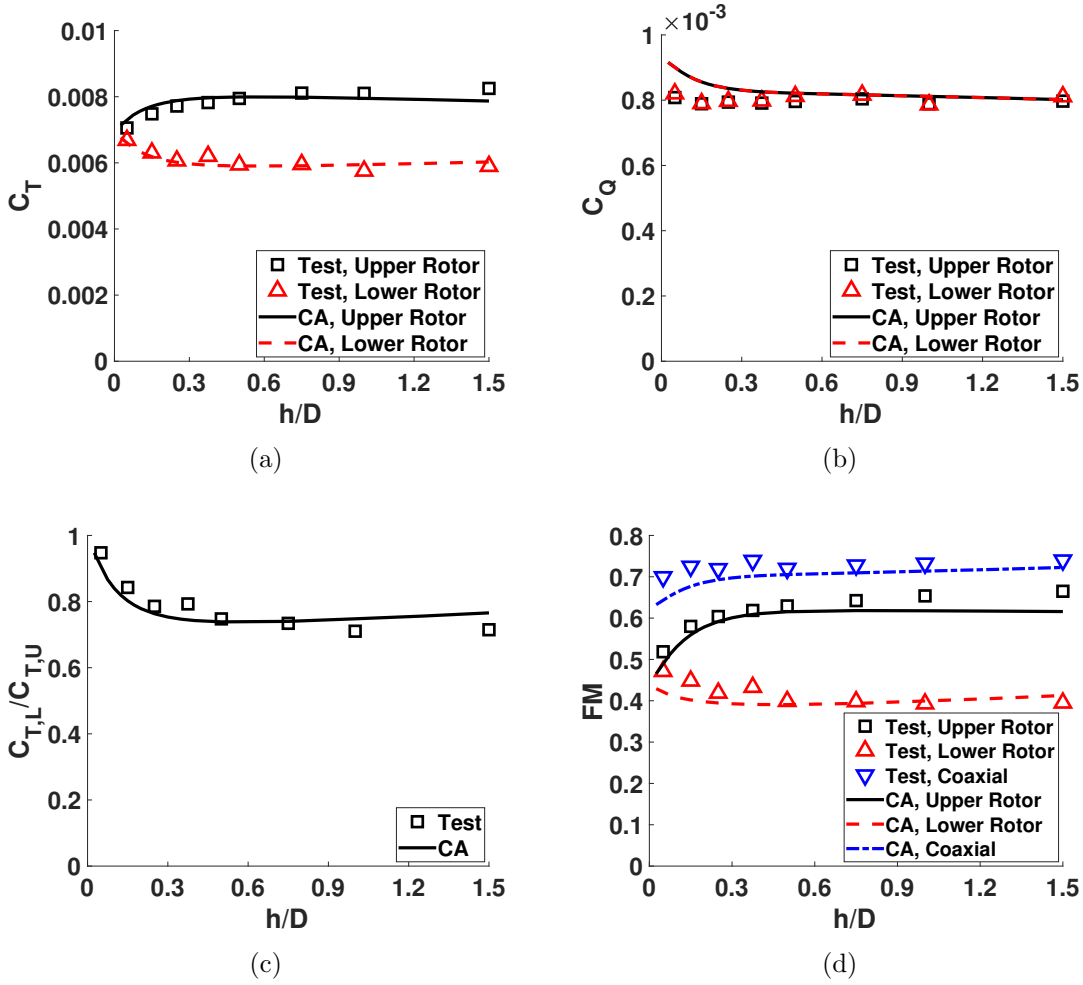

Figure 4.12: Performance of coaxial rotor over separation sweep, at 800 RPM, $C_T \approx 0.014$.

on thrust sharing and performance. The two target thrust levels were nominally $C_T \approx 0.007$ and $C_T \approx 0.014$. The measured values were in fact $C_T = 0.0077$ and $C_T = 0.0139$ on average, which are also the values used in the analysis, but the intended targets are quoted here for brevity.

Figure 4.11 shows the thrust and power sharing at the low thrust level, $C_T \approx 0.007$; plotted versus the inter-rotor separation, h/D. The upper rotor collective is trimmed to achieve the total thrust $C_T \approx 0.007$, and the lower rotor collective is trimmed to balance torque, $Q_u + Q_l = 0$. Similar to the thrust sweep, the thrust sharing, Figures 4.11(a), and 4.11(c), matches the data well. The thrust

sharing naturally has a much stronger dependence on the inter-rotor separation. At low separations the sharing is equally split, but as the separation increases the thrust share levels out near $T_l/T_u = 0.75$. This is close to the momentum theory result of 0.70. Similar to the thrust sweep, there is an over-prediction in torque, Figure 4.11(b), which results in an under-prediction in Figure of Merit, Figure 4.11(d). Below $h/D < 0.6$, as separation decreases there is a sharp increase in torque. The data does not exhibit this trend. Similarly, above $h/D > 0.6$, the rotor performance does not change. This behavior suggests that by then, the upper rotor wake is already fully contracted.

A similar sweep is also carried out at a high thrust level, $C_T \approx 0.014$, shown in Figure 4.12. The trends are similar but the predictions are improved. The thrust sharing, Figures 4.12(a) and 4.12(c), match well–once again. Again, the sharing begins nearly equal, and as separation increases, the upper rotor carries more, roughly $T_l/T_u = 0.75$. The torque prediction, Figure 4.12(b), matches well across the sweep. The prediction shows an increase in torque at low separation distances that again for some reason is missing in the data. At higher thrust, the thrust and torque level out quicker, by $h/D = 0.3$. This is because the wake contracts faster with higher thrust. Having matched the thrust and torque well, the Figure of Merit prediction, Figure 4.12(d), also matches very well.

In summary, except for the sharp increase in torque at very low inter-rotor separation, where the analysis predicts greater power than data, the predictions are satisfactory. As the axial separation approaches zero, the coaxial rotor conceptually approaches a single rotor with twice the blades; rendered impractical only by the fact that they must rotate in opposite directions. Therefore the coaxial rotor performance should in principle approach the single rotor performance as separation approaches zero. This is indeed observed in predictions. But not in test data. Thus it is the data that may be suspect at low separations, not the predictions. Figure 4.13 plots coaxial

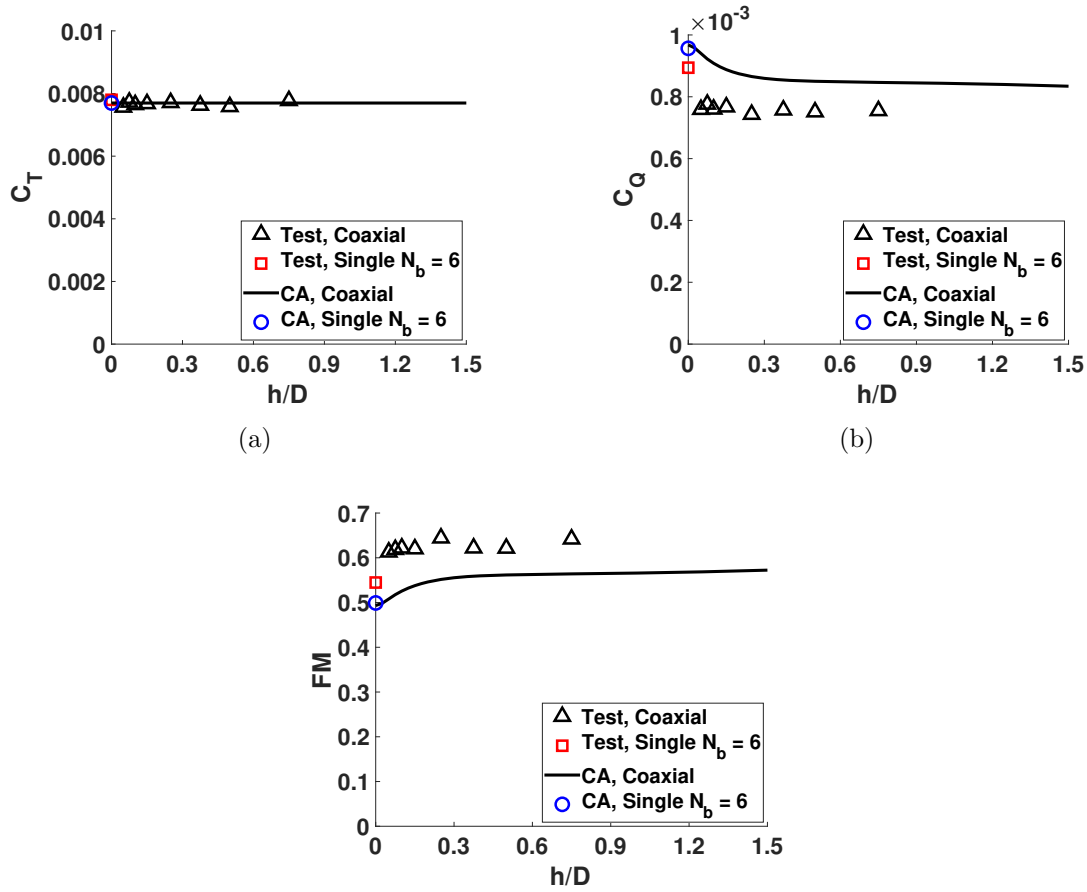

Figure 4.13: Performance of coaxial rotor with varying inter-rotor spacing shown together with the limit of single rotor with twice the blades ($N_b = 6$); 800 RPM, $C_T \approx 0.007$.

performance together with a single rotor performance with $N_b = 6$ at the limit of zero separation. Figure 4.13 shows the thrust levels are not suspect (Figure 4.13(a)), just the torque (Figure 4.13(b)). The measured torque appeared to be independent of inter-rotor separation and does not approach the single rotor data.

4.3 Structural Dynamics

The finite element structural model was developed in Chapter 3 and the non-rotating frequencies of the hingeless blade were measured and validated, Table 3.6 in Section 3.6.1. Here the analysis will be expanded to the rotating frame. The

Table 4.3: Model Mars rotor per-revolution (/rev) frequencies.

Mode	Articulated [/rev]	Hingeless [/rev]
1 **(F-T)**	1.11	1.58
2 **(T-F)**	2.16	2.20
3 **(L)**	4.02	4.02
4 **(T-F)**	5.27	6.43
5 **(T-F)**	8.20	8.44

frequencies are given in Table 4.3 and the fan plots for hingeless and articulated (in flap only) hubs are shown in Figure 4.14.

The hingeless fan plot, Figure 4.14(a), includes the measured non-rotating frequencies. **F** stands for flap, **L** for lag, and **T** for torsion. If there are two letters, the mode is coupled, with the first letter marking the dominant mode. For example, the first mode for both hubs is a flap dominated flap-torsion mode, **F-T**. The hingeless hub is very stiff (1.58/rev), with a first flap frequency slightly above full scale lift-offset rotors. The articulated hub is softer, but with a first flap frequency still quite high, 1.11/rev closer to classical hingeless hubs on Earth than an articulated hub. The higher flap frequencies are desired for handling qualities on Mars.

The large offset between the pitch axis at quarter-chord and center of gravity at half-chord causes strong flap-torsion coupling. Therefore all flap modes also have torsion and vice versa. Out of the first five modes, only the third includes lag motion. This mode is pure lag with no coupling. Because the articulation only affects flap (and torsion through coupling), the lag mode remains the same for both the hub types.

At the rotor operating speed, the lag frequency is 4.02/rev, which might result in resonance, but the academic nature of the study did not warrant a re-design of the blades. The other modes are sufficiently removed from resonance crossings.

The operating speed on Mars is 2400 RPM, but the vacuum chamber hover tests, described in Chapter 2, were conducted at 1000 RPM (due to motor heating

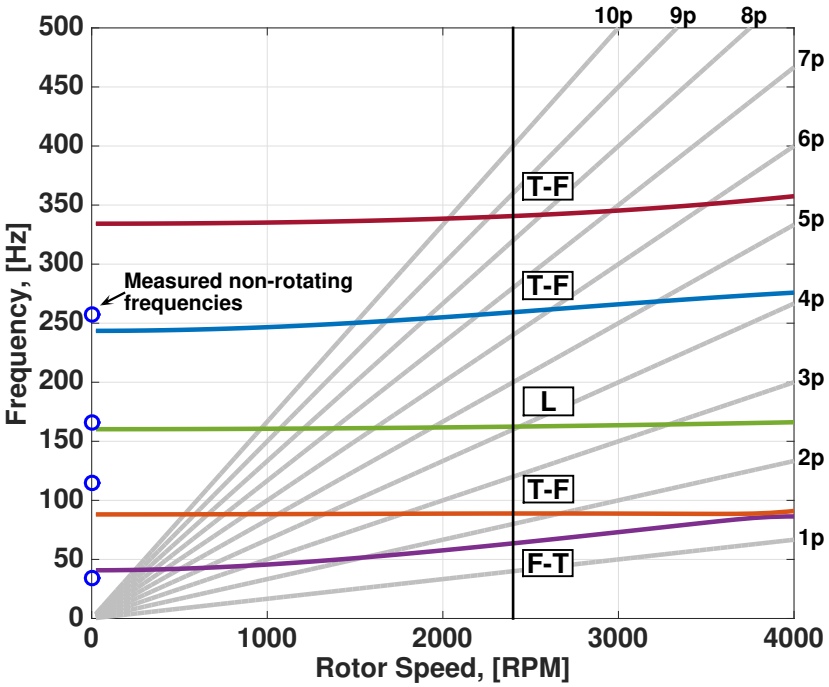

(a) Hingeless Hub Fan Plot

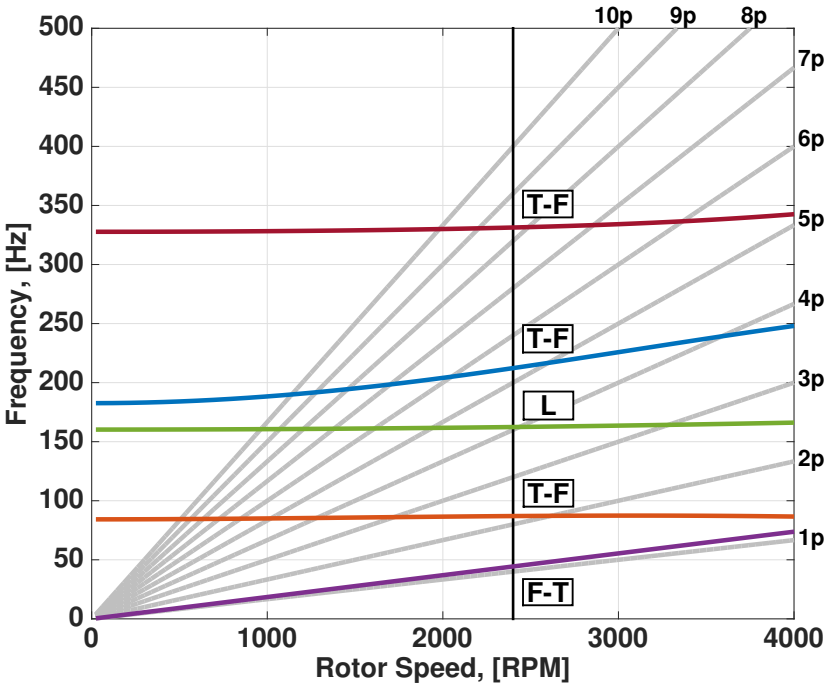

(b) Articulated Hub Fan Plot

Figure 4.14: Fan plots for hingeless and articulated hubs; operating RPM 2400, is designated by vertical black line.

restrictions). At this lower rotational speed, the hingeless hub is even stiffer, with the first flap frequency at 2.74/rev and the first lag frequency at 9.64/rev.

4.4 Mars Hover in Vacuum Chamber

Hover tests were carried out in a vacuum chamber; reproducing conditions similar to Mars. The tests are described in Chapter 2. Recall, collective sweeps were conducted at different Reynolds numbers, $3,000$ and $10,000$; at a constant Mach number. The data from these tests are used now for validating analysis in hover. Note that such validation is restricted to hover only, as forward flight is not feasible without a Martian wind-tunnel (or very large chamber).

The data in Chapter 2 includes three Reynolds numbers, $3,000$, $5,000$, and $10,000$, but the predictions are only conducted at the minimum and maximum Reynolds numbers to capture the extremes.

Figure 4.15 shows the blade loading coefficient C_T/σ versus collective. The predictions match well with the data at high collective-high thrust values. The maximum thrust achieved is also reasonably predicted. At negative thrust the CA predictions do not match the data, and in fact collapse to the same prediction for both Reynolds numbers. Additionally, the predicted onset of stall is premature. In the data, the onset of stall is delayed until very high collectives, $\theta > 30°$. The rotor achieves high thrust levels, $C_T/\sigma \approx 0.2 - 0.25$; above the typical stall limit of $C_T/\sigma = 0.16$ for conventional rotors. For positive thrust, the prediction captures the trend of greater thrust for higher Reynolds number.

More difficult at low Reynolds numbers is prediction of power, or torque. The power versus collective is shown in Figure 4.16. The power at low collective is now predicted better than at high collectives, quite the opposite trend from thrust. The power is over-predicted at high collectives, but better at lower collectives, near zero thrust. This suggests that the contributing factor to the over-prediction is the

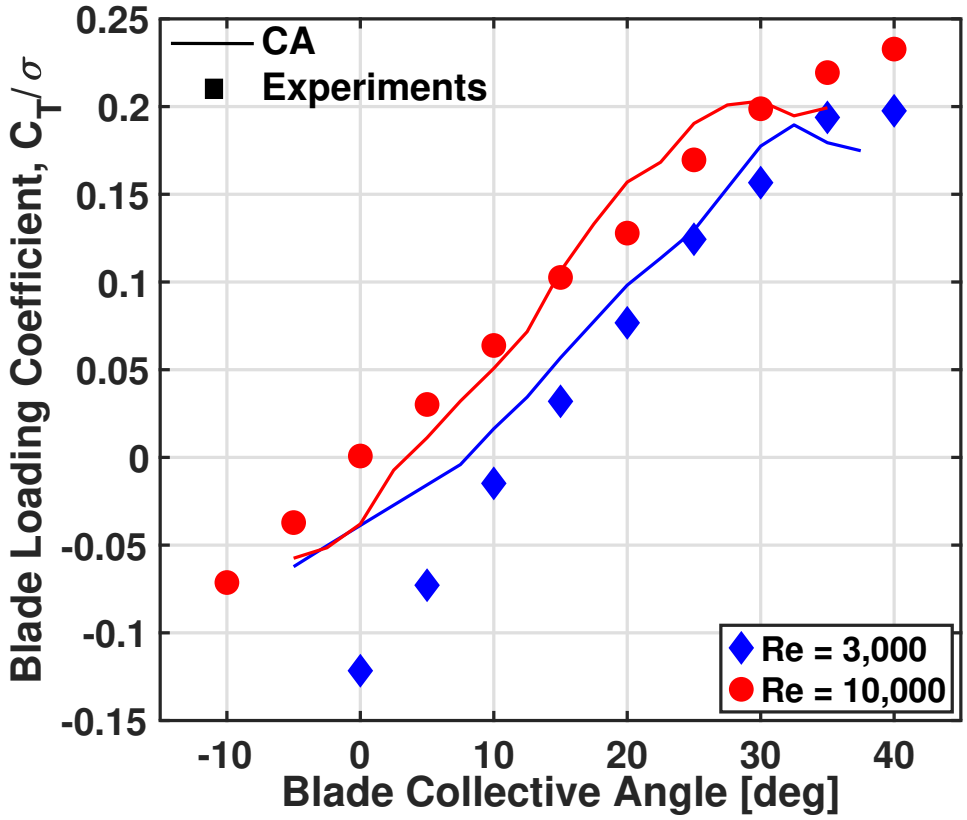

Figure 4.15: Measured and predicted thrust, C_T/σ, with collective, at different Reynolds numbers.

induced power. In general, unlike thrust, the power is more or less Reynolds number independent. Both the data and predictions show this trend–power at both $3,000$ and $10,000$ Reynolds numbers are the same.

Although analysis does not predict the thrust or power perfectly, it captures the general trends with collective and Reynolds number. The thrust is plotted versus power in Figure 4.17. For positive thrust, the key trend of increasing power with decreasing Reynolds number is well captured. For negative thrust, the trend flips in data, but not in predictions. At the lower Reynolds number $(3,000)$ the thrust-power relationship is better captured. For the higher Reynolds number $(10,000)$, the power is over-predicted above $C_T/\sigma = 0.1$. Stall is also premature. Overall, the gross trends match well with the data, and where they differ the deviation is on the conservative

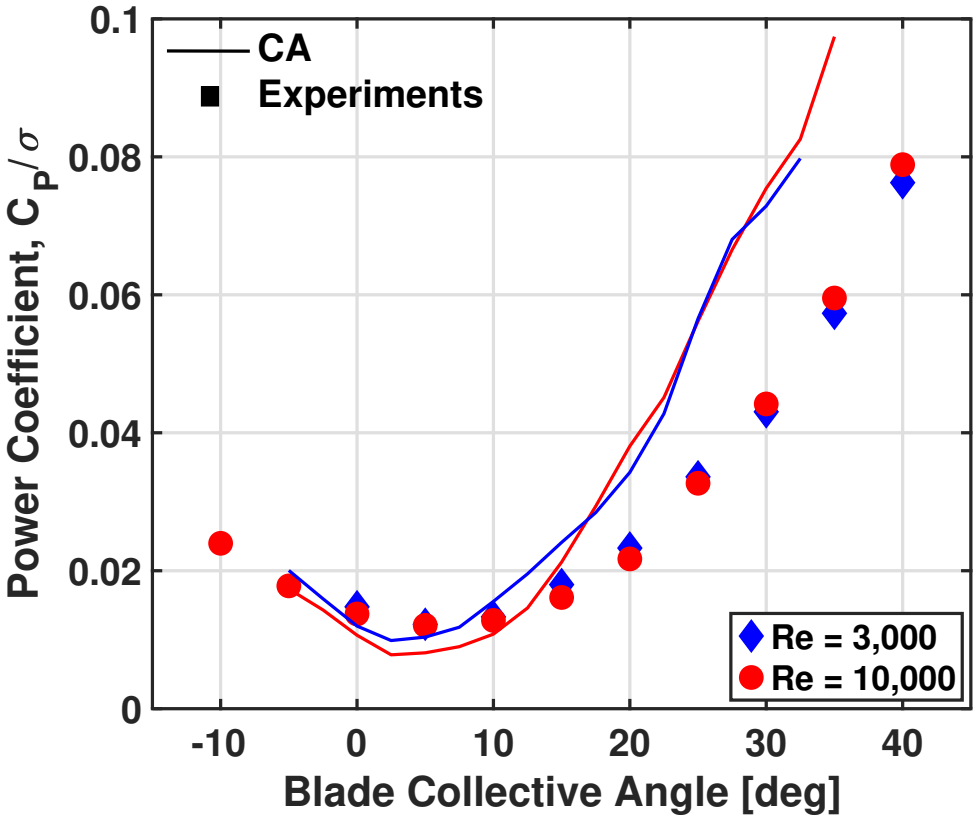

Figure 4.16: Data and CA prediction of variation of power coefficient, C_P/σ, with collective, at different Reynolds numbers.

side.

The Figure of Merit versus thrust is shown in Figure 4.18. The Reynolds number trends are predicted correctly, with higher Reynolds numbers achieving higher Figures of Merit. At the lower Reynolds number, the maximum Figure of Merit is slightly under-predicted. For the higher Reynolds number, the over-prediction in power seen earlier in the thrust-power curve appears as a much more pronounced under-prediction in Figure of Merit. Additionally, for the high Reynolds number, the maximum achievable blade loading, C_T/σ is under-predicted. The discrepancies between predictions and data can be accounted for by the inability of the analysis to include three-dimensional aerodynamics, which can have significant impact on rotor performance at low Reynolds numbers.

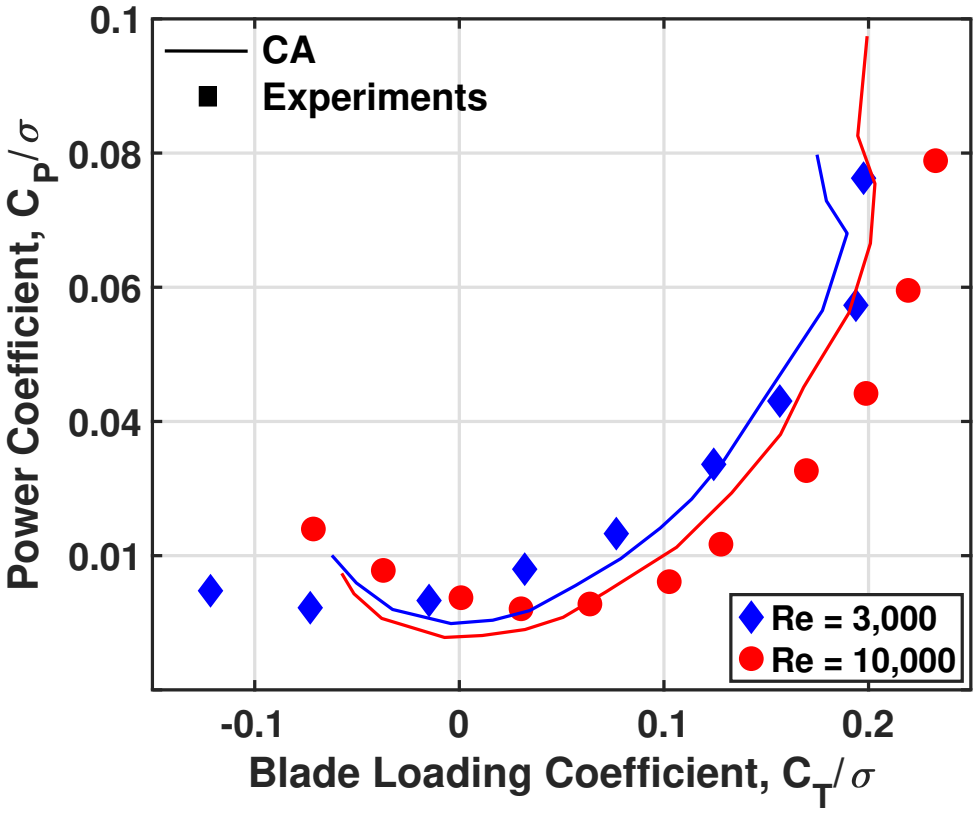

Figure 4.17: Data and CA prediction of variation of coefficient of power, C_P/σ, with blade loading, C_T/σ, at different Reynolds numbers.

The validated analysis is now ready for extension to coaxial flight on Mars.

4.5 Baseline Comprehensive Analysis

The single rotor analysis validated in Mars conditions is now synthesized into a coaxial rotor, validated with the best available conditions on Earth. The single rotor was a hingeless rotor (similar to the Mars helicopter), the coaxial analysis will compare both hingeless and articulated hubs. The articulation is in flap-only, both rotors are stiff in-plane to avoid ground resonance. First, a baseline is established for both. Then the effect of rotor separation, shaft angle and advance ratio are investigated as the important parametric variations.

The baseline flight conditions are described in Table 4.4 . The rotor was

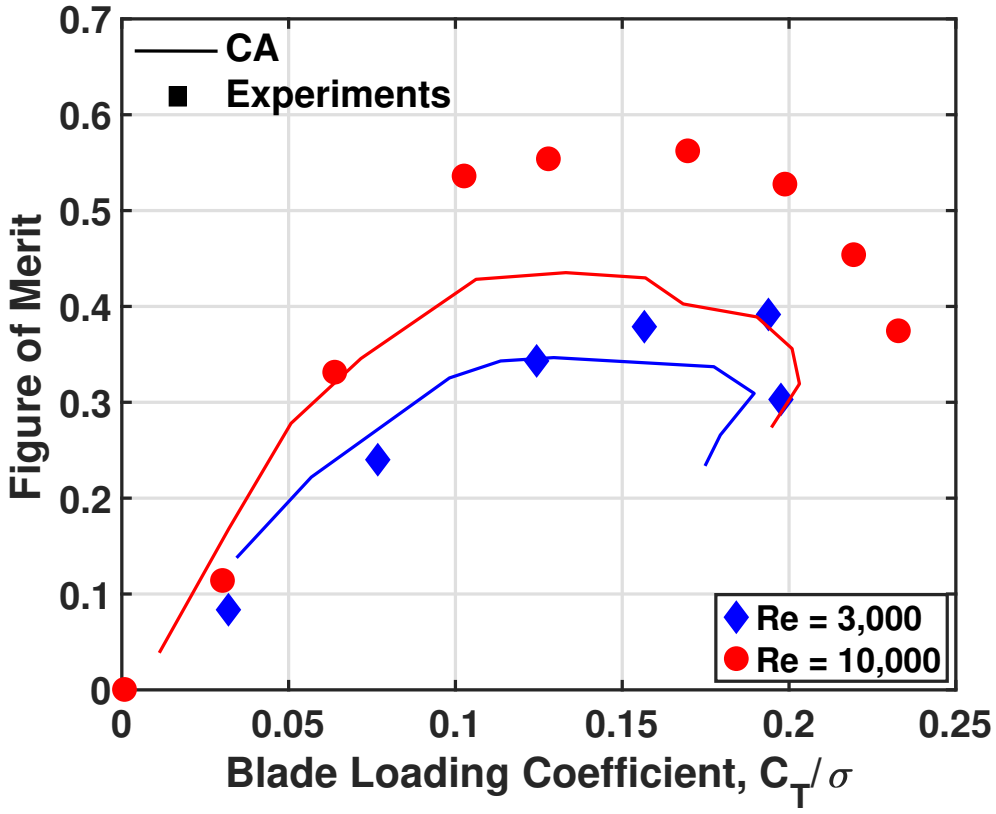

Figure 4.18: Data and CA prediction of variation of Figure of Merit, with blade loading coefficient C_T/σ, at different Reynolds numbers.

trimmed to zero lateral and longitudinal hub moments, zero total torque, and a thrust target of $C_T/\sigma = 0.08$. The trim procedure is described in Section 3.3.3. Using the same initial guess, the hingeless and articulated hubs converged in 86 and 126 iterations, respectively. The articulated rotor was expected to encounter greater difficulty converging because of the low aerodynamic damping on Mars and the proximity of its flap frequency to 1/rev. Table 4.5 lists the predicted trim control angles. The lower rotor has significantly larger collective, 75% and 96% more, for the hingeless and articulated rotors respectively. The hingeless hub has greater collective angles for both the upper and lower rotors compared to the articulated; 17% and 4% more, respectively. The hingeless rotor has higher hub loads and requires in general larger controls to trim to zero moments. Yet the blade motions are lower due to

Table 4.4: Baseline forward flight conditions.

Parameter	Value
Rotational Speed [RPM]	2400
Tip Reynolds	4687
Tip Mach	0.255
Lock number	0.075
Advance Ratio	0.10
Blade Loading, C_T/σ	0.08
Shaft Angle (nose down)	5.0°

Table 4.5: CA trimmed control angles.

	Hingeless	Articulated
Upper rotor: θ_o	6.28°	5.38°
Upper rotor: θ_{1c}	1.63°	1.58°
Upper rotor: θ_{1s}	−0.30°	−0.28°
Lower rotor: θ_o	10.94°	10.55°
Lower rotor: θ_{1c}	2.24°	2.18°
Lower rotor: θ_{1s}	1.54°	1.78°

higher stiffness.

Figures 4.19(a) and 4.19(b) show the tip deflections for the hingeless and articulated rotors respectively. The position of the quarter-chord at the tip is shown by the dashed line. It is banded by the projection of the blade chord at the tip. Thus, the edges of the colored bands represent the leading and trailing edge trajectories. The deflections include flexibility and control angles. The articulated hub experiences greater flap deflection when compared to the hingeless hub, as expected. The rotors are located at 0 and 0.1R ($h/D = 0.05$). Without any elastic deflection the position of the quarter-chord at the tip will fall directly on 0.0 and $0.1R$. The upper and lower rotors have no clocking angle so the blade passage occurs at azimuth angles of 0°, 90°, 180° and 270°. Vertical lines represent these blade passing locations, when the upper and lower blades might strike if separation were low. The minimum separations at blade passage azimuths are $6.87\%R$ and $6.86\%R$ for the hingeless and articulated hubs, respectively. These are remarkably similar, unlike on Earth were

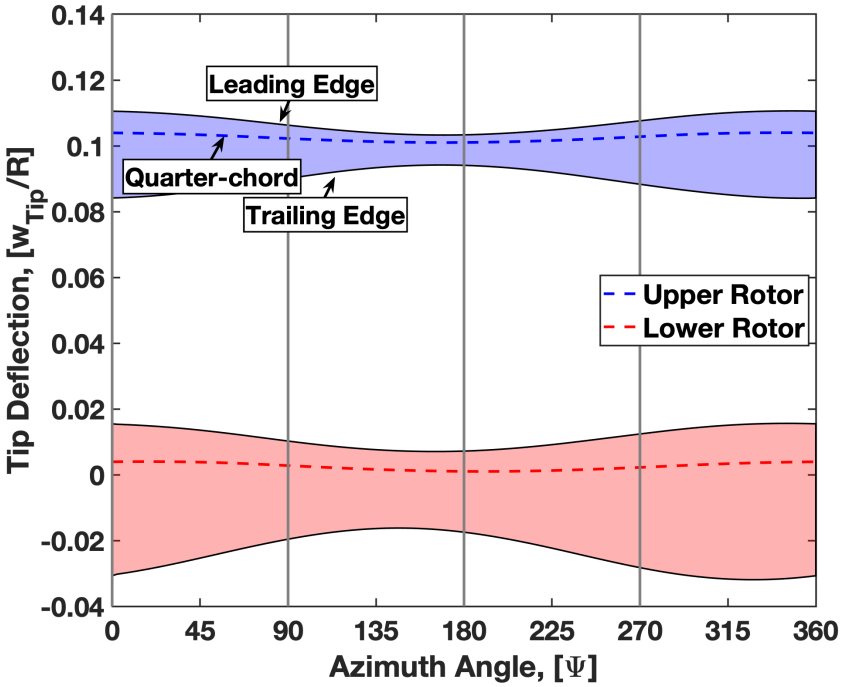

(a) Tip deflection for hingeless coaxial rotor

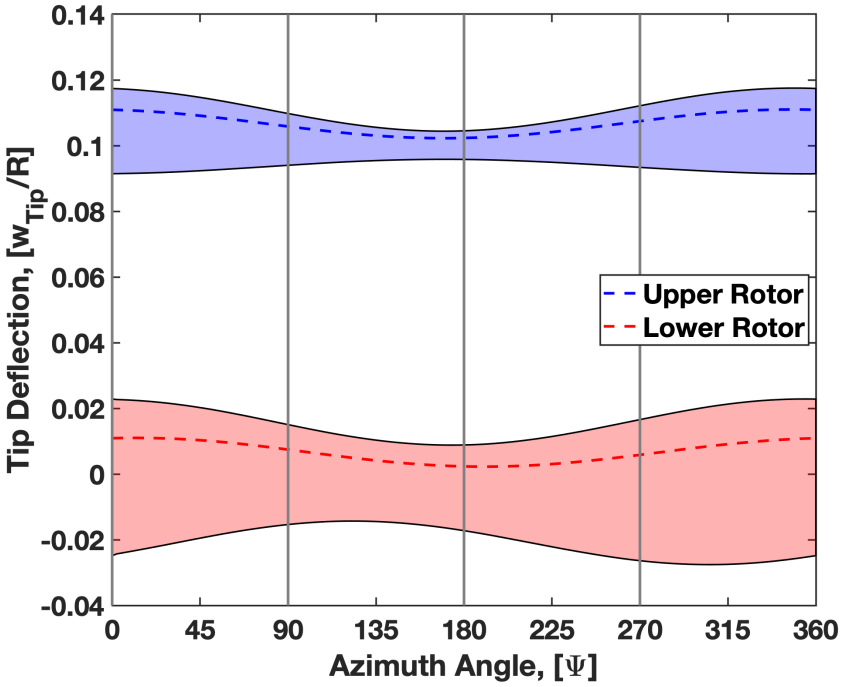

(b) Tip deflection for articulated coaxial rotor

Figure 4.19: Tip deflections for hingeless and articulated rotors from CA predictions; bands include full chord length with control angles and elastic deflections.

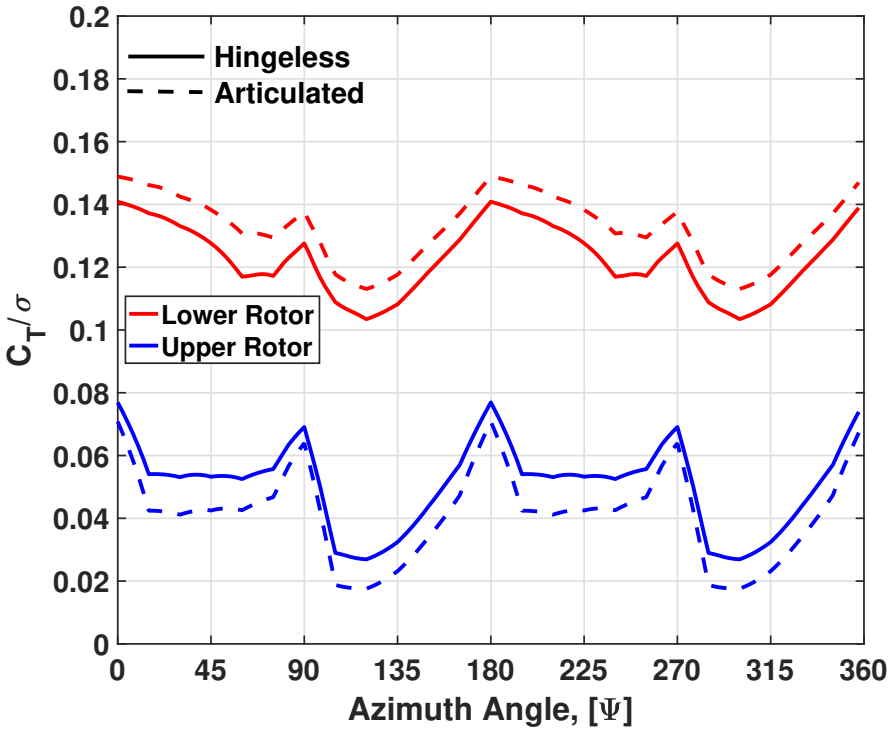

Figure 4.20: Thrust C_T/σ over the rotor azimuth for both hingeless and articulated rotors shown separately for upper and lower rotors; σ is solidity of each rotor.

the articulated hub would be expected to produce significantly larger motions and closer encounters at blade passage.

The deflection of the quarter-chord does not dictate separation, the motion of the leading and trailing edges due to control pitch is more important. The larger collective of the lower rotor resulted in significantly larger bands swept by the lower rotor compared to the upper rotor. On Mars, control angles would make the blades strike, not deflections, because of the large chord needed to mitigate the low Reynolds number. Note also, it is the hingeless hub that would in general require greater cyclic, aggravating the danger of blade strike. Thus, on Mars, the hingeless hub might be at a greater risk of blade strike, not the articulated hub. This is a conclusion contrary to our understanding on Earth.

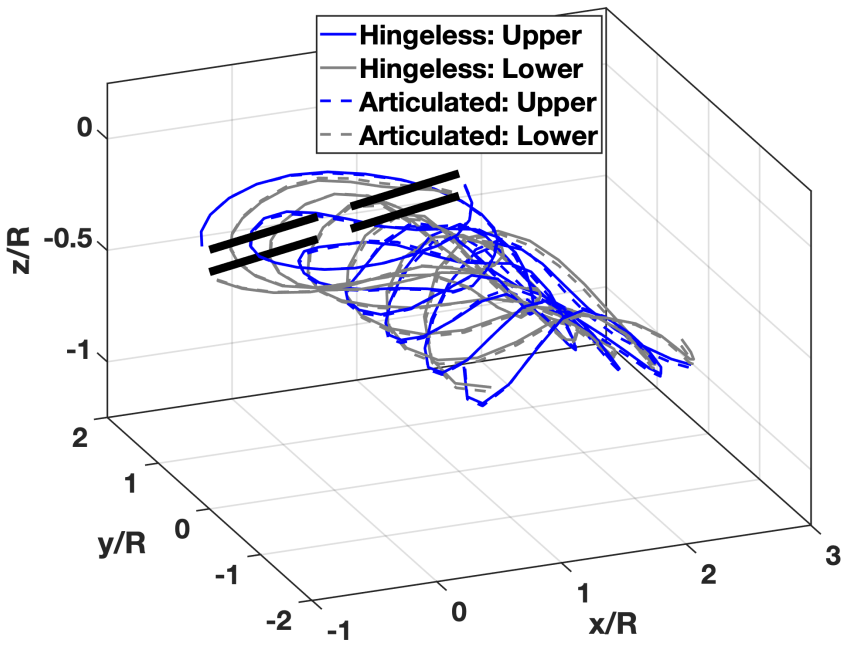

Figure 4.21: Isometric view of free wake geometry showing similarity of the wake from both rotors; at 0° and 180° azimuths when the upper and lower blades are aligned.

4.5.1 Rotor Thrust

Figure 4.20 shows the individual rotor thrust around the azimuth. The lower rotor, red lines, produces significantly more thrust than the upper rotor, a difference much more dramatic than in hover. The articulated hub, dashed lines, has a larger thrust sharing disparity. The upper rotor produces a smaller portion of the total thrust, $T_u/T = 23.6\%$, for the articulated hub compared to the hingeless, $T_u/T = 29.0\%$. All rotors show impulsive loading at 4/rev from blade passage. The impulsive loadings are in phase for all rotors, but the upper rotor experiences larger magnitudes.

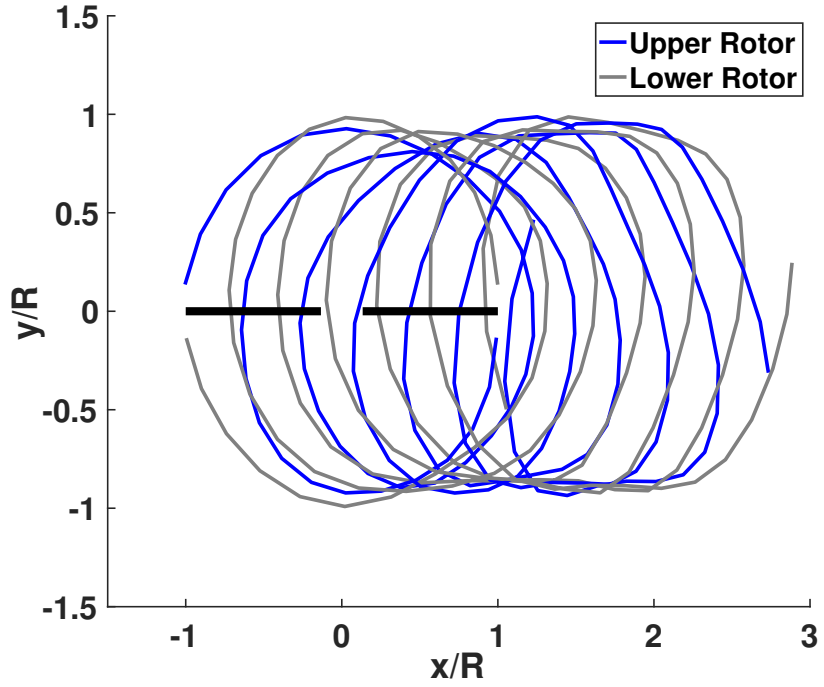

Figure 4.22: Top view of free wake geometry of the hingeless rotor; at 0° and 180° azimuths when the upper and lower blades are aligned.

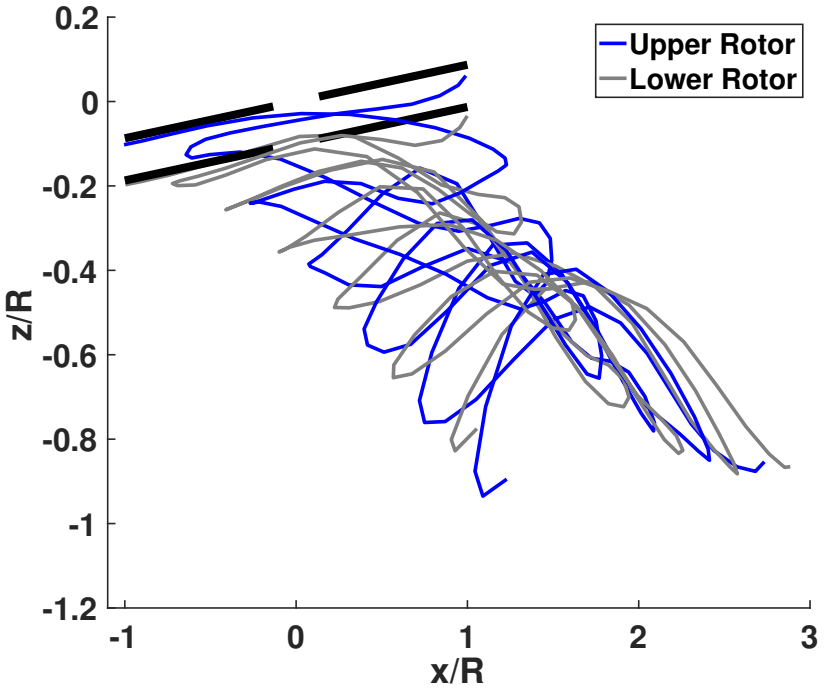

Figure 4.23: Side view of free wake geometry of the hingeless rotor; at 0° and 180° azimuths when the upper and lower blades are aligned.

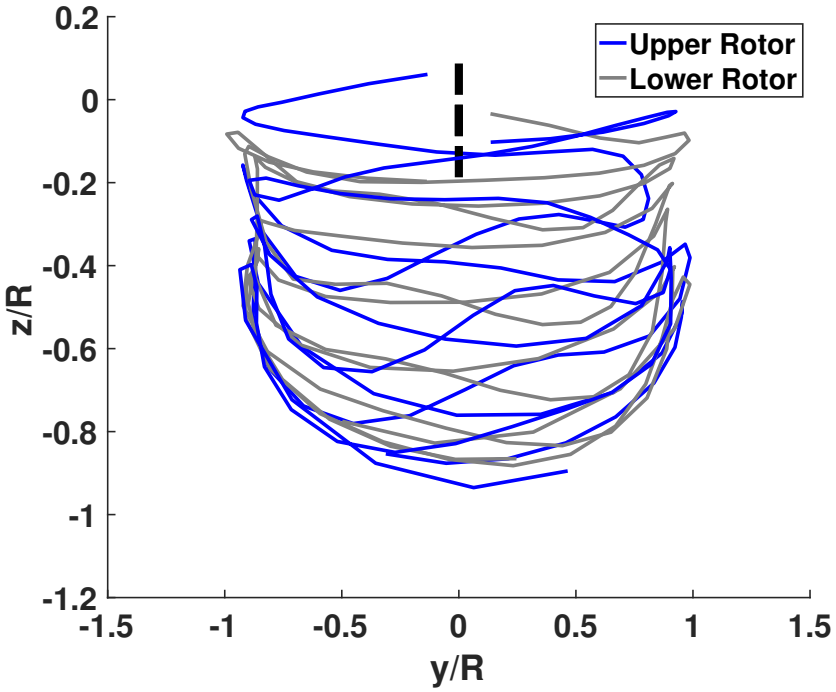

Figure 4.24: Rear view of free wake geometry of the hingeless rotor; at 0° and 180° azimuths when the upper and lower blades are aligned.

4.5.2 Wake Geometry

The patterns of the free wake geometry can often aid in better understanding of the behavior of rotor thrust. Figure 4.21 shows the wake geometry for both the hingeless and articulated hubs. They are difficult to distinguish as they are very similar overall. Each line traces the trajectory of a single tip trailer released from the blade tip. Figures 4.22, 4.23, 4.24, show only the hingeless wake from three views. These views show the propagation and distortion of the wake and the ingestion of the upper wake through the lower. Geometries only show trajectory not the core growth. Note that even though core growth is modeled, there is no dissipation of vorticity. These wake geometries reveal the overall nature of the flow field qualitatively, the sectional airloads, next, will provide more insight on core growth through interactions, and the chapter on CFD later will capture the dissipation of vorticity if any.

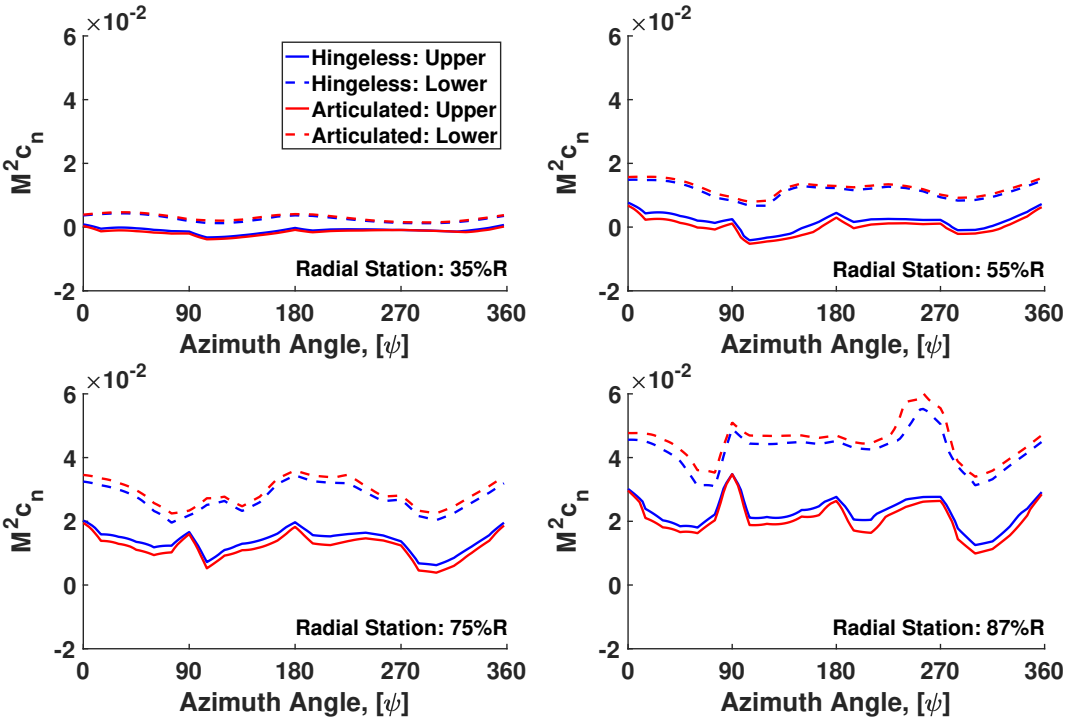

Figure 4.25: Sectional normal force at multiple radial stations from CA; for both hingeless and articulated rotors.

4.5.3 Sectional Airloads

Figures 4.25, 4.26, and 4.27 show the sectional normal force, chord force, and quarter-chord pitching moment in non-dimensional form:

$$M^2 c_n = \frac{dN/dr}{\frac{1}{2}\rho c a^2}; \quad M^2 c_c = \frac{dC/dr}{\frac{1}{2}\rho c a^2}; \quad M^2 c_{m_{25}} = \frac{dM_{25}/dr}{\frac{1}{2}\rho c^2 a^2} \tag{4.4}$$

This is the proper non-dimensionalization for rotor sectional aerodynamics, where the pure coefficients and the Mach number are both undefined but the product is well-defined. Each airload is shown at four radial stations: 35%R, 55%R, 75%R, and 87%R. The airloads are at the same time, hence in their own rotor azimuth, to facilitate direct comparison. An azimuth of 90° for example, means the blades are on their respective advancing sides, at the same time, but on two different sides of the disk.

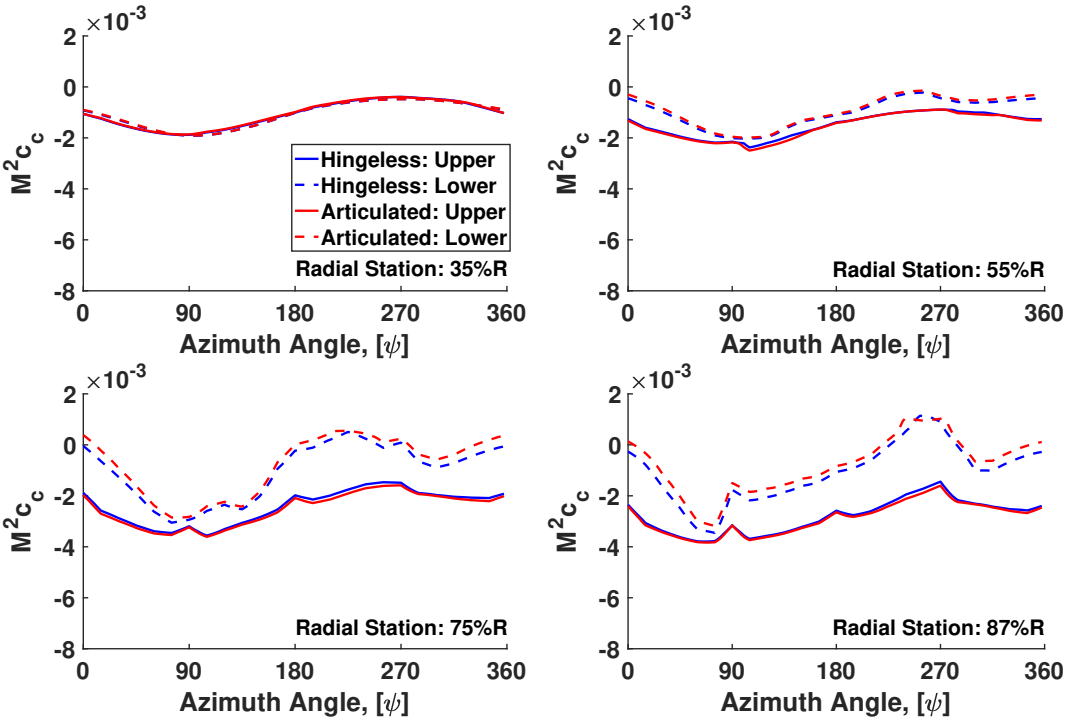

Figure 4.26: Sectional chord force at multiple radial stations from CA; for both hingeless and articulated rotors.

For the normal force, Figure 4.25, the mean value increases almost 4 fold from the root to tip. The magnitude of the oscillatory loads (peak-to-peak) increases roughly 8 fold from root to tip. There is the same 4/rev impulsive loading from blade passage. These impulsive loads become more pronounced near the blade tip. The magnitude is slightly larger on the upper rotor compared to the lower, which was also reflected in the integrated thrust (Figure 4.20). The differences between the hingeless and articulated hubs are negligible, only the steady loads show slightly larger thrust sharing for the articulated rotor.

For the chord force, Figure 4.26, the mean value increases nearly 3 times on the upper rotor from the root to tip while the lower rotor remains roughly constant. The magnitude of the oscillatory loads increases almost 2 fold on the upper rotor and 3 fold on the lower rotor from root to tip. There is the same 4/rev impulsive loading from blade passage. These impulsive loads become more pronounced near the

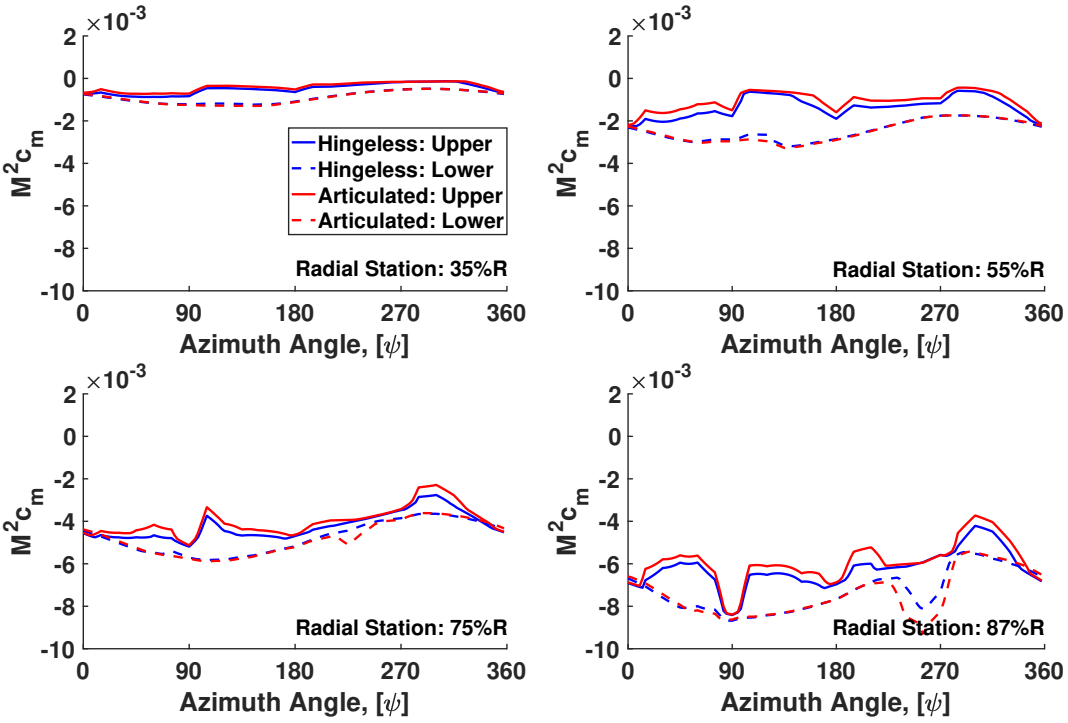

Figure 4.27: Sectional quarter-chord pitching moment at multiple radial stations from CA; for both hingeless and articulated rotors.

blade tip. The magnitude of the oscillatory loads is larger on the lower rotor which is opposite to the normal force trend. The differences between the hingeless and articulated hubs are negligible. Other than the 4/rev blade passage, the dominant loading is largely 1/rev. The 4/rev load is much smaller in chord force and barely noticeable.

For the quarter-chord pitching moment, Figure 4.27, the mean value increases nearly 7 fold from the root to tip. The magnitude of the oscillatory loads increases almost 8 fold from root to tip. There is the same 4/rev impulsive loading from blade passage. These impulsive loads become more pronounced near the blade tip. The magnitude is similar between upper and lower rotors. The differences between the hingeless and articulated hubs only appear in impulsive loads.

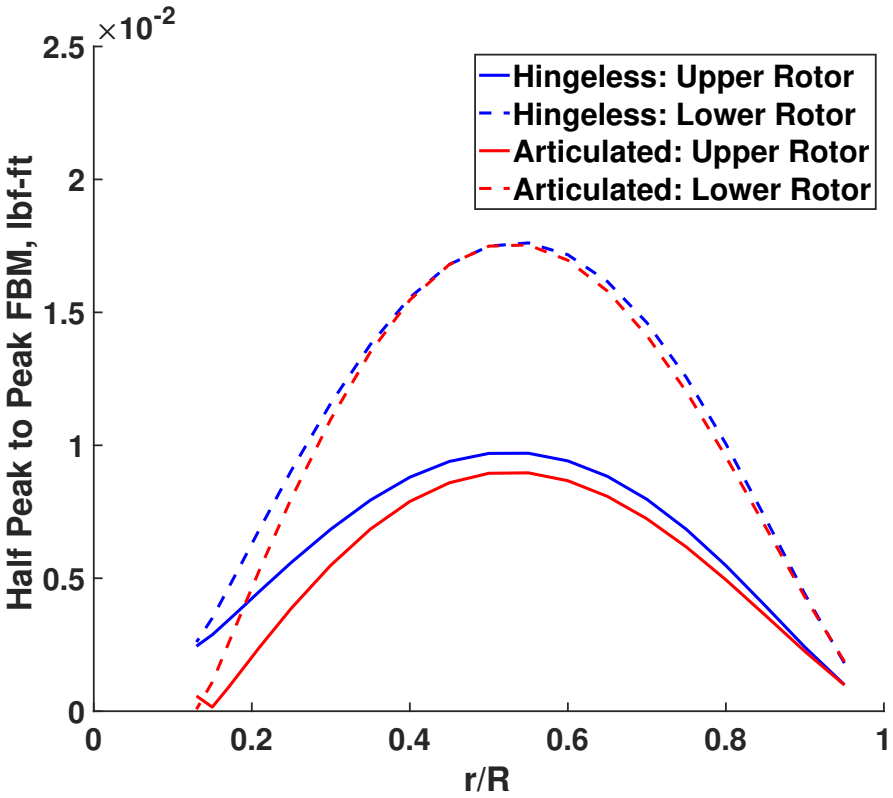

Figure 4.28: Flap bending moment half peak-to-peak oscillatory magnitude from CA.

4.5.4 Blade Structural Loads

For blade design, ultimately structural loads are needed. Higher loads mean more structure to absorb them, hence more weight. Even a gram of additional weight, when carried over 80 million miles, has an impact on the overall mission. For a rotor blade spinning at 2400 RPM the principal concern is the oscillatory loads. The oscillatory loads are transmitted to the aircraft. These accumulate cycles and can lead to fatigue of many hub and aircraft components. These can also lead to inter-laminar failure on the blades. The flap and lag bending moments and torsional moments are shown next in different formats. Figures 4.28, 4.31, and 4.34 show the half peak to peak load along the span. Figures 4.29, 4.32, and 4.35 show only the oscillatory, mean removed, loads at three radial stations: 30%R, 50%R, and 70%R.

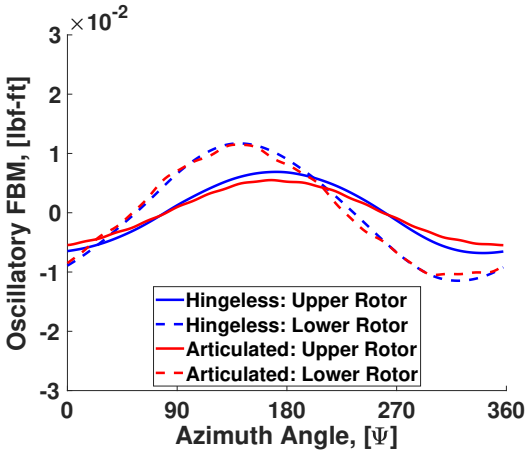

(a) Flap bending moment at 30%R

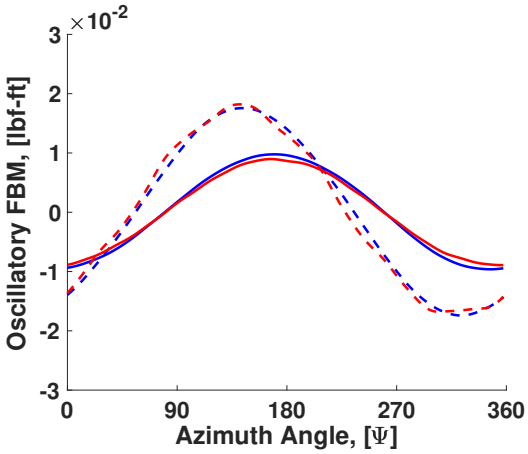

(b) Flap bending moment at 50%R

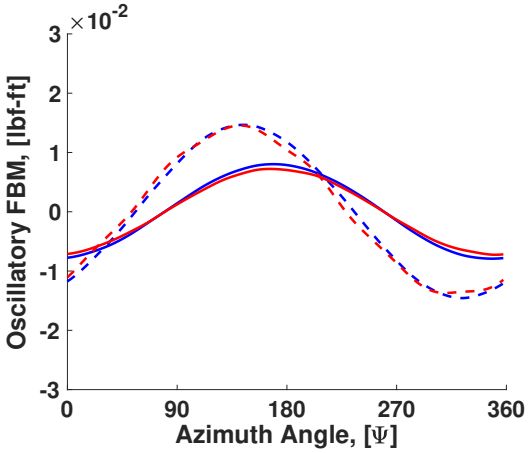

(c) Flap bending moment at 70%R

Figure 4.29: Oscillatory flap bending moment from CA.

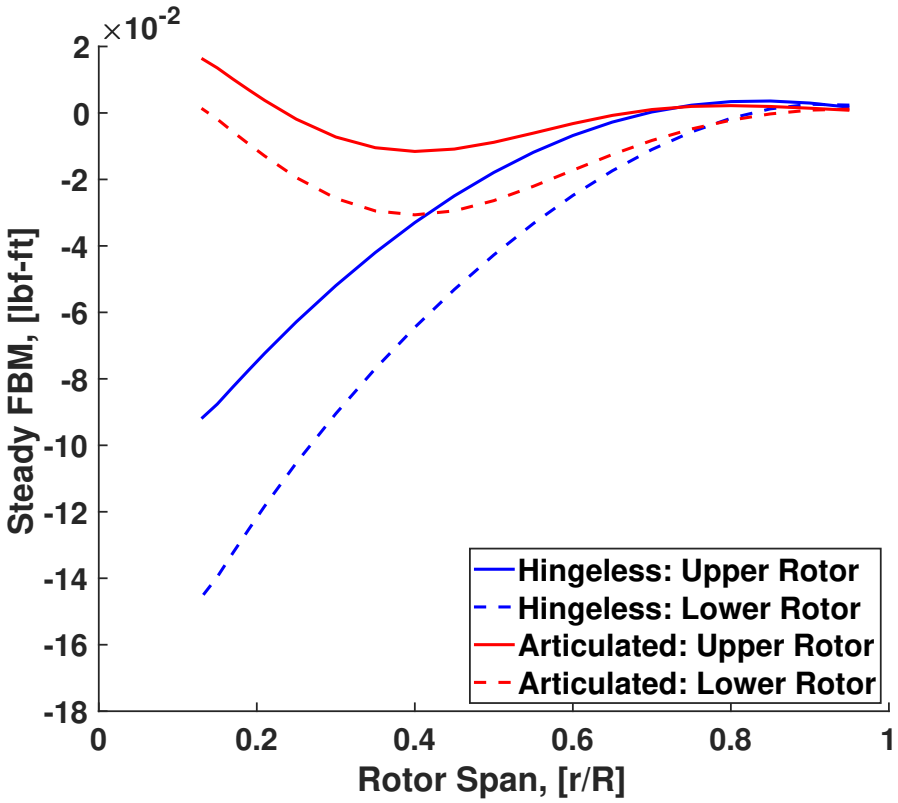

Figure 4.30: Steady flap bending moment from CA.

Figures 4.30, 4.33, and 4.36 show the steady load along the span.

Figure 4.28 shows the oscillatory flap bending moment (half peak-to-peak) versus span. The lower rotors have a nearly twice the loading compared to the upper. This follows the difference in thrust between the upper and lower rotors. At the hinge, the articulated loads reduce to zero whereas the hingeless carry some load as expected. What is surprising is that the hingeless hub does not show significantly greater loading as typical on Earth. This is due to the fact that the airloads in the thin atmosphere are very small. There simply is not enough aerodynamic loading to cause a difference in oscillatory flap bending loads. Figure 4.29 shows the waveform of the oscillatory flap bending moment. The load is entirely 1/rev caused by the forward flight velocity. There is negligible higher frequency content. Thus, the blade passage impulses so conspicuous in airloads do not appear in the structural loads. In the steady flap bending moment (Figure 4.30) the hingeless hub does have greater

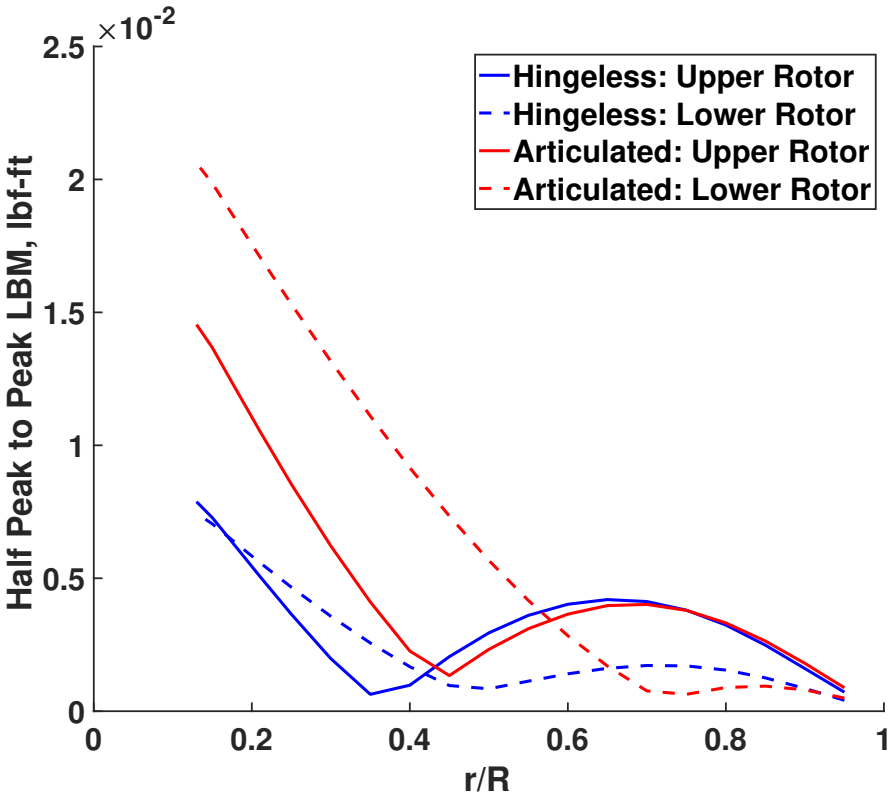

Figure 4.31: Lag bending moment half peak-to-peak oscillatory magnitude from CA.

loading as typical on Earth. The hingeless load is 8 and 5 times greater on the upper and lower rotors, respectively.

Figure 4.31 shows the oscillatory lag bending moment (half peak-to-peak) versus span. The upper and lower rotors carry a similar load for the hingeless hub. On the (flap-)articulated hub, except close to the blade tip, lower rotor has a greater load. The maximum load occurs at the root, as expected as there is no lag hinge for either hub. The (flap-)articulated hub has a greater load compared to the hingeless. The difference is larger on the lower rotor with a peak load nearly 3 times that of the hingeless, while on the upper rotor it is approximately twice. Figure 4.32 shows the mean removed waveform of the lag bending moment which consists of both 1/rev and higher frequency content (primarily 4/rev). These higher frequency content is a result of interactions with the blade lag mode (4.02/rev for both hubs). For the

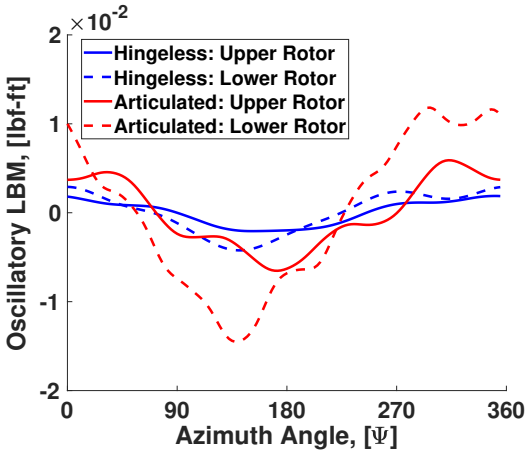

(a) Lag bending moment at 30%R

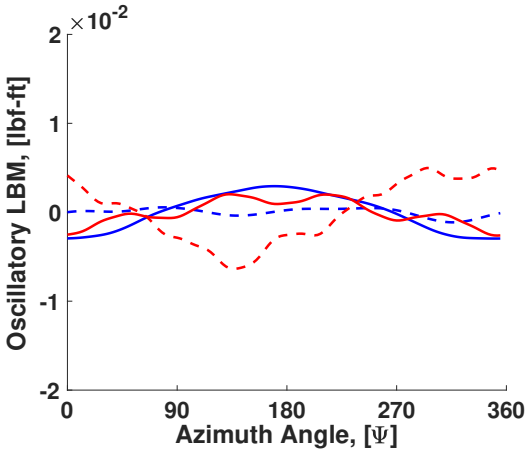

(b) Lag bending moment at 50%R

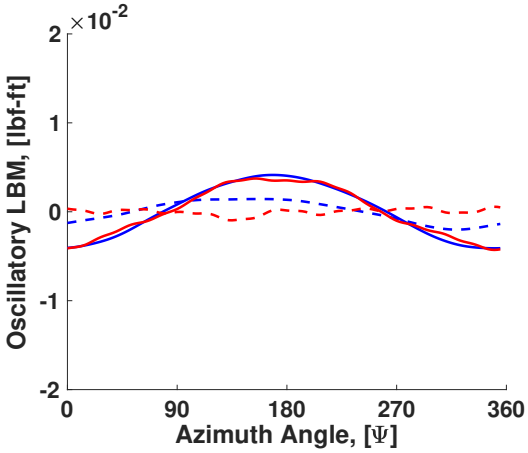

(c) Lag bending moment at 70%R

Figure 4.32: Oscillatory lag bending moment from CA.

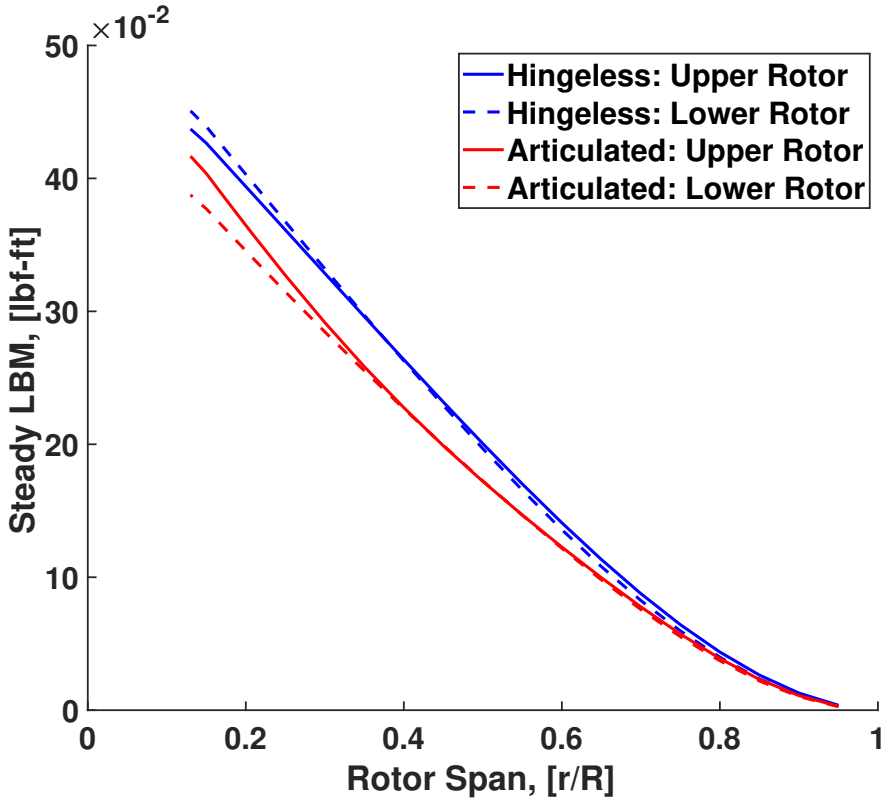

Figure 4.33: Steady lag bending moment from CA.

steady lag bending moment (Figure 4.33), both rotors have very similar loads and the hub types have negligible differences. This steady load is large because of the high centrifugal loading from a high RPM (2400 RPM) and 50% center of gravity offset.

In Figure 4.31 the oscillatory lag bending moment (half peak-to-peak) appears to have a discontinuity. The load in fact does not have a discontinuity. This is simply the oscillatory load reducing in magnitude, approaching zero (no oscillations), and reversing in phase so peaks become troughs and vice versa. The apparent discontinuity is simply an artifact of plotting the peak-to-peak magnitude.

Figure 4.34 shows the oscillatory torsion moment (half peak-to-peak) versus span. The lower rotors have a almost twice the loading compared to the upper. This follows the difference in flap bending due to the pitch-flap coupling caused by the center of gravity offset. The maximum load occurs at the root. The articulated hub

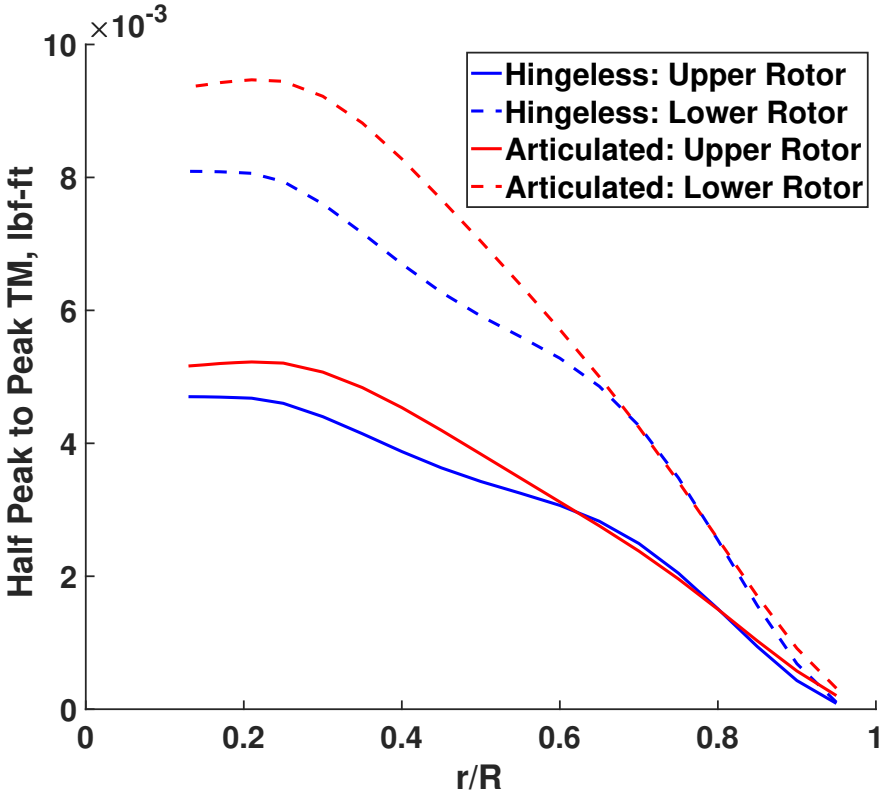

Figure 4.34: Torsion moment half peak-to-peak oscillatory magnitude from CA.

has moderately higher (14%) loads. At the blade tip, the loads reduce to zero. The peak magnitude is nearly half of the peak flap and chord bending magnitudes. For conventional, full scale rotorcraft the difference is substantially greater. Figure 4.35 shows the mean removed waveform of the torsion moment. The load is entirely 1/rev, again, following the flap bending moment. There is negligible higher frequency content. For the steady torsion moment (Figure 4.36) the hingeless hub has larger loading at the root although both reduce toward the tip uniformly. The hingeless hub has torsion moments 8 and 5 times higher on the upper and lower rotors, respectively.

For both hubs, the loads show a phase difference between the upper and lower rotors. The lower rotor leads the upper rotor by $30 - 35°$.

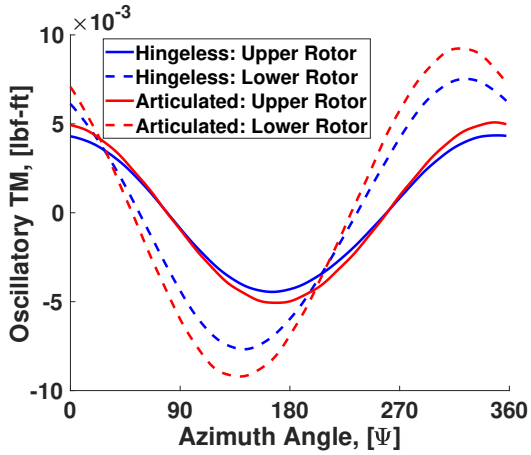

(a) Torsion moment at 30%R

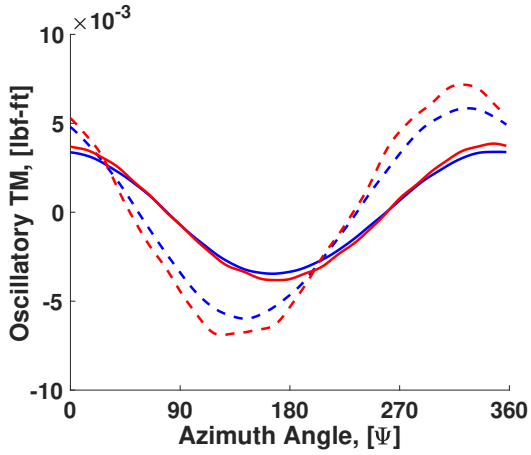

(b) Torsion moment at 50%R

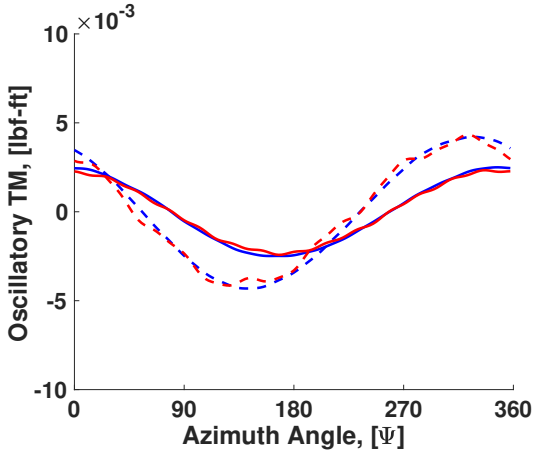

(c) Torsion moment at 70%R

Figure 4.35: Oscillatory torsion moment from CA.

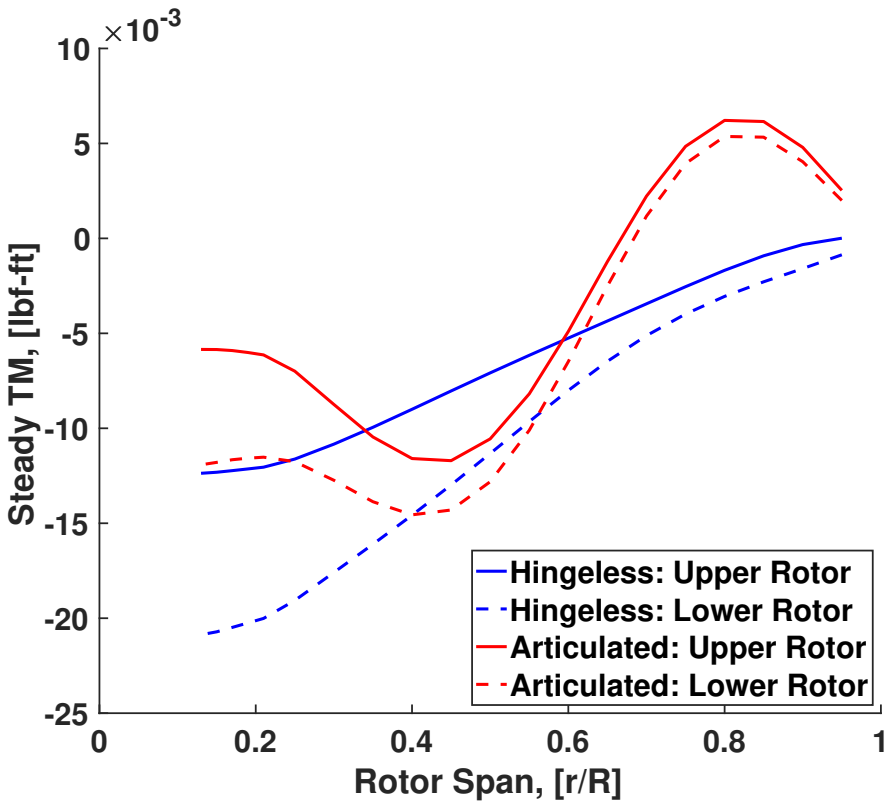

Figure 4.36: Steady torsion moment from CA.

4.5.5 Pitch Link Loads

Pitch link loads are important for sizing the control system. For a small aircraft, high steady pitch link loads can cause serious problems for controller bandwidth. The prediction of pitch link loads are shown in Figure 4.37. The oscillatory (mean-removed) and steady loads are shown separately. The oscillatory loads (Figure 4.37(a)) follow the same pattern as the torsion moments. The lower rotor has a higher magnitude due to the higher thrust level and the differences between hingeless and articulated hubs are negligible. The waveform is dominated by 1/rev. The steady pitch link loads (Figure 4.37(b)) also follow the same pattern as the torsion moments. There are significant differences between both upper and lower rotors and between hingeless and articulated hubs. The hingeless has twice the steady pitch link loads; this trend holds for both rotors.

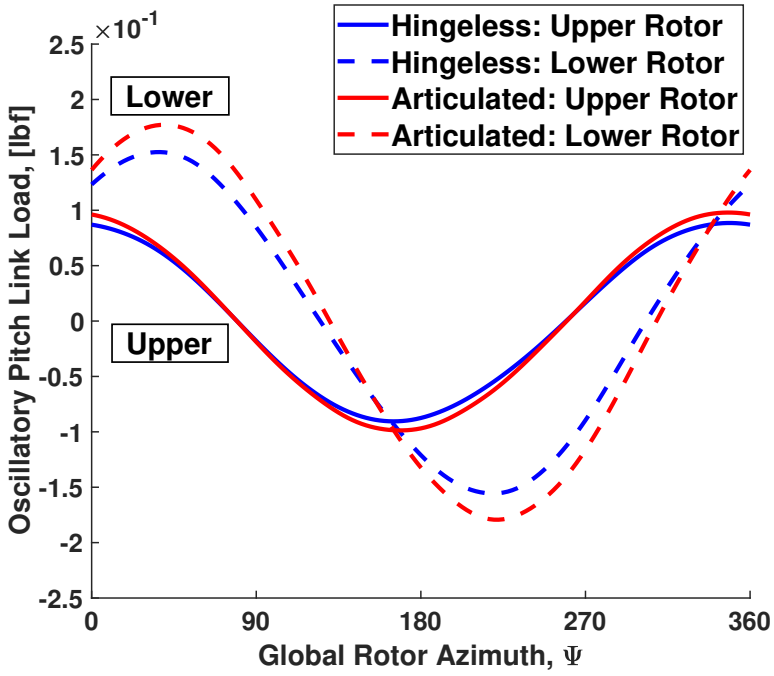

(a) Oscillatory pitch link loads.

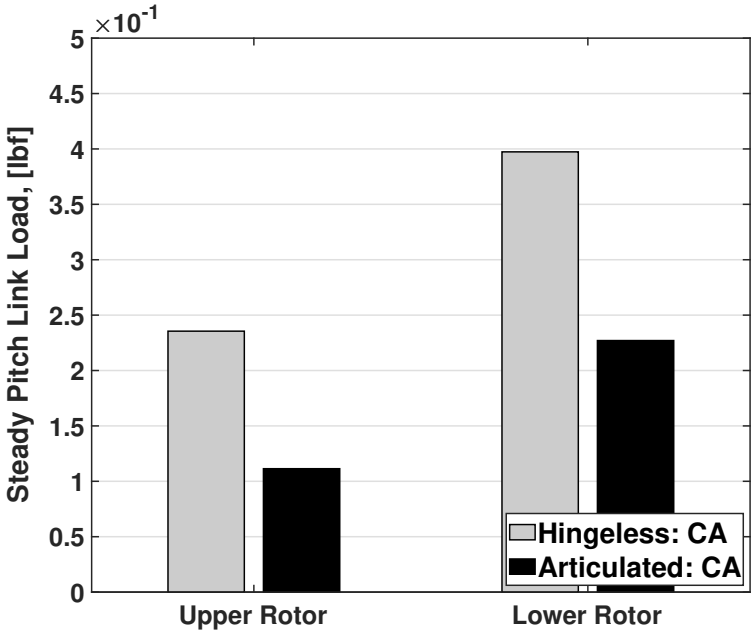

(b) Steady pitch link loads.

Figure 4.37: Pitch link loads for hingeless and articulated rotors from CA.

For a simple physical understanding, consider a rigid blade with isolated torsion. The total torsion moment at the blade root is

$$\text{Torsion Moment} = \gamma \overline{M}_{\text{aero}} - I_f(\ddot{\theta} + \nu_\theta^2 \theta) \tag{4.5}$$

where

$$\text{Aerodynamic Moment} : \gamma \overline{M}_{\text{aero}} \tag{4.6}$$

$$\text{Inertial Moment} : I_f \ddot{\theta} \tag{4.7}$$

$$\text{Propeller Moment} : I_f \nu_\theta^2 \theta \tag{4.8}$$

and γ is the Lock number, $\overline{M}_{\text{aero}}$ is the aerodynamic moment, I_f is moment of inertia about pitch axis, θ is the pitch angle (positive leading-edge up), ν_θ is the rotating natural frequency for torsion, and the dots denote azimuthal derivatives (time derivatives multiplied by rotation speed). The aerodynamic component is normally nose down (except for certain extreme angles of attack). However, when there is blade flapping and center of gravity offset, one additional moment needs to be considered. This is a pitch-flap coupling term introduced by the chordwise center of gravity offset which is nose-up for center of gravity behind pitch axis.

$$\text{Torsion Moment} = \gamma \overline{M}_{\text{aero}} - I_f(\ddot{\theta} + \nu_\theta^2 \theta) + I_x(\ddot{\beta} + \beta) \tag{4.9}$$

where β is the flap angle and I_x is flapping inertia of the offset $\int mxrdr$ with x as the offset.

The articulated hub has a lower nose down steady pitch link load because of this nose-up term from higher flapping. The hingeless hub flaps less, creating a smaller nose-up pitch flap coupling and therefore carries a larger nose-down pitch link load. This means it is in fact beneficial to carry a chordwise center of gravity

offset to reduce the steady pitch link loads. The pitch-flap coupling term disappears with no center of gravity offset. Allowing the chordwise center of gravity to remain at 50%c permits the use of the best airfoil for the aerodynamics and reduces the steady pitch link loads.

4.6 Excursions from Baseline Flight Condition

Having established the loads in the baseline flight condition, the effect of advance ratio, shaft angle, rotor separation, and blade loading are now investigated for certain important excursions. Only the above variables are changed, one at a time; the rest remain same as the baseline given earlier in Table 4.4.

4.6.1 Effect of Advance Ratio

The advance ratio is swept from 0.02 to 0.12, Figure 4.38. The baseline advance ratio was 0.10. The tip separation is insensitive to advance ratio and remains similar between the hubs. The oscillatory flap bending moment, torsion moment, and pitch link load all exhibit similar behavior in time. However the peak-to-peak magnitudes reveal interesting trends with advance ratio. The upper rotor increases continuously up to $\mu = 0.08$, but then reverses. The lower rotor increases continuously without any reversal. Both hubs carry similar loads. The lag bending moment shows more distinction between hubs, the articulated hub carrying higher loads at higher advance ratios. The hingeless hub carries twice the steady pitch link load for all advance ratios.

4.6.2 Effect of Shaft Angle

The shaft angle is swept from $-30°$ (nose-down) to $40°$ (nose-up), Figure 4.39. This is a far greater excursion than what is usual on Earth in anticipation of high

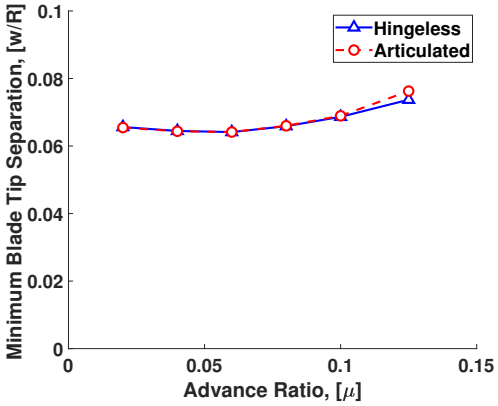

(a) Inter-rotor Separation

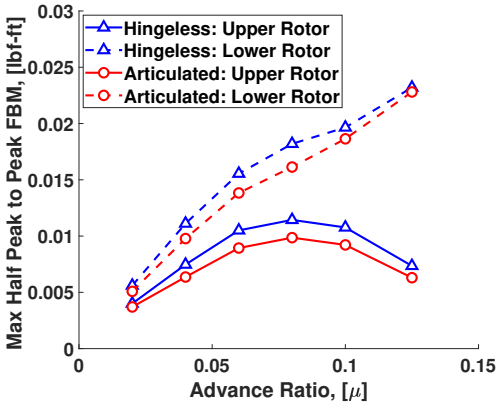

(b) Flap Bending Moment

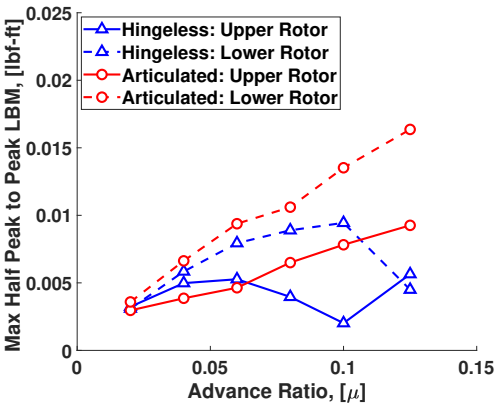

(c) Lag Bending Moment

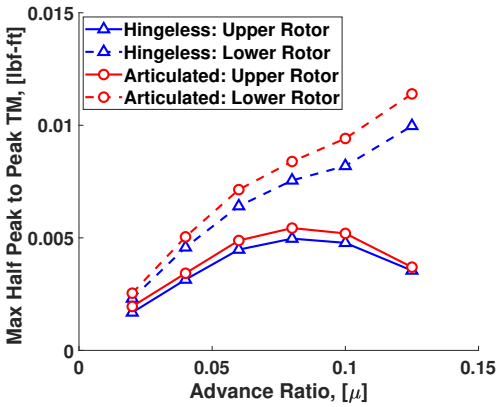

(d) Torsion Moment

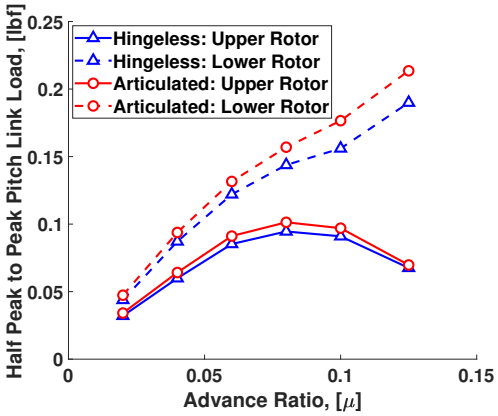

(e) Oscillatory Pitch Link Load

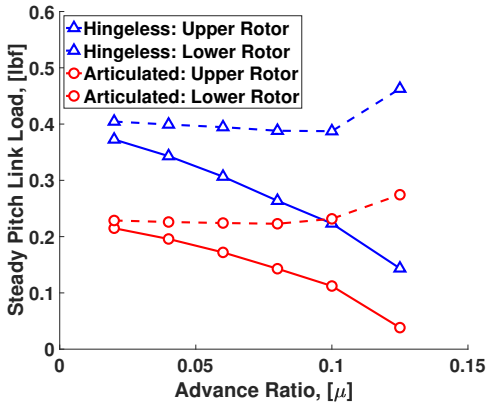

(f) Steady Pitch Link Load

Figure 4.38: Effect of advance ratio; at $C_T/\sigma = 0.08$, $\alpha = 5.0°$, $z/R = 0.10$.

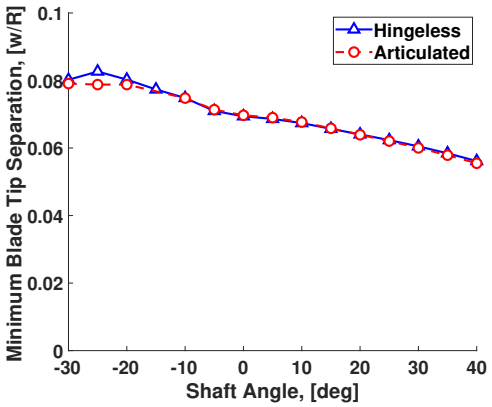

(a) Inter-rotor Separation

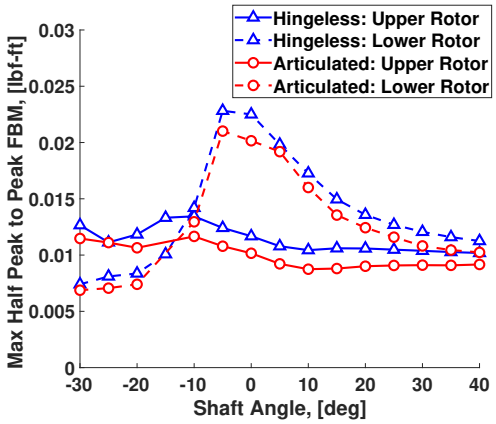

(b) Flap Bending Moment

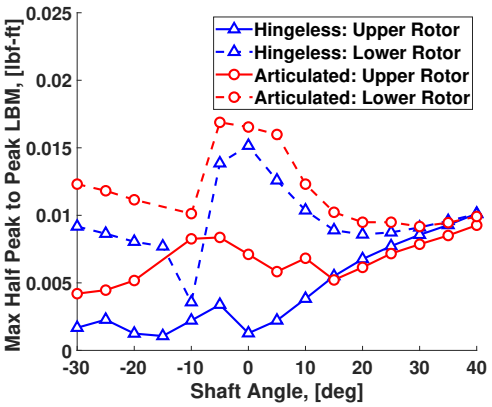

(c) Lag Bending Moment

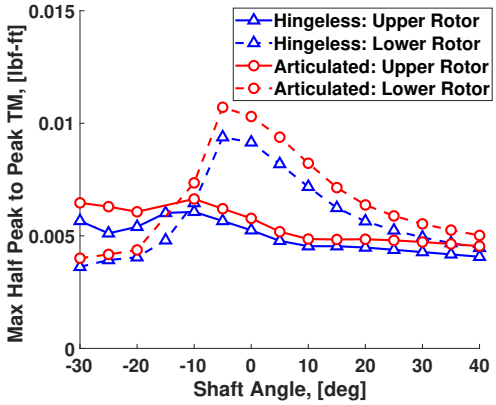

(d) Torsion Moment

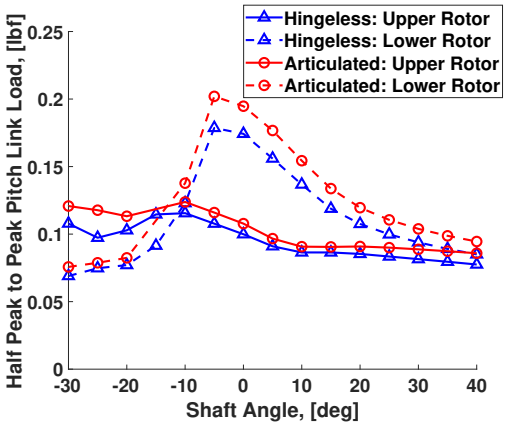

(e) Oscillatory Pitch Link Load

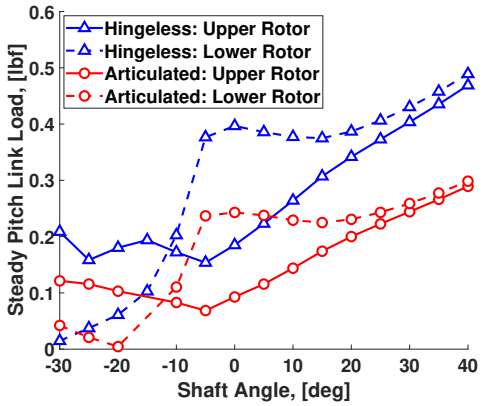

(f) Steady Pitch Link Load

Figure 4.39: Effect of shaft angle; at $C_T/\sigma = 0.08$, $\mu = 0.10$, $z/R = 0.10$.

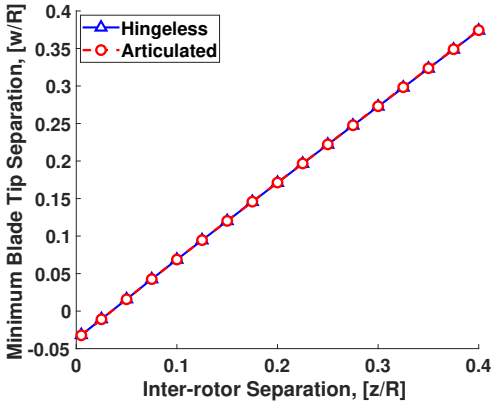

(a) Inter-rotor Separation

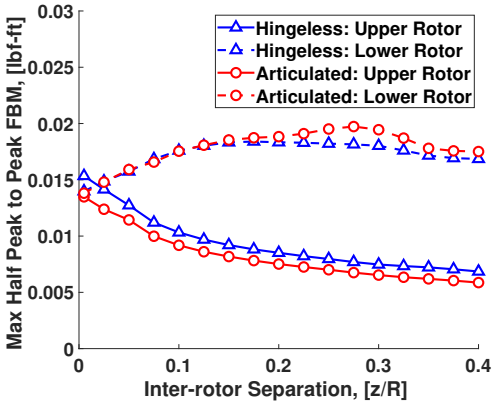

(b) Flap Bending Moment

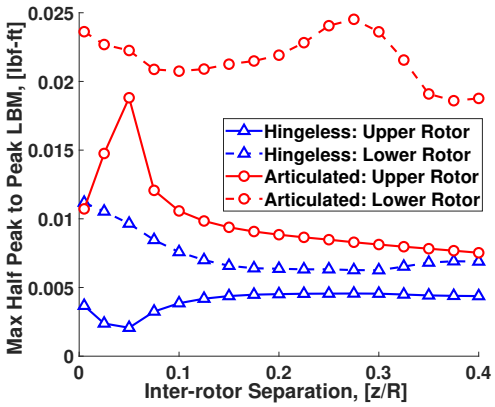

(c) Lag Bending Moment

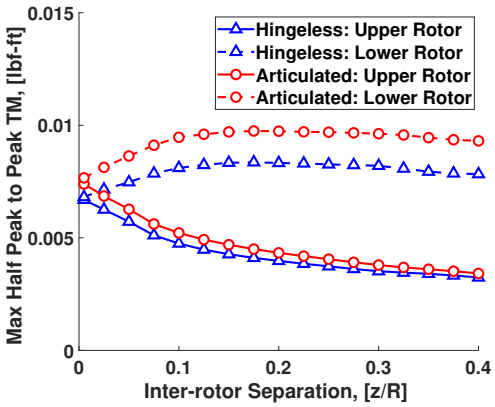

(d) Torsion Moment

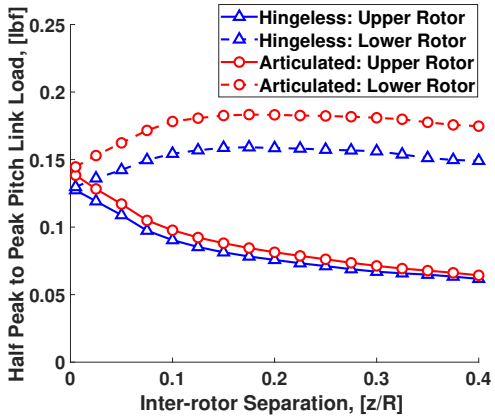

(e) Oscillatory Pitch Link Load

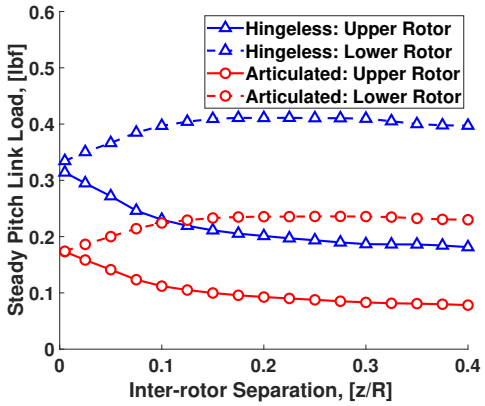

(f) Steady Pitch Link Load

Figure 4.40: Effect of inter-rotor separation; at $C_T/\sigma = 0.08$, $\mu = 0.10$, $\alpha = 5.0°$.

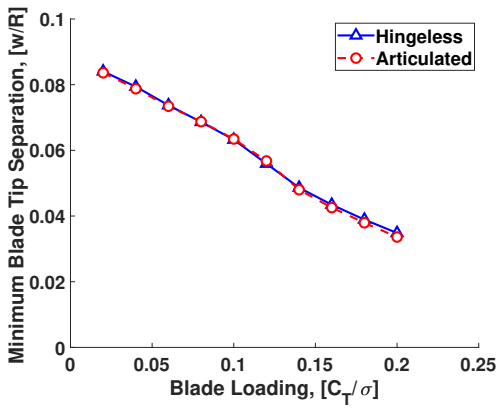

(a) Inter-rotor Separation

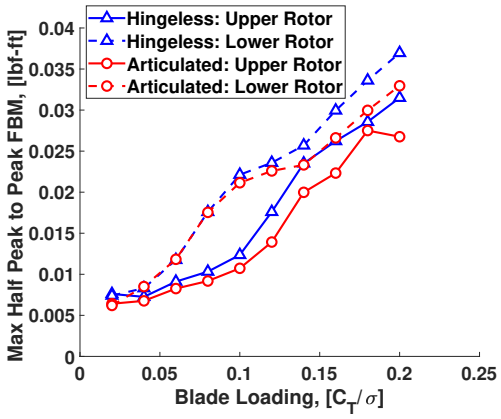

(b) Flap Bending Moment

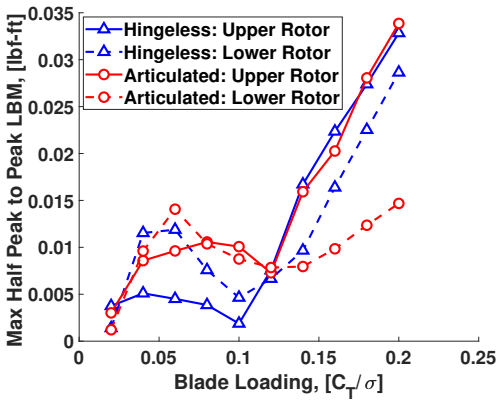

(c) Lag Bending Moment

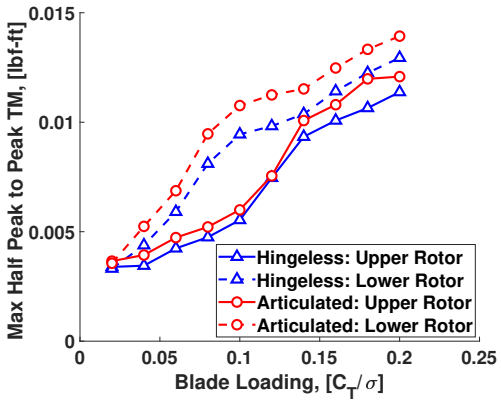

(d) Torsion Moment

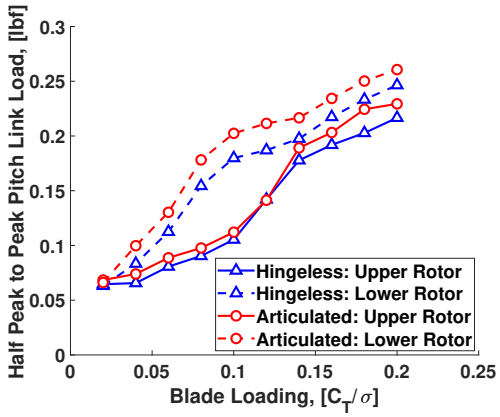

(e) Oscillatory Pitch Link Load

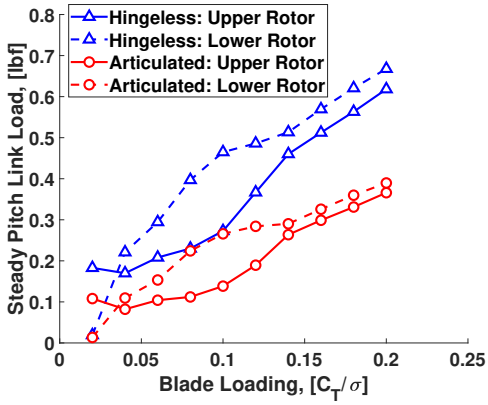

(f) Steady Pitch Link Load

Figure 4.41: Effect of blade loading C_T/σ; at $\mu = 0.10$, $\alpha = 5.0°$, $z/R = 0.10$.

gusts on Mars. The baseline C_T/σ of 0.08 and the margin available from test data ($\Delta C_T/\sigma$ of another 0.08, Figure 2.15) would allow these excursions. The baseline case had a shaft angle of 5°. The tip separation reduces with shaft angle but remains similar between the hubs. The oscillatory flap bending moment, lag bending, torsion moment, and pitch link load all exhibit similar trends. The upper rotor remains relatively constant, while the lower rotor peaks at zero shaft angle. This is the wake impingement effect the brunt of which is borne by the lower rotor. Both hubs carry similar loads. The steady pitch link load increases with shaft angle and the hingeless hub carries roughly twice the load throughout.

4.6.3 Effect of Inter-rotor Separation

The inter-rotor separation is swept from 0.01R to 0.40R, Figure 4.40. The baseline case had a separation of 0.10R. The tip separation is proportional to inter-rotor separation and as found for the baseline remains similar between the hubs. The oscillatory flap bending moment, torsion moment, and pitch link load all exhibit similar trends. The upper rotor decreases with separation, while the lower rotor increases. Both hubs carry similar loads. The lag bending moment shows deviation between hubs with the articulated hub carrying higher loads. There is a strange peak at low separation, thee physical justification of which is not clear. The steady pitch link load shows the hingeless hub carries twice the load for all separations.

4.6.4 Effect of Blade Loading

The blade loading is swept from 0.02 to 0.20, Figure 4.41. The baseline case had a blade loading of 0.08. The tip separation decreases with blade loading but remains similar between the hubs. The oscillatory flap bending moment, torsion moment, and pitch link load all exhibit similar trends and remain similar between the hubs. Both upper and lower rotors increase with blade loading, but the lower

rotor carries a larger load. Once again, the hingeless hub carries twice the load.

4.7 Summary and Conclusions

The comprehensive analysis was validated in hover for both coaxial rotors and at the Mars low Reynolds. First at a baseline flight condition, then for sweeps of advance ratio, shaft angle, rotor separation, and blade loading. The following key conclusions are noted.

1. The hingeless and articulated hubs surprisingly have similar tip separation and oscillatory flap bending moments.

2. The articulated hub has 9% higher oscillatory torsion loads.

3. The articulated hub has nearly twice the lag bending loads.

4. The hingeless hub has twice the steady control loads due to pitch-flap coupling.

5. The chordwise center of gravity offset reduce steady control loads.

6. For the shaft angle sweep, oscillatory blade loads peak around zero due to free wake and decrease for both positive and negative tilts, as the wake clears. Tip separation reduces while steady control loads increase with nose down shaft tilt.

7. For the inter-rotor separation sweep, oscillatory blade loads and steady control loads increase on the lower rotor and decrease on the upper as inter-rotor separation increases, while tip separation remains proportional to inter-rotor separation.

8. For the blade loading sweep, oscillatory blade loads and steady control loads increase with blade loading while tip separation decreases.

9. The blade passage impulses are seen in airloads only, not in structural loads.

Chapter 5: Coupled CFD/CA Analysis

5.1 Overview

Having applied CA to the Mars rotor, this chapter deals with the advancement of these tools to higher-fidelity coupled CFD/CA analysis.

The first section covers validation of the CFD analysis with the low Reynolds number hover data from Chapter 2. In the following sections, the same conditions explored earlier with CA in Chapter 4 are re-examined to gain additional insights. The conditions at which the high-fidelity analysis is essential and the predictions on which they have a significant impact are identified.

5.2 Mars Hover in Vacuum Chamber

The hover data from Chapter 2 is used for validating the 3D CFD analysis using fixed collective pitch. Figure 5.1 shows the blade loading C_T/σ versus collective. The higher Reynolds number is better predicted. The maximum blade loading is reasonably matched but not near stall where CFD predicts similar behavior to CA. For negative blade loading, predictions do not match the data at all. Even though this region is of no practical importance it is a problematic sign to have this level of error. CFD captures the basic trend of blade loading increasing with Reynolds number, but over predicts at any given collective compared to the data and CA.

At low Reynolds numbers predicting power is more difficult because of the viscous effects on transition and separation. Figure 5.2 shows the power versus col-

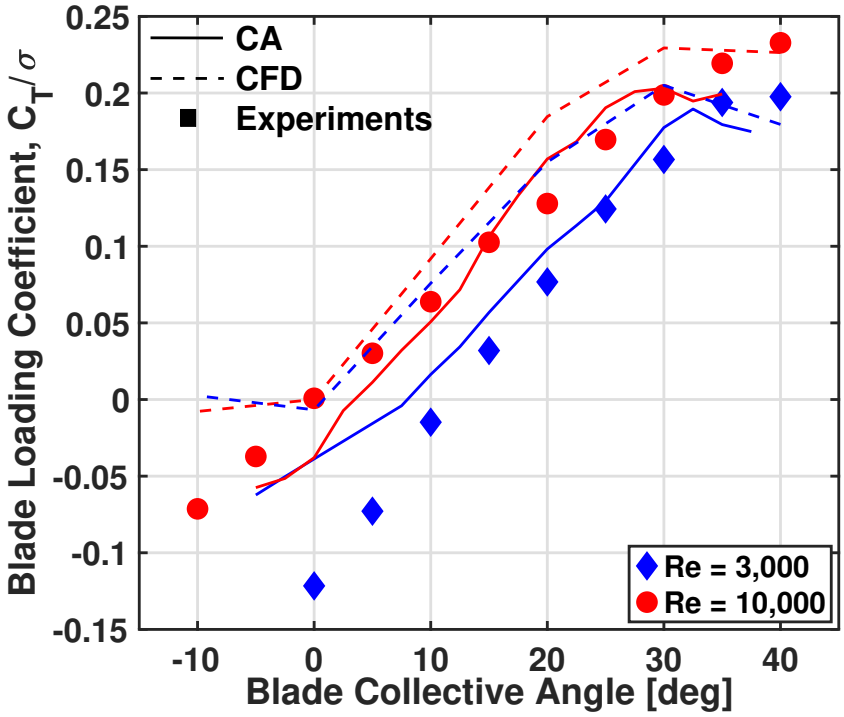

Figure 5.1: Data, CA prediction, and CFD prediction of blade loading, C_T/σ, with collective, at different Reynolds numbers.

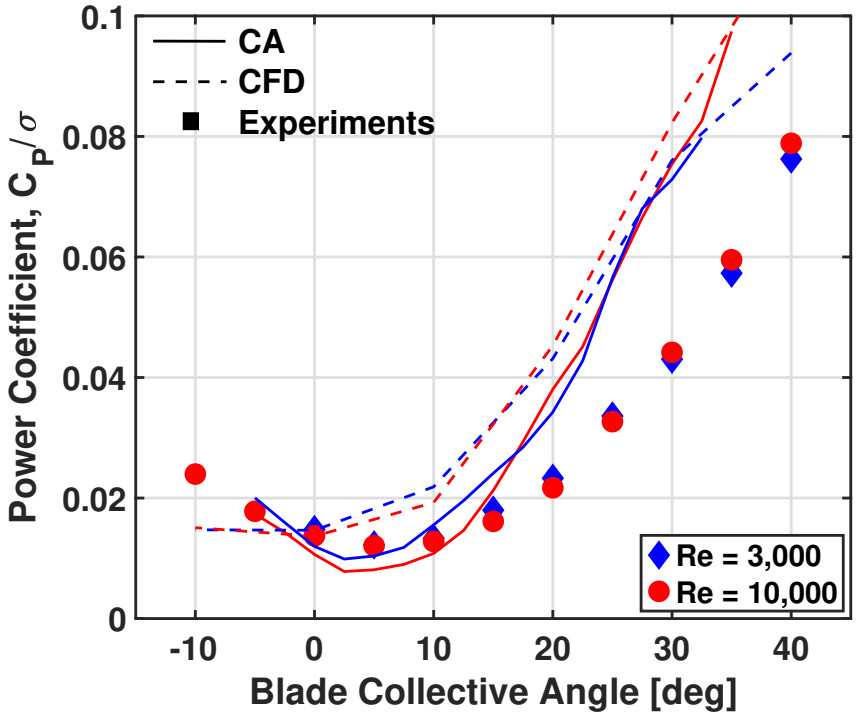

Figure 5.2: Data, CA prediction, and CFD prediction of power coefficient, C_P/σ, with collective, at different Reynolds numbers.

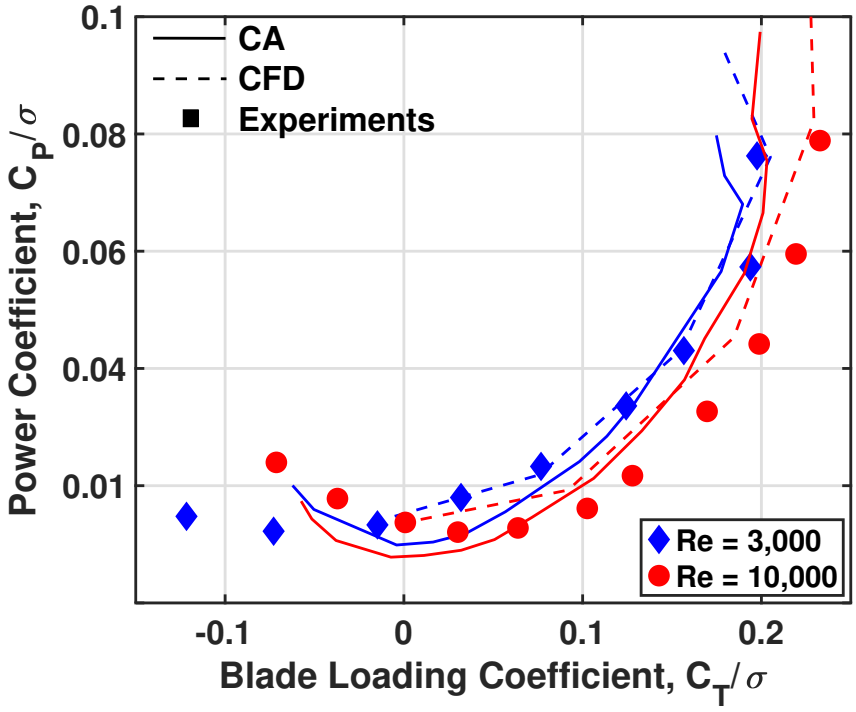

Figure 5.3: Data, CA prediction, and CFD prediction of variation of coefficient of power, C_P/σ, with blade loading, C_T/σ, at different Reynolds numbers.

lective. CFD over-predicts power consistently but better than CA. At low collectives, CFD does not accurately predict the minimum power. Unlike blade loading, the data and predictions show power is more or less Reynolds number independent.

Although CFD does not predict the blade loading or power versus collective with much accuracy. Figure 5.3 shows blade loading versus power is captured far better. This is partly due to compensating errors in thrust and power but also likely from errors in collective. Collective measurements are often prone to steady errors. The general trend of increase in power with decrease in Reynolds number is captured by both analyses but CFD matches the higher blade loadings much better. At the higher Reynolds number $10,000$ CFD matches significantly better. CFD even captures the highest blade loadings.

Figure 5.4 shows the Figure of Merit versus blade loading. The differences between CA and CFD predictions are evident. CFD predicts the maximum Figure

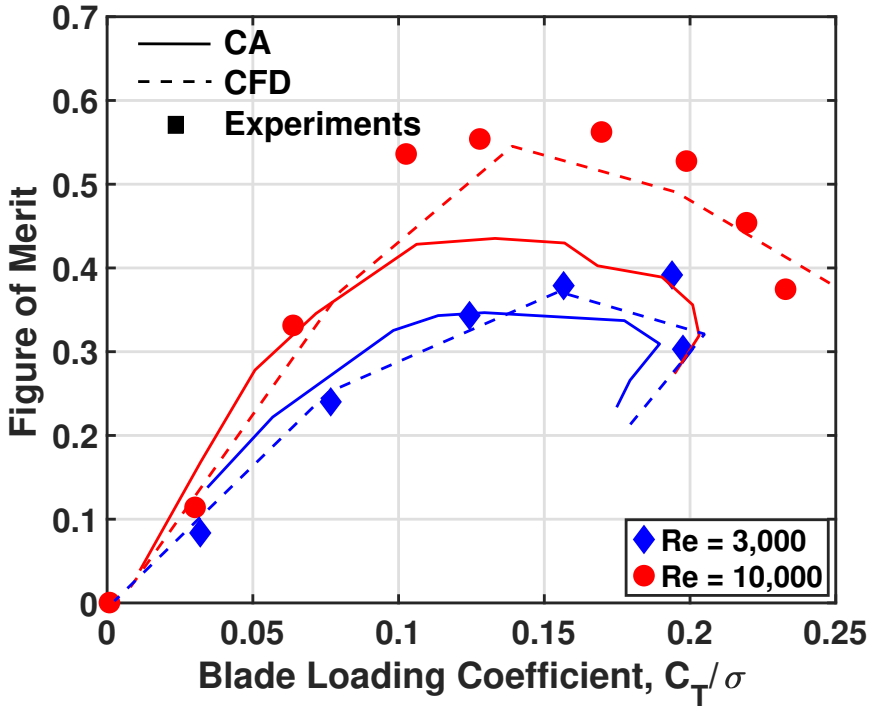

Figure 5.4: Data, CA prediction, and CFD prediction of variation of Figure of Merit, with blade loading coefficient C_T/σ, at different Reynolds numbers.

of Merit with significantly greater accuracy. Both predict the increase in Figure of Merit with Reynolds number correctly. The discrepancies between CA and CFD can be attributed to three-dimensional aerodynamic effects and their impact on low Reynolds number phenomena such as laminar separation bubbles.

Figure 5.5 shows the streamlines from CFD at Reynolds number $10,000$ for four collective angles $\theta_o = 10°,\ 20°,\ 30°$, and $40°$. The streamlines originate from three spanwise planes $r/R = 0.25,\ 0.50$, and 0.75. At the lower collectives, the flow is attached and mostly chordwise (2D). As the collective increases ($\theta_o > 20°$), the flow separates and is dominated by radial flow from root to tip. This explains the differences in predictions. The 3D flow phenomena cannot be captured by the 2D lifting-line methods in CA.

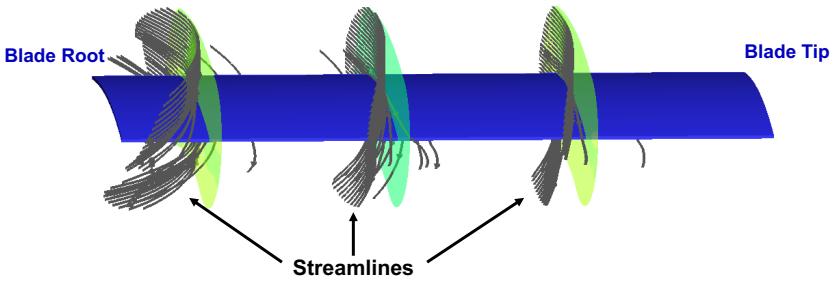

(a) Collective of 10°

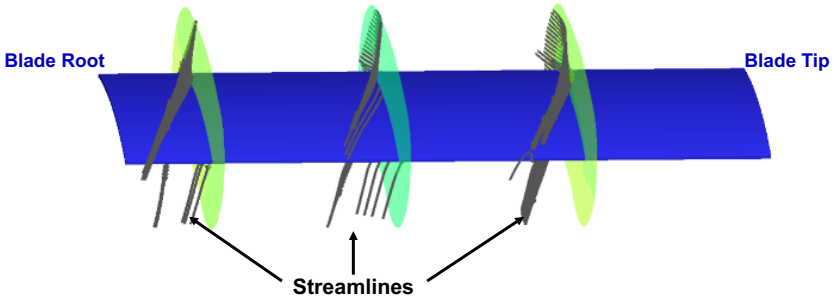

(b) Collective of 20°

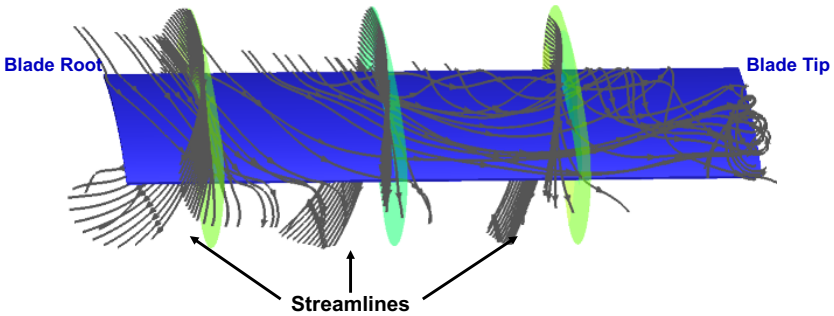

(c) Collective of 30°

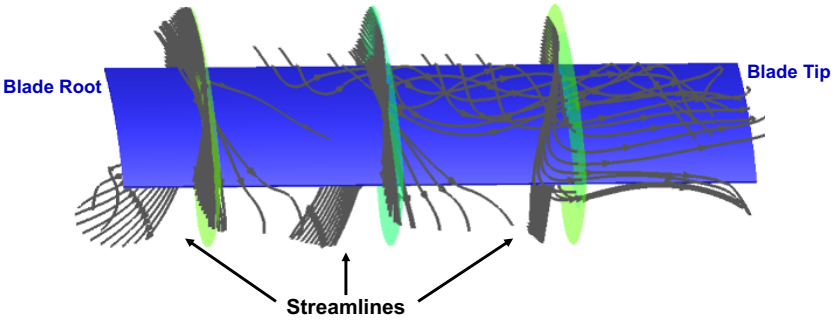

(d) Collective of 40°

Figure 5.5: Streamlines from three radial stations ($r/R = 0.25,\ 0.50,\ 0.75$) at four different collective angles ($\theta_o = 10°,\ 20°,\ 30°,\ 40°$); $Re = 10,000$ and $M = 0.07$.

Table 5.1: Baseline forward flight conditions.

Parameter	Value
Rotorational Speed, [RPM]	2400
Advance Ratio	0.10
Tip Reynolds number	4687
Tip Mach number	0.255
Density, [kg/m^3]	0.0167
Speed of Sound, [m/s]	230.1
Temperature, [K]	210

5.3 Coupled CFD/CA Analysis

As described in Chapter 3, the relaxed delta-coupling method was used to couple high-fidelity 3D CFD and CA analyses. The coupled CFD/CA analysis is now used to analyze the same flight conditions as Section 4.5, and as described in Table 5.1, to study the differences between hingeless and articulated hubs as well as between CA and CFD/CA. Recall, the articulated rotor is only articulated in flap. The trim procedure remains the same as CA with the rotor trimmed to zero hub moments, zero net torque, and a thrust target of $C_T/\sigma = 0.08$. The advance ratio is $\mu = 0.10$, shaft angle is $\alpha_s = 5°$ (tilted forward into the flow). The rotational speed is 2400 RPM, with a tip Mach number of 0.255 and Reynolds number of 4687.

5.3.1 Convergence and Control Angles

Two full revolutions of CFD were completed before the first coupling iteration, thereafter a single revolution was used. Convergence of the control angles was achieved after ten coupling iterations, that is, eleven total rotor revolutions in CFD. The control angle history is shown in Figure 5.6 and the converged results are given in Table 5.2. The CA control predictions are shown as the #0 iteration in the figures. The oscillations are due to the very low aerodynamic damping in the thin Martian air. Greater relaxation reduces the oscillations but delays convergence.

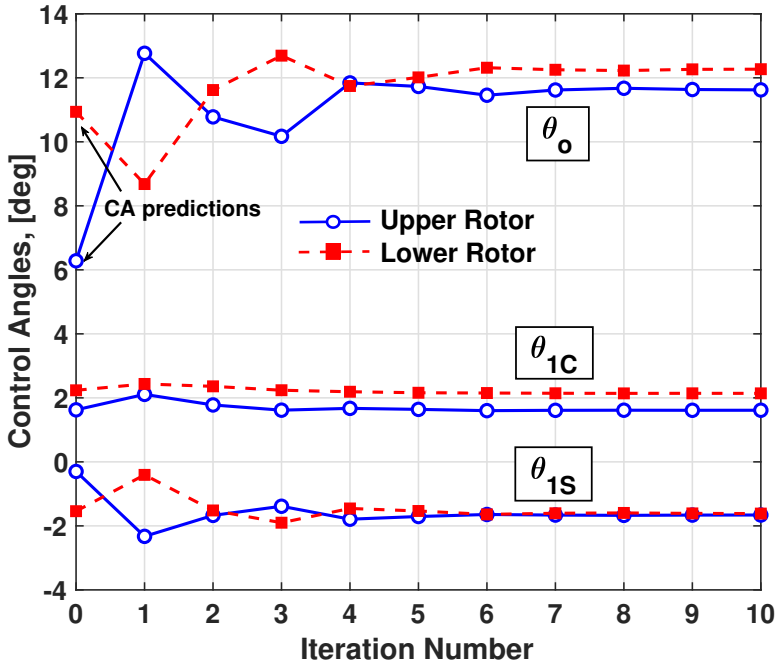

(a) Hingeless hub control angle coupling iteration history

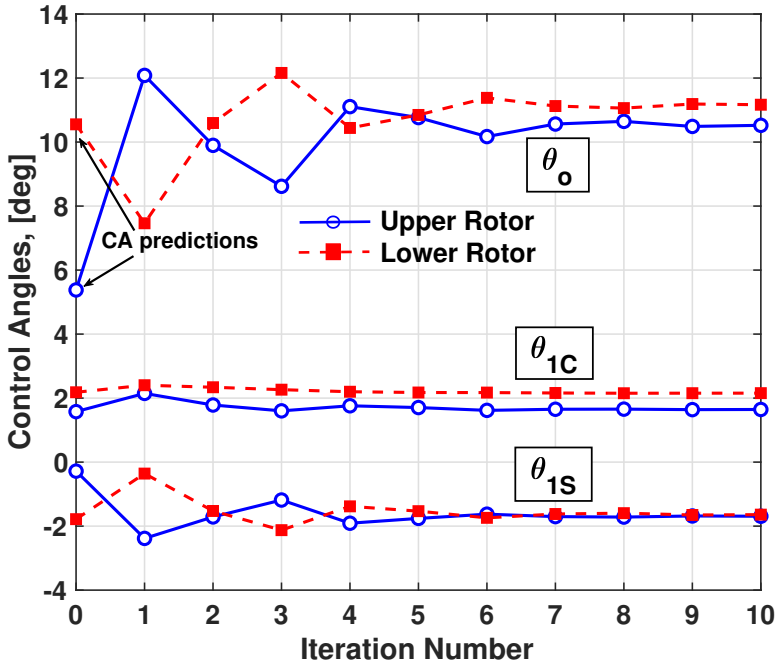

(b) Articulated hub control angle coupling iteration history

Figure 5.6: Control angle trim history for both hingeless and articulated during coupled CFD/CA analysis.

Table 5.2: CFD/CA trimmed control angles.

	Hingeless	Articulated
Upper rotor: θ_o	11.62°	10.52°
Upper rotor: θ_{1c}	1.61°	1.64°
Upper rotor: θ_{1s}	−1.66°	−1.69°
Lower rotor: θ_o	12.27°	11.17°
Lower rotor: θ_{1c}	2.14°	2.16°
Lower rotor: θ_{1s}	1.62°	1.64°

From CA to CFD/CA, for both hubs, the collective pitch increases on both rotors. Additionally, the difference in upper and lower collective is now less than 1° instead of 5° predicted by CA. The hingeless hub requires moderately larger collective pitch, but nearly identical cyclic pitch compared to the articulated hub. While CFD/CA shows very little change in the lateral cyclic, θ_{1c}, there is significant change in the longitudinal cyclic, θ_{1s}. Typically on Earth, the lateral cyclic is affected more by the wake, but because of low Lock number and stiff rotor the phase delay nearly disappears and it is the longitudinal cyclic that is influenced more by the wake. Differences in the free-wake and CFD wakes cause the change in lateral cyclic.

5.3.2 Rotor Thrust

Figures 5.7 and 5.8 show the azimuthal variation of thrust or blade loading C_T/σ for the CA predictions and the last three coupling iterations. Each rotor is shown individually in its local azimuth. The last three iterations have nearly identical waveforms for both hubs showing good convergence. The CFD/CA thrust is dominated by a large 4/rev impulsive loading. This is a result of blade passage. There is an increase in thrust before the blades pass because of the mutual up-wash caused by the bound circulation. Once the blades pass, the bound circulation causes a down-wash on the other rotor. The impulsive loading is comparable between hingeless and articulated hubs, but has significantly larger influence on the upper

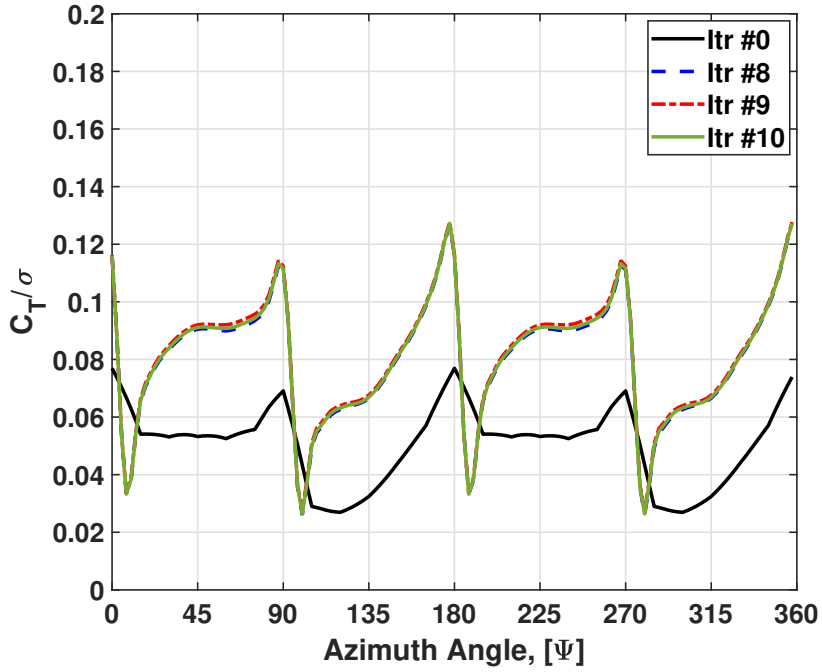

(a) Hingeless, Upper Rotor

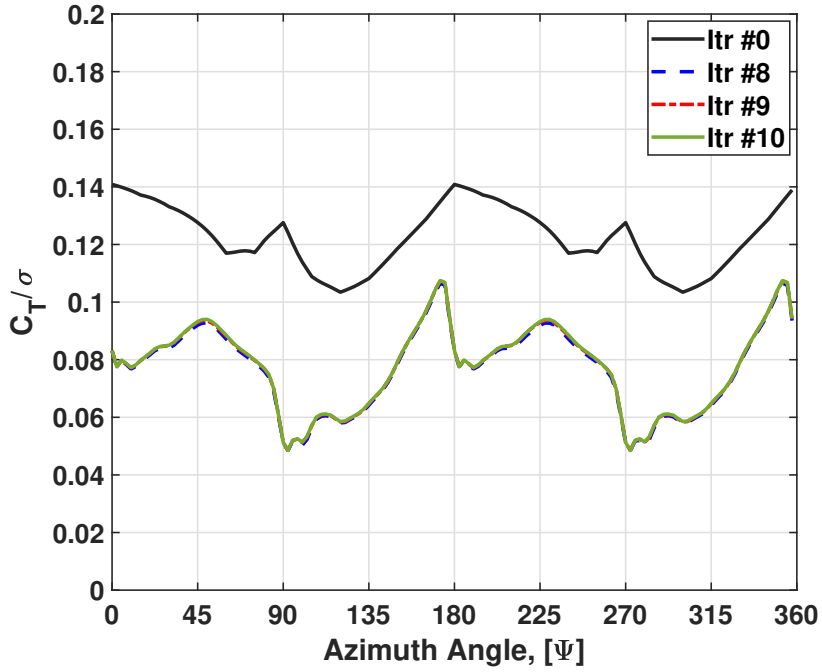

(b) Hingeless, Lower Rotor

Figure 5.7: Thrust C_T/σ of upper and lower rotors versus azimuth for the hingeless hub; iteration #0 is lifting-line comprehensive analysis; σ is solidity of each rotor.

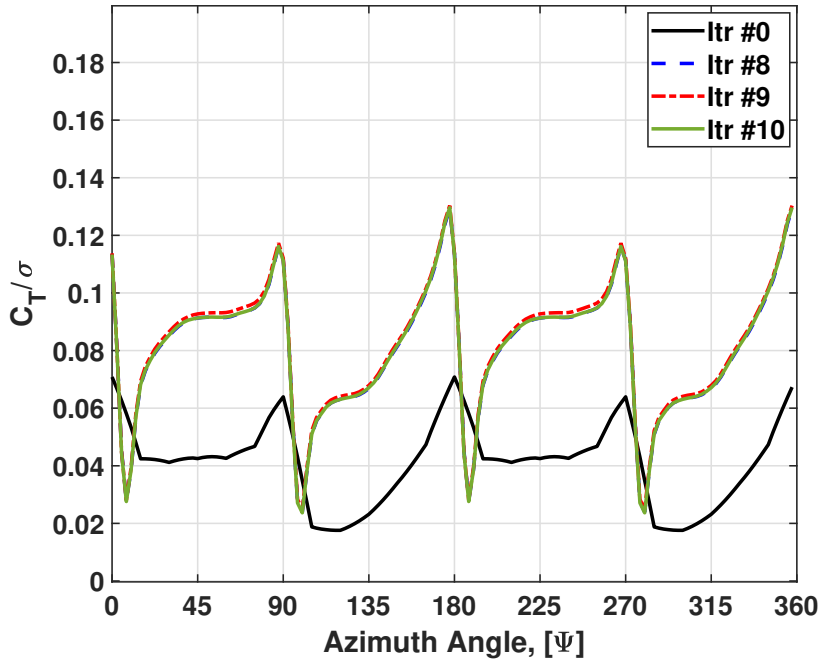

(a) Articulated, Upper Rotor

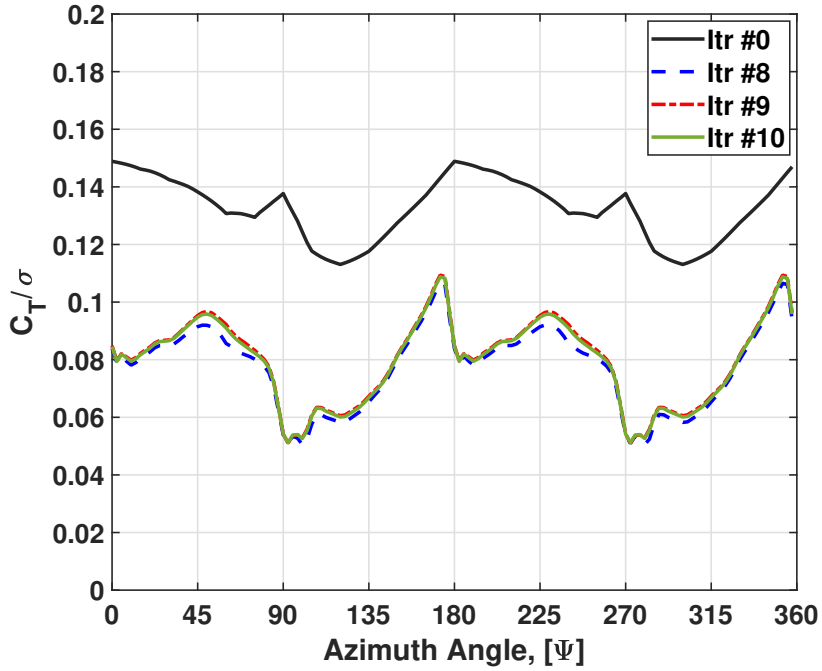

(b) Articulated, Lower Rotor

Figure 5.8: Thrust C_T/σ of upper and lower rotors versus azimuth for the articulated hub; iteration #0 is lifting-line comprehensive analysis; σ is solidity of each rotor.

rotor compared to the lower.

CA and CFD/CA predict very different thrust sharing. With CA the upper rotor produced a smaller portion of the total thrust, $T_u/T = 29.0\%$ and 23.6% for the hingeless and articulated hubs respectively while with CFD/CA the thrust sharing is nearly equally, $T_u/T = 50.4\%$ for both hubs. Additionally, the blade passage interactions in CA did not adequately capture the large impulsive load found in CFD/CA.

5.3.3 Wake Geometry

Figures 5.9, 5.10, and 5.11 show the flow fields as iso-surfaces of Q-criterion at 0.003 and colored by vorticity. Both wakes have very similar roll up, symmetric structures, strong interactions, and rapid breakdown. The wake is expected to dissipate quickly at low Reynolds number due to a core growth that scales with $1/Re$. Therefore, the tip vortices do not appear to produce the usual intertwining downstream typical of rotor flows on Earth. Thus, blade passage impulses dominate the airloads and appear more pronounced than the usual first and fourth quadrant interactions typically found on Earth. It also appears that at the given advance ratio, the upper wake is ingested by the lower rotor which slices through the tip vortex causing a faster dissipation. There are other more subtle differences between the wakes. For instance, the vortex roll up is tighter for the hingeless upper rotor on the retreating side, due to less flapping. Over-all the nature of wake evolution, dissipation, and skew angles are very similar between the two hubs.

5.3.4 Tip Deflections

Figure 5.12 shows the tip deflections for the hingeless and articulated hubs (compare with Figure 4.19 for CA). The upper rotor is plotted with $10\%R$ vertical offset. The dashed lines represent the quarter-chord motion, the upper line is the

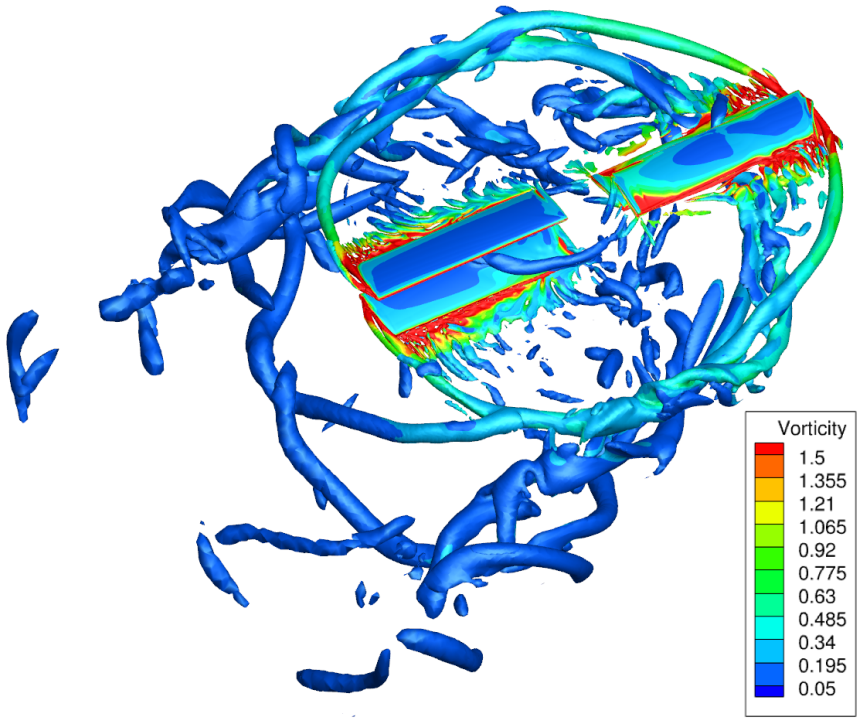

(a) Converged CFD solution for the hingeless hub

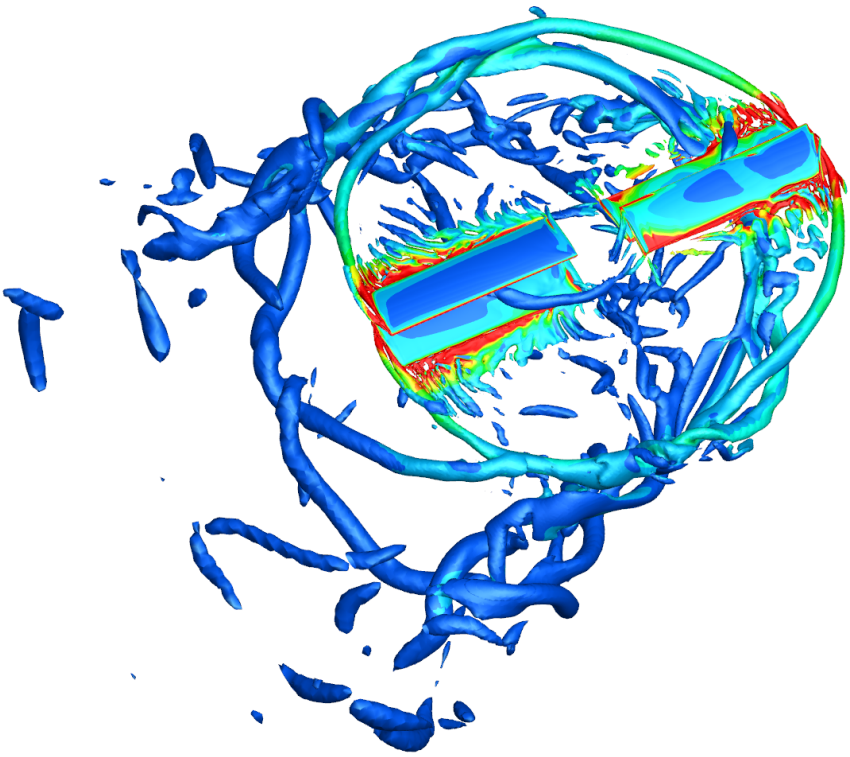

(b) Converged CFD solution for the articulated hub

Figure 5.9: Converged CFD/CA flow solutions for both hubs; iso-surface of Q-criterion, 0.003, colored by vorticity.

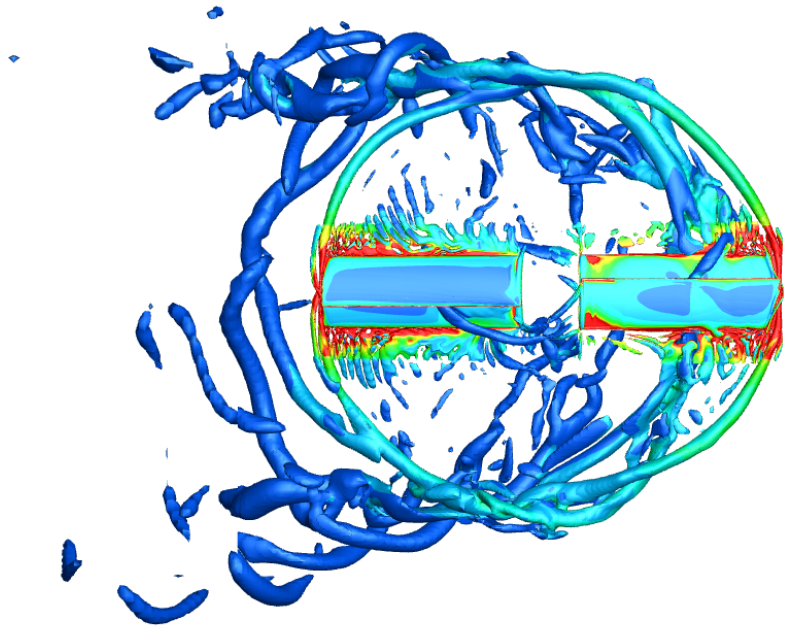

(a) Converged CFD solution for the hingeless hub, top view

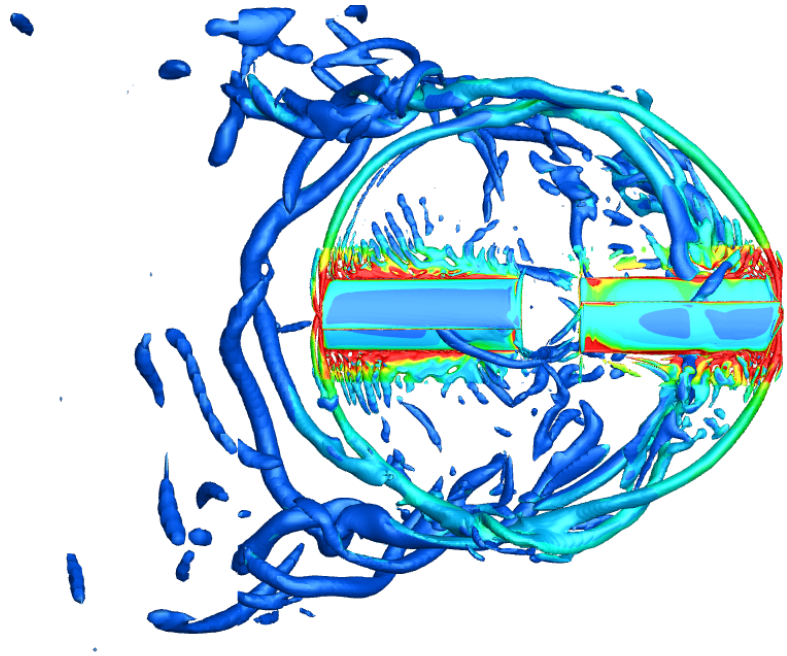

(b) Converged CFD solution for the articulated hub, top view

Figure 5.10: Converged CFD/CA flow solutions for both hubs; iso-surface of Q-criterion, 0.003, colored by vorticity.

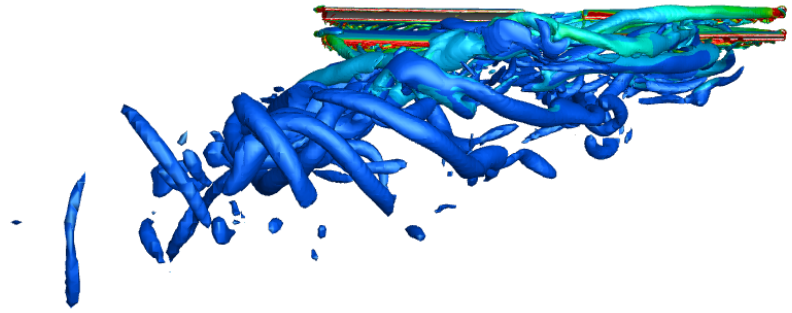

(a) Converged CFD solution for the hingeless hub, side view

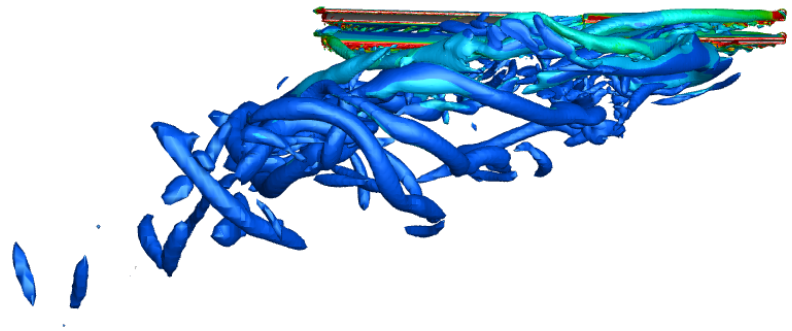

(b) Converged CFD solution for the articulated hub, side view

Figure 5.11: Converged CFD/CA flow solutions for both hubs; iso-surface of Q-criterion, 0.003, colored by vorticity.

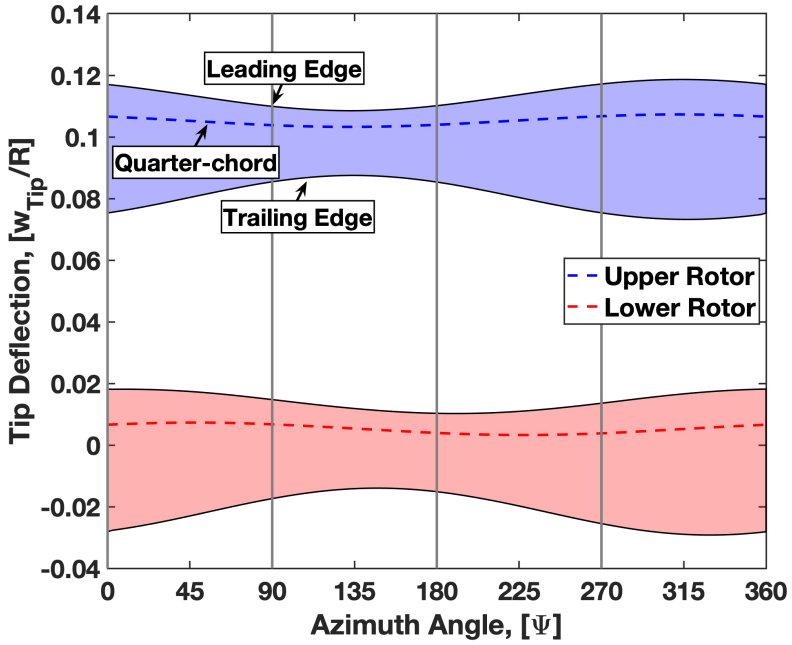

(a) Tip deflections for hingeless hub from CFD/CA

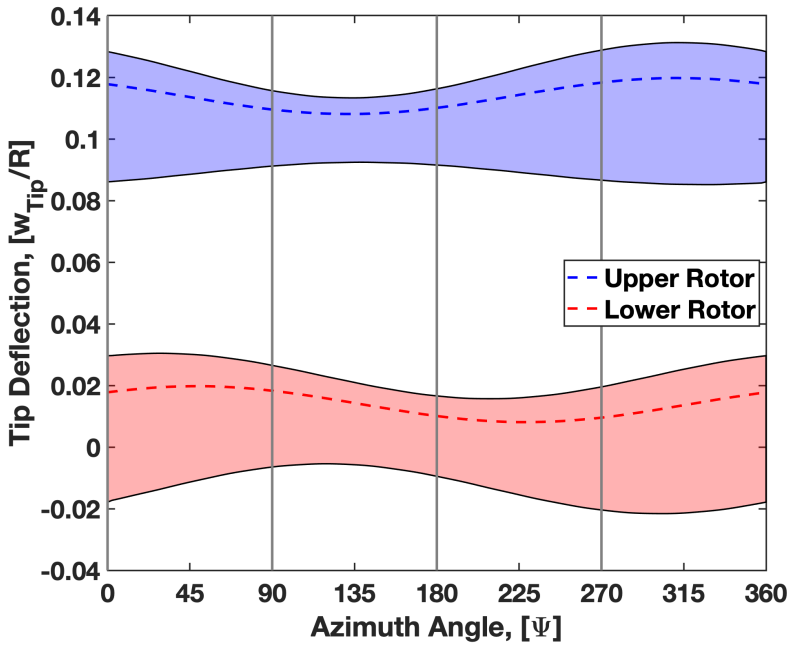

(b) Tip deflection for flap-articulated hub CFD/CA

Figure 5.12: Tip deflections for hingeless and articulated rotors from CFD/CA predictions; bands include full chord length with control angles and elastic deflections.

leading edge motion, and the lower line is the trailing edge motion. The band is due to the chord and pitch angles; so greater the pitch, the wider the band. CFD/CA shows a similar waveform as CA, but greater pitch. This is more apparent on the upper rotor. Blade passage occurs at azimuths of $\psi = 0°,\ 90°,\ 180°$, and $270°$, and are denoted by vertical lines. For the given flight condition, the hubs were safe from blade strike. The minimum separation at blade passage are $5.89\%R$ and $5.83\%R$ for the hingeless and articulated hubs respectively. This is about $1\%R$ less separation than predicted by CA so the difference is negligible and does not warrant high-fidelity. On Mars, blade strike depends less on flapping and torsion than chord and pitch inputs. With a large chord, the hingeless hub with greater hub moments to cancel could be at a greater danger of blade strike. This is a key difference from Earth. Both CA and CFD/CA predict this consistently.

5.3.5 Sectional Airloads

Figure 5.13 compares the sectional airloads for the hingeless and articulated hubs, and shows the remarkable similarity in airloads between the two hubs. This holds true at all radial stations, so for brevity, only the hingeless airloads are shown henceforth. Figures 5.14, 5.15, and 5.16 show the sectional airloads at four radial stations, 35%, 55%, 75%, and 87% R, comparing CA and CFD/CA. The impact of CFD/CA analyses is apparent.

For the normal force (Figure 5.14), the CA slightly under-predicts the mean on the upper rotor and significantly over-predicts it on the lower. This is a result of the different thrust sharing between analyses. Additionally, CA under-predicts the the impulsive loadings from blade passage. This is more pronounced on the upper rotor where they are under-predicted by a factor of $2 - 3$. Both analyses predict the upper rotor having significantly larger impulsive loading than the lower.

For the chord force (Figure 5.15) the CA predicts the mean of the upper rotor

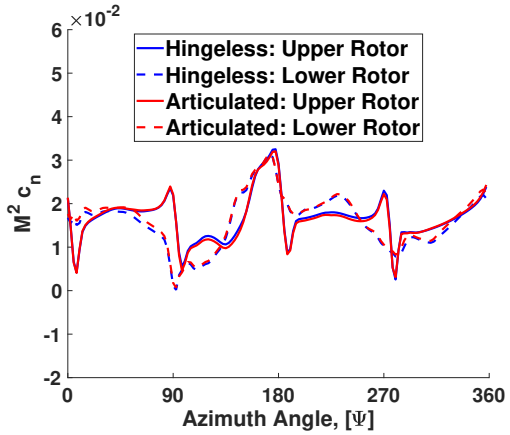

(a) Normal force

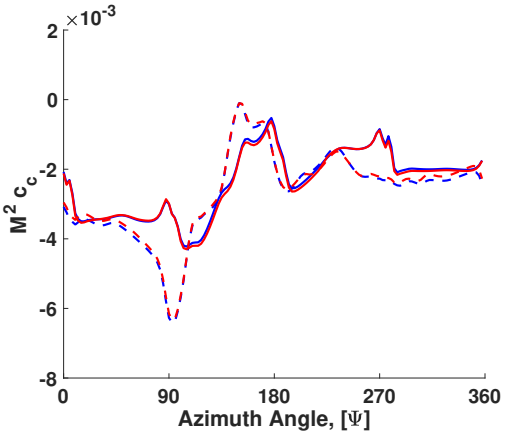

(b) Chord force

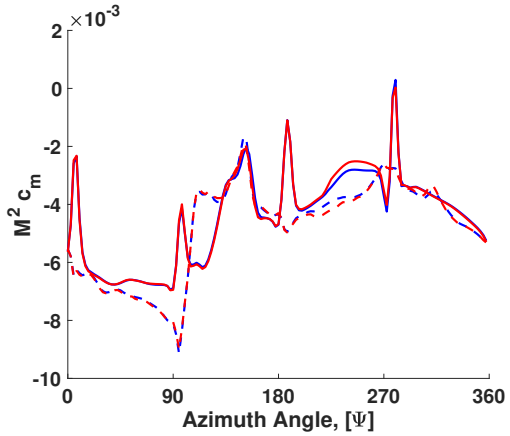

(c) Quarter-chord pitching moment

Figure 5.13: Comparison of sectional airloads between hingeless and articulated hubs using coupled analysis; 75%R.

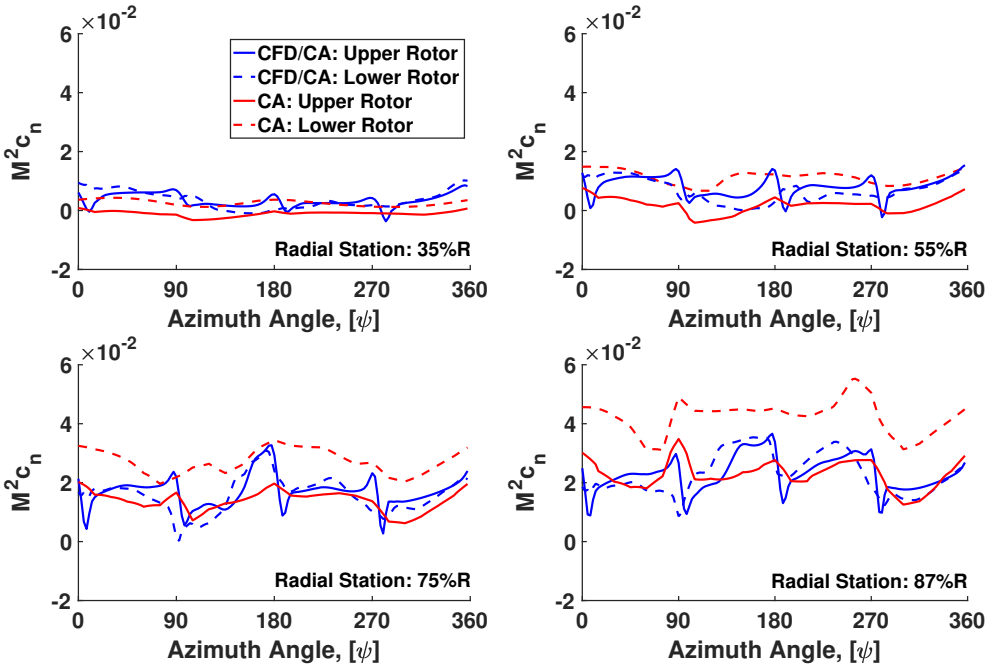

Figure 5.14: Sectional normal force at four radial stations.

well but significantly over-predicts the lower chord force. Additionally, the CA under-predicts the impulsive loadings from blade passage. This is more pronounced on the upper rotor where they are under-predicted by a factor of 2. Unlike the normal force, chord force shows similar impulsive loading for the upper and lower rotors.

For the quarter-chord pitching moment (Figure 5.16) the CA under-predicts the mean of the inboard sections, but shows better agreement outboard. Additionally, CA severely under-predicts the impulsive loadings from blade passage. CFD/CA predicts large 4/rev impulsive loading with peak to peak variation roughly equal to the mean pitching moment. These are up to 5 times the CA predictions and more pronounced on the upper rotor. Additionally, the impulsive loading is larger than what was seen in the normal and chord forces.

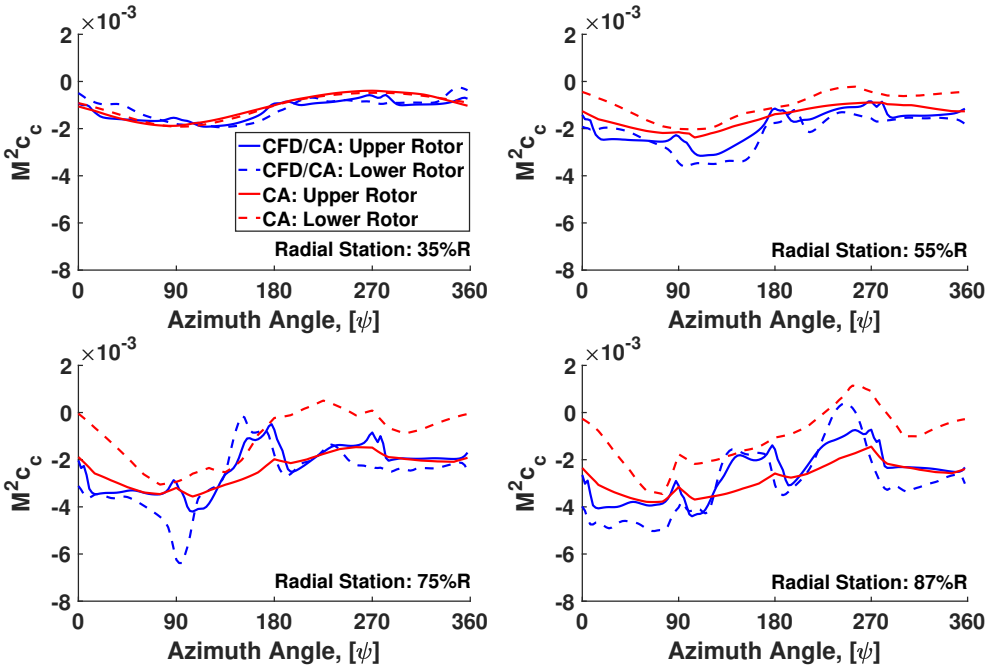

Figure 5.15: Sectional chord force at four radial stations.

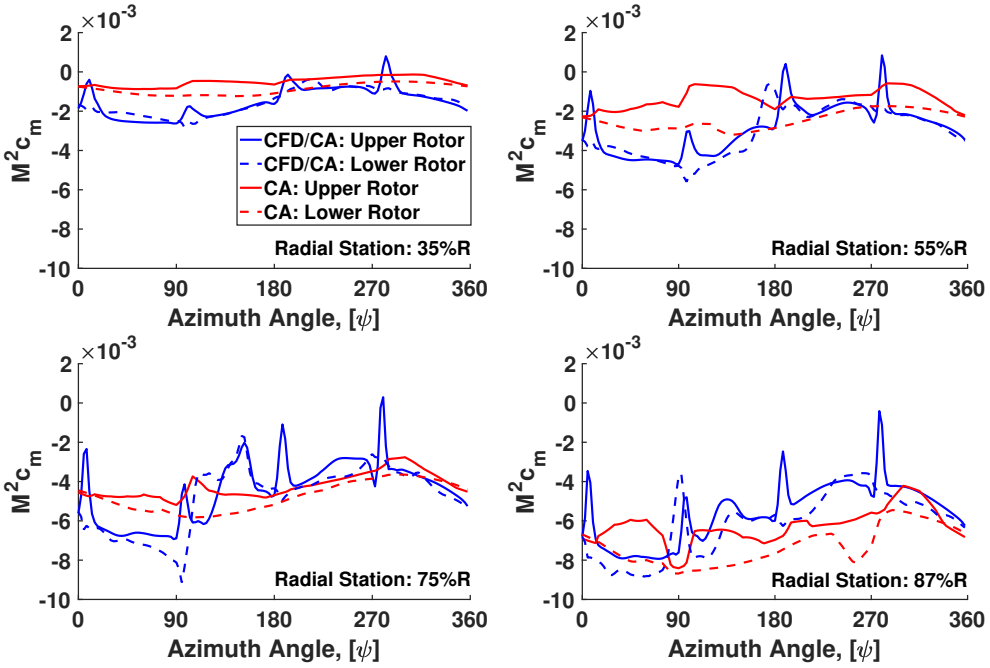

Figure 5.16: Sectional quarter-chord pitching moment at four radial stations.

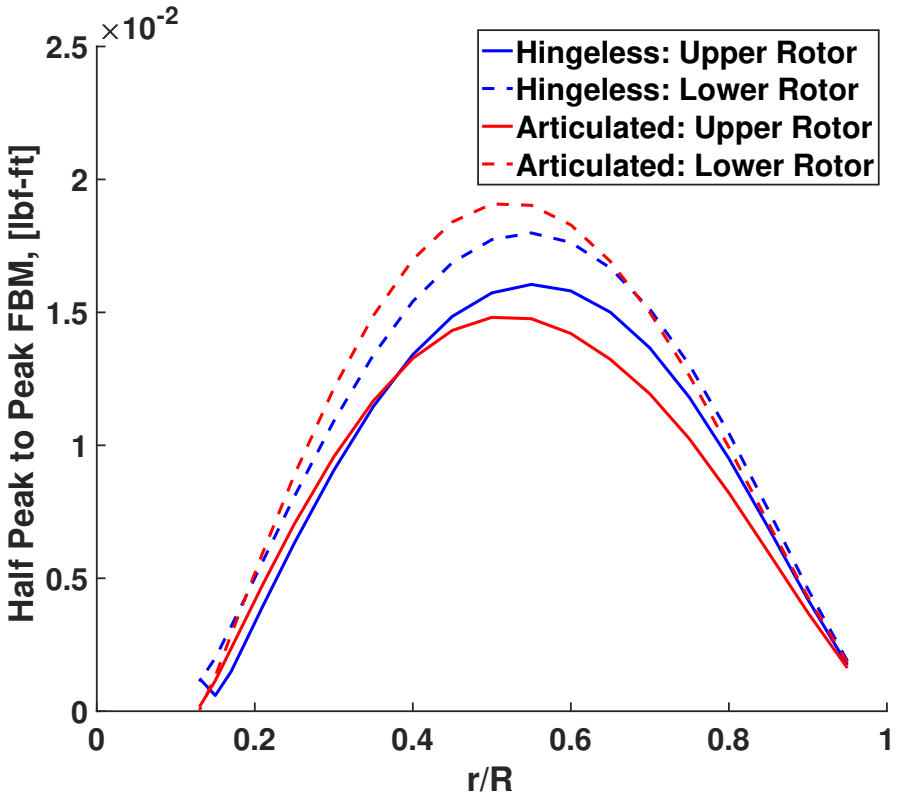

Figure 5.17: Flap bending moment half peak-to-peak oscillatory magnitude from CFD/CA.

5.3.6 Structural Loads

The structural loads are ultimately the determining factor in blade design. These loads size the blade weight for an aircraft where every gram must be carried 300 million miles. Both steady and oscillatory loads need to be considered but with the rotor spinning at 2400 RPM (hence accruing cycles rapidly) the principal concern is oscillatory loads. Figures 5.17, 5.20, and 5.23 show the half peak to peak loads along span. Figures 5.18, 5.21, and 5.24 show only the oscillatory, mean removed, loads at three radial stations: 30%R, 50%R, and 70%R. Figures 5.19, 5.22, and 5.25 show the steady loads along span.

Figure 5.17 shows the oscillatory flap bending moment (half peak-to-peak) versus span. The trends are similar to CA, but not the magnitudes. The hingeless

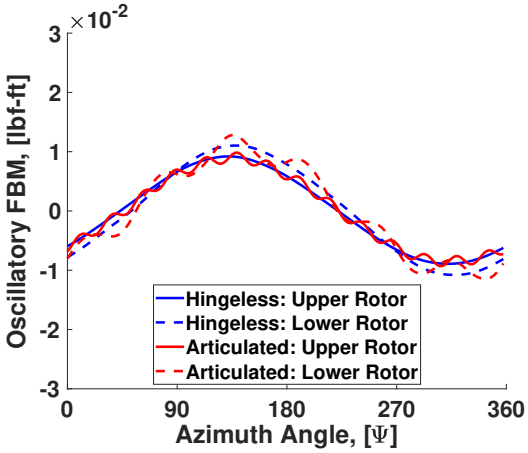

(a) Flap bending moment at 30% R

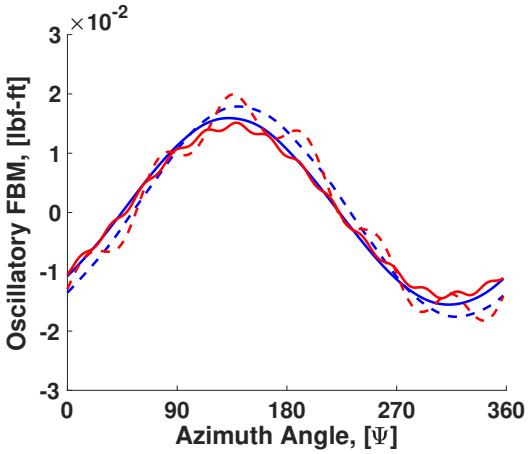

(b) Flap bending moment at 50% R

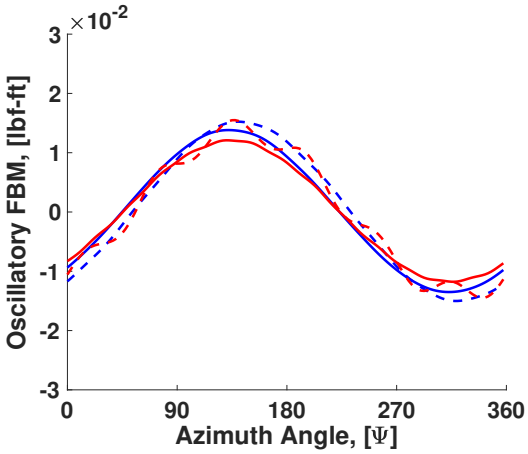

(c) Flap bending moment at 70% R

Figure 5.18: Oscillatory flap bending moment from CFD/CA.

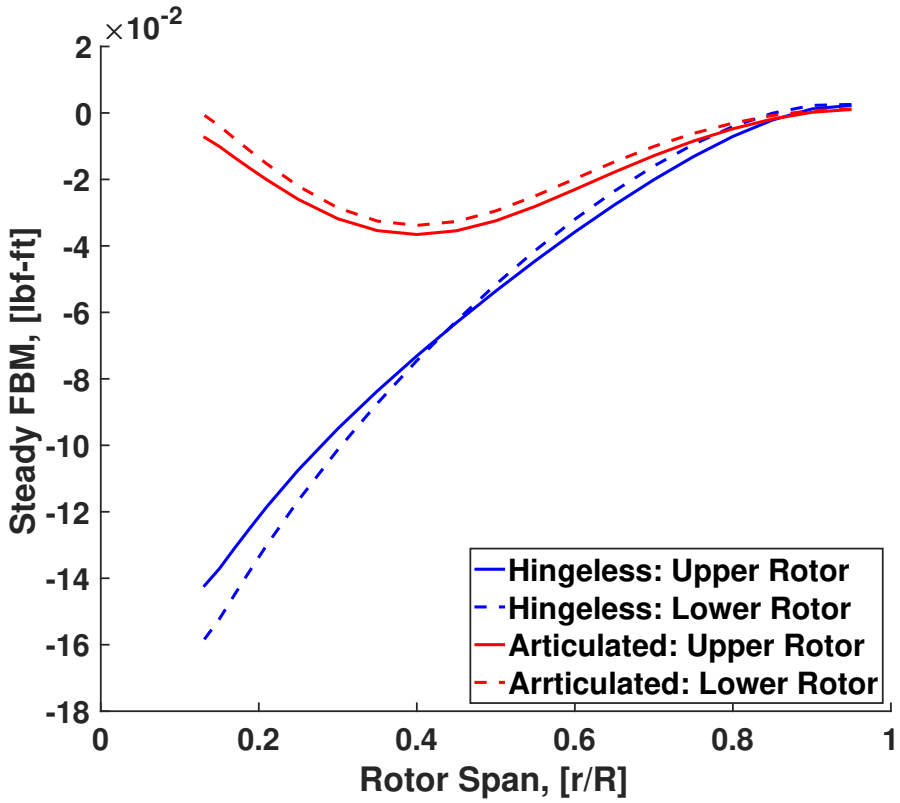

Figure 5.19: Steady flap bending moment from CFD/CA.

and articulated hubs have very similar loads, but now the upper and lower rotors also have similar loads. This follows from thrust balance. It is surprising that the hingeless does not have significantly greater loading as typical on Earth, but it is because the airloads in the thin atmosphere are small. There simply is not enough aerodynamic loading to cause a difference in bending loads. Figure 5.18 shows the mean removed waveform moment. It is predominantly 1/rev, but for the articulated hub there is small higher frequency content as well. Figure 5.19 shows the steady moment. The maximum on the hingeless hub is 5 times the maximum on the articulated, which occurs near 30%R. Again, due to similar thrust share the upper and lower rotors experience similar loads compared to CA. Additionally, the loads are greater than those predicted by CA, twice as large for the hingeless hub (64.3% and 14.1% for the upper and lower rotors respectively).

Figure 5.20 shows the oscillatory lag bending moment (half peak-to-peak)

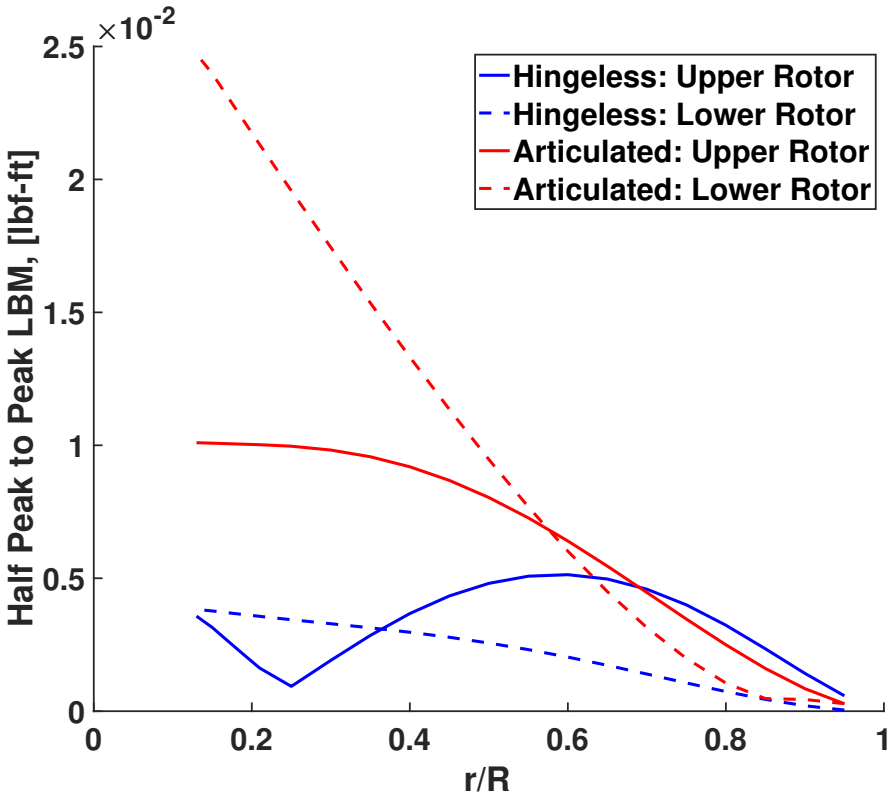

Figure 5.20: Lag bending moment half peak-to-peak oscillatory magnitude from CFD/CA.

versus span from CFD/CA. There is a significant difference between hubs. The trends are similar to CA, but with different magnitudes. CFD/CA predicts a 39% decrease in maximum load, except for the articulated hub, where CFD/CA predicts a 20% increase on the lower rotor. The articulated hub has significantly greater loads; 2 and 5 times the hingeless hub for the upper and lower rotors respectively. Both hubs can carry lag bending moment although it is surprising that the articulated is greater. Figure 5.21 shows the mean removed waveform of the lag bending moment. It is predominantly 1/rev, but on the articulated hub there is suspicious high frequency content. For the lower rotor, high frequency content contribute significantly to the half peak to peak oscillations. The physical cause of these high frequency (6 and 14/rev) oscillations is unclear. These oscillations were absent in CA predictions. Also note that the upper rotor loading is completely out of phase from what was

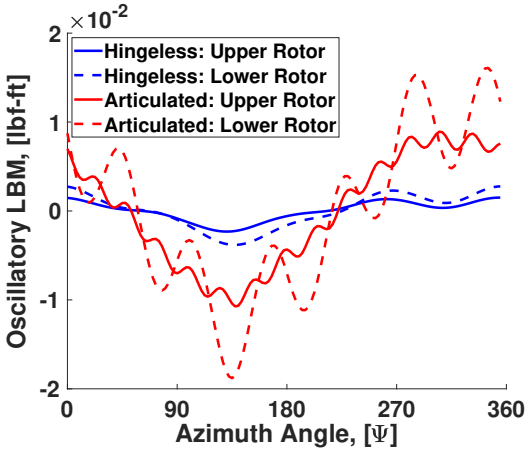

(a) Lag bending moment at 30%R

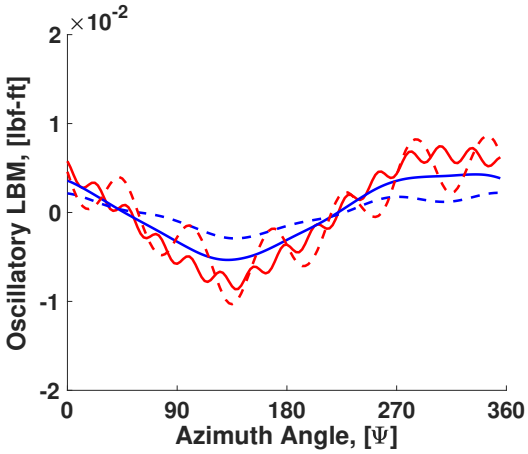

(b) Lag bending moment at 50%R

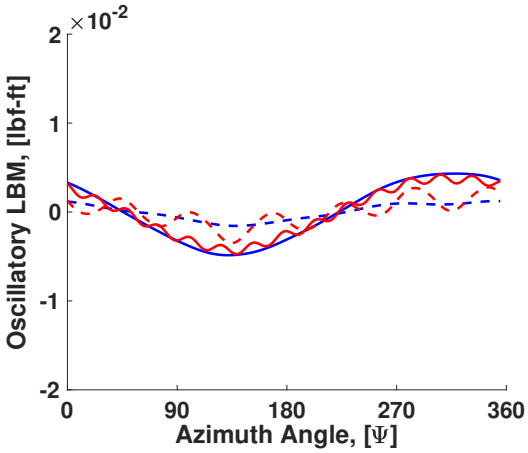

(c) Lag bending moment at 70%R

Figure 5.21: Oscillatory lag bending moment from CFD/CA.

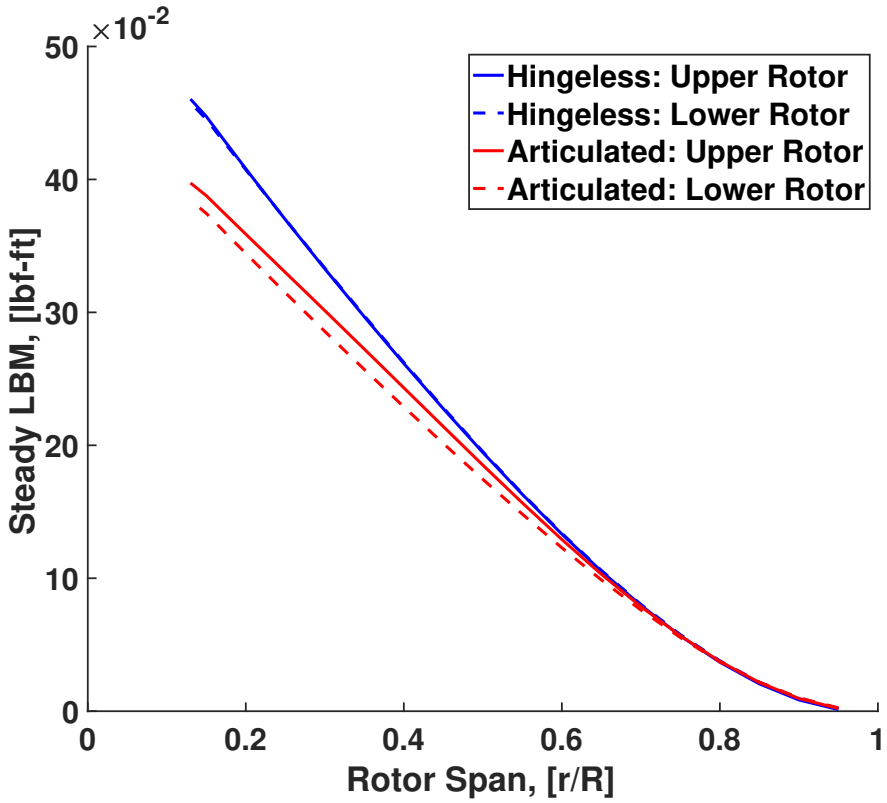

Figure 5.22: Steady lag bending moment from CFD/CA predictions.

predicted earlier by CA alone. Figure 5.22 shows the steady lag bending moment. The differences between hingeless and articulated are small and between upper and lower rotors even smaller. The maximum on the hingeless hub is only 15% greater than on the articulated, and both are near the root. The steady loads are marginally greater than those predicted by CA, with an average increase between the two hubs of 12.6% and 9.1% for the upper and lower rotors respectively. Higher oscillatory loads in any direction are not desirable, but a high lag bending moment can perhaps be more easily absorbed by the large chord length and low aspect ratio blade design necessary for the Mars rotor.

Figure 5.23 shows the oscillatory torsion moment (half peak-to-peak) versus span from CFD/CA. The trends are similar to the flap bending moment, which is not surprising because of the pitch-flap coupling. Additionally, they are similar to CA predictions. The articulated hub experiences maximum loads 9% greater than

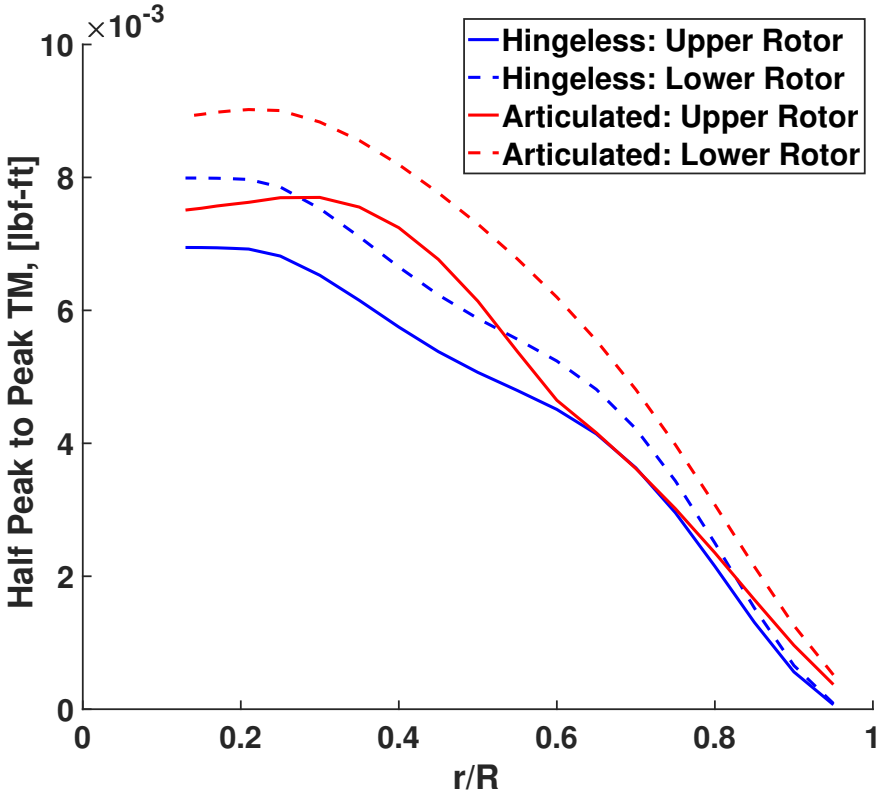

Figure 5.23: Torsion moment half peak-to-peak oscillatory magnitude from CFD/CA.

the hingeless hub. The maximum for the hingeless hub occurs at the root, but at $25-35\%$R for the articulated. The largest difference between CFD/CA and CA is the high increase (average of 58%) on the upper rotors because of the change in thrust balance. The lower rotors remain similar. Figure 5.24 shows the mean removed waveform. It is predominantly 1/rev, but there is again high frequency content on the articulated hub. For the lower rotor, high frequency content contributes to the half peak to peak oscillations. The physical cause of these high frequency (6 and 14/rev) oscillations is unclear. Figure 5.25 shows the steady moment. The maximum on the hingeless hub compared to the articulated is 84% higher on the upper rotor and 62% higher on the lower. Again, the maximum occurs near 30%R for the articulated and near the root for the hingeless. The loads are similar to CA, except for the 83.6% increase on the hingeless hub upper rotor.

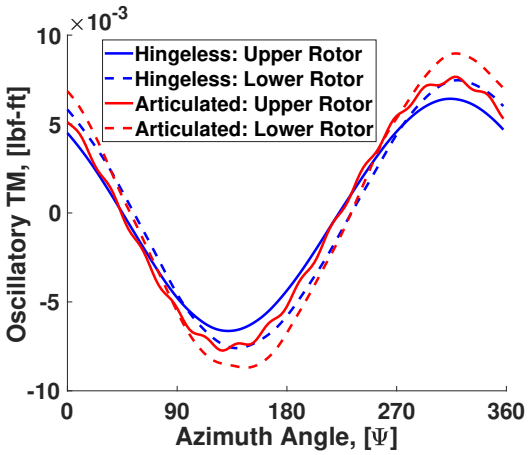

(a) Torsion moment at 30% R

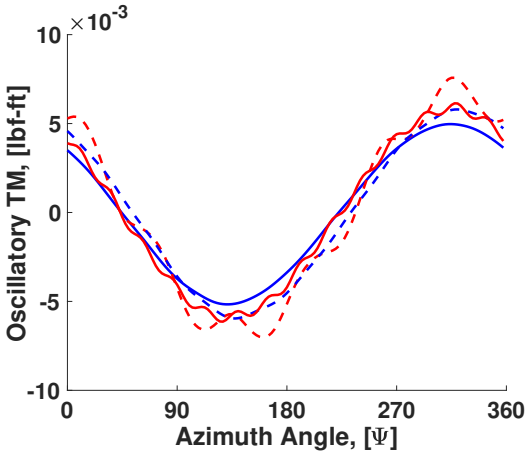

(b) Torsion moment at 50% R

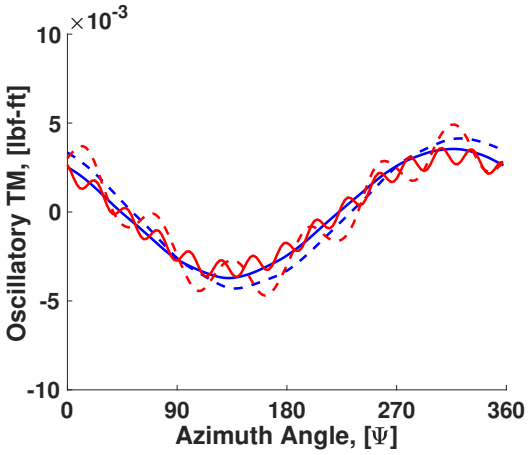

(c) Torsion moment at 70% R

Figure 5.24: Oscillatory torsion moment from CFD/CA.

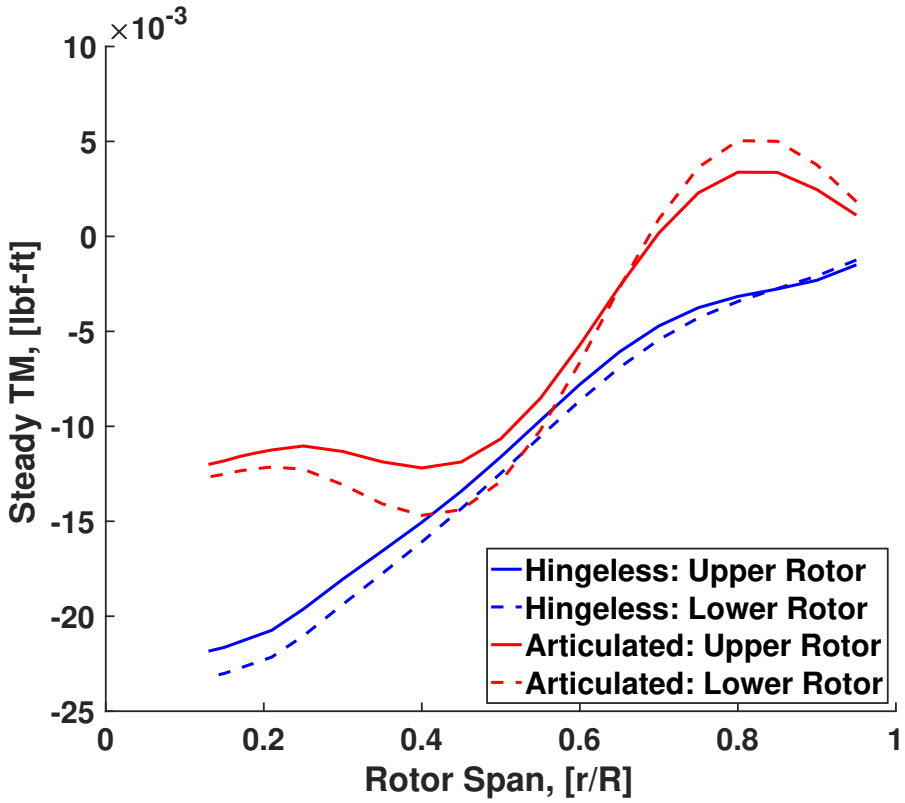

Figure 5.25: Steady torsion moment from CFD/CA.

5.3.7 Pitch Link Loads

Figure 5.26 shows the oscillatory (mean-removed) pitch link loads predicted by CA and CFD/CA. With CFD/CA the upper and lower rotors show similar magnitude, which is different than the CA prediction. The waveform is dominated by 1/rev and there is no high frequency content. Figure 5.27 provides the steady pitch link loads for both hubs, and shows an under-prediction by CA for the upper rotor loads by almost one half. That the hingeless hub has a significantly larger steady load, approximately twice the articulated is also predicted by CFD/CA. This is expected, as the cause is pitch-flap coupling from center of gravity offset, not aerodynamic moments. The mean is still nose down. Chordwise C.G. offset introduces a nose-up moment. The articulated hub has a larger steady flap angle which creates a larger nose-up pitching moment. This moment in turn reduces the nose-down pitching

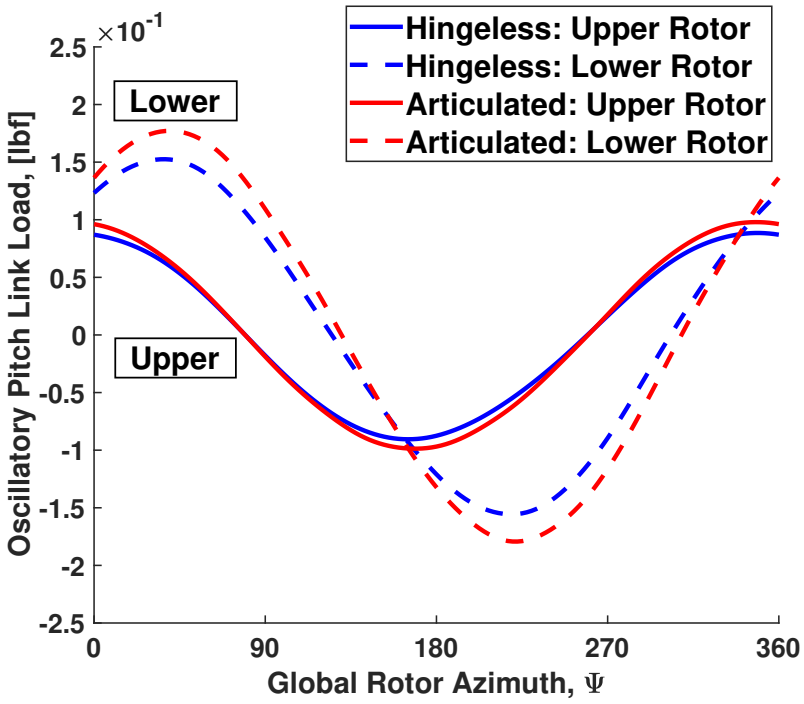

(a) Oscillatory pitch link loads from CA

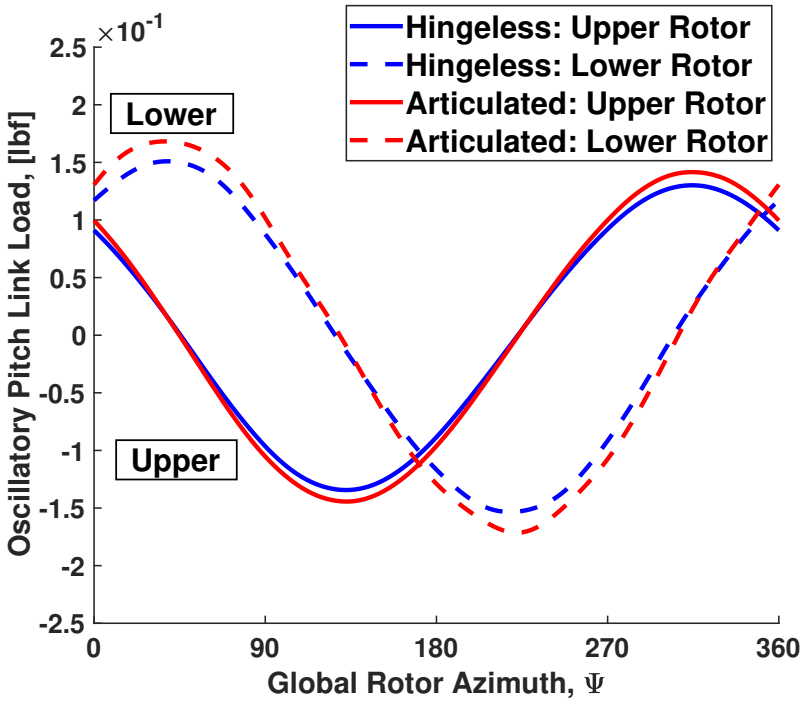

(b) Oscillatory pitch link loads from CFD/CA

Figure 5.26: Oscillatory (mean-removed) pitch link loads from CA and coupled CFD/CA analyses.

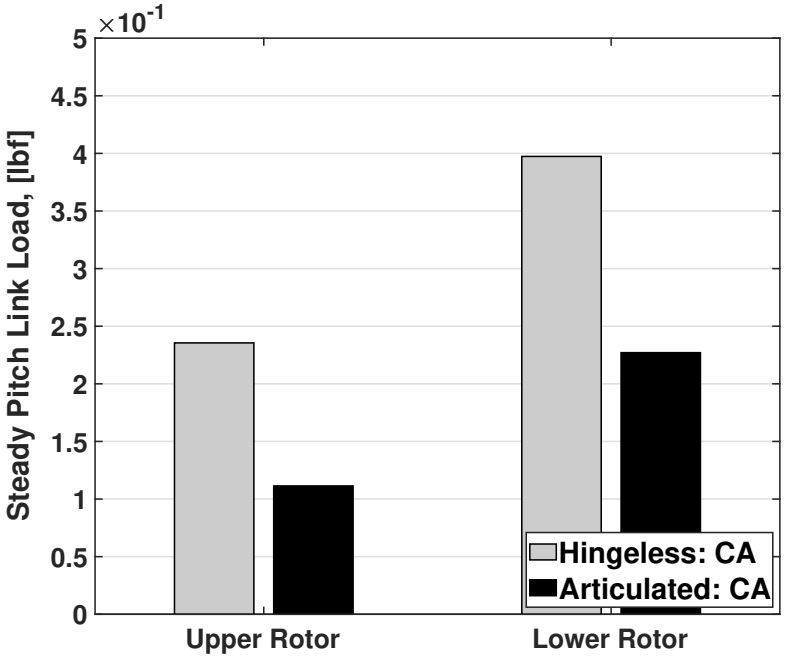

(a) Predictions from CA

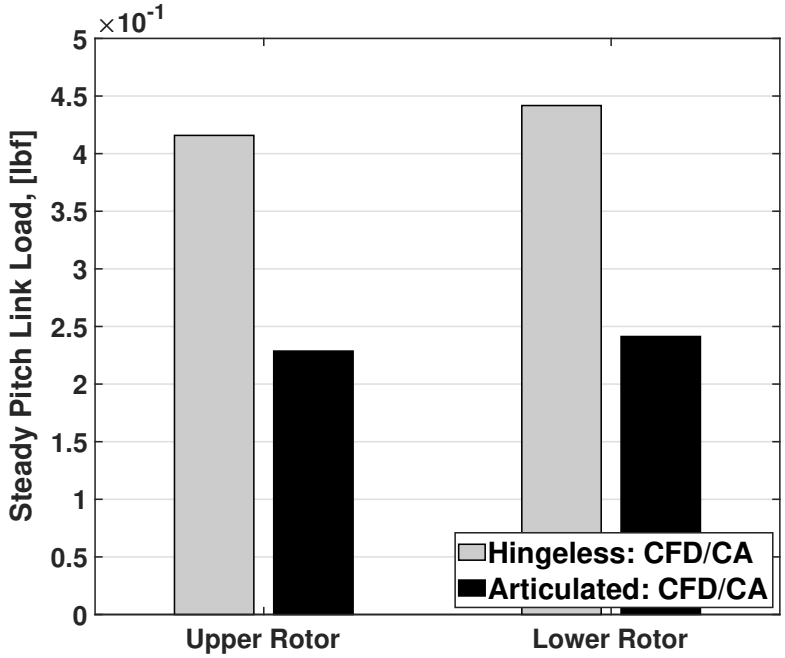

(b) Predictions for coupled CFD/CA

Figure 5.27: Mean pitch link loads from CA and coupled CFD/CA analyses.

moment. It is in fact beneficial to have a chordwise center of gravity offset, in order to reduce the mean pitch link loads. The contributions from aerodynamic pitching moments from CFD are also significant, particularly for the upper rotor where there is almost a 100% increase, for both hubs.

5.4 Summary and Conclusions

CFD was validated in hover at the Mars low Reynolds number conditions. Then forward flight was explored with emphasis on hub type. The impact of the high-fidelity analysis was assessed. The following conclusions are drawn.

1. CFD is able to predict the low Reynolds number data better than CA.
2. CFD/CA predicts an equal thrust sharing between upper and lower rotors in forward flight.
3. CFD/CA predicts significantly larger impulsive loading due to blade passage compared to CA.
4. The wake dissipates quickly and does not propagate as long as typical on Earth.
5. The distinctions between hingeless and articulated hubs predicted by CA hold true.
6. In general, magnitudes of the oscillatory and steady change increase from CA.
7. CA is able to predict the performance and mean loads but not the oscillatory loads critical for fatigue and vibration.

Chapter 6: Helios–Coupled CFD/CA Analysis of US Army

6.1 Overview

Chapters 4 and 5 dealt with forward flight but no validation. There are no Martian wind-tunnels for rotors. Therefore, in this chapter the in-house (UMD) coupled CFD/CA analysis is compared with the Department of Defense's CREATE™-AV Helios software. This software contains a different CA and CFD. Like UMD CFD/CA, Helios is also a state-of-art high-fidelity rotorcraft simulation tool on Earth (see Refs [95–99] for recent efforts). The same baseline forward flight conditions as investigated in Chapters 4 and 5 are repeated again. Then, with the readily available fuselage capability of Helios, the effect of a notional fuselage is also studied.

6.2 Helios

Developed as part of the Department of Defense's Computational Research and Engineering Acquisition Tools and Environment – Air Vehicles (CREATE™-AV), Helios is a software framework (a driver routine to call various disciplinary codes). It uses a multi-mesh paradigm to combine structured and unstructured CFD solvers and can couple them with CA. The near body solver is a semi-structured strand solver, mStrand (unstructured on the surface for ease of meshing complex bodies, but structured outward for ease of resolving boundary layer). The background solver is a Cartesian solver, SAMCart. Overset meshing is used for the interface between the two CFD solvers. The CFD/CA coupling methodology is identical to UMD. The

Table 6.1: Helios mesh convergence results at $Re_{Tip} = 5000$, $M_{Tip} = 0.255$, and $C_T/\sigma = 0.08$.

Mesh	Time/step	FM
Fine	33.58 s	0.3540
Medium	21.54 s	0.3476
Coarse	16.73 s	0.3207

CA is Rotorcraft Comprehensive Analysis System (RCAS). RCAS employs the same finite element approach as UMARC only the response calculated via time marching. The Helios CFD has even higher-fidelity in certain areas. For example, Helios uses an Adaptive Mesh Refinement (AMR) which can identify regions of higher vorticity and refine the mesh locally in this region. Using this approach allows the complex vortical flows to be well resolved without a blanket refinement of the entire background mesh. It is already clear from Chapters 4 and 5 however that vorticity is not an important mechanism in Mars hence this capability is not expected to impact results. In general then, close approximations to the solution is to be expected, and if achieved, would serve as the best verification Earth has to offer. In the following sections, the UMD Mars rotor is modeled in Helios and the same flight conditions are executed.

6.3 Setup

The near body mesh uses similar resolution as used in the UMD solver. The cell sizes at the outer limit of the blade mesh were set to be the same as the UMD mesh and extended up to $0.4c$ away from the blade surface. In Helios both the nearbody and background mesh are automatically generated at run time. The structured mesh covers up to 20 R in all directions with 15 levels of refinement for maximum fidelity.

To verify the blade mesh a convergence study on the wall normal spacing was conducted (wall normal is the structured direction, hence easy to refine). Three meshes were tested. A summary of the mesh convergence is given in Table 6.1. The

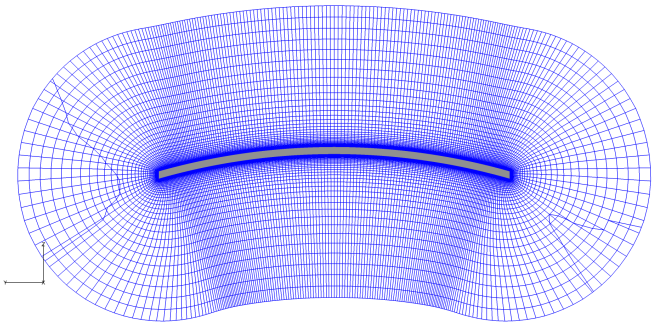

Figure 6.1: Nearbody airfoil mesh used in DoD Helios.

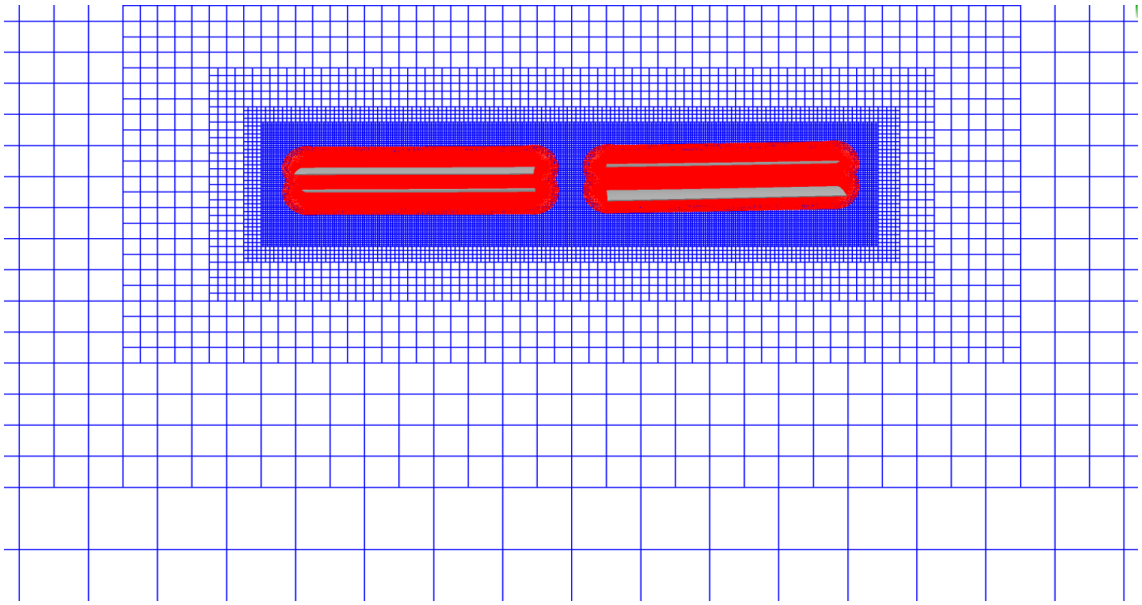

Figure 6.2: Background Cartesian mesh from DoD Helios showing the first few levels of mesh refinement.

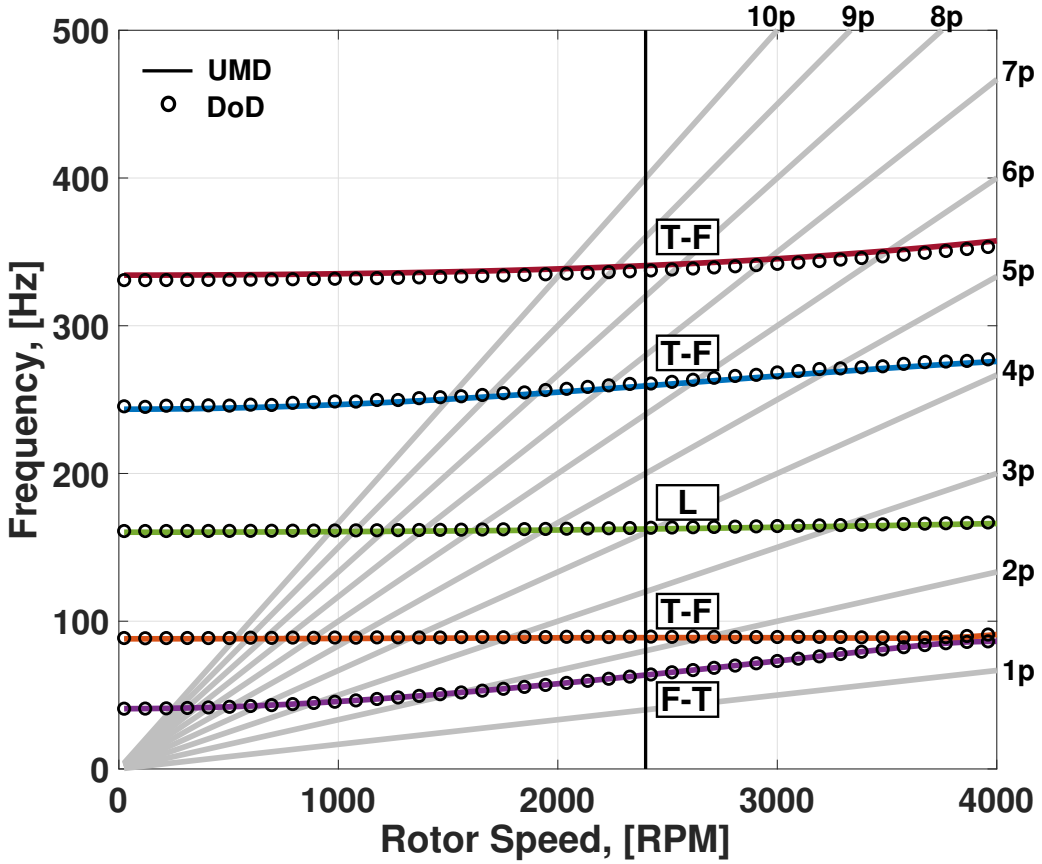

Figure 6.3: Comparison of UMARC and RCAS fan plots to verify similar structural modeling.

coarsest mesh under-predicted the Figure of Merit of the fine mesh by 9.5% while the medium mesh was only off by 1.8%. Therefore to minimize runtime the medium mesh was selected. This mesh has a wall normal spacing of 0.001c. The mesh is shown in Figure 6.1 and the background mesh in Figure 6.2.

The same baseline forward flight conditions were used (see Table 4.4). For this comparison, only the hingeless rotor was selected. To verify the structural inputs, the fan plots from the two analyses were compared, Figure 6.3. The frequencies are identical. The coupling solution procedure was also identical. Both analyses ran for two full revolutions before the first coupling, and then coupled once per revolution until converged. Six coupling iterations were considered sufficient based on the convergence pattern seen earlier with UMD CFD/CA.

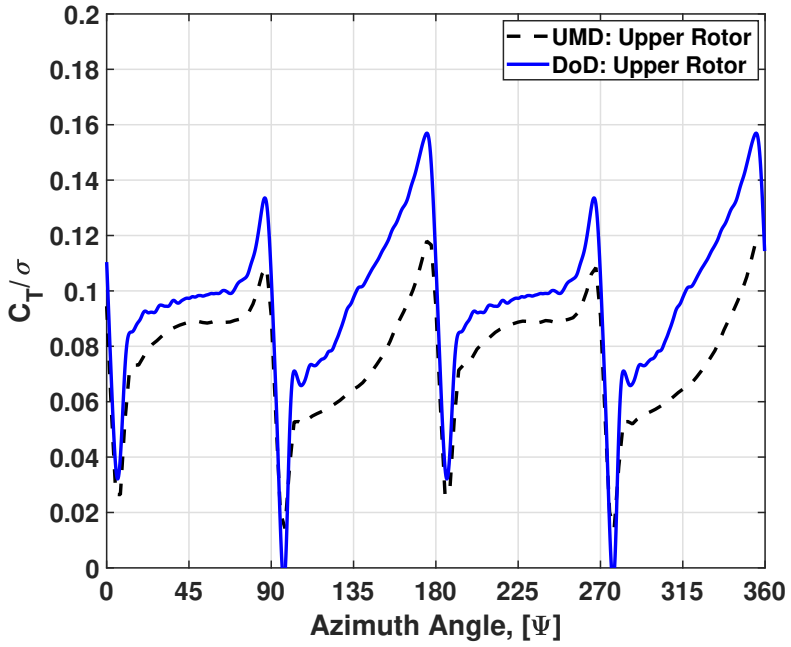

(a) Upper Rotor

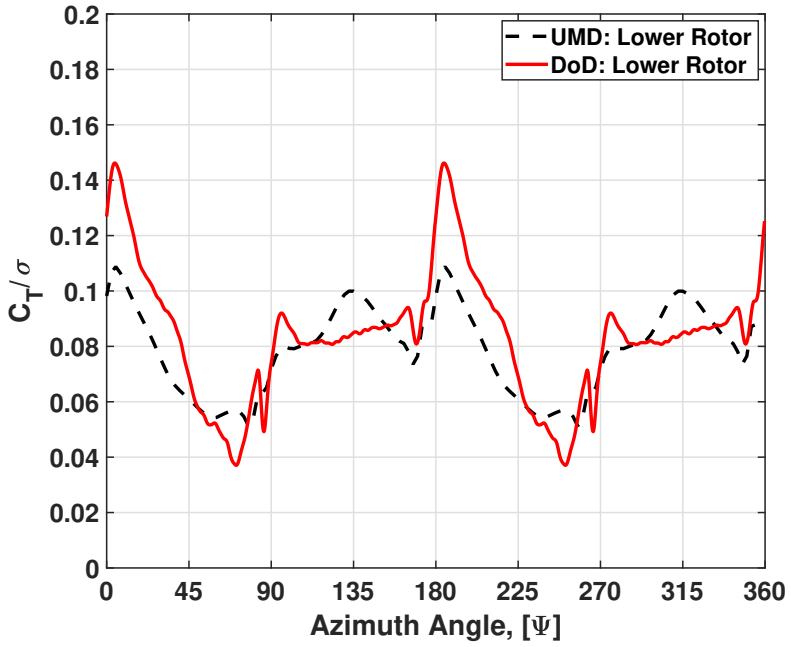

(b) Lower Rotor

Figure 6.4: Thrust coefficient C_T/σ of upper and lower rotors around the rotor azimuth; UMD in-house versus Helios.

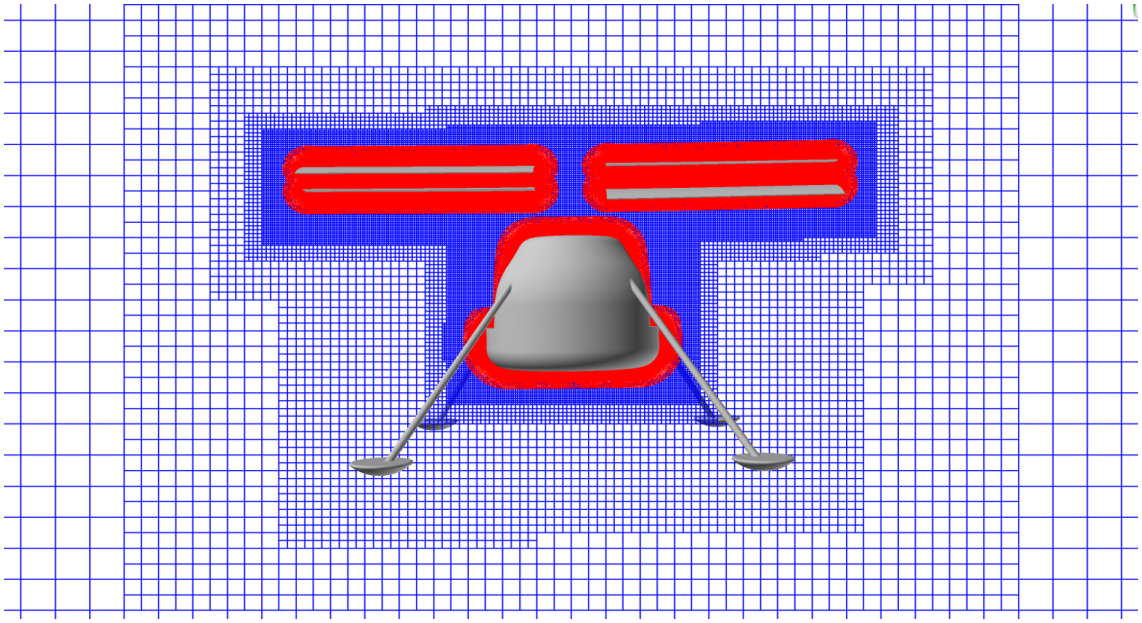

Figure 6.5: Aircraft with fuselage mesh.

6.4 Coaxial Rotor Results

Figure 6.4 shows the thrust for the two sets of analyses (UMD in-house and Helios). The analyses show similar trends and waveform. Helios predicts larger impulsive loads on both upper and lower rotors. The impulsive loads are verified. Even greater impulses are predicted suggesting more blade passage interaction, possibly due to the finer mesh.

6.5 Effect of Fuselage

The mesh with fuselage is shown in Figure 6.5. The rotor mesh is identical. The CFD/CA coupling naturally only considers the rotor. There is no structural model of the fuselage.

The flow field around the aircraft is shown in Figure 6.6. The wake has similar roll up, symmetric structures, strong interactions, and quick breakdown as the isolated rotor wake shown earlier in Section 5.3.3. The adaptive mesh refinement

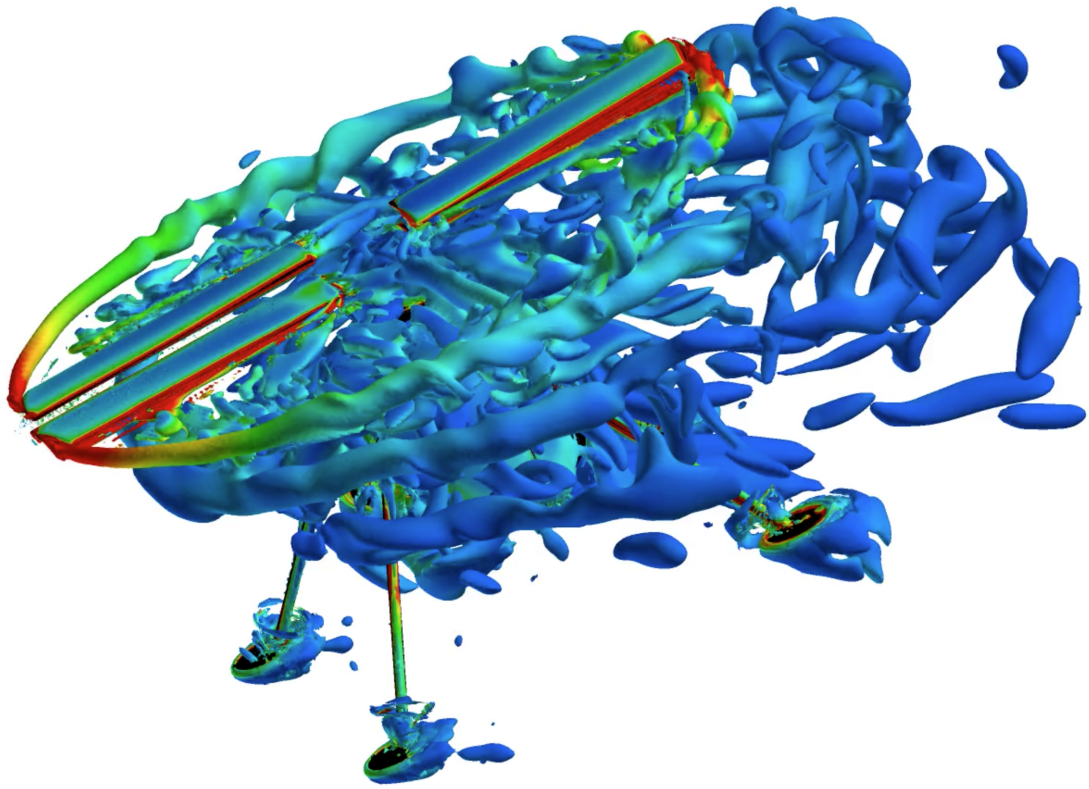

Figure 6.6: Converged Helios CFD/CA flow solution for aircraft; iso-surface of Q-criterion, 0.003, colored by vorticity.

confirms the wake indeed does not propagate far downstream. It also appears that at the given advance ratio, the upper wake is ingested and sliced by the lower rotor which causes faster dissipation. There is no interesting interaction with the fuselage.

Figure 6.7 shows the thrust with and without the fuselage, from the upper and lower rotors separately. The predictions are remarkably similar. The impulsive loadings remain and the general waveforms are almost identical. The only difference is a small steady offset. This offset is too small to affect the trim solution. Thus, the inclusion of the fuselage aerodynamics is not important for rotor airloads and structural loads. The high rotational speed and and thin Martian atmosphere cause the fuselage to not meaningfully impact the rotor flow field. The implication is that

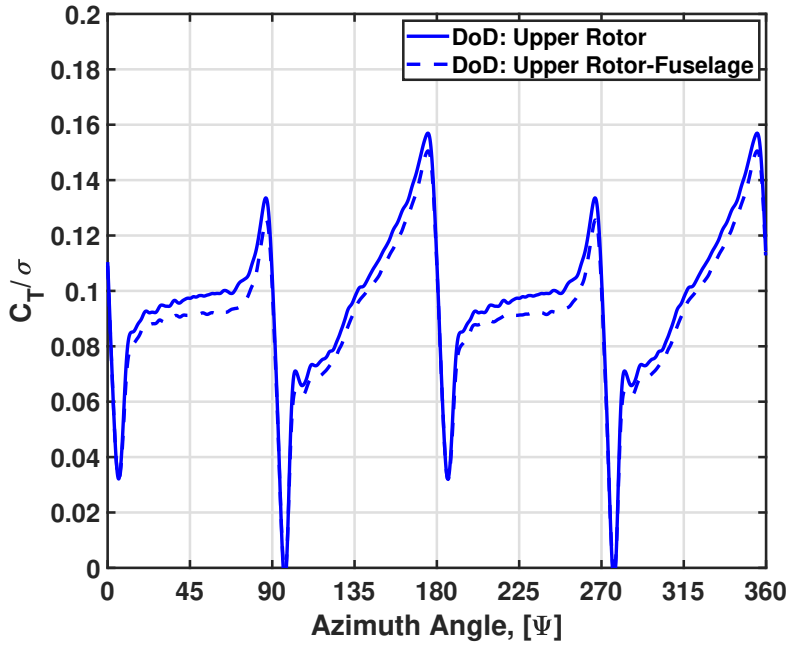

(a) Upper Rotor

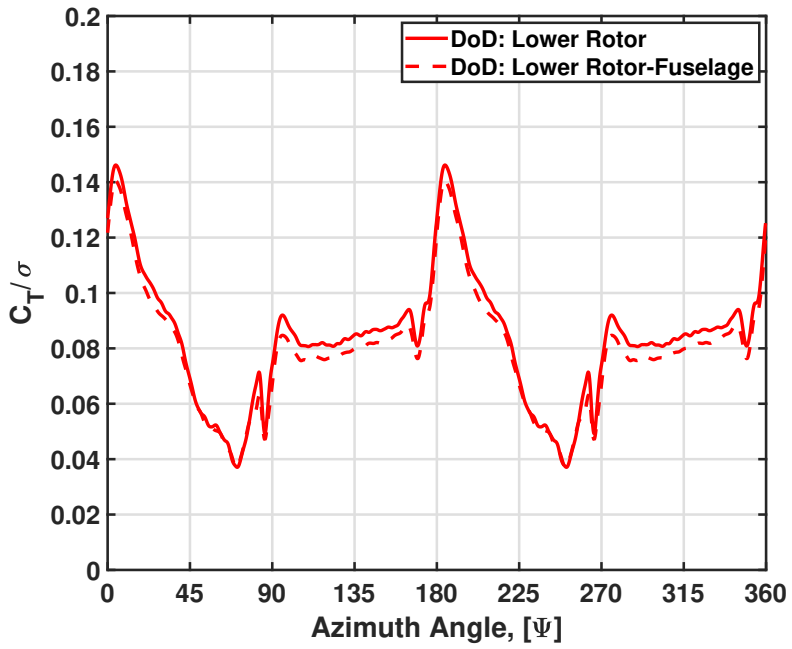

(b) Lower Rotor

Figure 6.7: Thrust coefficient C_T/σ of upper and lower rotors around the rotor azimuth; isolated rotors versus full aircraft.

fuselages of any shape might perhaps be acceptable as needed by the science mission without being constrained by aerodynamics.

6.6 Summary and Conclusions

The UMD CFD/CA developed in-house was verified in forward flight with the US Department of Defense Helios software. The same problem and conditions were set up and executed in Helios and the results provided independent verification of the predictions. The impact of the fuselage on the rotor flow field was explored. The following conclusions are drawn.

1. The conclusions from UMD CFD/CA are all verified by Helios results. In absence of test data this serves to provide the best possible independent confirmation. There were however certain finer details that were different.

2. Helios predicts larger impulsive loads, although the general trends and waveform are similar.

3. The inclusion of fuselage aerodynamics does not have a meaningful impact on the rotor airloads and structural loads. This is because of the high rotational speed, quick wake dissipation and the thin Martian air.

Chapter 7: Summary and Conclusions

This chapter summarizes this dissertation. It includes: key conclusions, the principal contributions, and recommendations of future research.

7.1 Summary

The fundamental aeromechanics of rotary-wing flight on Mars was explored. The exploration included chamber testing of Mars-like low Reynolds number rotors and the development of comprehensive analysis and comprehensive analysis coupled with computational fluid dynamics for systematic investigation of aeromechanical phenomena–critical for weights and packaging for Mars. The investigation included rotor airloads, structural loads, and control loads, comparison of hingeless and articulated hubs, hover and forward flight, and the impact of fuselage aerodynamics. The coaxial configuration was used as the baseline platform for this work.

The technical approach consisted of fabrication and chamber testing of a small rotor and multi-fidelity analysis from comprehensive analysis (CA) to computational fluid dynamics (CFD) coupled with comprehensive analysis (CFD/CA). In absence of flight or wind-tunnel data on Mars innovative methods of validation and verification were devised.

Low Reynolds number hover tests were conducted on a small 1.5 ft diameter hingeless rotor inside a 3 ft diameter vacuum chamber. The two-bladed model rotor had a hingeless hub and a swashplate with full pitch controls. The tests covered a range of 3000 to $10,000$ tip Reynolds number at a constant Mach number of 0.07 and

collective sweeps of $-10°$ to $40°$ at $5°$ increments. The data agreed with the limited data published later by JPL at similar conditions (Re $= 11,000$) on the actual Mars Helicopter scheduled onboard the Mars 2020 mission.

Next, the structural and aerodynamic models for the blades and rotor were developed. The structural properties were measured and calculated from the test blades. Flap stiffness was measured and chord and torsion calculated from a 3D FEA (X3D) after calibration of material properties using the flap data. The blades were too stiff and unconventional to measure chord and torsion accurately. Predictions matched the measured non-rotating frequencies validating the basic structural model. The pitch link stiffness could not be measured either. The pitch link was modeled but assumed to be rigid. So the pitch link loads are torsion loads at the pitch bearing. The aerodynamic properties were generated using in-house 2D CFD. Sectional lift, drag, and quarter-chord pitching moment coefficients were calculated at Reynolds numbers of 1000, 3000, 5000, 7000, and $10,000$ and Mach numbers of 0.05, 0.10, and 0.30.

Using the above properties, a refined comprehensive analysis (CA) was set up using University of Maryland Advanced Rotorcraft Code (UMARC) as the baseline platform. The CA was validated with state-of-art coaxial low Re (tip Re $210,000$–$315,000$) hover data from US Army / NASA Ames. Then, the rotor model was validated at Martian Re (tip Re 3000–$10,000$), using the vacuum chamber hover data. After validation, the analysis was converted to forward flight. The focus of the investigation was on hub type, comparing hingeless and articulated. The baseline conditions were: advance ratio $\mu = 0.10$, shaft angle $\alpha = 5°$ (positive nose-down), inter-rotor separation $h/D = 0.05$, and thrust $C_T/\sigma = 0.08$ with excursions of key flight and design parameters: advance ratio (0.02 to 0.12), shaft angle ($-30°$ to $40°$), inter-rotor separation (0.01R to 0.40R), and blade loading (0.02 to 0.20).

Next, a coupled CFD/CA analysis was developed to replace the lifting-line/free

wake aerodynamic model with 3D CFD and obtain higher fidelity predictions. This analysis was also validated with the same in-house vacuum chamber data. Once validated the same baseline forward flight conditions was explored again, to investigate 3D effects of the low Reynolds number blades, propagation of the wake, and distortion and dissipation of the vortices. The two analyses were compared to observe the impact of the higher fidelity analysis and assess the need to be used during design of future Mars helicopters.

Finally, due tot the complete absence of any sort of forward flight data in Mars conditions, or any past precedence of any sort, the in-house CFD/CA predictions were verified by modeling and testing the same case on another state-of-art CFD/CA–US Department of Defense Helios. Helios contains a different structural and CFD solver. Predictions from Helios served as an independent verification of the results. Helios was also used to assess the need for aerodynamic modeling of the fuselage. Based on all of these studies the following key conclusions are drawn.

7.2 Key Conclusions

The key conclusions of this dissertation are as follows. They are listed in the order they were established, not in order of importance. They are all equally important.

1. It was observed from test data that thin cambered plate airfoils are suitable for Mars in both hover and forward flight. The 2% thick 6% cambered circular arc airfoil studied here was capable of hover with a maximum Figure of Merit of 0.57 at tip Re = $10,000$. The data showed the expected Reynolds number trends, that performance increased with Reynolds number, from 0.39 at Re = 3000 to 0.42 at Re = 5000.

2. Lifting-line comprehensive analysis (CA) predicted lower Reynolds numbers

hover trends, but under-predicted maximum Figure of Merit, especially for Re $= 10,000$.

3. In forward flight, blade strike was found to be equally likely for the hingeless and articulated hubs. This is because at the very low Lock numbers rotor separation is dictated by control angles and chord, not flap angle. This is contrary to the trends found on Earth.

4. The peak to peak airloads are determined by impulses from blade passage. This is particularly true for the upper rotor. The peak to peak structural loads are determined more by trim solution and global aerodynamics of airfoils and wake. This is true for both the upper and lower rotor. This conclusion holds for both hub types.

5. Thee impulses from blade passage were significant only in airloads but not in structural loads. Only their low harmonic content is filtered into the structural loads.

6. The oscillatory flap bending and torsion moments were comparable between hubs, while lag bending were 4 fold higher for the hingeless.

7. The hingeless hub had steady control loads 2 fold the articulated. This is due to pitch-flap coupling from the chordwise center of gravity offset and flapping angle. The higher flipping of the articulated hub further reduces the control loads.

8. The trends between hubs hold for all excursions of advance ratio, shaft angle, inter-rotor separation, and thrust. Oscillatory blade loads increase with advance ratio, shaft angle, and thrust. For the inter-rotor separation sweep, they increase on the lower rotor and decrease on the upper. Steady control loads increase with shaft angle, inter-rotor separation and thrust.

9. CFD predicts low Reynolds number hover and Figure of Merit. Even for performance, CFD is beneficial over lifting-line.

10. In forward flight, CFD/CA predicts airloads with higher blade passage impulses, higher chord force, and more even thrust sharing. CFD captures unsteady phenomena such as vortex core growth, wake interaction, and blade passage interactions.

11. CFD/CA predicts the same trends between hubs for loads as found with CA, but the magnitudes differ. The oscillatory loads are significantly higher. These differences impact deflections and trim solution.

12. Blade center of gravity at mid-chord is beneficial for aerodynamics and structural dynamics. Thin cambered plates are best aerodynamics. Unlike Earth, no instability due to low Reynolds number and relieves steady control loads.

13. The fuselage aerodynamics had insignificant impact on airloads. Meaning fuselage shape can be dictated by the science mission and not aerodynamics.

7.3 Principal Contributions

There are three main contributions of this thesis. These are listed below.

1. Laid the foundation of Mars helicopter aeromechanics. Behavior of the aircraft, rotor, hub, blades and controls are different than Earth. They are all intimately coupled also, and therefore cannot be studied or analyzed in isolation. Conventions from Earth do not hold and therefore cannot extrapolate for Mars.

2. Developed new high-fidelity tools that can faithfully predict these physics. Validated in hover with state-of-art coaxial low Re (tip Re $210,000$–$315,000$) data and with single rotor at Martian Re (tip Re 3000–$10,000$). CFD/CA

predictions verified in forward flight by modeling and testing the same case on another state-of-art CFD/CA–US Department of Defense Helios.

3. New understanding of the trade-offs between the hingeless and articulated hubs on Mars. Inter-rotor separation is not dictated by hub type. The low Lock number strongly influences loads. Control loads are relieved by pitch-flap coupling due to blade flapping and chordwise center of gravity offset.

7.4 Future Work

There are many factors that go into the design of a Mars helicopter. The present work focused only on the rotor aeromechanics, specifically the rotor airloads and structural loads. It was also limited to the coaxial configuration. There are two major gaps related to the aircraft modeling that must be addressed in near future.

1. **Aircraft Gust Stability and Controls** – The light-weight low inertia Mars helicopter will be particularly susceptible to high gusts. Maneuvers must be autonomous (4 to 24 minute communication time) and perhaps largely vision based (no GPS). The present work only considered level flight trim solution (equilibrium flight). In future, capability to predict loads in transient maneuvers and under gusts is needed. Flight dynamics and controllability are crucial for Mars because of the lack of aerodynamic damping in the very thin atmosphere.

2. **Fuselage Structural Model** – Chapter 6 covered the impact of fuselage aerodynamic model. Including a structural finite element model of the fuselage is especially important for this aircraft because of the danger of rotor-body frequency coalescence with such a large rotor and small fuselage. In addition, science payloads must be shielded adequately from vibrations.

While this work explored the fundamentals of aeromechanics on Mars, many

gaps in testing capability remained. This thesis identified the key areas to focus on in the future.

1. **Control Loads** – A measurement of the pitch link loads in the rotating frame would provide crucial validation data. It will also provide insights into the control system loads. The use of a small load cell in the pitch link and slip ring should allow for these measurements.

2. **Unsteady Hub Moments** – The validation was conducted using mean thrust and torque values. It would be beneficial to also measure the unsteady hub loads. A good test case would be to input cyclic pitch control, and record the 1/rev hub moments. The current setup will be capable to measuring these loads with the addition of a shaft encoder for azimuthal position.

3. **Larger Chamber** – A larger vacuum chamber is desired. Recirculation is an issue in a small vacuum chamber. Presently, the larger 9 ft vacuum chamber has no swashplate. But at least fixed collective cases could be tested and compared with the current data set. Larger chamber would also allow higher motor speeds (tip Mach numbers) with less heating.

4. **Coaxial Test Stand** – Even though A wealth of data can be collected from an isolated rotor, the best validation of coaxial analysis require a coaxial rig. Significant work would be needed to develop a two rotor system, ideally with the capability to synchronize the rotors, balance torque, and measure loads on each rotor independently.

Whereas the above areas emphasize basic understanding, targeted research on an actual Mars aircraft will also become important. A vision for future Mars helicopters was recently published by NASA/UMD/JPL team. Future work should involve building, testing and analyzing these blades. The fundamental parameters would remain the same. Thus, testing should emphasize the following.

1. **Chordwise Center of Gravity** – Explore the benefits of center of gravity placement near quarter chord.

2. **Airfoil Geometry** – Exploration of airfoil design should include parameters such as thickness, camber, leading edge shape (sharp versus blunt), and boundary layer trips.

3. **Rotor Geometry** – Low Reynolds number research suggests taper could be beneficial for performance. Additionally, sweep should be explored because Mars helicopters may encounter transonic effects due to high rotational speeds and lower speed of sound on Mars.

These and many other fascinating issues remain the topics of future research. No one knows what awaits the Mars Helicopter upon its arrival. But regardless of how it unfolds, it will usher in a brave and bold new world of aerial exploration of Mars.

Appendix A: Vacuum Chamber Wiring Schematics

The vacuum chamber wiring schematics are documented here for future researchers. Figure A.1 shows the vacuum chamber wire diagram for exterior wires. Figure A.2 shows the vacuum chamber wire harness labels for exterior wires. Figure A.3 shows the vacuum chamber wire diagram for interior wires. Figure A.4 shows the vacuum chamber wire harness labels for interior wires.

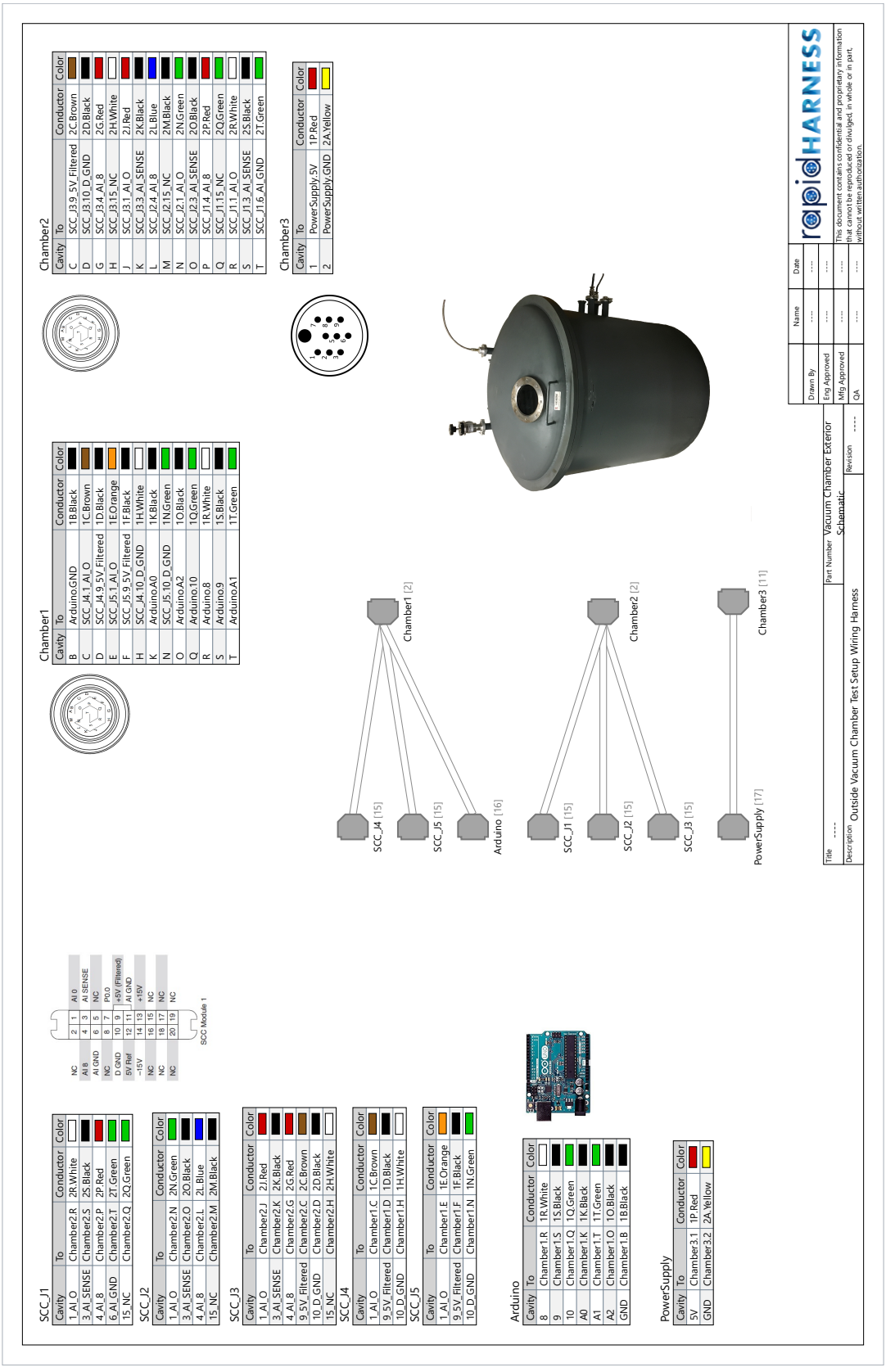

Figure A.1: Vacuum chamber wire diagram for exterior wires.

Title:	I-Wiring Harness
Part Number:	Vacuum Chamber Exterior Schematic
Description:	Outside Vacuum Chamber Test Setup Wiring Harness

rapidHARNESS

From	To	Conductor	Conductor PN	Twist With	Gauge	Length	From Contact PN	Notes
Chamber1.B	Arduino.GND	1B.Black	24 AWG Black		24 AWG			
Chamber1.C	SCC_J4.1_AI_O	1C.Brown	24 AWG Brown		24 AWG			
Chamber1.D	SCC_J4.9_5V_Filtered	1D.Black	24 AWG Black		24 AWG			
Chamber1.E	SCC_J5.1_AI_O	1E.Orange	24 AWG Orange		24 AWG			
Chamber1.F	SCC_J5.9_5V_Filtered	1F.Black	24 AWG Black		24 AWG			
Chamber1.H	SCC_J4.10_D_GND	1H.White	24 AWG White		24 AWG			
Chamber1.K	Arduino.A0	1K.Black	24 AWG Black		24 AWG			
Chamber1.N	SCC_J5.10_D_GND	1N.Green	24 AWG Green		24 AWG			
Chamber1.O	Arduino.A2	1O.Black	24 AWG Black		24 AWG			
Chamber1.Q	Arduino.10	1Q.Green	24 AWG Green		24 AWG			
Chamber1.R	Arduino.8	1R.White	24 AWG White		24 AWG			
Chamber1.S	Arduino.9	1S.Black	24 AWG Black		24 AWG			
Chamber1.T	Arduino.A1	1T.Green	24 AWG Green		24 AWG			
Chamber2.C	SCC_J3.9_5V_Filtered	2C.Brown	24 AWG Brown		24 AWG			
Chamber2.D	SCC_J3.10_D_GND	2D.Black	24 AWG Black		24 AWG			
Chamber2.G	SCC_J3.4_AI_8	2G.Red	24 AWG Red		24 AWG			
Chamber2.H	SCC_J3.15_NC	2H.White	24 AWG White		24 AWG			
Chamber2.J	SCC_J3.1_AI_O	2J.Red	24 AWG Red		24 AWG			
Chamber2.K	SCC_J3.3_AI_SENSE	2K.Black	24 AWG Black		24 AWG			
Chamber2.L	SCC_J2.4_AI_8	2L.Blue	24 AWG Blue		24 AWG			
Chamber2.M	SCC_J2.15_NC	2M.Black	24 AWG Black		24 AWG			
Chamber2.N	SCC_J2.1_AI_O	2N.Green	24 AWG Green		24 AWG			
Chamber2.O	SCC_J2.3_AI_SENSE	2O.Black	24 AWG Black		24 AWG			
Chamber2.P	SCC_J1.4_AI_8	2P.Red	24 AWG Red		24 AWG			
Chamber2.Q	SCC_J1.15_NC	2Q.Green	24 AWG Green		24 AWG			
Chamber2.R	SCC_J1.1_AI_O	2R.White	24 AWG White		24 AWG			
Chamber2.S	SCC_J1.3_AI_SENSE	2S.Black	24 AWG Black		24 AWG			
Chamber2.T	SCC_J1.6_AI_GND	2T.Green	24 AWG Green		24 AWG			
Chamber3.1	PowerSupply.5V	1P.Red	24 AWG Red		24 AWG			
Chamber3.2	PowerSupply.GND	2A.Yellow	24 AWG Yellow		24 AWG			

Page 1 of 1

Figure A.2: Vacuum chamber wire harness labels for exterior wires.

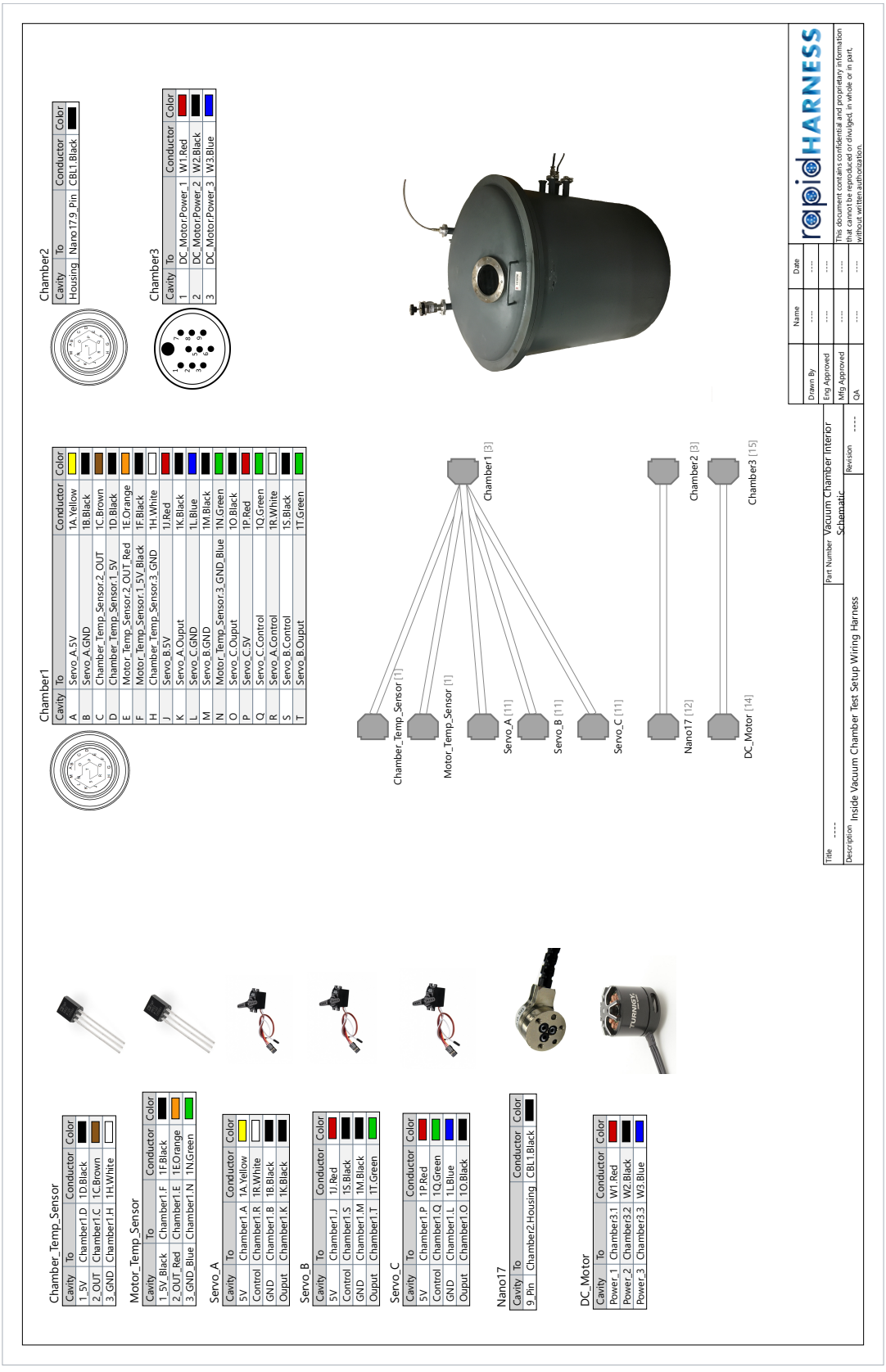

Figure A.3: Vacuum chamber wire diagram for interior wires.

Title:	I-Wiring Harness
Part Number:	Vacuum Chamber Interior Schematic
Description:	Inside Vacuum Chamber Test Setup Wiring Harness

rapidHARNESS

From	To	Conductor	Conductor PN	Twist With	Gauge	Length	From Contact PN	Notes
Chamber1.C	Chamber_Temp_Sensor.2_OUT	1C.Brown	24 AWG Brown		24 AWG			
Chamber1.D	Chamber_Temp_Sensor.1_5V	1D.Black	24 AWG Black		24 AWG			
Chamber1.H	Chamber_Temp_Sensor.3_GND	1H.White	24 AWG White		24 AWG			
DC_Motor.Power_1	Chamber3.1	W1.Red	20 AWG Red		20 AWG			
DC_Motor.Power_2	Chamber3.2	W2.Black	20 AWG Black		20 AWG			
DC_Motor.Power_3	Chamber3.3	W3.Blue	20 AWG Blue		20 AWG			
Motor_Temp_Sensor.1_5V_Black	Chamber1.F	1F.Black	24 AWG Black		24 AWG			
Motor_Temp_Sensor.2_OUT_Red	Chamber1.E	1E.Orange	24 AWG Orange		24 AWG			
Motor_Temp_Sensor.3_GND_Blue	Chamber1.N	1N.Green	24 AWG Green		24 AWG			
Nano17.9_Pin	Chamber2.Housing	CBL1.Black	9 Wire 24 AWG shielded		24 AWG			
Servo_A.5V	Chamber1.A	1A.Yellow	24 AWG Yellow		24 AWG			
Servo_A.Control	Chamber1.R	1R.White	24 AWG White		24 AWG			
Servo_A.GND	Chamber1.B	1B.Black	24 AWG Black		24 AWG			
Servo_A.Ouput	Chamber1.K	1K.Black	24 AWG Black		24 AWG			
Servo_B.5V	Chamber1.J	1J.Red	24 AWG Red		24 AWG			
Servo_B.Control	Chamber1.S	1S.Black	24 AWG Black		24 AWG			
Servo_B.GND	Chamber1.M	1M.Black	24 AWG Black		24 AWG			
Servo_B.Ouput	Chamber1.T	1T.Green	24 AWG Green		24 AWG			
Servo_C.5V	Chamber1.P	1P.Red	24 AWG Red		24 AWG			
Servo_C.Control	Chamber1.Q	1Q.Green	24 AWG Green		24 AWG			
Servo_C.GND	Chamber1.L	1L.Blue	24 AWG Blue		24 AWG			
Servo_C.Ouput	Chamber1.O	1O.Black	24 AWG Black		24 AWG			

Page 1 of 1

Figure A.4: Vacuum chamber wire harness labels for interior wires.

Bibliography

[1] Seiff, A. and Kirk, D.B., "Structure of the Atmosphere of Mars in Summer at Mid-Latitudes," *Journal of Geophysical Research*, Vol. 82, No. 28, September 1977, pp. 4364–4378.

[2] Magalhaesl, J.A., Schofield, J.T., and Seiff, A., "Results of the Mars Pathfinder Atmospheric Structure Investigation," *Journal of Geophysical Research*, Vol. 104, No. E4, April 1999, pp. 8943–8955.

[3] Portree, D. S. F., "Humans to Mars: Fifty Years of Mission Planning, 1950-2000," *NASA-SP-2001-4521*, 2001.

[4] Ley, W. and von Braun, W., *The Exploration of Mars*, 1st ed., Viking Publishers, New York, NY, USA, 1956.

[5] The NASA History Office, "Astronautics and Aeronautics, 1978: A Chronology," *NASA-SP-4023*, 1978.

[6] Kuhl C.A., "Design of a Mars Airplane Propulsion System for the Aerial Regional-scale Environmental Survey (ARES) Mission Concept," 44th AIAA/ASME/SAE/ASEE Joint Propulsion Conference and Exhibit, AIAA, July 2008, Paper No. 2008-5246, Hartford, CT.

[7] Kuhl, C. A., "Design of a Mars Airplane Propulsion System for the Aerial Regional-Scale Environmental Survey (ARES) Mission Concept," Tech. Rep. NASA-TM-2009-215700, 2009.

[8] Seemann, G.R., "A Concept Study of A Remotely Piloted Vehicle for Mars Exploration," Tech. Rep. NASA-CR-157942, 1978.

[9] Reed, R.D., "High-Flying Mini-Sniffer RPV - Mars Bound," *Astronautics and Aeronautics*, Vol. 16, No. 1, June 1978, pp. 26–39. NASA-SP-4023.

[10] French, J.R., "The Mars Airplane," *Marshall Space Flight Center Manned Mars Missions: Working Group Papers*, Vol. 1, No. 1-4, May 1986, pp. 406–414.

[11] Colozza, A.J., "Preliminary Design of a Long-Endurance Mars Aircraft," Tech. Rep. NASA-CR-185243, 1990.

[12] Smith, S.C., Hahn, A.S., Johnson, W.R., Kinney, D.J., Pollitt, J.A., and Reuther, J.J., "The Design of the Canyon Flyer, An Airplane for Mars Exploration," 38th AIAA Aerospace Sciences Meeting and Exhibit, AIAA, January 10-13 2000, Paper No. 2000-0514, Reno, NV.

[13] Hall, J., Pauken, M., Kerzhanovich, V., Walsh, G., Kulczycki, E., Fairbrother, D., Shreves, C., and Lachenmeier, T., "Mars Balloon Flight Test Results," AIAA Balloon Systems Conference, AIAA, May 2009, Paper No. 2009-2809, Seattle, WA.

[14] Kerzhanovich, V., Cutts, J., Cooper, H., Hall, J., McDonald, B., Pauken, M., White, C. Yavrouin, A., Castano, A., Cathey, H., Fairbrother, D., Smith, S., Shreves, C., Lachenmeier, T., Rainwater, E., and Smith, M., "Breakthrough in Mars Balloon Technology," COSPAR Balloon Technology Conference, Committee on Space Research, October 2002, Houston, TX.

[15] Nock, K.T., Balaram, J., Heun, M. K., Smith, I. S., and Gamber, T., "Mars 2001 Aerobot/Balloon System Overview," International Balloon Technology Conference, AIAA, June 3-5 1997, Paper No. 1997-1500, San Francisco, CA.

[16] Heun, M., Cathey, H. Jr., and Haberle, R., "Mars Balloon Trajectory Model for Mars Geoscience Aerobot Development," International Balloon Technology Conference, AIAA, June 3-5 1997, Paper No. 1997-1500, San Francisco, CA.

[17] Savu, G., and Trifu, O., "Photovoltaic Rotorcraft for Mars Missions," 31st AIAA/ASME/SAE/ASEE Joint Propulsion Conference and Exhibit, AIAA/ASME/SAE/ASEE, July 10-12 1995, Paper No. 1995-2644, San Diego, CA.

[18] Young, L., Gulick, V., and Briggs, G., "Rotorcraft as Mars Scouts," IEEE Aerospace Conference, Institute of Electrical and Electronics, March 9-16 2002, Big Sky, MT.

[19] Young, L. A., "Vertical Lift – Not Just For Terrestrial Flight," AHS/AIAA/RaeS/SAE International Powered Lift Conference, AHS/AIAA/RaeS/SAE, November 1 2000, Arlington, VA.

[20] Young, L., Aiken, E., Derby, M., Demblewski, R., and Navarrete, J., "Design Opportunities and Challenges in the Development of Vertical Lift Planetary Aerial Vehicles," American Helicopter Society International Vertical Lift Aircraft Design Specialist's Meeting, American Helicopter Society, January 19-21 2000, San Francisco, CA.

[21] Young, L., Aiken, E., Derby, M., Demblewski, R., and Navarrete, J., "Experimental Investigation and Demonstration of Rotary-Wing Technologies for Flight in the Atmosphere of Mars," American Helicopter Society 58th Annual Forum, American Helicopter Society, June 11-13 2002, Montreal, Canada.

[22] Datta, A., Bao, J., Gamard, O., Griffiths, D., Liu, L., Pugliese, G., Roget, B., and Sitamaran, J., "The Martian Autonomous Rotary-Wing Vehicle (MARV)," American Helicopter Society Student Design Competition Report, June 1 2000.

[23] Datta, A., Roget, B., Griffiths, L., Pugliese, G., Sitamaran, J., Bao, D., Liu, J., and Gamard, O., "Design of a Martian Autonomous Rotary-Wing Vehicle," *Journal of Aircraft*, Vol. 40, No. 3, May-June 2003, pp. 461–472.

[24] Corfeld, K., Strawn, R., and Long L., "Computational Aerodynamics Analysis of a Martian Rotorcraft," *Journal of the American Helicopter Society*, Vol. 49, No. 3, July 2004, pp. 350–356.

[25] Anyoji, M., Nose, K., Ida, S., Numata, D., Nagai, H., and Asai, K., "Low Reynolds Number Airfoil Testing in a Mars Wind Tunnel," 51st AIAA Aerospace Sciences Meeting, AIAA, June 28 - July 1 2010, Paper No. 2010-4627, Chicago, IL.

[26] Suwa, T., Nose, K., Numata, D., Nagai, H., and Asai, D., "Compressibility Effects on Airfoil Aerodynamics at Low Reynolds Number," 30th AIAA Applied Aerodynamics Meeting, AIAA, June 25-28 2012, Paper No. 2012-3029, New Orleans, LA.

[27] Nagai, H., Asai, D., Numata, D., and Suwa, T., "Characteristics of Low-Reynolds Number Airfoils in a Mars Wind Tunnel," 51st AIAA Aerospace Sciences Meeting, AIAA, January 7-10 2013, Paper No. 2013-0073, Dallas/Fort Worth, TX.

[28] Shrestha, R., Benedict, M., Hrishikeshavan, V., and Chopra, I., "Hover Performance of a Small-Scale Helicopter Rotor for Flying on Mars," *Journal of Aircraft*, Vol. 53, No. 4, July-August 2016, pp. 1160–1167.

[29] Winslow, J., Otsuka, H., Govindarajan, B., and Chopra, I., "Basic Understanding of Airfoil Characteristics at Low Reynolds Numbers (10E4 to 10E5)," *Journal of Aircraft*, Vol. 55, No. 3, December 2017, pp. 1050–1061.

[30] Lv, P., Fu, J.M., Xia, Z.F., Mohd-Zawawi, F., Benard, E., and Moschetta, J.M., "Numerical Investigation of a Proof-of-Concept Rotor in Martian Atmosphere," International Micro Air Vehicle Conferences and Competitions, IMAVS, October 17-21 2016, Beijing, China.

[31] Pelletier, A., and Mueller, T.J, "Low Reynolds Number Aerodynamics of Low-Aspect-Ratio, Thin/Flat/Cambered-Plate Wings," *Journal of Aircraft*, Vol. 37, No. 5, September 2000, pp. 825–832.

[32] Koning, W.J.F., Johnson, W., and Grip, H.F., "Improved Mars Helicopter Aerodynamic Rotor Model for Comprehensive Analyses," *AIAA Journal*, Vol. 57, No. 9, September 2019, pp. 3969–3979.

[33] Balaram, J., Canham, T., Duncan, C., Golombek, M., Grip, H., Johnson, W., Maki, J., Quon, A., Stern, R., and Zhu, D., "Mars Helicopter Technology Demonstrator," AIAA SciTech Forum, AIAA, January 2018, Paper No. 2018-0023, Kissimmee, FL.

[34] Grip, H, Scharf, D., Malpica, C., Johnson, W., Mandic, M., Singh, G., and Young, L., "Guidance and Control for a Mars Helicopter," AIAA SciTech Forum, AIAA, January 2018, Paper No. 2018-1849, Kissimmee, FL.

[35] Grip, H., Lam, J., Bayard, D., Conway, D., Singh, G., Brockers, R., Delaune, J., Matthies, L., Malpica, C., Brown, T., Jain, A., San Martin, A., and Merewether, G., "Flight Control System for NASA's Mars Helicopter," AIAA SciTech Forum, AIAA, January 2019, Paper No. 2019-1289, San Diego, CA.

[36] Grip, H, Johnson, W., Malpica, C., Scharf, D., Mandic, M., Young, L., Allan, B., Mettler, B., San Martin, M., and Lam, J., "Modeling and Identification of Hover Flight Dynamics for NASA's Mars Helicopter," *Journal of Guidance, Control, and Dynamics*, Vol. 43, No. 2, February 2020, pp. 179–193.

[37] Pipenberg, B., Keennon, M., Tyler, J., Langberg, S., Hibbs, B., Balaram, J., Grip, H., and Pempejian, J., "Design and Fabrication of the Mars Helicopter Rotor, Airframe, and Landing Gear Systems," AIAA SciTech Forum, AIAA, January 7-11 2019, Paper No. 2019-0620, San Diego, CA.

[38] Pipenberg, B., Keennon, M., Langberg, S.A., and Tyler, J.D., "Development of the Mars Helicopter Rotor System," 75th VFS Annual Forum and Technology Display, Vertical Flight Society International, May 13-16 2019, Philadelphia, PA.

[39] Coleman, C. P., "A Survey of Theoretical and Experimental Coaxial Rotor Aerodynamic Research," Tech. Rep. NASA-TP-3675, 1997.

[40] Burgess, R.K., "The ABC Rotor–A Historical Perspective," AHS 60th Annual Forum, AHS International, June 2004, Baltimore, MD.

[41] Linden, A.W., and Rudell, A.J., "An ABC Status Report," AHS 37th Annual Forum, AHS International, June 1981, New Orleans, LA.

[42] Arents, D. N., "An Assessment of The Hover Performance of The XH-59A Advancing Blade Concept Demonstration Helicopter," Tech. Rep. ADA042063, 1977.

[43] Ruddell, A.J., "XH-59A ABC Technology Demonstrator Altitude Expansion and Operational Tests," Tech. Rep. ADA111114, 1981.

[44] Blackwell, R., and Millot, T., "Dynamics Design Characteristics of the Sikorsky X2 TechnologyTM Demonstrator Aircraft," AHS 64th Annual Forum, AHS International, May 2008, Montreal, Canada.

[45] Bagai, A., "Aerodynamic Design of the X2 TechnologyTM Demonstrator Main Rotor Blade," AHS 64th Annual Forum, AHS International, May 2008, Montreal, Canada.

[46] Walsh, D., Weiner, S., Arifian, K., Bagai, A., Lawrence, T., and Blackwell, R., "Development Testing of the Sikorsky X2 TechnologyTM Demonstrator," AHS 65th Annual Forum, AHS International, May 2009, Grapevine, TX.

[47] Walsh, D., Weiner, S., Arifian, K., Lawrence, T., Wilson, M., Millott, T., and Blackwell, R., "High Airspeed Testing of the Sikorsky X2 TechnologyTM Demonstrator," AHS 67th Annual Forum, AHS International, May 2011, Virginia Beach, VA.

[48] Lorber, P. F., Law, G. K., O'Neill, J. J., Matalanis, C., and Bowles, P., "Overview of S-97 RaiderTM Scale Model Tests," AHS 72th Annual Forum, AHS International, May 17-19 2016, West Palm Beach, FL.

[49] McAlister, K., Tung, C., Rand, O., Khromov, V., and Wilson, J., "Experimental and Numerical Study of a Model Coaxial Rotor," AHS 62rd Annual Forum, AHS International, May 2006, Phoenix, AZ.

[50] McAlister, K., and Tung, C., "Experimental Study of a Hovering Coaxial Rotor with Highly Twisted Blades," AHS 64th Annual Forum, AHS International, May 2008, Montreal, Canada.

[51] Ramasamy, M., "Hover Performance Measurements Toward Understanding Aerodynamic Interference in Coaxial, Tandem, and Tilt Rotors," *Journal of the American Helicopter Society*, Vol. 60, No. 3, July 2015, pp. 1–17.

[52] Cameron, C. G., Karpatne, A., and Sirohi, J., "Performance of a Mach-Scale Coaxial Counter-Rotating Rotor in Hover," *Journal of Aircraft*, Vol. 53, No. 3, May-June 2016, pp. 746–755.

[53] Cameron, C. G., and Sirohi, J., "Performance and Loads of a Lift Offset Rotor: Hover and Wind Tunnel Testing," *Journal of the American Helicopter Society*, Vol. 64, No. 2, April 2019, pp. 1–12.

[54] Cameron, C. G., Sirohi, J., Schmaus, J., and Chopra, I., "Performance and Loads of a Reduced-Scale Coaxial Counterrotating Rotor," *Journal of the American Helicopter Society*, Vol. 64, No. 4, October 2019, pp. 1–15.

[55] Johnson, W., "Influence of Lift Offset on Rotorcraft Performance," Tech. Rep. NASA-TP-2009-215404, 2009.

[56] Johnson, W., Moodie, A. M., and Yeo, H., "Design and Performance of Lift-Offset Rotorcraft for Short-Haul Missions," AHS Future Vertical Lift Aircraft Design Conference, AHS International, January 2012, San Francisco, CA.

[57] Yeo, H., and Johnson, W., "Investigation of Maximum Blade Loading Capability of Lift-Offset Rotors," *Journal of the American Helicopter Society*, Vol. 59, No. 1, January 2014, pp. 1–12.

[58] Schmaus, J., and Chopra, I., "Aeromechanics of Rigid Coaxial Rotor Models for Wind-Tunnel Testing," *Journal of Aircraft*, Vol. 54, No. 4, July-August 2017, pp. 1486–1497.

[59] Schmaus, J. H., "Aeromechanics of a High Speed Coaxial Helicopter Rotor," *PhD Thesis*, 2017. University of Maryland.

[60] Ruzicka, G. C., and Strawn, R. C., "Computational Fluid Dynamics Analysis of a Coaxial Rotor Using Overset Grids," The AHS Specialist's Conference on Aeromechanics, AHS International, January 2008, San Francisco, CA.

[61] Lakshminarayan, V.K., and Baeder, J.D., "High-Resolution Computational Investigation of Trimmed Coaxial Rotor Aerodynamics in Hover," *Journal of the American Helicopter Society*, Vol. 54, No. 4, October 2009, pp. 42008–42008.

[62] Harrington, R.D., "Full-scale-tunnel Investigation of the Static-thrust Performance of a Coaxial Helicopter Rotor," Tech. Rep. NACA-TN-2318, March 1951.

[63] Juhasz, O., Syal, M., Celi, R., Khromov, V., Rand, O., Ruzicka, G. C., and Strawn, R. C., "Comparison of Three Coaxial Aerodynamic Prediction Methods Including Validation with Model Test Data," *Journal of the American Helicopter Society*, Vol. 59, No. 3, October 2014, pp. 1–14.

[64] Reed, E., and Egolf, T. A., "Coaxial Rotor Wake and Prop Induction Impact on a Horizontal Tail Using HPCMP CREATE™-AV Helios," 53rd AIAA Aerospace Sciences Meeting, AIAA, January 2015, Kissimmee, FL.

[65] Bowles, P.O, Matalanis, C., Battisti, M., Min, BY., Wake, B. E., Tuozzo, N., and Lorber, P. F., "Full-Configuration CFD Analysis of the S-97 RAIDERTM," Vertical Flight Society 75th Annual Forum, Vertical Flight Society International, May 2019, Philadelphia, PA.

[66] Seokkwan, Y., Lee, H. C., and Pulliam, T. H., "Computational Study of Flow Interactions in Coaxial Rotors," Tech. Rep. ARC-E-DAA-TN24718, 2016.

[67] Barbely, N. L., Komerath, N. M., and Novak, L. A., "A Study of Coaxial Rotor Performance and Flow Field Characteristics," AHS Technical Conference on Aeromechanics Design for Transformative Vertical Flight, American Helicopter Society, January 20-22 2016, San Francisco, CA.

[68] Xu, H., and Ye, Z., "Coaxial Rotor Helicopter in Hover Based on Unstructured Dynamic Overset Grids," *Journal of Aircraft*, Vol. 47, No. 5, September 2010, pp. 1820–1824.

[69] Datta, A., Nixon, M., and Chopra, I., "Review of Rotor Loads Prediction with the Emergence of Rotorcraft CFD," *Journal of the American Helicopter Society*, Vol. 52, No. 4, October 2007, pp. 287–317.

[70] Singh, R., and Kang, H., "Computational Investigation of Transient Loads and Blade Deformations on Coaxial Rotor Systems," AIAA Aviation Forum, 33rd AIAA Applied Aerodynamics Conference, AIAA, June 22-26 2015, Paper No. 2015-2884, Dallas, TX.

[71] Singh, R., Kang, H., and Bhagwat, M., "Computational and Experimental Study of Coaxial Rotor Steady and Vibratory Loads," AIAA SciTech Forum; 54th AIAA Aerospace Sciences Meeting, AIAA, January 4-8 2016, Paper No. 2016-1787, San Diego, CA.

[72] Passe, B., Sridharan A., and Baeder, J., "Computational Investigation of Coaxial Rotor Interactional Aerodynamics in Steady Forward Flight," AIAA Aviation Forum, 33rd AIAA Applied Aerodynamics Conference, AIAA, June 22-26 2015, Paper No. 2015-2883, Dallas, TX.

[73] Passe, B., Sridharan A., Baeder, J., and Singh, R., "Identification of Rotor-Fuselage Aerodynamic Interactions in a Compound Coaxial Helicopter using CFD-CSD Coupling," AHS Technical Conference on Aeromechanics Design for Transformative Vertical Flight, American Helicopter Society, January 20-22 2016, San Francisco, CA.

[74] Klimchenko, V., and Baeder, J. D., "CFD/CSD Study of Interactional Aerodynamics of a Coaxial Compound Helicopter in High-Speed Forward Flight," , AIAA SciTech 2020 Forum, AIAA, January 2020, Orlando, FL.

[75] Bagai, H., and Leishman, J.G., "Free-Wake Analysis of Tandem, Tilt-Rotor and Coaxial Rotor Configurations," *Journal of the American Helicopter Society*, Vol. 41, No. 3, July 1996, pp. 196–207.

[76] Brown, R. E., "Rotor Wake Modeling for Flight Dynamic Simulation of Helicopters," *AIAA Journal*, Vol. 38, No. 1, January 2000, pp. 57–63.

[77] Lim, J., McAlister, K. W., and Johnson, W., "Hover Performance Correlation for Full-Scale and Model-Scale Coaxial Rotors," *Journal of the American Helicopter Society*, Vol. 54, No. 3, July 2009, pp. 1–14.

[78] Singh P., and Friedmann, P. P., "Application of Vortex Methods to Coaxial Rotor Wake and Load Calculations in Hover," *Journal of Aircraft*, Vol. 55, No. 1, January 2018, pp. 373–381.

[79] Datta, A., and Chopra, I., "Validation and Understanding of UH-60A Vibratory Loads in Steady Level Flight," *Journal of the American Helicopter Society*, Vol. 49, No. 3, July 2004, pp. 271–287.

[80] Datta, A., Sitaraman, J., Chopra, I., and Baeder, J., "CFD/CSD Prediction of Rotor Vibratory Loads in High Speed Flight," *Journal of Aircraft*, Vol. 43, No. 6, November-December 2006, pp. 1698–1709.

[81] Datta, A., "Fundamental Understanding, Prediction and Validation of Rotor Vibratory Loads in Steady Level Flight," *PhD Thesis*, 2004. University of Maryland.

[82] Jude, D., Sitaraman, J., Lakshminarayan, V., and Baeder, J., "An Overset Generalised Minimal Residual Method for the Multi-solver Paradigm," *International Journal of Computational Fluid Dynamics*, Vol. 34, No. 1, January 2020, pp. 61–74.

[83] Jude, D., and Baeder, J. D., "Extending a Three-Dimensional GPU RANS Solver for Unsteady Grid Motion and Free-Wake Coupling," AIAA SciTech Forum; 54th AIAA Aerospace Sciences Meeting, AIAA, January 4-8 2016, Paper No. 2016-1811, San Diego, CA.

[84] Jude, D., Lee, B., Jung, Y.S., Petermann, J., Govindarajan, B., and Baeder, J. D., "Application of a Heterogeneous CFD Framework Towards Simulating Complete Rotorcraft Configurations," American Helicopter Society 74th Annual Forum, May 2018, Phoenix, AZ.

[85] Lee, B., Jung, Y.S., Jude, D., and Baeder, J. D., "Prediction of Rotor Hub Flow Using Mercury Framework," Vertical Flight Society 75th Annual Forum, Vertical Flight Society International, May 2019, Philadelphia, PA.

[86] Tung, C., Caradonna, F.X., and Johnson, W.R., "The Prediction of Transonic Flows on an Advancing Rotor," *Journal of the American Helicopter Society*, Vol. 31, No. 3, July 1986, pp. 4–9.

[87] Datta, A., and Chopra, I., "Prediction of the UH-60A Main Rotor Structural Loads Using Computational Fluid Dynamics/Comprehensive Analysis Coupling," *Journal of the American Helicopter Society*, Vol. 53, No. 4, October 2008, pp. 351–365.

[88] Potsdam, M., Yeo, H., and Johnson, W., "Rotor Airloads Prediction Using Loose Aerodynamic/Structural Coupling," *Journal of Aircraft*, Vol. 43, No. 3, May-June 2006, pp. 732–742.

[89] Ament, G.A., and Koning, W.J.F., "Isolated Rotor Forward Flight Testing From One Atmosphere Down to Martian Atmospheric Densities," , AHS Technical Conference on Aeromechanics Design for Transformative Vertical Flight, American Helicopter Society, January 2018, San Francisco, CA.

[90] Rieper, F., "A Low-Mach Number Fix for Roe's Approximate Riemann Solver," *Journal of Computational Physics*, Vol. 230, No. 13, June 2011, pp. 5263–5287.

[91] Medida, S., and Baeder, J., "Application of the Correlation-Based $\gamma - \overline{Re_{\theta t}}$ Transition Model to the Spalart-Allmaras Turbulence Model," 20th AIAA Computational Fluid Dynamics Conference, AIAA, June 27 - 30 2011, Paper No. 2011-3979, Honolulu, HI.

[92] Yamauchi, G., and Johnson, W., "Trends of Reynolds Number Effects on Two-Dimensional Airfoil Characteristics for Helicopter Rotor Analyses," Tech. Rep. NASA-TM-84363, April 1983.

[93] McAlister, and Kenneth W., "Rotor Wake Development During the First Revolution," *Journal of the American Helicopter Society*, Vol. 49, No. 4, October 2004, pp. 371–390.

[94] Ho, J., Yeo, H., and Bhagwat, M., "Validation of Rotorcraft Comprehensive Analysis Performance Predictions for Coaxial Rotors in Hover," *Journal of the American Helicopter Society*, Vol. 62, No. 2, April 2016, pp. 1–13.

[95] Wissink, A., Potsdam, M., Jain, R., Leffell, J., Jayaraman, B., Roget, B., Lakshminarayan, V., Sitaraman, J., Bauer, A., and Forsythe, J., "Improvements in the Helios Rotorcraft Simulation Code," AHS 72th Annual Forum, AHS International, May 17-19 2016, West Palm Beach, FL.

[96] Yeo, H., and Potsdam, M., "Rotor Structural Loads Analysis Using Coupled Computational Fluid Dynamics/Computational Structural Dynamics," *Journal of Aircraft*, Vol. 53, No. 1, January-February 2016, pp. 87–105.

[97] Ho, J., Jayaraman, B., and Yeo, H., "Coupled Computational Fluid Dynamics and Comprehensive Analysis Calculations of a Gimballed Tiltrotor," *AIAA Journal*, Vol. 57, No. 10, October 2019, pp. 4433–4446.

[98] Yeo, H., Potsdam, M., "Rotor Structural Loads Analysis Using Coupled Computational Fluid Dynamics/Computational Structural Dynamics," *Journal of Aircraft*, Vol. 53, No. 1, January-February 2016, pp. 87–105.

[99] Roget, B., Sitaraman, J., Wissink, A., Saberi, H., and Chen, W., "Maneuvering Rotorcraft Simulations Using HPCMP CREATE™-AV Helios," AIAA SciTech Forum; 54th AIAA Aerospace Sciences Meeting, AIAA, January 4-8 2016, Paper No. 2016-1057, San Diego, CA.